The Design, Synthesis, and Properties of Strained Alkyne Cycloparaphenylenes

by

Julia M. Fehr

A dissertation accepted and approved in partial fulfillment of the

requirements for the degree of

Doctor of Philosophy

in Chemistry

Dissertation Committee:

Michael D. Pluth, Chair

Ramesh Jasti, Advisor

Darren W. Johnson, Core Member

Raghuveer Parthasarathy, Institutional Representative

University of Oregon

Fall 2023

DISSERTATION ABSTRACT

Julia M. Fehr

Doctor of Philosophy in Chemistry

Title: The Design, Synthesis, and Properties of Strained Alkyne Cycloparaphenylenes

Strained molecules possess the potential energy required to do work in the form of further chemical transformations. Strained alkynes in particular are an attractive handle for such applications as they can undergo the metal-free strain-promoted azide-alkyne cycloaddition (SPAAC). Beyond heightening reactivity, imparting strain also affects other properties, as has been shown in the study of strained conjugated molecules. In this context, strain modulates the electronics of the molecules and typically heightens their conductivity and solubility. These ideas are described in detail in Chapter 1.

This work includes published and unpublished coauthored material that highlights both of these applications by focusing on the design and study of strained alkyne-containing carbon nanohoops (also known as [*n*+1] cycloparaphenylenes or [*n*+1]CPPs). Carbon nanohoops are highly strained conjugated macrocycles composed primarily of *para*-substituted phenylene units. Incorporation of an alkyne into the backbone of these molecules provides a handle for controlled strain-promoted reactivity. Modulating the topology and electronics of [*n*+1]CPPs to in turn alter reactivity towards the SPAAC reaction is the focus of Chapter 2 of this work. Chapter 3 focuses on exploring other types of strain-promoted reactivity, in particular alkyne cyclotrimerization resulting in the formation of pinwheel-shaped large molecules. Finally, early efforts to modulate the emission color of a [*n*+1]CPP, to synthesize a thermally-activated delayed fluorescence nanohoop, and to synthesize a di-alkyne carbon nanohoop are described in Chapter 4.

ACKNOWLEDGMENTS

I would first like to thank my advisor, Professor Ramesh Jasti, for being a mentor of the highest caliber over the course of my Ph.D. From the very beginning, it has been an honor and a privilege to be a part of the Jasti Lab. Ramesh has made me feel empowered, valued, and welcomed every step of the journey, and those are feelings that will always stick with me, and leadership qualities I will strive to embody as I move forward in my career.

I would next like to thank my lab mates—Dr. Tavis Price, Dr. James May, Tara Clayton, Harrison Reid, Veronica Spaulding, Gabriela Bailey, Lan Chen, Vi Baird, Victor Salpino, and our gone-but-not-forgotten visiting students Viktor Pedersen and Masafumi Sugiyama. There are no better friends than you all, and it's been nothing but a joy to work with you every day. Thank you from the bottom of my heart for your support and friendship over the years, it really has meant the world to me.

I would also like to thank my previous lab mates and mentors Dr. Tobias Schaub, Dr. Jeff Van Raden, Dr. Curtis Colwell, Dr. Terri Lovell, Dr. Erik Leonhardt, Dr. Ruth Maust, and Dr. Claire Otteson, my rotation mentors Dr. Matthew Cerda, Dr. Ngoc-Minh Phan, and Dr. Sean Fontenot, my mentors at UNC, Dr. Catherine McKenas and Prof. Matthew Lockett, and finally all the Jasti Lab alumni I did not cross paths with but whose research laid the foundations for the hoopsters of today. You all are an inspiration, and I am forever in your debt for the chemistry and life skills that you taught me.

Next, I want to thank the chemistry department staff for their unending help and patience with me as I navigated the world of graduate school. I would like to give a special shout-out to Christi Mabinuori, Janet Macha Kneller, Kathy Noakes, Leah O'Brien, Amy Lane, and Jim Rasmussen for their help in keeping me on track with graduate school, making sure deadlines were met, scheduling endless office hours and committee meetings for me, helping me figure out conference travel, and assisting me with chemical ordering.

Thank you to my committee: my committee chair Prof. Michael Pluth, core member Prof. Darren Johnson, and outside member Prof. Raghuveer Parthasarathy. I am especially indebted to Profs. Pluth and Johnson for excellent experiences in their labs as a rotation student, and again to Darren for hosting me during my summer REU experience which ultimately led me to choose UO for graduate school.

I would also like to thank the Haley Lab, past and present: Prof. Michael Haley, Dr. Jeremy Bard, Dr. Chun-lin Deng, Dr. Justin Dressler, Dr. Joshua Barker, Dr. Gabrielle Warren, Nolan McNeill, Efrain Vidal, Bella Demachkie, Michael Miller, Megan Rammer, and Nathan Boone. It has been an absolute blast to spend every group meeting, departmental event, and conference with you all. Special thanks to Prof. Haley who has taught me much about organic chemistry as well as how to convey science clearly and effectively. Also special thanks to Dr. Gabrielle Warren, who has been a truly excellent friend since my very first day of graduate school.

Finally I would like to thank my family. My dad, Fred, who has encouraged me and supported me every step of the way. My mom, Robin, who is my greatest supporter, biggest inspiration, and best friend in the world. My brother Alex and sister-in-law Jessica, who are always there to cheer me up when I'm feeling down. Finally, our beloved dogs, Leo and Smush, for their unconditional love.

DEDICATION

Dedicated to all the women in science who came before and forged a path.

TABLE OF CONTENTS

Chapter Page

LIST OF FIGURES

Figure Page

Figure Page

LIST OF TABLES

LIST OF SCHEMES

CHAPTER 1

INTRODUCTION

This chapter was written by myself with editorial assistance from Professor Ramesh Jasti.

1.1 Alkynes in Click Chemistry

The term *click chemistry* was coined by Sharpless and coworkers in 2001 to describe particularly high performing chemical transformations.[1] These *click reactions* are generally expected to have several qualities including: (1) high selectivity, (2) high yield, (3) no byproducts or easily removed byproducts, (4) straightforward product isolation, and (5) wide scope. In 2002, a crucial step forward in click chemistry was made by the independent development of the copper-catalyzed azide-alkyne cycloaddition (CuAAC) by the research groups of Meldal and Sharpless.[2,3] The uncatalyzed version of this reaction between a terminal alkyne and an azide to form a triazole product was first developed by Huisgen in the 1950s;[4,5] however, Huisgen's version of the reaction was thermally driven, occurring only at high temperatures and resulting in approximately 1:1 regioselectivity between the 1,4 and 1,5 isomers. In contrast, the CuAAC is a simple and modular reaction that exhibits regiospecificity towards the 1,4 isomer and proceeds in high yields with few—if any—byproducts.[6]

The CuAAC remains an important click reaction that has seen widespread use since its introduction due to its robustness and efficiency.[6] However, it does have limitations—namely, a tendency for the Cu (I) catalyst to become oxidized (usually necessitating the addition of a reducing agent such as sodium ascorbate to the reaction mixture) and the toxicity of copper, which makes the CuAAC unsuitable for *in vivo* biological studies.[3,6,7]

In 2004, an alternative to the CuAAC arose which, instead of a metal catalyst, employed strain to drive the reaction forward.[7] While the strain-promoted azide alkyne cycloaddition (SPAAC) had been known since at least the 1950s, Bertozzi and coworkers were the first to utilize it in the context of click chemistry. The strained alkyne scaffold used in the Bertozzi group for this initial publication was cyclooctyne—an eight-carbon ring containing one alkyne moiety. Generalized versions of the CuAAC and SPAAC are shown in **Scheme 1.1**.

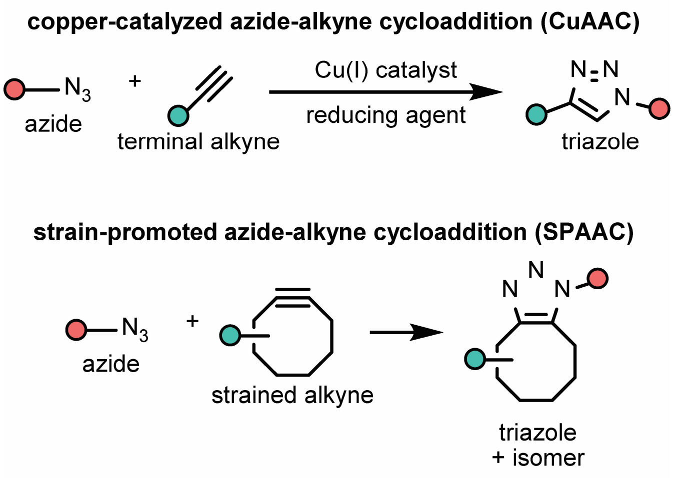

Scheme 1.1. Comparison of the copper-catalyzed azide-alkyne cycloaddition (CuAAC) and the metal-free strain-promoted azide-alkyne cycloaddition (SPAAC).

1.2 Bioorthogonal Chemistry

In the Bertozzi group's initial 2004 publication, they showcased that a cyclooctyne-functionalized probe reacted efficiently with azide-labeled biomolecules both *in vitro* and *in vivo* (see **Scheme 1.2**).[7] In 2007, the same group synthesized another cyclooctyne derivative with enhanced SPAAC kinetics (*vide infra*) covalently linked to a fluorophore.[8] Live cells were treated with azidosugars which resulted in incorporation of azide groups onto cell surface glycans; treatment of these cells with the cyclooctyne-containing fluorophore allowed for the fluorescent labeling of cell surface glycans and the visualization of glycan trafficking through time-lapse imaging.

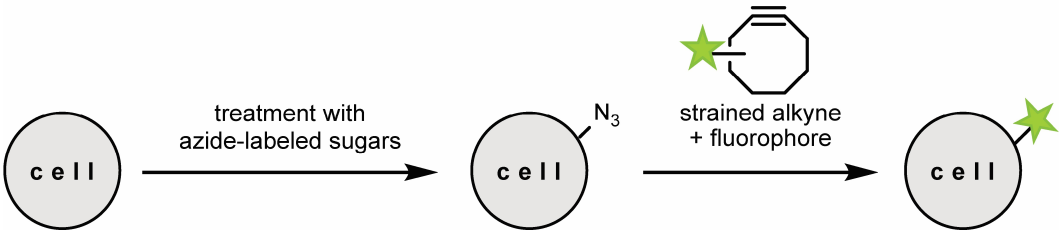

Scheme 1.2. Simplified workflow for the bioorthogonal labeling of azidoglycans on cell surfaces with a cyclooctyne-functionalized fluorophore.

This powerful new method for fluorescent labeling of biomolecules had several advantages over green fluorescent protein (GFP) incorporation, which was the method typically used at the time.[9] It was generally simpler to execute and could be adapted to any biomolecule and probe that could be functionalized with azide and cyclooctyne moieties. This idea of using click chemistry in biological systems became known as *bioorthogonal chemistry*.[10] Like click chemistry, a bioorthogonal reaction must adhere to specific criteria such as: (1) fast kinetics to avoid removal of the probe by the cell prior to the reaction occurring, (2) high selectivity and stability to avoid side reactivity with the native biological environment, (3) high yields, and (4) the bioorthogonal reagents and the reaction product must not disrupt the native functions of the targets.[11] Since the early 2000s, much research effort has been focused on the development of new bioorthogonal reactions and their implementation in the field of biological imaging. In 2022, Bertozzi was awarded the Nobel Prize in Chemistry (alongside Meldal and Sharpless) for her contributions to the field of click chemistry.[12]

1.3 The Distortion-Interaction Model

The enhancement of cyclooctyne reaction kinetics has been a topic of significant interest since the Bertozzi group's first use of the moiety in 2004.[7] Fast reaction rates will ensure that the target is sufficiently labeled before the probe is cleared by the organism.[13] By utilizing the concepts of physical organic chemistry, more reactive versions of the cyclooctyne handle (as well as many other moieties) can be designed, then synthesized *via* synthetic organic chemistry.

The distortion-interaction model, developed independently by Houk and Bickelhaupt, provides an excellent framework for understanding the factors which determine the kinetics of many reactions, including SPAAC.[14–16] The distortion-interaction model is best understood in terms of a reaction coordinate diagram (**Figure 1.1**). For a straightforward reaction under kinetic control, the height of the activation barrier (*i.e.* the $\Delta E^{\ddagger}_{\text{actinvation}}$, which is the difference in energy level between the ground state reagents and the transition state) will dictate the rate constant for the reaction. The distortion-interaction model proposes that the magnitude of $\Delta E^{\ddagger}_{\text{activation}}$ is composed of two terms: $\Delta E^{\ddagger}_{\text{distortion}}$ and $\Delta E^{\ddagger}_{\text{interaction}}$. $\Delta E^{\ddagger}_{\text{distortion}}$ represents the energy *input* required to distort/bend the reactants from their ground state to transition state geometries. $\Delta E^{\ddagger}_{\text{interaction}}$ describes the stabilizing interactions between the frontier molecular orbitals involved in the reaction at the transition state (*e.g.* the interaction of an electron-rich highest occupied molecular orbital, or HOMO, with an electron-poor lowest unoccupied molecular orbital, or LUMO). Summing together the positive energy term $\Delta E^{\ddagger}_{\text{distortion}}$, which destabilizes the transition state and increases its energy, with the negative energy term $\Delta E^{\ddagger}_{\text{interaction}}$, which lowers and stabilizes the energy of the transition state, provides the overall $\Delta E^{\ddagger}_{\text{activation}}$. Therefore, minimizing $\Delta E^{\ddagger}_{\text{distortion}}$ and maximizing $\Delta E^{\ddagger}_{\text{interaction}}$ will lead to the lowest $\Delta E^{\ddagger}_{\text{activation}}$, which will in turn lead to the fastest rate of reaction.

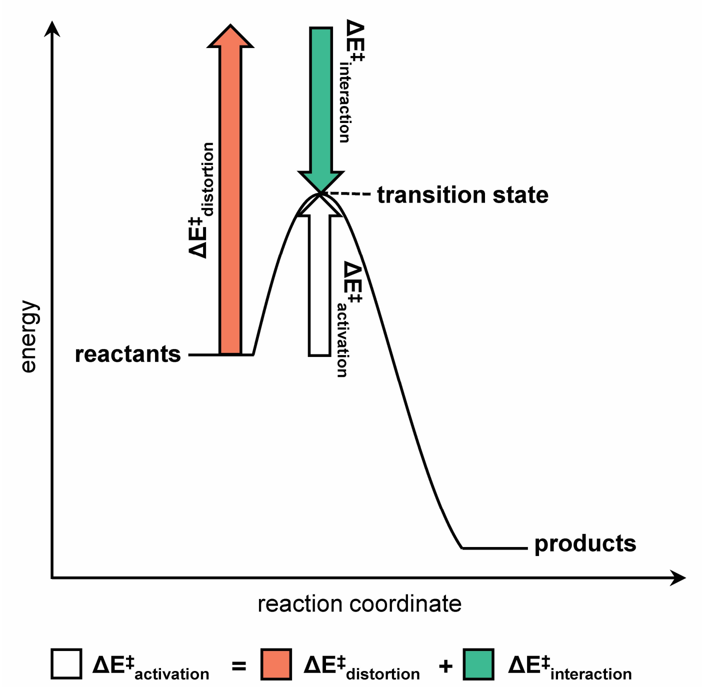

Figure 1.1. Distortion-interaction model for exothermic, kinetically controlled reactions.

1.4 Modifications to the Cyclooctyne Scaffold

Many variations of cyclooctyne have now been developed for use in the SPAAC reaction as well as other cycloadditions (**Figure 1.2**).[17] In the context of the distortion-interaction model, modifications to the *strain* of the cyclooctyne scaffold can be thought to decrease the $\Delta E^{\ddagger}_{\text{distortion}}$ term by pre-distorting the ground state geometry of the alkyne reactant such that less energy input will be required to bend it into its transition state geometry. Modifications to the *electronics* of the cyclooctyne, upon which the LUMO is normally situated, generally pull electron density away from the alkyne to enhance orbital interactions with the HOMO on the electron-rich azide and therefore increase the magnitude of $\Delta E^{\ddagger}_{\text{interaction}}$.[16,17]

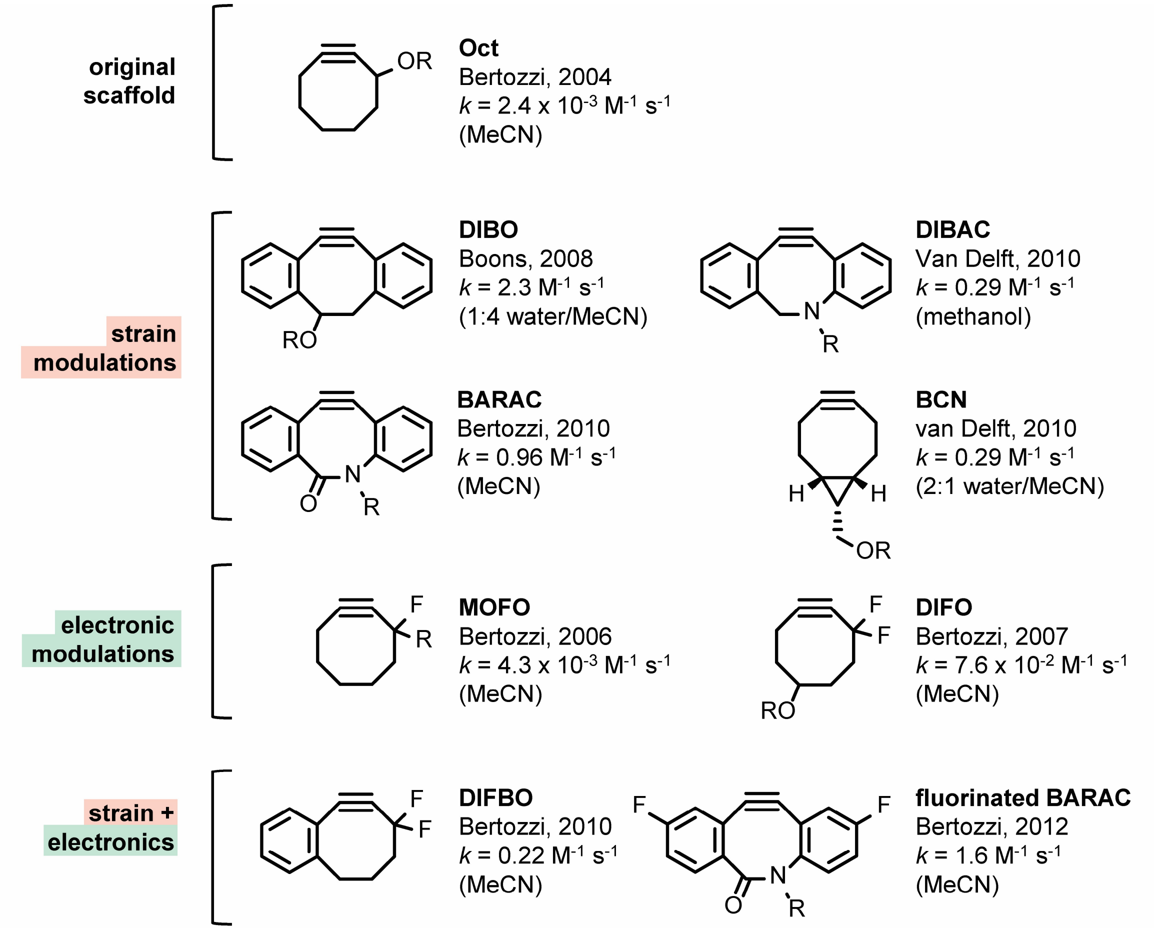

Figure 1.2. Variations of the cyclooctyne scaffold studied since 2004. *k* refers to the second-order rate constant for the SPAAC reaction with an azide; the solvent used for the measurement is written in parentheses.

A common strategy for modulating the strain of the cyclooctyne scaffold is to increase its number of sp^2 hybridized carbons, thereby rigidifying the molecule and locking it into a more strained conformation. Boons and coworkers were the first to employ this strategy with the synthesis of cyclooctyne derivative DIBO, which possessed two benzene units fused close to the alkyne moiety.[18] Van Delft and coworkers employed a similar strategy in the synthesis of DIBAC, with the addition of an sp^3 hybridized N center which aided in future functionalization of the scaffold (*e.g.* sulfonation to enhance aqueous solubility).[19] The Bertozzi group took this strategy a step further with the synthesis of BARAC, which adds another sp^2 hybridized center in the form of an amide group to the cyclooctyne scaffold.[20] In all of these cases, significant rate enhancement was observed over the unfunctionalized cyclooctyne system.

In these benzo-fused examples, it has been noted that the "flagpole" hydrogens of the benzene rings located *ortho* to the alkyne may introduce some steric interference between the alkyne and other reactive species.[13,21] Theoretical studies suggest that the A-1,3 strain introduced by the interaction of the flagpole hydrogens with the alkyne could diminish SPAAC reactivity.[21] An interesting and synthetically straightforward strategy for enhancing strain without benzo-fusion was introduced by van Delft et al. with the synthesis of their cyclooctyne derivative BCN.[22] This bicyclo-[6.1.0]nonyne analogue essentially involves the fusion of a cyclopropane ring on cyclooctyne directly across from the alkyne. Van Delft and coworkers measured an impressive near 100-fold increase in reactivity compared to Oct through this simple but effective strategy.

Electronic modulations to cyclooctyne have also received much attention. The first of such molecules, dubbed MOFO, was synthesized by Bertozzi and coworkers in 2006.[23] In MOFO, a single fluorine atom was appended to the cyclooctyne scaffold on the carbon directly adjacent to the alkyne moiety which led to a modest increase in SPAAC kinetics in comparison to the original Oct reagent.[23] This result was followed up in 2007 by the introduction of DIFO, another molecule synthesized by the Bertozzi group which featured two fluorine atoms at the same position and led to a noted increase in SPAAC rate constant.[8]

Efforts to combine both electronic and strain modulations into one cyclooctyne derivative have seen mixed success. For example, DIFBO, first described by the Bertozzi group in 2010, united difluorination adjacent to the alkyne with the fusion of a single benzene unit on the opposite side of the scaffold.[24] While these modifications did significantly enhance the rate of SPAAC reaction, they rendered the molecule unstable, and it was prone to spontaneous alkyne cyclotrimerization at the final reaction step. As such, the alkyne could not be readily isolated, and only *in situ* trapping of the SPAAC product by the addition of benzyl azide to the final alkyne formation step was possible. In a 2012 publication, the Bertozzi group showed that fluorination of benzo-fused BARAC *meta* to the alkyne modestly increased the SPAAC reaction kinetics.[25]

1.5 Strained Carbon Nanomaterials

In the above examples, strain has been incorporated into a molecule's architecture in order to predispose it towards certain reactivity; however, there are other motivations for incorporating strain into molecules. In the realm of conjugated carbon nanomaterials, imparting strain by bending otherwise flat aromatic/conjugated units has several advantages. Firstly, bending the p orbitals of the conjugated material out of alignment forces the p orbitals to overlap less efficiently, weakening the pi bonds of the molecule, which in turn increases the energy of the HOMO and lowers the energy of the LUMO. A narrow HOMO-LUMO gap is advantageous for many applications in organic electronics.[26] Secondly, imparting curvature tends to heighten the solubility of the molecule limiting self-stacking.[27] Additionally, imparting curvature can make other intermolecular interactions, such as convex-concave π-π interactions, more efficient which is significant for a range of host-guest applications.[28]

The strained alkyne moiety is present in several types of macrocyclic strained carbon nanomaterials (**Figure 1.3**). In 1996, Kawase and Oda published the syntheses of fully conjugated hoops of alternating phenylene and acetylene units which they dubbed cyclic [*n*]paraphenyleneacetylenes or [*n*]CPPAs.[29] The molecules synthesized in this study, [6]CPPA and [8]CPPA, were fluorescent with modest quantum yields but fairly unstable. The authors reported that the most strained of the two macrocycles, [6]CPPA, would "explosively" decomposed if heated to 80 °C in the presence of air, while [8]CPPA underwent decomposition at 120 °C.

Further investigation of [*n*]CPPAs has been undertaken by the research groups of Moore and Lee. In 2016, Moore et al. reported the synthesis of [3]CPP^{3}A *via* a high-yielding molybdenum-catalyzed alkyne methathesis route of bent three-ring precursors and subsequent reductive aromatization.[30] While the compound was unstable under ambient conditions, [3]CPP^{3}A was shown to co-crystalize effectively with C_{70}, and was capable of undergoing a SPAAC reaction with azides at each alkyne site. Following the same alkyne metathesis strategy with alternative four- and five-ring bent precursors, Lee *et al.* presented the syntheses of [3]CPP^{4}A and [3]CPP^{5}A (shown to be particularly stable due to its much larger size) in a 2019 follow-up publication.[31] Finally, a 2021 publication from Lee et al. described the synthesis of [8]CPPA-Me^8, an iteration of the macrocycle decorated with methyl units situated *ortho* to alternating alkynes, via a *cis*-stilbene-based precursor to alkyne metathesis.[32] Bromination, then treatment with strong base for dehydrobromination resulted in high yields (80% over two steps) of the final target compound. Unfortunately, [8]CPPA-Me^8 was unstable to air, and thus the final reaction and workup was performed in the glovebox under nitrogen atmosphere.

Hoops composed exclusively of sp hybridized carbons, referred to as "cyclo[*n*]carbons," have invoked serious interest from chemists in the past several decades. In the 1980s and 1990s, Diederich and others explored the synthesis of cyclocarbon precursors that could then be "unmasked" to form a cyclocarbon through various methods (*e.g.* heating, UV light).[33] Mass spectroscopy evidence indicated that cyclo[18]carbon had been successfully formed from the demasking of a bridged-ethenoanthracene *via* a retro-Diels-Alder reaction initiated by flash vacuum pyrolysis.[34] Definitive characterization of cyclo[18]carbon through a combination of atomic force microscopy (AFM) and scanning tunneling microscopy (STM) was finally achieved in 2019 by Anderson *et al.*[35] At the very low temperature of 5 K, Decarbonylation of a cyclocarbon oxide—sublimed on a NaCl/Cu(III) bilayer—was induced with the STM-AFM tip to produce the cyclocarbon.

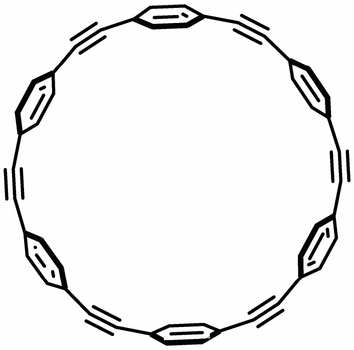

[6]CPPA
Kawase + Oda, 1996

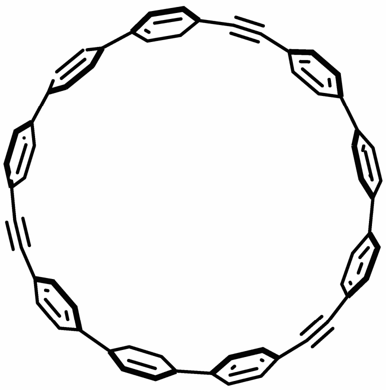

[3]CPP^{3}A
Lee + Moore, 2016

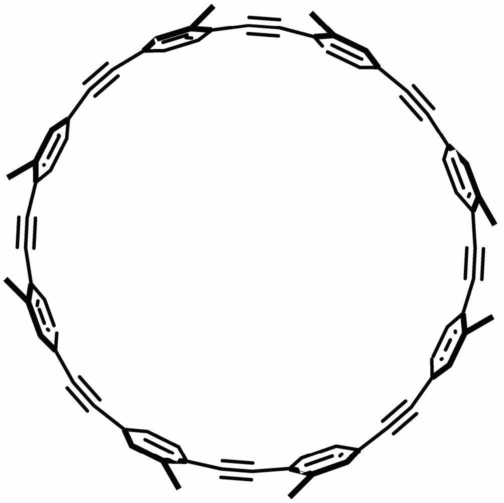

[8]CPPA-Me$_8$
Lee, 2021

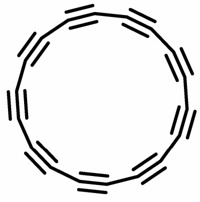

cyclo[18]carbon
Diederich (detected), 1989
Anderson (characterized), 2019

Figure 1.3. Examples of strained alkynes incorporated into carbon-based conjugated macrocycles.

1.6 Cycloparaphenylenes

The advantages of bending aromatic units in carbon nanomaterials is perhaps best exemplified by the popularity of carbon nanotubes[36] and fullerenes[37] over the past several decades. Carbon nanotube in particular have received much attention; these molecules can have a wide range of photophysical and electronic properties which are dictated by the helicity and diameter of the nanotube, amongst other factors.[38] Historically, however, carbon nanotubes have been difficult to both synthesize in a selective manner and isolate from a mixture resulting from a nonselective synthesis.[38]

Cycloparaphenylenes (**Figure 1.4**, also referred to as carbon nanohoops or [*n*]CPPs) represent the shortest cross-section of an armchair carbon nanotube. As such, they offer in some ways a much more synthetically accessible alternative to carbon nanotubes which can be selectively made *via* bottom-up organic synthesis. The first synthesis of [*n*]CPPs was accomplished by Jasti, Bertozzi, and coworkers in 2008.[39] Since this time, interest in carbon nanohoops has grown considerably due not only to their link with carbon nanotubes but also due to their own unique properties.[40]

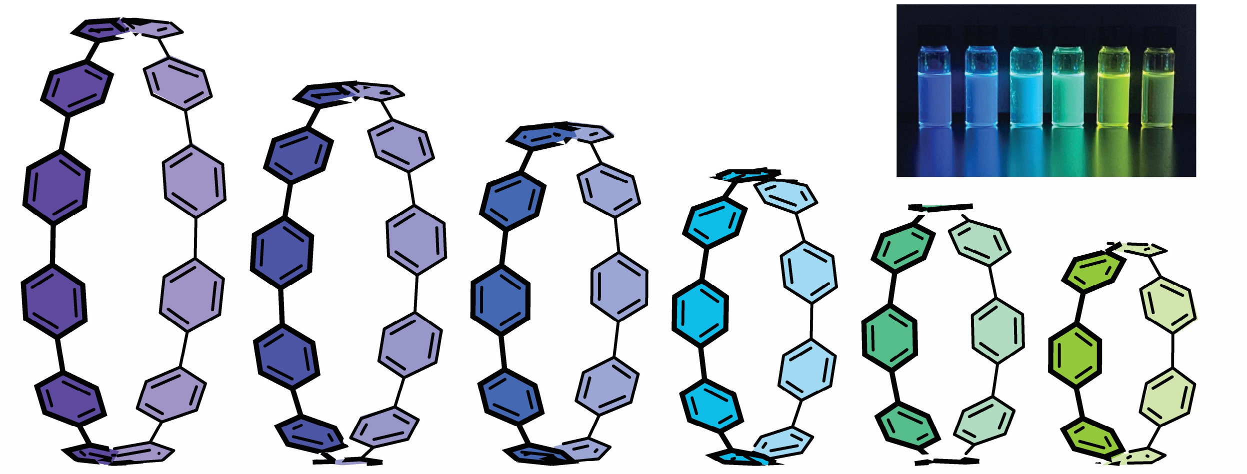

[12]CPP **[11]CPP** **[10]CPP** **[9]CPP** **[8]CPP** **[7]CPP**

Figure 1.4. *Para*-linked [12] through [7]CPP. Inset shows the fluorescence of these [*n*]CPPs upon illumination with 365 nm light.

Many variations of the all-hydrocarbon, fully *para*-linked [*n*]CPP scaffold have now been synthesized; examples include nanohoops incorporating heteroatoms and/or heterocycles,[41–47] as well as various topologies such as *meta*-linked nanohoops,[48] rotaxanes,[28,49–51] and catenanes.[52,53]

Focusing solely on the all-hydrocarbon, *para*-linked versions of the nanohoop scaffold, however, illuminates a few trends crucial for understanding carbon nanohoop chemistry.[54] Firstly, strain increases as the number of phenylene units in the molecule (*i.e.* the diameter), denoted by [*n*], decreases (**Figure 1.5**). Secondly, [*n*]CPPs generally have a narrowing HOMO-LUMO gap as the number of phenylene units decreases.[54] This is because smaller diameter nanohoops tend to have smaller dihedral angles between phenylenes, which heightens conjugation. This in turn results in a red-shifting of nanohoop fluorescence emission (**Figure 1.6**) as the diameter of the molecule decreases, as the energy of the emission is closely related to the energy of the HOMO-LUMO gap. Finally, most carbon nanohoops have an absorbance maxima at approximately 340 nm (**Figure 1.6**).[54] This is due to the fact that the absorbance depends not on the energy of the HOMO to LUMO transition (which is formally Laporte forbidden), but on a combination of allowed transitions between HOMO–1 to LUMO, HOMO–2 to LUMO, HOMO to LUMO+1, and HOMO to LUMO+2 which are all of approximately the same energy regardless of the identity of the nanohoop.[55]

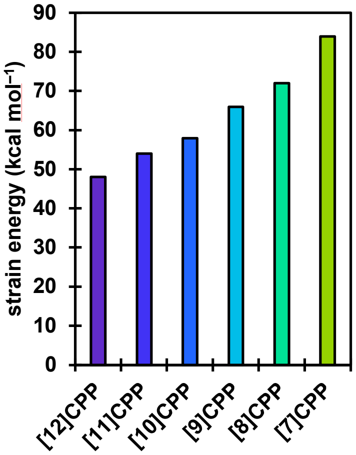

Figure 1.5. Strain energy (kcal mol^{-1}) as a function of [*n*]CPP size.

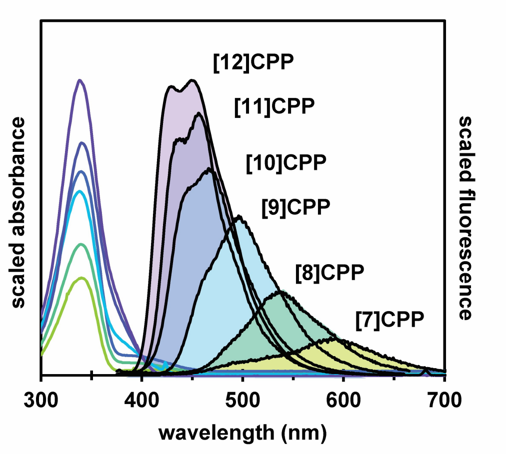

Figure 1.6. Absorbance (colored lines) and fluorescence (filled peaks) traces of [*n*]CPPs measured in dichloromethane (DCM).

1.7 Strained Alkyne Carbon Nanohoops

In 2018, Schaub, Jasti, and coworkers published the first iteration of the [*n*+1]CPP family of carbon nanohoops (**Figure 1.7**).[56] These molecules contain a strained alkyne moiety ("+1") incorporated directly into the carbon backbone of the nanohoop. This allows [*n*+1]CPPs to undergo strain-promoted reactions, including [2+2] cycloaddition-retrocyclization and the SPAAC reaction. In this initial publication, three sizes of [*n*+1]CPP were synthesized: [7+1]CPP, [9+1]CPP, and [11+1]CPP. The alkyne-containing nanohoops were shown to have strain-dependent reactivity towards reaction with tetracyanoethylene; [7+1]CPP reacted quickly at low temperatures while the least strained [11+1]CPP required more forcing conditions. The authors also demonstrated that typical carbon nanohoop properties, such as common absorption maxima at 340 nm and red-shifting emission with decreasing hoop diameter, were maintained even with the addition of the strained alkyne to the scaffold.

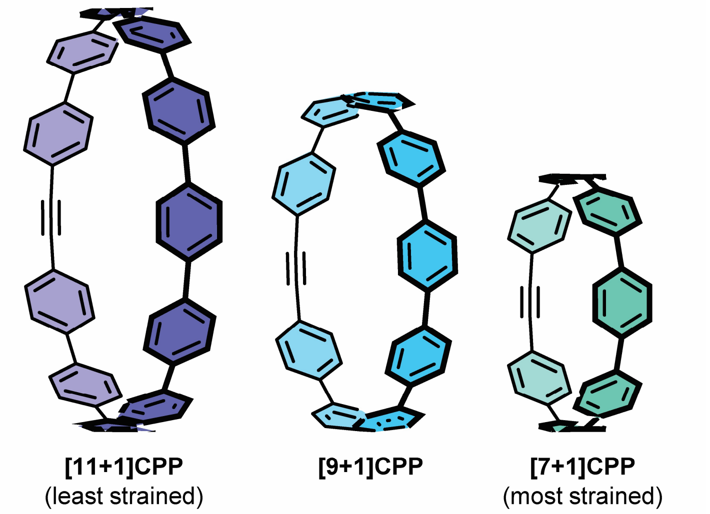

Figure 1.7. Strained alkyne-containing [*n*+1]CPPs initially published in 2018.

This initial publication demonstrated that the [*n*+1]CPP scaffold combines a tunable new SPAAC reagent with the unique photophysical properties of carbon nanohoops.[56] As evidenced by the variety of carbon nanohoops that have been synthesized to date, these molecules have highly modular syntheses. As such, we focused our attention on modulating the [*n*+1]CPP scaffold to systematically tune the kinetics of the SPAAC reaction and expand the chemical space of this new subset of nanohoops. Chapter II describes an in-depth study describing the synthesis of new [*n*+1]CPPs and thorough characterization of their SPAAC kinetics, photophysics, and general reactivity. Chapter III describes the cyclotrimerization of [*n*+1]CPPs at the alkyne moiety: a new strategy to synthesize large carbon nanostructures *via* this functional group. Chapter IV describes the synthesis and initial characterization of strained alkyne carbon nanohoops with unique features—namely an electron-accepting heterocycle and an additional strained alkyne moiety.

1.8 Bridge to Chapter II

This first chapter begins with a broad overview of the two key topics addressed in this dissertation—namely, strained alkynes and carbon nanohoops. It then narrows its focus to describe previous work done published in 2018 by Schaub *et al.* to unite these two topics into one type of molecule called [*n*+1]CPPs. Chapter II is a continuation of this area of study, with a special emphasis on the synthesis of new [*n*+1]CPPs, and an in-depth study of their reactivity and photophysical properties.

CHAPTER II

EXPERIMENTAL AND THEORETICAL ELUCIDATION OF SPAAC KINETICS FOR STRAINED ALKYNE-CONTAINING CYCLOPARAPHENYLENES

Chapter II is adapted from a study published in *Chemical Science* entitled "Experimental and Theoretical Elucidation of SPAAC Kinetics for Strained Alkyne-Containing Cycloparaphenylenes." Synthesis of the molecules described herein was performed by myself and Anna Garrison. Characterization, photophysical measurements, and kinetics experiments were carried out by myself. StrainViz calculations were performed by Tavis Price. All other calculations were performed by Dr. Nathalie Myrthil and Prof. Steven Lopez. The manuscript was written primarily by myself with contributions from Dr. Nathalie Myrthil, Tavis Price, and Prof. Steven Lopez. Editorial assistance was provided by Prof. Steven Lopez and Prof. Ramesh Jasti. Prof. Ramesh Jasti provided guidance on the project.

2.1 Introduction

Sharpless highlighted the challenge of covalently bonding two molecules as efficiently and selectively as possible by introducing the 'click chemistry' concept in 2001.[1] In 2002, the concurrent reports by the research groups of Sharpless and Meldal on the copper-catalyzed azide-alkyne cycloaddition (CuAAC) showcased 1,3-dipolar cycloadditions as an ideal way to address this challenge.[2,3] Since those early days, much scientific effort has been focused on optimizing click reactions with increased rate constants, selectivities, and scope. Building upon the CuAAC is the related strain-promoted azide-alkyne cycloaddition (SPAAC) from Bertozzi and coworkers, which accomplishes the same transformation as CuAAC without the need for a Cu(I) catalyst by using a strained alkyne with non-linear bond angles.[7] The most common alkyne scaffold for SPAAC, cyclooctyne (**Figure 2.1a**), has continued to interest chemical biology and materials science researchers striving to increase cycloaddition rate constants and selectivities.[7,8,57,22]

Strained alkynes have not been limited to their applications in click chemistry; they possess a rich history in the field of carbon nanomaterials (**Figure 2.1b**). In this context, strained alkynes can be found within radially π-conjugated macrocycles. For instance, the elusive 'all-carbon' molecules, dubbed cyclo[*n*]carbons, have been the subject of much scientific interest. Diederich and coworkers first observed cyclo[18]carbon by time-of-flight mass spectrometry after laser flash heating of annulene precursors in 1989.[34] More recently, in 2019, Anderson and coworkers observed cyclo[18]carbon on a NaCl-surface using high-resolution atomic force microscopy.[35] [*n*]Cycloparaphenyleneacetylenes ([*n*]CPPAs), comprised of alternating C-C triple bonds and phenylene units, are also intriguing cyclic structures that were first synthesized by Oda and coworkers in 1996.[29] From their onset, [*n*]CPPAs have been shown to be notably unstable, with Oda noting that [6]CPPA "explosively decomposed at about 80 °C." Recent work by Moore and Lee has introduced several different sizes and variations of the CPPA scaffold, including [3]CPP^{3}A which can successfully undergo a triple SPAAC reaction with three equivalents of an azido-compound.[30–32] Clearly, [*n*]CPPAs possess very interesting reactivity but some are relegated to the glovebox due to their low stability.[30,32]

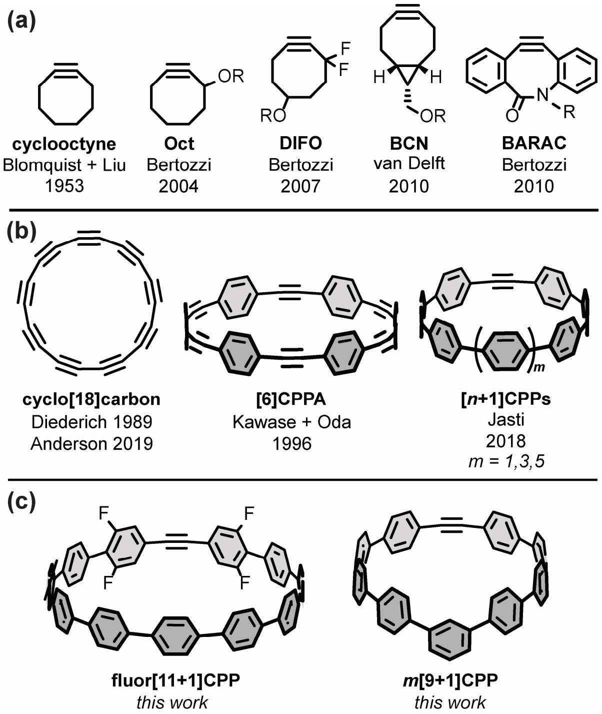

Figure 2.1. (a) Examples of strained alkynes developed for copper-free click chemistry. (b) Strained alkynes in the field of carbon nanomaterials. (c) New strained alkyne-containing [*n*+1]CPPs described in this work.

Our group has historically focused on a related, but generally more stable type of carbon nanomaterial: the cycloparaphenylene ([*n*]CPP) or carbon nanohoop.[39] These molecules possess a radially-oriented π-system which allows for increased solubility in organic solvents, unique photophysical properties (including bright fluorescence for most carbon nanohoops), tunable frontier molecular orbitals (FMOs), and host-guest capabilities (e.g. complexation with C_{60}).[54] In 2018, we introduced a new subclass of carbon nanohoops containing a single strained alkyne within the carbon backbone.[56] We refer to these structures as [*n*+1]CPPs, where the *n* denotes the number of phenylene units in the molecule "+1" alkyne moiety (**Figure 2.1b**). In that initial publication, we detailed the synthesis of three molecules—**[7+1]CPP**, **[9+1]CPP**, and **[11+1]CPP**—and demonstrated that these molecules (a) can undergo strain-promoted cycloadditions at the alkyne, (b) possess size-dependent (i.e. strain-dependent) levels of reactivity, and (c) maintain the photophysical properties typical of cycloparaphenylenes, including a common absorbance maximum, high molar absorptivities, bright fluorescence, and a size-dependent emission maximum. However, while **[9+1]CPP** and **[11+1]CPP** possessed good stability, **[7+1]CPP** was found to decompose quickly under ambient conditions.

Nonetheless, we were excited by the idea of a new strained alkyne scaffold that offered the radially-conjugated π-system of cyclic carbon nanomaterials, the synthetic manipulability of the well-studied cyclooctyne, and reasonable stability. Herein, we describe our efforts to (a) tune the reactivity of the [*n*+1]CPP scaffold *via* organic synthesis, (b) fully characterize the photophysical properties of these molecules, (c) quantify the rate constants for each described [*n*+1]CPP in the SPAAC reaction with benzyl azide, and (d) computationally illustrate the origin of these effects. In this work, we studied previously reported **[9+1]CPP** and **[11+1]CPP** as well as two new [*n*+1]CPPs: ***m*[9+1]CPP** and **fluor[11+1]CPP** (**Figure 2.1c**). In both cases, we observed heightened reactivity relative to the parent [*n*+1]CPPs which can be explained with quantum mechanical calculations provided by Lopez and coworkers. Our ultimate aim in this study is to understand the structural perturbations that can lead to increased reactivity for this new strained alkyne scaffold.

2.2 Results and Discussion

2.2.1 Synthesis of Strained Alkyne-Containing Cycloparaphenylenes

As we set out to expand our library of [*n*+1]CPPs, we focused on developing a modular synthesis. To do this, we centered the synthesis on five key molecules that could be Suzuki cross-coupled in different combinations to yield unique macrocyclic intermediates (the synthesis of two of these molecules—**II.1** and **II.2**—is described in **Scheme 2.1**). These coupling partners can be separated into two groups: (a) alkyne-containing molecules which are fluorinated or nonfluorinated (**II.1** and **II.3**, white in **Scheme 2.2**), and (b) boronic esters which will dictate the size and connectivity (**II.2**, **II.4**, and **II.5**, all *para* or singularly *meta*) of the final structure (shown in color in **Scheme 2.2**). Most of these coupling partners possess cyclohexadiene units; we refer to these as 'masked benzenes' as their sp^3-hybridized carbons help to impart curvature to the molecule. After assembly of the initial macrocyclic intermediate, these cyclohexadiene units can be reductively aromatized to form the final strained [*n*+1]CPP.

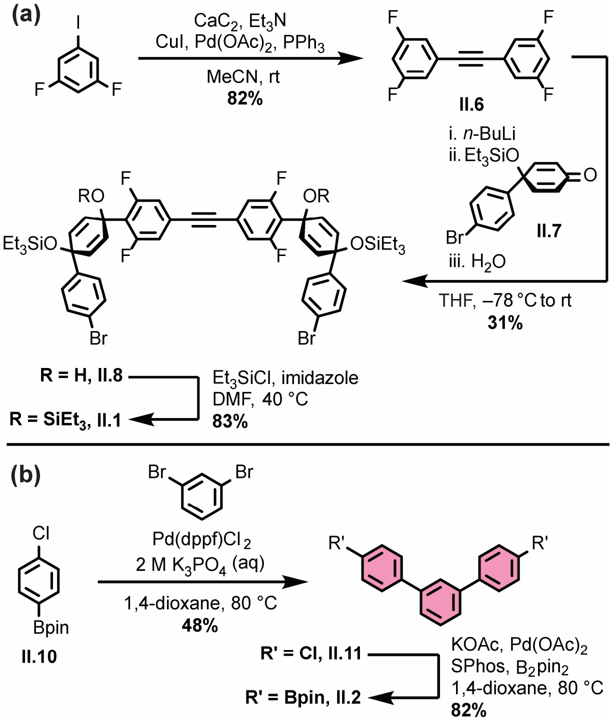

Scheme 2.1. (a) Synthesis of coupling partner **II.1**. (b) Synthesis of coupling partner **II.2**.

For completeness, **Scheme 2.2** also summarizes the synthesis of previously reported **[9+1]CPP** and **[11+1]CPP**. Readers are directed to our previous publication for full characterization of those molecules as well as the coupling partners utilized in their synthesis: **II.3**, **II.4**, and **II.5**.[56]

The first [*n*+1]CPP of interest, **fluor[11+1]CPP**, was inspired by the classic fluorinated cyclooctyne structure DIFO, which increases SPAAC rate constants *via* electronic modulations to the scaffold.[8] In the synthesis of **fluor[11+1]CPP**, we first focused our attention on the building block **II.1**, a fluorinated version of **II.3**. The synthesis (detailed in **Scheme 2.1**) began with a Sonogashira cross-coupling reaction between two equivalents of 1,3-difluoro-5-iodobenzene and acetylene (as the alkyne source) produced *in-situ* from water and calcium carbide.[56] The resulting alkyne-containing compound **II.6** underwent double deprotonation with *n*-BuLi at the *para* position relative to the alkyne, followed by nucleophilic addition into two equivalents of ketone **II.7**[58] and aqueous workup to yield precursor **II.8**. Subsequent silyl protection resulted in the desired coupling partner **II.1**. With this compound in hand, we could form the desired macrocycle, **II.9** (**Scheme 2.2**). Coupling of **II.1** with **II.5** (described previously) under Suzuki-Miyaura cross-coupling conditions furnished macrocycle **II.9** in 37% yield. Having formed the necessary carbon-carbon bonds to build the macrocycle, the final steps in the synthesis were to deprotect the silyl ethers and finally fully aromatize the molecule. Silyl ether deprotection with tetrabutylammonium fluoride (TBAF) was performed in the presence of acetic acid which resulted in conversion to the alcohol-containing macrocycle. Tin-mediated reductive aromatization of the crude product yielded **fluor[11+1]CPP** in 41% yield over two steps.

The second [*n*+1]CPP of interest, ***m*[9+1]CPP**, was inspired by StrainViz, a computational tool developed by our group to visualize local strain in molecules, and our previous study of the synthesis and properties of meta-linked [*n*]CPPs.[48,59] StrainViz analysis has shown that [*n*]CPPs with a *meta*-linked phenylene are most strained in the region directly across from this linkage.[59] We applied these findings in our design of ***m*[9+1]CPP**, which should possess greater strain around the alkyne than the all-*para* linked parent molecule, **[9+1]CPP**. The synthesis of ***m*[9+1]CPP** begins with preparation of coupling partner **II.2** as detailed in **Scheme 2.1**. A Suzuki cross-coupling reaction between two equivalents of the boronic ester **II.10** and 1,3-dibromobenzene furnished dichloride **II.11**. Miyaura borylation of **II.11** yielded our final coupling partner, boronic ester **II.2**.

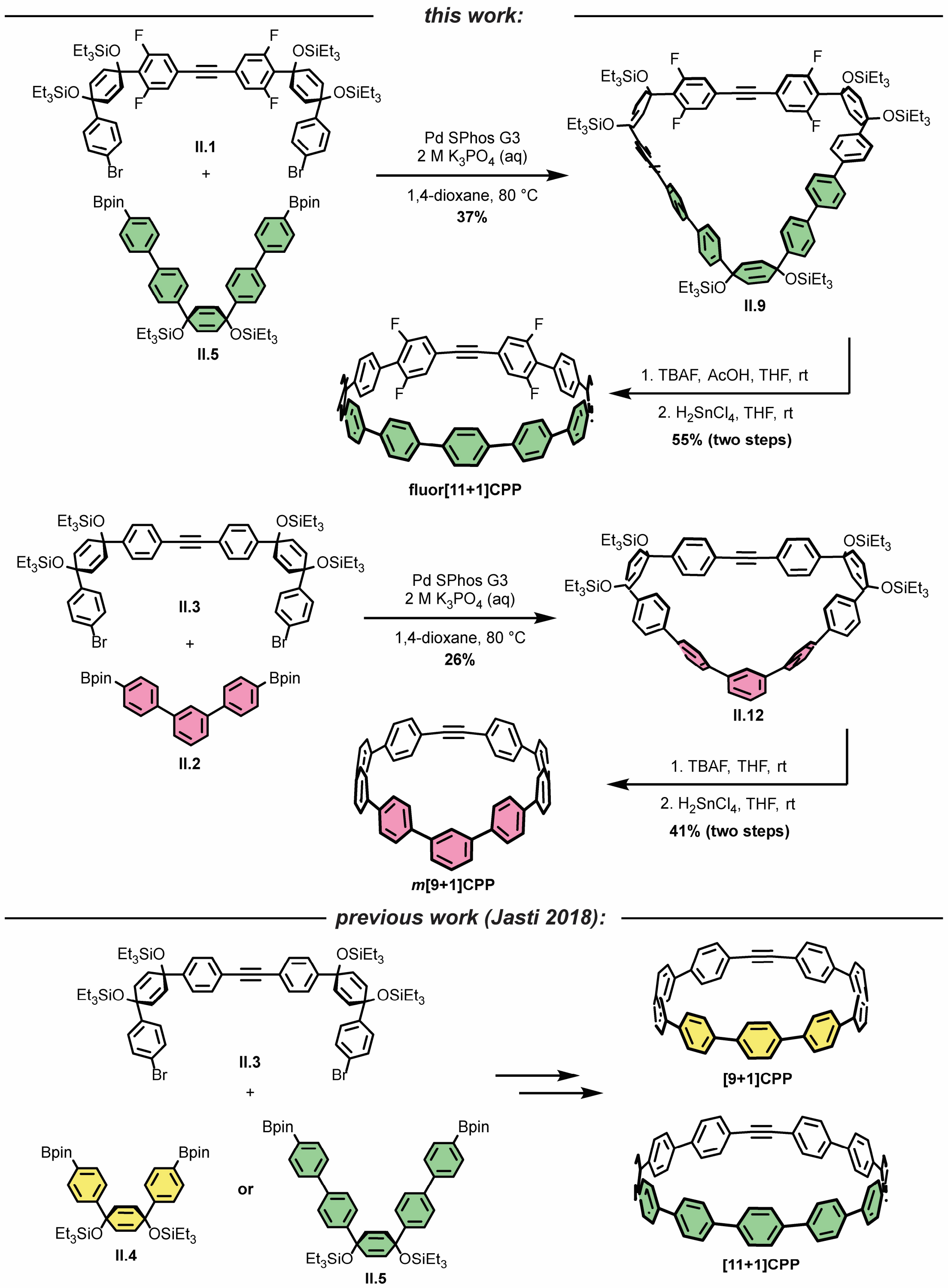

Scheme 2.2. Synthesis of the [*n*+1]CPPs analyzed in this study. Note that the synthesis of **[9+1]CPP** and **[11+1]CPP** was first detailed in 2018 and shown here for completeness. The colors denote three important coupling partners central to this synthesis; green represents the coupling which would impart the least strain to the overall structure, while the pink coupling partner would impart the most strain.

With **II.2** in hand, as well as **II.3** prepared as described by Schaub *et al.*,[56] we performed a Suzuki cross-coupling reaction under very dilute conditions to yield the unaromatized, silyl-protected macrocycle **II.12** in 26% yield (**Scheme 2.2**). Treatment of **II.12** with TBAF yielded the alcohol-containing macrocycle. Without rigorous purification, this material was then subjected to tin-mediated reductive aromatization with H_2SnCl_4 to furnish ***m*[9+1]CPP** in 41% yield over the last two transformations.

We previously reported[56] that **[9+1]CPP** could be stored as a solid without noticeable decomposition at –27 °C for several months, and **[11+1]CPP** could even be stored under ambient conditions for several months without decomposition. **Fluor[11+1]CPP** and ***m*[9+1]CPP** were both found to be stable at room temperature in air for a few days without noticeable decomposition, and could be stored as a solid at –27 °C or frozen in a solution of DMSO for several weeks without decomposition.

As a final step, each [*n*+1]CPP was combined with benzyl azide to yield the [*n*+1]CPP-BnAz SPAAC products, **[9+1]CPP-BnAz**, **[11+1]CPP-BnAz**, **fluor[11+1]CPP-BnAz**, and ***m*[9+1]CPP-BnAz** (**Scheme 2.3**). These were fully characterized in preparation for future kinetics experiments. Conveniently, the symmetric nature of the [*n*+1]CPPs means that only one regioisomer is produced for each cycloaddition reaction.

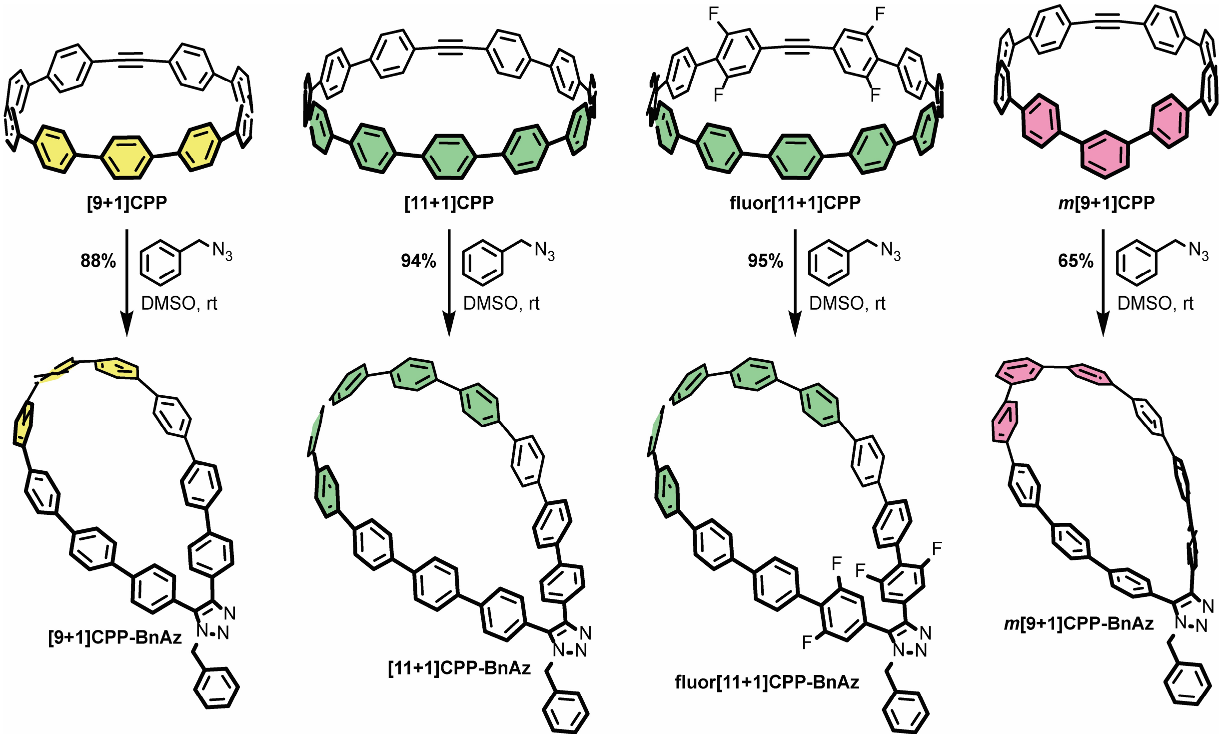

Scheme 2.3. Strain-promoted azide-alkyne cycloaddition reactions between the [*n*+1]CPPs described in this study and benzyl azide, a model compound. Yields were determined *in situ via* quantitative ^{1}H NMR in comparison to an internal standard, dimethyl sulfone.

2.2.2 Photophysical Characterization

CPPs often possess intriguing photophysical properties,[54] and we were keen to investigate those properties in this study. All [*n*+1]CPPs and [*n*+1]CPP-BnAz SPAAC products were characterized in terms of their absorbance/emission profiles, molar absorptivities, and quantum yields. All measurements were performed in DMSO to mirror our kinetics experiments, and quantum yields were also measured in dichloromethane (DCM) as a point of comparison (*vide infra*). The entirety of this data is available in experimental section 2.4, and we will highlight the main points here and in **Figure 2.2**.

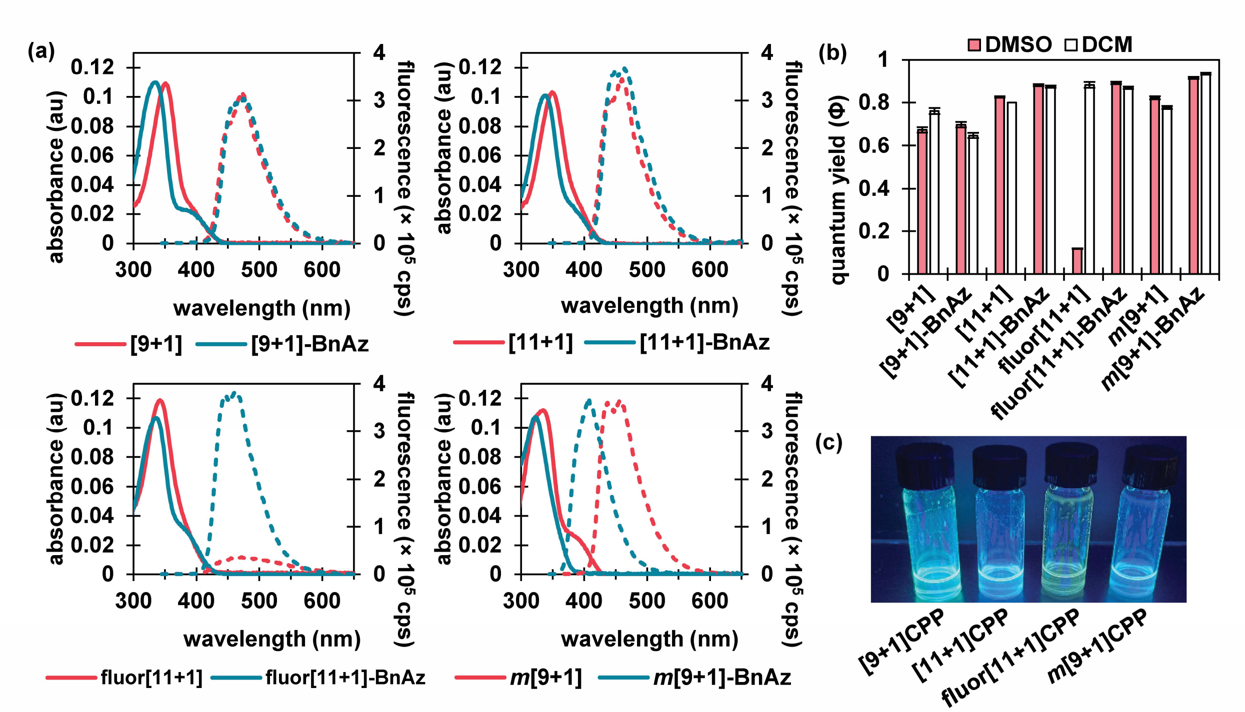

Figure 2.2. The photophysical data for the molecules described in this study. (a) Absorbance and emission for each [*n*+1]CPP (pink) and [*n*+1]CPP-BnAz (blue) in DMSO; each measurement was taken at an approximate absorbance of 0.1 au, and a fluorescence measurement was taken immediately afterwards, excited at 340 nm with the same slit widths (exc. and emm.) in all cases. (b) Quantum yields (Φ) in DMSO (pink) and DCM (white) measured *via* comparison to known standards. (c) Photograph of each CPP dissolved (to saturation) in deuterated DMSO and illuminated with 365 nm light.

Absorbance and emission traces in DMSO for each [*n*+1]CPP and [*n*+1]CPP-BnAz are shown in **Figure 2.2a**. A few general trends can be observed: the SPAAC products exhibit slightly blue-shifted $\lambda_{\text{max,abs}}$ values in comparison to the parent [*n*+1]CPP while the emission profiles are largely maintained. Another interesting feature of these traces is a small, redder secondary absorbance for [*n*+1]CPP-BnAz products. We attribute this to a symmetry-forbidden HOMO-LUMO transition which becomes allowed post-SPAAC.[48,54,60] An interesting exception to these trends is ***m*[9+1]CPP** and its SPAAC product ***m*[9+1]CPP-BnAz**. Here, we observe the allowed HOMO-LUMO transition in the CPP itself but not the SPAAC product. We also observe a significant blue-shift in the emission for ***m*[9+1]CPP-BnAz**. We hypothesize that this is due to a lowering in the overall strain of the molecule, which has been observed previously.[48]

The next point of interest is the quantum yields of the [*n*+1]CPPs and [*n*+1]CPP-BnAz products, which are shown in **Figure 2.2**. These values were measured by comparison to known standards.[61] While all of the other [*n*+1]CPPs (and [*n*+1]CPP-BnAz products) exhibited high quantum yields (ranging from 0.67 to 0.93) characteristic of large, non-donor-acceptor-type CPPs, **fluor[11+1]CPP** was the notable exception. While the molecule had a quantum yield of 0.88 in DCM, the quantum yield was reduced to 0.12 in DMSO. Interestingly, upon undergoing the SPAAC reaction with benzyl azide, high quantum yields of 0.87 and 0.89 in DCM and DMSO respectively were observed for the resulting product. We hypothesize that the electron-withdrawing fluorine atoms grant this molecule donor-acceptor-type properties; the non-emissive charge-transfer state of this CPP molecule is stabilized by polar solvents, leading to a diminished quantum yield in DMSO. Similar properties have been observed previously by Itami *et al.* in donor-acceptor-type CPPs.[43] While this 7.4-fold turn-on response is modest in comparison to some other fluorogenic probes, we are excited about the implications of this finding and anticipate using this principle in the design of future [*n*+1]CPPs with turn-on fluorescence.

2.2.3 Kinetics of the SPAAC Reaction with Benzyl Azide

We next set out to quantify second-order rate constants for the SPAAC reaction of each [*n*+1]CPP with benzyl azide. To accomplish this, we combined each [*n*+1]CPP with 2-12 equivalents of benzyl azide in deuterated dimethyl sulfoxide at 25 °C and monitored the reaction via quantitative ^{1}H NMR. Concentrations were determined by comparison to an internal standard of known concentration (dimethyl sulfone). From the results, we determined second-order rate constants for each reaction as shown in **Figure 2.3**.

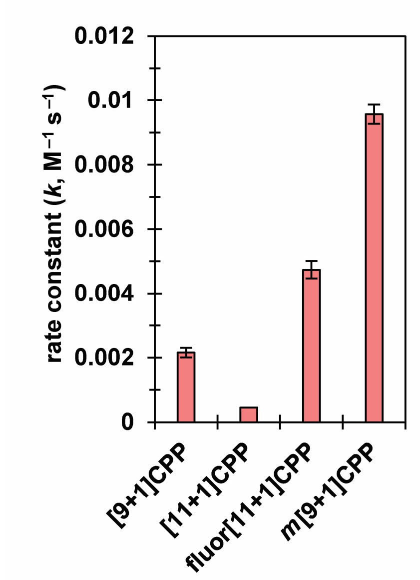

Figure 2.3. SPAAC second-order rate constants for [*n*+1]CPPs. These constants were measured *via* quantitative ^{1}H NMR in deuterated DMSO.

We found that the [*n*+1]CPP structure directly impacted the observed SPAAC rate constants. We had shown previously that the smaller **[9+1]CPP** possesses heightened reactivity over larger **[11+1]CPP** towards tetracyanoethylene (TCNE) in a [2+2]cycloaddition-retrocyclization reaction.[56] The same holds true in this study, where we observed an almost five-fold increase in rate constant for **[9+1]CPP** (2.2×10^{-3} M^{-1} s^{-1}) compared to **[11+1]CPP** (4.5×10^{-4} M^{-1} s^{-1}). The electronically modulated **fluor[11+1]CPP**, exhibiting fluorine atoms at all four positions *meta* to the alkyne moiety, displayed a second-order rate constant of 4.7×10^{-3} M^{-1} s^{-1} towards the SPAAC reaction with benzyl azide. This is an approximately 10-fold increase in comparison to **[11+1]CPP** just by fluorination of the scaffold. Lastly, we hypothesized that the *meta*-linked version of **[9+1]CPP**, ***m*[9+1]CPP**, would possess increased local strain at the alkyne due to its location opposite the *meta* linkage. We determined a second-order rate constant of 9.6×10^{-3} M^{-1} s^{-1} for the SPAAC reaction of ***m*[9+1]CPP** with benzyl azide. This corresponds to a 4.4-fold increase compared to **[9+1]CPP** just by changing the connectivity of the macrocycle.

2.2.4 Computational Methods

StrainViz. Computations were performed using Gaussian09 at the B3LYP/6-31+G(d) level of theory.[62] StrainViz calculations were performed using the scripts available through GitHub with an alternation to the "input_gen.py" script. Keywords "Opt=(rfo,NoSymm)" were added to account for the fragments with an alkyne. Output from individual StrainViz calculations were submitted with the maximum bond energy set as the highest strained bond between all four molecules. This setting recolors each bond to generate a comparative heat map. Replacing the "max(norm_values)" on line 171 in the "bond_scripts.py" with the max bond strain in the "total_bond.tcl" file, a recolored output is generated by rerunning the StrainViz script for each molecule.

Transition states and energies. Computations were performed using Gaussian 16 program.[63] The reactions between each [*n*+1]CPP and benzyl azide were optimized using M06-2X26[64] and 6-31+G(d,p)[65] basis set with the integral equation formalism variant of polarizable continuum model (IEF-PCM)[66] with parameters for DMSO. Conformational searches of the 10 lowest energy conformers were determined for the reactants, intermediates, and transition states using the Conformer-Rotamer Ensemble Sampling Tool (CREST).[67] After locating the lowest energy transition structure, we ran intrinsic reaction coordinate (IRC) calculations and optimized the reactive conformers corresponding to the reactants and products. We performed a vibrational analysis and confirmed that each stationary point was minima; we identified only positive vibrational frequencies. The optimized global minima transition structures showed only one negative vibrational frequency and was used to determine barrier heights and reaction energies.

2.2.5 Theoretical Analysis of [*n*+1]CPP Reactivity

In order to better understand the relationship between [*n*+1]CPP structure and the observed reactivity trends, we performed an in-depth computational analysis. First, we analyzed the ground state geometries of each [*n*+1]CPP with StrainViz to better understand the distribution of strain throughout each molecule (results displayed in **Figure 2.4** and **Table 2.1**).[59] A few trends can be observed. Notably, in each [*n*+1]CPP maximum local strain is located at the alkyne. We noted that **[11+1]CPP** and **fluor[11+1]CPP** displayed the lowest maximum local strains of 1.29 and 1.16 kcal mol^{-1}, respectively, while ***m*[9+1]CPP** has the highest local strain at the alkyne with 3.56 kcal mol^{-1}. For the unfunctionalized **[9+1]CPP**, **[11+1]CPP**, and ***m*[9+1]CPP**, it is clear from this analysis that the acuteness of the C–C≡C bond angle and therefore the local strain at the alkyne has a major effect on SPAAC rate constant. However, strain cannot account for the heightened reactivity of **fluor[11+1]CPP** in comparison to the similarly strained, unfunctionalized

[11+1]CPP. We therefore turned to transition state structure analysis and the distortion-interaction model developed by Houk to provide a more detailed explanation of our results.[15,16]

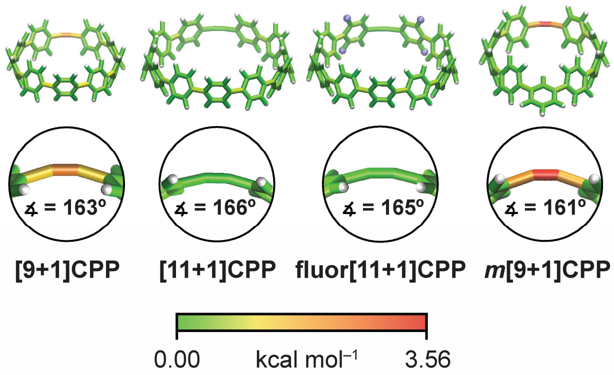

Figure 2.4. Strain analysis of the [*n*+1]CPPs described in this study with the StrainViz computational tool.

Table 2.1. Strain values determined from Strainviz for each [*n*+1]CPP; reported in kcal mol^{-1}.

[*n*+1]CPP	**Total strain**	**Max. local strain**
[9+1]CPP	58.0	2.94
[11+1]CPP	44.4	1.29
fluor[11+1]CPP	44.6	1.16
m[9+1]CPP	43.3	3.56

We computed the transition structures and activation free energies for the SPAAC of each [*n*+1]CPP with benzyl azide (**Figure 2.5** and **Table 2.2**). The transition structures are all concerted but asynchronous. The $\text{C–N}_{\text{internal}}$ and $\text{C–N}_{\text{external}}$ bond lengths in the [*n*+1]CPP transition states range from 2.15-2.17 Å and 2.26-2.30 Å, respectively. This observed asynchronicities can be attributed to the larger orbital coefficient and nucleophilicity of the $\text{N}_{\text{internal}}$ of benzyl azide with a natural bond orbital (NBO) charge of –0.40, in comparison to –0.078 for $\text{N}_{\text{external}}$.

Table 2.2. Activation free energies for the [*n*+1]CPPs in this study; reported in kcal mol^{-1}.

[*n*+1]CPP	$\Delta G^{\ddagger}_{\text{experimental}}$	$\Delta G^{\ddagger}_{\text{computational}}$
[9+1]CPP	21.1	24.2
[11+1]CPP	22.0	25.3
fluor[11+1]CPP	20.6	24.2
m[9+1]CPP	20.2	23.0

The computed activation free energies ($\Delta G^{\ddagger}_{\text{comp}}$) ranged from 23.0 to 25.3 kcal mol^{-1}. We observed an acceptable agreement between computations and experiments; when plotting $\Delta G^{\ddagger}_{\text{exp}}$

against $\Delta G^{\ddagger}{}_{\text{comp}}$, we observed a linear correlation ($R^2 = 0.94$; $\Delta G^{\ddagger}{}_{\text{comp}} = 1.17\Delta G^{\ddagger}{}_{\text{exp}} - 0.62$; see section 2.4 for details).

We next implemented the distortion/interaction model to understand the origin of the reactivity differences of the [*n*+1]CPPs towards benzyl azide. The distortion/interaction model[15,16] is an energy-decomposition scheme that has been used extensively to understand the origin of unimolecular[68–71] and bimolecular[72–76] reactions. The distortion/interaction model dissects activation energies into distortion and interaction energies. The distortion energy ($\Delta E^{\ddagger}{}_{\text{dist}}$) is the energy required to distort the reactants from their equilibrium geometries to their transition state geometries without allowing them to interact. The interaction energy ($\Delta E^{\ddagger}{}_{\text{int}}$) captures the interactions between the two distorted reactants in the transition state. A generalization of the distortion-interaction model and a summary of the results of this analysis is displayed in **Figure 2.5**. We note that the activation electronic energies (*i.e.* $\Delta E^{\ddagger}$) are different from the activation free energies (*i.e.* $\Delta G^{\ddagger}$) because the electronic energies omit zero point energy and thermochemical energetic corrections. The distortion/interaction model uses energies without zero point energies because the distorted and frozen geometries of the cycloaddends are extracted from the optimized transition structures.

Notably, **fluor[11+1]CPP** has the highest $\Delta E^{\ddagger}{}_{\text{int}}$ of all the [*n*+1]CPPs in this study (–11.7 kcal mol^{-1}). This, in conjunction with its slightly lower $\Delta \text{E}^{\ddagger}{}_{\text{dist}}$ (20.4 kcal mol^{-1}) relative to parent **[11+1]CPP** (21.0 kcal mol^{-1}), is responsible for the relatively low $\Delta E^{\ddagger}$ and superior SPAAC rate constant.

The reactivity trend for **[9+1]CPP**, **[11+1]CPP**, and ***m*[9+1]CPP** can also be explained *via* the distortion-interaction model. [*n*+1]CPPs with more acute C–C≡C bond angles in the ground state geometry displayed slightly decreased $\Delta E^{\ddagger}{}_{\text{int}}$, but this was counteracted by significant lowering of $\Delta E^{\ddagger}{}_{\text{dist}}$ since less energy input was required to distort pre-bent reactants into their transition state geometries. This phenomenon is known as distortion-acceleration.

Finally, we sought to explain the large $\Delta E^{\ddagger}{}_{\text{int}}$ of **fluor[11+1]CPP** in comparison to the other [*n*+1]CPPs in this study. We turned to frontier molecular orbital (FMO) analysis (see experimental section 2.4).[15,77–83] Tetrafluorination resulted in an overall lowering in energy of the HOMO–1 and LUMO orbitals in comparison to the parent **[11+1]CPP**. This leads to a smaller FMO gap with benzyl azide (6.64 eV for **fluor[11+1]CPP** vs. 6.85 eV for **[11+1]CPP**). In line with FMO theory, smaller FMO gaps lead to stronger orbital interactions in the transition state structure; this effect is captured in $\Delta E^{\ddagger}_{\text{int}}$. The $\Delta E^{\ddagger}_{\text{int}}$ values for **fluor[11+1]CPP** and **[11+1]CPP** are –11.7 vs. –10.7 kcal mol^{-1}. The 1.0 kcal mol^{-1} increase in stabilizing interaction energy is caused by relatively strong FMO interactions of **fluor[11+1]CPP** with benzyl azide relative to **[11+1]CPP**.

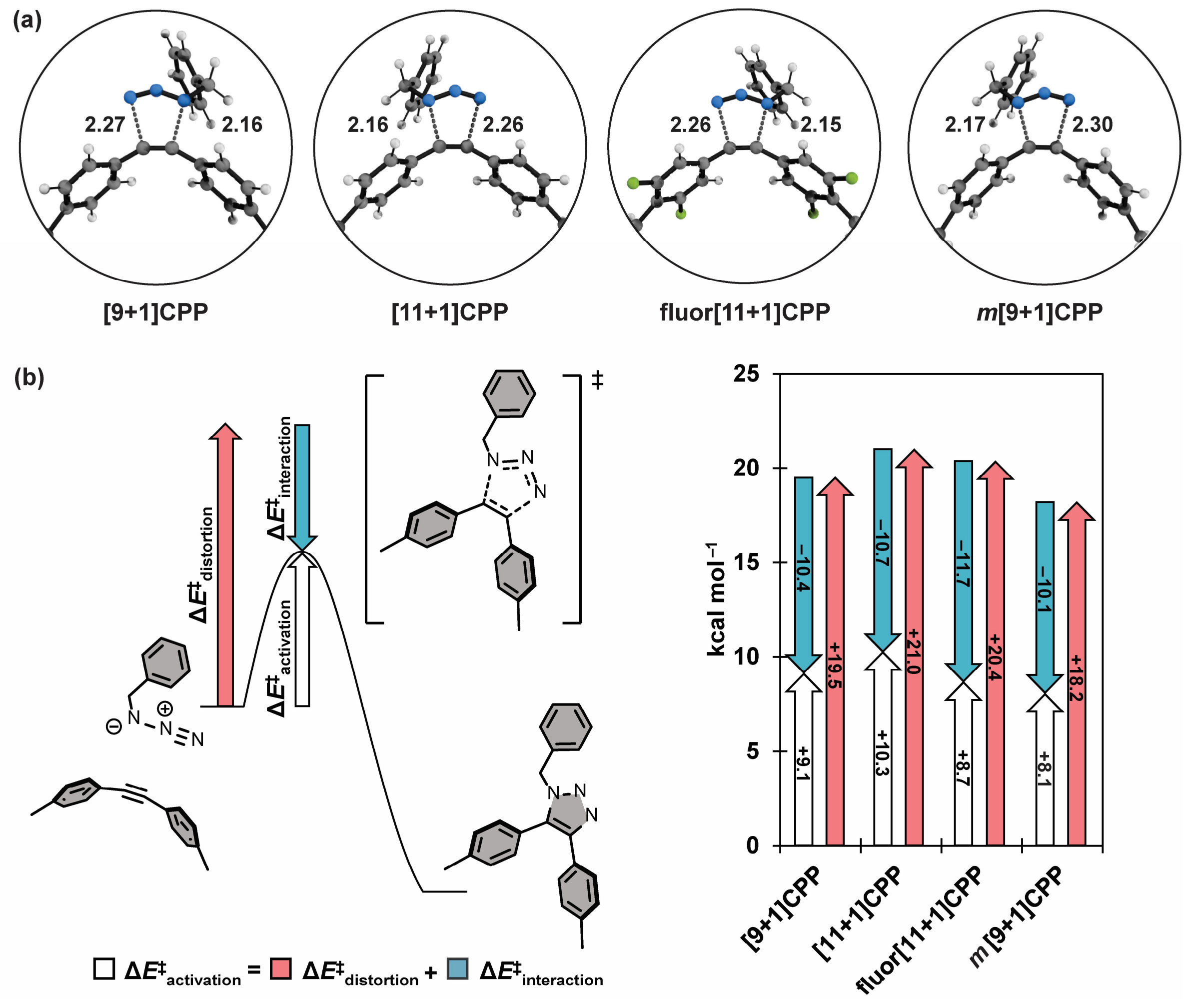

Figure 2.5. (a) Transition structures for each SPAAC reaction with benzyl azide; distances shown in Angstroms (Å). (b) Generalization of the distortion-interaction model and $\Delta E^{\ddagger}_{\text{activation}}$ of each SPAAC reaction broken down into its $\Delta E^{\ddagger}_{\text{distortion}}$ and $\Delta E^{\ddagger}_{\text{interaction}}$ components.

2.2.6 Reactivity Predictions for Cyano-Containing [*n*+1]CPPs

We performed additional computations to test our hypotheses of FMO effects on the cycloaddition reactivities towards benzyl azide. To that end, we computed the activation free energies of two theoretical tetra-cyano **[11+1]CPPs** (**Figure 2.6**) with cyano groups installed at the four *meta* positions (**II.13**) or four *ortho* positions (**II.14**). We hypothesized that the cooperative effect of the four π-electron withdrawing groups (π-EWGs) at the *ortho* position would lower LUMO energy of **II.14** more than that of **II.13**, where the cyano groups are electron-withdrawing *via* induction (the Hammett parameters for cyano are σ_p and σ_m = 0.66 and 0.56, respectively). The $\Delta G^{\ddagger}$ for **II.13** and **II.14** are 22.5 and 20.0 kcal mol^{-1}. The $\Delta\Delta G^{\ddagger}$ of 2.5 kcal mol^{-1} corresponds to a nearly 100-fold higher rate constant for **II.14** vs. **II.13** and at least 1,000-fold higher rate constant for **II.14** vs. **[11+1]CPP**. We performed a distortion-interaction analysis to understand the origin of the substantially lower $\Delta G^{\ddagger}$ of **II.13** and **II.14** relative to **[11+1]CPP**. The $\Delta E^{\ddagger}$ of **II.13** and **II.14** are 6.0 and 2.6 kcal mol^{-1}; the $\Delta E^{\ddagger}_{\text{dist}}$ of **II.13** and **II.14** are 21.9 and 20.5 kcal mol^{-1}. The $\Delta E^{\ddagger}_{\text{int}}$ of **II.13** and **II.14** are –15.8 and –17.9 kcal mol^{-1}, respectively. These interaction energies are the most stabilizing for those computed in this study and suggest that stronger FMO interactions in the transition state accelerate the reaction. We demonstrate this effect by computing the FMOs for **II.13** and **II.14**; the LUMOs for these molecules are –2.05 and –2.37 eV. The lower LUMO for **II.14** is consistent with the enhanced π-electron withdrawing effect of four cyano groups and leads to more stabilizing interaction energies and lower $\Delta G^{\ddagger}$. We will explore this effect further in subsequent manuscripts.

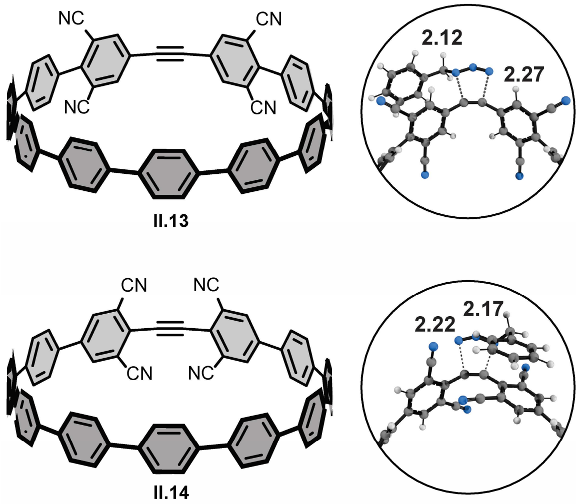

Figure 2.6. Theoretical tetra-cyano, isomeric **[11+1]CPPs**; distances shown in Angstroms (Å).

2.3 Conclusion

We have expanded the [n+1]CPP library to include two new molecules with unique properties: fluorinated **fluor[11+1]CPP** and *meta*-linked ***m*[9+1]CPP**. We fully characterized these two molecules as well as previously reported **[9+1]CPP** and **[11+1]CPP** in terms of their photophysics and quantitative SPAAC reaction kinetics with benzyl azide. Finally, we performed quantum mechanical calculations to identify the origins of these differences in reactivity.

Ultimately, we have endeavored to show that the SPAAC reaction kinetics of [*n*+1]CPPs can be finely tuned *via* organic synthesis. By changing a phenylene linkage or installing electron-withdrawing groups, it is possible to alter reactivity by as much as an order of magnitude without changing the size of the [*n*+1]CPP. We have also shown that functionalizing these CPPs can sometimes lead to interesting photophysical properties such as donor-acceptor-type [*n*+1]CPPs which display fluorescence turn-on post click reaction in polar solvents. Additionally, using quantum mechanical calculations, we have shown that we can predict the reactivities of these molecules towards benzyl azide. Finally, we predicted the reactivities of two theoretical [*n*+1]CPPs, **II.13** and **II.14**, with a 102- and 104-fold rate increase relative to **[11+1]CPP** due to four π-EWGs.

In this study we noted that these structures can be made with common building blocks. In theory, the coupling partners described herein could be combined to make six unique macrocyclic intermediates and therefore six unique [*n*+1]CPPs each with different reactivities. It was our experience that the most reactive of the possibilities, a fluorinated **[9+1]CPP** and a fluorinated ***m*[9+1]CPP**, were either not isolable or began to immediately react upon isolation. These results are intriguing in and of themselves and we will elaborate further on this topic in a future publication.

2.4 Experimental Section

2.4.1 General Experimental Details

Unless otherwise noted, commercially available materials were used without purification. Compounds **[9+1]CPP**, **[11+1]CPP**, **[11+1]CPP-BnAz**, **II.3**, **II.4**, **II.5**, **II.7**, and Pd Sphos G3 were prepared according to the literature.[56,58,84] Moisture and oxygen sensitive reactions were carried out in flame-dried glassware and under an inert atmosphere of purified nitrogen using syringe/septa technique. Tetrahydrofuran (THF), dimethylformamide (DMF), and 1,4-dioxane were dried by filtration through alumina according to the methods described by Grubbs.[85] Thin-layer chromatography (TLC) was performed on aluminium plates coated with 0.20 mm thickness of Silica Gel 60 F254 (Macherey-Nagel). Developing plates were visualized using UV light at wavelengths of 254 and 365 nm. Silica column chromatography was conducted with Zeochem

Zeoprep n60 Eco 40-63 μm silica gel. Alumina column chromatography was conducted with SorbTech basic alumina (pH 10), Act. II-III, 50-200 μm. ^{1}H and ^{13}C NMR spectra were recorded on either a Bruker Avance III HD 500 (^{1}H: 500 MHz, ^{13}C: 126 MHz) or Bruker Avance III HD 600 MHz (^{1}H: 600 MHz, ^{13}C: 151 MHz) NMR spectrometer. The samples were measured at 25 °C. The chemical shifts (δ) were reported in parts per million (ppm) and were referenced to the residual protio-solvent (CD_2Cl_2, ^{1}H: $\delta = 5.32$ ppm and ^{13}C: $\delta = 53.84$ ppm; DMSO-d_6, ^{1}H: $\delta = 2.50$ ppm and ^{13}C: $\delta = 39.52$ ppm) or to tetramethylsilane (for $CDCl_3$, TMS, $\delta = 0.00$ ppm). Coupling constants (J) are given in Hz and the apparent resonance multiplicity is reported as s (singlet), d (doublet), t (triplet), q (quartet), dd (doublet of doublets) or m (multiplet). For all [*n*+1]CPPs and [*n*+1]CPP-BnAz, ^{1}H NMR spectra were collected in DMSO-d_6 as a point of reference for rate experiments, and in some cases an additional ^{1}H spectrum was collected in CD_2Cl_2. ^{13}C NMRs for these compounds were attempted in DMSO-d_6, but in cases of limited solubility, the ^{13}C NMRs were collected in CD_2Cl_2 instead. The SPAAC reaction yields reported in Scheme 3 of the paper were determined *in-situ* without purification in DMSO-d_6 doped with dimethyl sulfone internal standard (14.5 mM, preparation described in section 2.4.4). Infrared absorption (IR) spectra were recorded on a Thermo Scientific Nicolet 6700 spectrometer equipped with a diamond crystal Smart ATR or as a cast film on KCl plates (CH_2Cl_2 as drop-casting solvent). Characteristic IR absorptions are reported in cm^{-1} and denoted as strong (s), medium (m), and weak (w). UV/Vis absorption and fluorescence spectra were recorded on an Agilant Cary 100 spectrophotometer and a Horiba Jobin Yvon Fluoromax-4 Fluorimeter, respectively. All measurements were carried out under ambient conditions in QS Quartz Suprasil cells (10 mm light path). The absorption maxima (λ_{max}) are reported in nm and the extinction coefficient (ε) in M^{-1} cm^{-1}.

2.4.2 Synthetic Details

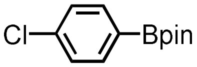

Compound II.10. 1-bromo-4-chlorobenzene (7.00 g, 36.6 mmol, 1.00 equiv.) was dissolved in THF (91 mL, 0.4 M) and the solution cooled to –78 °C over the course of 45 minutes. *n*-Butyllithium (2.5 M in hexanes, 15.4 mL, 38.3 mmol, 1.05 equiv.) was added dropwise. After allowing the reaction mixture to stir for 10 minutes, 2-isopropoxy-4,4,5,5-tetramethyl-1,3,2-

dioxaborolane (9.70 mL, 47.5 mmol, 1.3 equiv.) was added dropwise. The reaction mixture was allowed to stir for 30 minutes after the addition at –78 °C, at which point it was allowed to warm to room temperature over the course of 30 minutes. Deionized water (25 mL) was added. The resulting mixture was concentrated (*ca.* 100 mL) *via* rotary evaporator and extracted with EtOAc (3 × 100 mL). The combined organic layers were washed with brine (3 × 100 mL), dried over sodium sulfate, filtered, and concentrated *via* rotary evaporator to yield the crude product as an off-white low-melting solid. The crude product was purified *via* automated column chromatography (SiO_2, 0 – 42% CH_2Cl_2/hexanes) yielding a white solid (3.92 g, 16.4 mmol, 45%). R_f = 0.63 (SiO_2, 40% CH_2Cl_2/hexanes; product slowly decomposes on silica); ^{1}H NMR (500 MHz, Chloroform-*d*) δ 7.73 (d, *J* = 8.1 Hz, 2H), 7.34 (d, *J* = 8.2 Hz, 2H), 1.33 (s, 12H) ppm; ^{13}C NMR (126 MHz, Chloroform-*d*) δ 137.5, 136.1, 128.0, 84.0, 24.9 ppm (5 signals, one signal does not appear); IR (ATR) ṽ 3053 (w), 3007 (w), 2974 (m), 1595 (s), 1564 (w), 1464 (w), 1394 (m), 1357 (s), 1331 (s), 1260 (m), 1138 (s), 1091 (s), 1014 (m), 852 (m), 823 (s), 725 (s), 647 (s); HRMS (ASAP, positive mode) *m*/*z* calcd for $C_{12}H_{17}BO_2Cl$: 239.1010 [M+H]$^+$, found 239.1025.

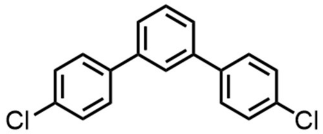

Compound II.11. II.10 (3.11 g, 13.0 mmol, 2.05 equiv.) and Pd(dppf)Cl_2 (0.519 g, 0.64 mmol, 0.1 equiv.) were dissolved in deoxygenated 1,4-dioxane (211 mL, 0.03 M, sparged with N_2 for one hour prior to use). 1,3-dibromobenzene (0.77 mL, 6.4 mmol, 1.0 equiv.) was added to the reaction mixture via syringe. The resulting solution was sparged with N_2 for an additional 15 minutes. The reaction mixture was heated to 80 °C over the course of 15 minutes. Deoxygenated aqueous K_3PO_4 solution (21 mL, 2.0 M, sparged with N_2 for one hour prior to use) was added via syringe. The reaction mixture was allowed to stir at 80 °C overnight. It was then cooled to room temperature and filtered through a plug of Celite (CH_2Cl_2). The filtrate was dried over sodium sulfate and concentrated to yield the crude product as a brown solid. The crude product was purified *via* a short plug (SiO_2, 2% EtOAc/hexanes), then triturated with methanol to yield a white solid (0.91 g, 3.1 mmol, 48%). R_f = 0.67 (SiO_2, 30% CH_2Cl_2/hexanes); ^{1}H NMR (500 MHz, Chloroform-*d*) δ 7.69 (t, *J* = 1.9 Hz, 1H), 7.56 – 7.47 (m, 7H), 7.42 (d, *J* = 8.5 Hz, 4H) ppm; ^{13}C NMR (126 MHz, Chloroform-*d*) δ 140.66, 139.36, 133.63, 129.41, 128.97, 128.43, 126.21, 125.68 ppm (8 signals);

IR (ATR) ṽ 3023 (w), 2911 (w), 1602 (m), 1494 (m), 1465 (m), 1106 (s), 1011 (s), 834 (s), 788 (s), 698 (s); HRMS (ASAP, positive mode) *m*/*z* calcd for $C_{18}H_{12}Cl_2$: 298.0316 $[M]^+$, found 298.0321.

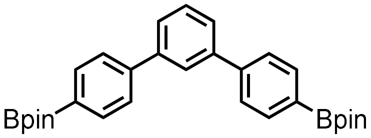

Compound II.2. II.11 (0.500 g, 1.7 mmol, 1.00 equiv), KOAc (1.08 g, 11 mmol, 6.6 equiv), palladium acetate (0.002 g, 0.008 mmol, 0.005 equiv.), SPhos (0.086 g, 0.21 mmol, 0.125 equiv.), and bis(pinacolato)diboron (1.697 g, 6.7 mmol, 4.0 equiv) were dissolved in 1,4-dioxane (9 mL, 0.19 M) and the resulting reaction mixture was sparged with N_2 for 15 minutes. The reaction mixture was heated to 90 °C and allowed to stir overnight. The reaction mixture was cooled to room temperature. Ethyl acetate was added and the reaction mixture was sonicated. It was then filtered through a plug of Celite (EtOAc). The filtrate was concentrated to yield the crude product as a brown solid. Trituration with methanol yielded the final product as a white solid (0.660 g, 1.36 mmol, 82%). $R_f = 0.52$ (SiO_2, 100% CH_2Cl_2, product is slowly decomposing on silica); ^{1}H NMR (500 MHz, Chloroform-*d*) δ 7.90 (d, *J* = 7.9 Hz, 4H), 7.83 (t, *J* = 1.9 Hz, 1H), 7.66 (d, *J* = 8.1 Hz, 4H), 7.60 (d, *J* = 7.5 Hz, 2H), 7.51 (t, *J* = 8.1 Hz, 1H), 1.37 (s, 24H) ppm; ^{13}C NMR (126 MHz, Chloroform-*d*) δ 143.80, 141.65, 135.31, 129.22, 126.58, 126.50, 126.25, 83.84, 24.89 ppm (9 signals, one signal does not appear); IR (ATR) ṽ 3043 (w), 3031 (w), 2980 (m), 1608 (m), 1550 (w), 1516 (w), 1465 (w), 1398 (m), 1358 (s), 1322 (s), 1270 (m), 1142 (s), 1091 (s), 1018 (m), 962 (s), 858 (s), 829 (m), 795 (s), 741 (s), 699 (m), 655 (s); HRMS (ASAP, positive mode) *m*/*z* calcd for $C_{30}H_{37}B_2O_4$: 483.2878 $[M+H]^+$, found 483.2911.

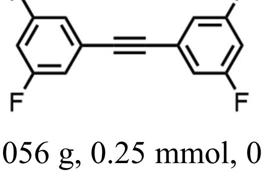

Compound II.6. Palladium acetate (0.056 g, 0.25 mmol, 0.02 equiv.), triphenylphosphine (0.164 g, 0.63 mmol, 0.05 equiv.), and copper iodide (0.119 g, 0.63 mmol, 0.05 equiv.) were dissolved in wet acetonitrile (62.5 mL, 0.2 M, sparged with N_2 for 30 minutes prior to use) and the resulting mixture was sparged with nitrogen for an additional 30 minutes. Triethylamine (5.23 mL, 37.5

mmol, 3 equiv.), 3,5-difluoroiodobenzene (1.5 mL, 12.5 mmol, 1 equiv.), and calcium carbide (2.40 g, 37.5 mmol, 3 equiv.) were added in rapid succession. The reaction mixture was stirred at room temperature for 24 hours. Additional portions of calcium carbide (0.200 g, 3.1 mmol, 0.25 equiv.), palladium acetate (0.020 g, 0.09 mmol, 0.007 equiv.), and deionized water (500 µL), were added to drive the reaction to completion. After two additional hours, dichloromethane was added and the reaction mixture was sonicated. It was then filtered through a plug of Celite (CH_2Cl_2). The filtrate was concentrated to yield the crude product as a dark brown solid. The crude product was purified first *via* a short plug (SiO_2, 100% CH_2Cl_2) and then more vigorously *via* automated column chromatography (SiO_2, 100% hexanes) to yield a white solid (1.28 g, 5.13 mmol, 82%). R_f = 0.52 (SiO_2, 100% hexanes); ^{1}H NMR (500 MHz, Chloroform-*d*) δ 7.07 – 6.99 (m, 4H), 6.83 (tt, *J* = 8.9, 2.4 Hz, 2H) ppm; ^{13}C NMR (126 MHz, Chloroform-*d*) δ 162.79 (dd, *J* = 249.5, 13.3 Hz), 125.01 (t, *J* = 11.6 Hz), 114.76 (dd, *J* = 19.9, 6.8 Hz), 105.15 (t, *J* = 25.3 Hz), 88.79 (t, *J* = 3.9 Hz) (5 signals); ^{19}F NMR (471 MHz, Chloroform-*d*) δ -109.15 – -109.23 (m) ppm; IR (ATR) ṽ 3091 (w), 1614 (s), 1583 (s), 1507 (w), 1479 (m), 1428 (s), 1366 (s), 1215 (m), 1179 (s), 1121 (s), 989 (s), 850 (s), 666 (s); HRMS (ASAP, positive mode) *m/z* calcd for $C_{14}H_7F_4$: 251.0484 $[M+H]^+$, found 251.0509.

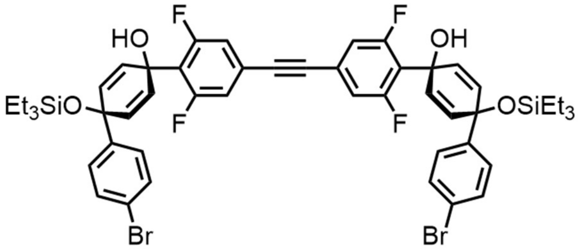

Compound II.8. II.6 (1.88 g, 7.53 mmol, 1 equiv.) was dissolved in THF (79 mL, 0.2 M) and the solution cooled to –78 °C over the course of 45 minutes. *n*-Butyllithium (2.4 M in hexanes, 6.43 mL, 15.4 mmol, 2.05 equiv.) was added dropwise, turning the solution an opaque gray. The reaction mixture was allowed to stir for ten minutes. Then, **II.7** (6.00 g, 15.8 mmol, 2.1 equiv., dissolved in 5 mL THF) was added dropwise, turning the solution a cloudy yellow. The reaction mixture was allowed to stir for an additional ten minutes at –78 °C. The reaction mixture was then transferred to a 0 °C bath and allowed to stir for 40 minutes; the mixture turned a clear turquoise over this time period. Deionized water (50 mL) was added. The resulting mixture was concentrated (ca. 75 mL) *via* rotary evaporator and extracted with EtOAc (3 × 100 mL). The combined organic layers were washed with brine (3 × 100 mL), dried over sodium sulfate, filtered, and concentrated *via* rotary evaporator to yield the crude product as an orange low-melting solid. The crude product was purified *via* automated column chromatography (40 – 80% CH_2Cl_2/hexanes), followed by recrystallization in minimal CH_2Cl_2 and hexanes to yield a white crystalline solid (2.34 g, 2.3 mmol, 31%). R_f = 0.33 (SiO_2, 80% CH_2Cl_2/hexanes); ^{1}H NMR (500 MHz, Methylene Chloride-*d*$_2$) δ 7.39 (d, *J* = 8.2 Hz, 4H), 7.25 (d, *J* = 8.2 Hz, 4H), 7.15 – 7.07 (m, 4H), 6.33 (dt, *J* = 10.4, 2.9 Hz, 4H), 5.96 (d, *J* = 9.8 Hz, 4H), 2.74 (t, *J* = 2.6 Hz, 2H), 1.00 (t, *J* = 7.9 Hz, 18H), 0.71 (q, *J* = 7.9 Hz, 12H) ppm; ^{13}C NMR (126 MHz, Methylene Chloride-*d*$_2$) δ 160.85 (dd, *J* = 250.7, 9.2 Hz), 144.97, 133.42, 131.49, 128.87 (t, *J* = 2.3 Hz), 127.87, 124.29 (t, *J* = 13.5 Hz), 121.95 (t, *J* = 13.8 Hz), 121.26, 116.49 (dd, *J* = 22.0, 7.3 Hz), 89.25 (t, *J* = 3.5 Hz), 71.56, 67.86 (t, *J* = 1.9 Hz), 7.22, 6.74 ppm (15 signals); ^{19}F NMR (471 MHz, Chloroform-*d*) δ -106.97 – -107.06 (m) ppm; IR (ATR) ṽ 3596 (w), 3091 (w), 3039 (w), 2953 (m), 2910 (w), 2874 (m), 1625 (m), 1585 (w), 1550 m), 1456 (m), 1417 (m), 1194 (m), 1164 (m), 1107 (w), 1075 (m), 1004 (s), 970 (m), 937 (m), 856 (s), 709 (s), 601 (s); HRMS (ASAP, positive mode) *m*/*z* calcd for $C_{50}H_{52}O_4F_4Si_2Br_2$: 1006.1707 $[M]^+$, found 1006.1714.

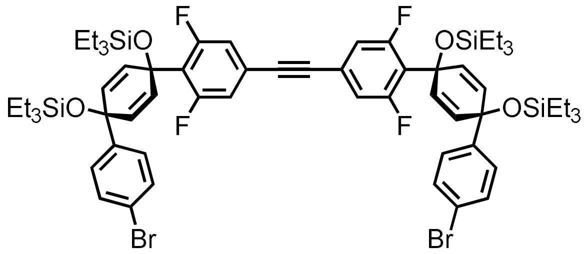

Compound II.1. II.8 (2.70 g, 2.67 mmol, 1.0 equiv.) and imidazole (0.820 g, 12 mmol, 4.5 equiv.) were dissolved in *N,N*-dimethylformamide (46.8 mL, 0.2 M). Chlorotriethylsilane (1.57 mL, 9.36 mmol, 3.5 equiv.) was added *via* syringe. The reaction mixture was heated to 40 °C and allowed to stir overnight. It was then cooled to room temperature and saturated aqueous solution of sodium bicarbonate (150 mL) was added. The reaction was extracted with ethyl acetate (3 × 100 mL). The combined organic layers were then washed with aqueous 5% LiCl (5 × 100 mL), washed with brine (3 × 100 mL), dried over sodium sulfate, filtered, and concentrated *via* rotary evaporator to yield the crude product as a white solid. The crude product was purified *via* automated column chromatography (SiO_2, 0 – 20% CH_2Cl_2/hexanes) to yield a white solid (2.73 g, 2.22 mmol, 83%). R_f = 0.48 (20% CH_2Cl_2/hexanes); ^{1}H NMR (500 MHz, Chloroform-*d*) δ 7.32 (d, *J* = 8.6 Hz, 4H), 7.14 (d, *J* = 8.6 Hz, 4H), 7.04 – 6.96 (m, 4H), 6.39 (dt, *J* = 10.3, 3.2 Hz, 4H), 5.89 (d, *J* = 10.1 Hz, 4H), 0.96 (t, *J* = 7.9 Hz, 18H), 0.90 (t, *J* = 7.9 Hz, 18H), 0.66 (q, *J* = 7.9 Hz, 12H), 0.56 (q, *J* = 7.9 Hz, 12H) ppm; ^{13}C NMR (126 MHz, Chloroform-*d*) δ 160.44 (dd, *J* = 252.6, 9.3 Hz), 144.77, 131.96, 131.10, 129.63 (t, *J* = 2.8 Hz), 127.29, 123.64 (t, *J* = 13.2 Hz), 123.00 (t, *J* = 13.7 Hz), 120.90, 115.95 (dd, *J* = 20.9, 7.1 Hz), 89.02 (t, *J* = 3.1 Hz), 71.15, 69.35 (t, *J* = 2.7 Hz), 7.04, 6.80, 6.38, 6.18 ppm (17 signals); ^{19}F NMR (471 MHz, Chloroform-*d*) δ -104.72 (d, *J* = 10.2 Hz) ppm; IR (ATR) ṽ 3041 (w), 2951 (m), 2909 (w), 2873 (m), 1622 (m), 1549 (m), 1476 (m), 1455 (m), 1414 (m), 1238 (m), 1193 (m), 1173 (w), 1161 (w), 1108 (m), 1071 (s), 1017 (s), 953 (s), 855 (s), 829 (m), 733 (s), 711 (s), 603 (s); HRMS (ASAP, positive mode) *m*/*z* calcd for $C_{62}H_{80}O_4F_4Si_4Br_2$: 1234.3437 [M]$^+$, found 1234.3463.

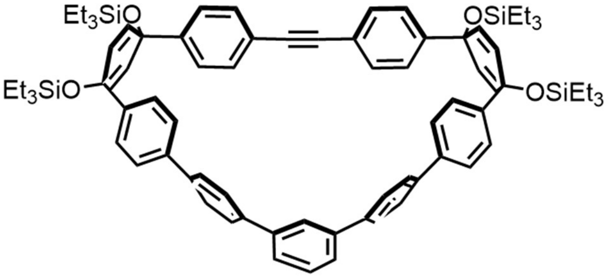

Compound II.12. II.2 (0.150 g, 0.311 mmol, 1.1 equiv.), **3** (0.33 g, 0.283 mmol, 1.0 equiv.), and Pd SPhos Gen III (0.023 g, 0.028 mmol, 0.1 equiv.) were dissolved in 1,4-dioxane (445 mL, 0.0007 M, sparged with N_2 for one hour prior to use). The resulting solution was sparged with N_2 for an additional 15 minutes. The reaction mixture was heated to 80 °C over the course of 15 minutes. Deoxygenated aqueous K_3PO_4 solution (45 mL, 2.0 M, sparged with N_2 for one hour prior to use) was added via syringe. The reaction mixture was allowed to stir at 80 °C overnight. It was then cooled to room temperature and the aqueous layer was removed. Concentration *via* rotary evaporator yielded the crude product as a brown solid, which was redissolved in CH_2Cl_2, dried over sodium sulfate, and reconcentrated. The crude product was purified *via* automated column chromatography (SiO_2, 0 – 30% CH_2Cl_2/hexanes). This was followed by sonication in ethanol and vacuum filtration to yield the final product as a white solid (0.0892 g, 0.072 mmol, 26%). R_f = 0.34 (30% CH_2Cl_2/hexanes); ^{1}H NMR (500 MHz, Methylene Chloride-d_2) δ 7.59 – 7.52 (m, 6H), 7.51 – 7.45 (m, 5H), 7.42 (d, *J* = 8.4 Hz, 4H), 7.30 (d, *J* = 8.4 Hz, 4H), 7.23 (d, *J* = 8.4 Hz, 4H), 7.14 (d, *J* = 8.4 Hz, 4H), 7.10 (t, *J* = 1.9 Hz, 1H), 6.01 (d, *J* = 10.1 Hz, 4H), 5.90 (d, *J* = 10.1 Hz, 4H), 0.93 – 0.83 (m, 36H), 0.63 – 0.51 (m, 24H); ^{13}C NMR (126 MHz, CD_2Cl_2) δ 146.52, 145.06, 142.59, 141.72, 140.14, 140.12, 134.08, 132.51, 131.64, 131.54, 129.58, 128.74, 127.61, 127.29, 126.78, 126.58, 124.41, 122.41, 89.46, 72.07, 72.00, 7.24, 7.21, 6.86, 6.80 (25 signals); IR (ATR) ṽ 3029 (w), 2951 (m), 2910 (w), 2873 (m), 1600 (w), 1558 (w), 1505 (w), 1456 (w), 1238 (w), 1172 (w), 1111 (m), 1074 (s), 1003 (m), 960 (s), 859 (m), 820 (m), 792 (m), 719 (s); HRMS (ASAP, positive mode) *m/z* calcd for $C_{80}H_{96}O_4Si_4$: 1232.6386 [M]$^+$, found 1232.6281.

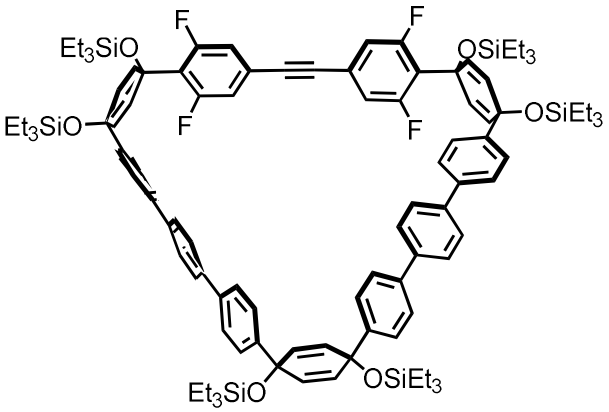

Compound II.9. II.1 (0.460 g, 0.371 mmol, 1.0 equiv.), **5** (0.367 g, 0.408 mmol, 1.1 equiv.), and Pd SPhos Gen III (0.029 g, 0.037 mmol, 0.1 equiv.) were dissolved in 1,4-dioxane (464 mL, 0.0008 M, sparged with N_2 for one hour prior to use). The resulting solution was sparged with N_2 for an additional 15 minutes. The reaction mixture was heated to 80 °C over the course of 15 minutes. Deoxygenated aqueous K_3PO_4 solution (46.4 mL, 2.0 M, sparged with N_2 for one hour prior to use) was added via syringe. The reaction mixture was allowed to stir at 80 °C for 2 hours. It was then cooled to room temperature and filtered through a plug of Celite (CH_2Cl_2) and dried over sodium sulfate. Concentration *via* rotary evaporator yielded the crude product as a brown solid. The crude product was purified *via* automated column chromatography (0 – 33% CH_2Cl_2/hexanes). The resultant solid was washed with pentanes and ethanol to yield the final product as a white solid (0.239 g, 0.139 mmol, 37%). R_f = 0.57 (40% CH_2Cl_2/hexanes); ^{1}H NMR (500 MHz, Chloroform-*d*) δ 7.64 (d, *J* = 8.2 Hz, 4H), 7.61 (d, *J* = 8.2 Hz, 4H), 7.55 (d, *J* = 8.1 Hz, 4H), 7.50 (d, *J* = 8.1 Hz, 4H), 7.40 (dd, *J* = 13.1, 8.1 Hz, 8H), 7.08 – 7.00 (m, 4H), 6.42 (dt, *J* = 10.3, 3.1 Hz, 4H), 6.04 (s, 4H), 5.96 (d, *J* = 9.8 Hz, 4H), 1.04 – 0.94 (m, 36H), 0.91 (t, *J* = 7.9 Hz, 18H), 0.75 – 0.61 (m, 24H), 0.57 (q, *J* = 7.9 Hz, 12H); ^{13}C NMR (126 MHz, Chloroform-*d*) δ 160.53 (dd, *J* = 252.6, 9.1 Hz), 145.01, 144.81, 139.66, 139.39, 139.30, 139.14, 132.31, 131.56, 129.14 (t, *J* = 3.1 Hz), 127.31, 127.21, 126.65, 126.52, 126.47, 125.93, 123.58 (t, *J* = 13.2 Hz), 123.28 (t, *J* = 13.7 Hz), 116.04 (dd, *J* = 21.4, 6.6 Hz), 89.02 (t, *J* = 2.7 Hz), 71.69, 71.36, 69.43 (t, *J* = 2.7 Hz), 7.11, 7.08, 6.81, 6.52, 6.45, 6.20; ^{19}F NMR (471 MHz, Chloroform-*d*) δ -104.52 (d, *J* = 10.4 Hz); IR (ATR) ṽ 3028 (w), 2951 (m), 2909 (w), 2874 (m), 1619 (m), 1550 (m), 1485 (m), 1456 (m), 1412 (m), 1237 (m), 1193 (m), 1173 (m), 1114 (m), 1066 (s), 1004 (s), 952 (s), 857 (s), 812 (s), 716 (s); HRMS (ASAP, positive mode) *m/z* calcd for $C_{104}H_{130}O_6F_4Si_6$: 1718.8419 $[M]^+$, found 1718.8438.

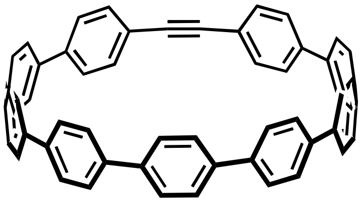

[9+1]CPP. The synthesis of **[9+1]CPP** has been described previously. As our kinetics experiments were performed in *d*-DMSO, we include here NMR information for this compound in *d*-DMSO; ^{1}H NMR (600 MHz, DMSO-d_6) δ 7.70 – 7.63 (m, 32H), 7.39 (d, *J* = 8.2 Hz, 4H); ^{13}C NMR (126 MHz, DMSO) δ 139.16, 137.79, 137.36, 137.27, 137.15, 136.99, 136.84, 131.00, 127.21, 127.17, 127.15, 126.68, 122.17, 98.76 (14 signals, five unaccounted for).

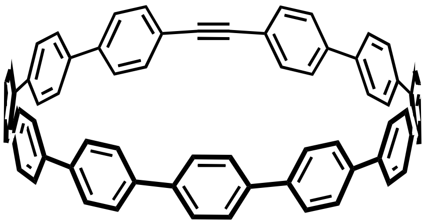

[11+1]CPP. The synthesis of **[11+1]CPP** has been described previously. As our kinetics experiments were performed in *d*-DMSO, we include here NMR information for this compound in *d*-DMSO; ^{1}H NMR (500 MHz, DMSO-d_6) δ 7.76 – 7.69 (m, 40H), 7.48 (d, *J* = 8.2 Hz, 4H); ^{13}C NMR (126 MHz, DMSO) δ 139.24, 138.10, 137.71, 137.55, 137.45, 137.42, 137.19, 131.29, 127.14, 127.10, 126.70, 121.96, 96.75 (13 signals, 10 unaccounted for).

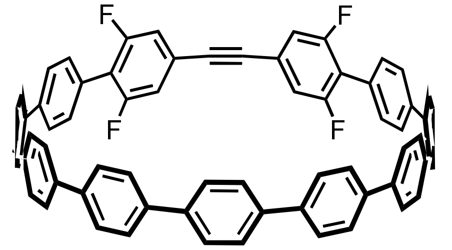

fluor[11+1]CPP. *Deprotection of silyl ether groups.* **II.9** (0.100 g, 0.0581 mmol, 1.0 equiv.) was dissolved in tetrahydrofuran (7.3 mL, 0.008 M) at room temperature. Acetic acid (0.17 mL, 2.91 mmol, 50 equiv.) was added dropwise, closely followed by dropwise addition of tetra-*n*-butylammonium fluoride (1 M solution in tetrahydrofuran, 1.45 mL, 1.45 mmol, 25 equiv.). The reaction mixture was allowed to stir for 18 hours at room temperature. Deionized water (15 mL) was added. The organic layer was almost completely removed *via* rotary evaporator, and the resultant white suspension was vigorously sonicated. The now-deprotected intermediate (a white solid) was isolated *via* vacuum filtration and thorough washing with DI water and dichloromethane. *Reductive aromatization*. $SnCl_2{\cdot}2H_2O$ (0.181 g, 0.8 mmol, 1.0 equiv. with respect to HCl) was dissolved in tetrahydrofuran (20 mL, 0.040 M). HCl (0.13 mL, 1.6 mmol, 2.0 equiv with respect to $SnCl_2{\cdot}2H_2O$) was added and the reaction was allowed to stir for 30 minutes. Concurrently in a separate flask, the deprotected macrocycle (0.060, 0.0581 mmol, 1.0 equiv.) was dissolved in tetrahydrofuran (8 mL, 0.0073 M). After the 30 minutes had elapsed, prepared H_2SnCl_4 solution (8.72 mL, 0.349 mmol, 0.040 M, 6 equiv.) was added to the solution of deprotected macrocycle. The reaction was allowed to stir for 1.5 hours. The reaction was diluted with hexanes (15 mL) then subjected directly to purification *via* a short plug (basic AlO_x, 50% CH_2Cl_2/hexanes). Subsequent sonication in acetone and vacuum filtration yielded the final product as a white solid (0.030 g, 0.032 mmol, 55% over two steps); R_f = 0.60 (50% CH_2Cl_2/hexanes, compound is slowly decaying on silica). ^{1}H NMR (500 MHz, Methylene Chloride-*d*$_2$) δ 7.72 – 7.58 (m, 34H), 7.52 (d, *J* = 8.2 Hz, 4H), 7.04 (d, *J* = 8.4 Hz, 4H); ^{1}H NMR (500 MHz, DMSO-*d*$_6$) δ 7.76 (td, *J* = 15.9, 13.8, 8.2 Hz, 34H), 7.50 (d, *J* = 8.1 Hz, 4H), 7.41 (d, *J* = 8.6 Hz, 4H); ^{19}F NMR (471 MHz, Methylene Chloride-*d*$_2$) δ -114.18 (d, *J* = 9.9 Hz); ^{19}F NMR (471 MHz, DMSO-*d*$_6$) δ -113.88 (d, *J* = 6.1 Hz); ^{13}C NMR (126 MHz, Methylene Chloride-*d*$_2$) δ 160.30 (dd, *J* = 249.9, 8.5 Hz), 141.05, 139.17, 139.14, 139.12, 138.96, 138.86, 138.79, 138.56, 131.33 (t, *J* = 2.8 Hz), 128.14, 127.96, 127.87, 127.83, 127.75, 127.71, 127.63, 127.55, 127.32, 125.00 (t, *J* = 12.8 Hz), 119.00 (t, *J* = 17.6 Hz), 115.35 (dd, *J* = 20.2, 7.3 Hz), 96.76 (t, *J* = 3.5 Hz) (23 signals); IR (ATR) ṽ 3025 (w), 1617 (w), 1597 (w), 1556 (w), 1483 (s), 1393 (w), 1363 (w), 1195 (m), 1177 (m), 1021 (m), 1001 (m), 809 (s), 747 (s); HRMS (ESI, positive mode) *m*/*z* calcd for $C_{68}H_{40}F_4$: 932.3066 $[M]^+$, found 932.3083.

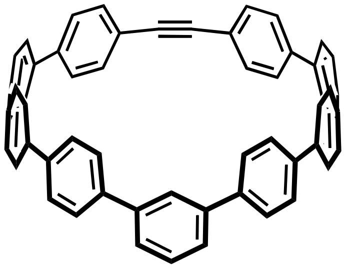

***m*[9+1]CPP.** *Deprotection of silyl ether groups.* **II.12** (0.060 g, 0.0486 mmol, 1.0 equiv.) was dissolved in tetrahydrofuran (6.1 mL, 0.008 M) at room temperature. Tetra-*n*-butylammonium fluoride (1 M solution in tetrahydrofuran, 0.21 mL, 0.21 mmol, 4.4 equiv.) was added dropwise to the solution. The reaction mixture was allowed to stir for 1 hour at room temperature. Deionized water (5 mL) was added. The organic layer was almost completely removed *via* rotary evaporator, and the resultant white suspension was vigorously sonicated. The now-deprotected intermediate (a white solid) was isolated *via* vacuum filtration and thorough washing with DI water and dichloromethane. *Reductive aromatization*. $SnCl_2{\cdot}2H_2O$ (0.181 g, 0.8 mmol, 1.0 equiv. with respect to HCl) was dissolved in tetrahydrofuran (20 mL, 0.040 M). HCl (0.13 mL, 1.6 mmol, 2.0 equiv with respect to $SnCl_2{\cdot}2H_2O$) was added and the reaction was allowed to stir for 30 minutes. Concurrently in a separate flask, deprotected OH-*m*[9+1]macrocycle (0.038 g, 0.0486 mmol, 1.0 equiv.) was dissolved in tetrahydrofuran (8 mL, 0.006 M). After the 30 minutes had elapsed, prepared H_2SnCl_4 solution (2.7 mL, 0.11 mmol, 0.040 M, 2.2 equiv.) was added to the solution of deprotected OH-*m*[9+1]macrocycle. The reaction was allowed to stir for 1 hour. The reaction was diluted with hexanes (20 mL) then subjected directly to purification *via* a short plug (basic AlO_x, 45% CH_2Cl_2/hexanes). Subsequent sonication in ether and vacuum filtration yielded the final product as a light yellow solid (0.014 g, 0.020 mmol, 41% over two steps); R_f = 0.43 (45% CH_2Cl_2/hexanes); ^{1}H NMR (500 MHz, Methylene Chloride-*d*$_2$) δ 7.66 – 7.51 (m, 27H), 7.43 (d, *J* = 8.1 Hz, 4H), 7.38 (d, *J* = 8.3 Hz, 4H), 6.71 (t, *J* = 2.0 Hz, 1H); ^{1}H NMR (600 MHz, DMSO-*d*$_6$) δ 7.76 (dd, *J* = 8.7, 7.1 Hz, 8H), 7.73 – 7.62 (m, 20H), 7.58 (t, *J* = 7.6 Hz, 1H), 7.50 (d, *J* = 8.4 Hz, 3H), 7.41 (d, *J* = 8.6 Hz, 4H), 6.70 (t, *J* = 1.9 Hz, 1H); ^{13}C NMR (126 MHz, CD_2Cl_2) δ 142.82, 141.60, 140.48, 139.75, 139.66, 139.03, 138.76, 138.51, 135.00, 131.18, 129.54, 129.05, 127.97, 127.78, 127.70, 127.65, 127.19, 124.36, 123.76, 101.44 (20 signals, one unaccounted for); IR (ATR) ṽ 3025 (w), 1592 (m), 1480 (s), 1391 (w), 1107 (w), 1000 (m), 909 (w), 858 (m), 830 (s), 806 (s), 797 (s), 746 (s), 726 (m), 708 (m); HRMS (ESI, positive mode) *m/z* calcd for $C_{56}H_{36}$: 708.2812 $[M]^+$, found 708.2835.

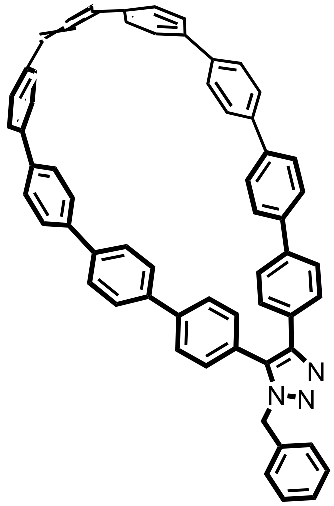

[9+1]CPP-BnAz. [9+1]CPP (0.013 g, 0.0181 mmol, 1 equiv.) was dissolved in toluene (2.0 mL, 0.009 M). Benzyl azide (0.0125 mL, 0.100 mmol, 5.5 equiv.) was added and the reaction was allowed to proceed for 4 hours at 50 °C. The toluene was removed *via* rotary evaporator. The crude product was purified *via* a short plug (basic AlO_x, 100% CH_2Cl_2). The resultant solid was sonicated in ethanol and vacuum filtered to yield the final product as a yellow solid (0.008 g, 0.010 mmol, 55%); $R_f = 0.52$ (SiO_2 4% MeOH/CH_2Cl_2); ^{1}H NMR (500 MHz, DMSO-d_6) δ 7.75 – 7.61 (m, 28H), 7.51 (d, *J* = 8.5 Hz, 2H), 7.44 (d, *J* = 8.4 Hz, 2H), 7.37 – 7.25 (m, 7H), 7.12 (d, *J* = 6.5 Hz, 2H), 5.62 (s, 2H); ^{13}C NMR (126 MHz, DMSO) δ 144.82, 140.19, 139.38, 138.57, 138.41, 138.10, 137.83, 137.62, 137.28, 137.23, 137.11, 136.78, 136.75, 136.70, 136.68, 136.65, 135.81, 134.49, 130.71, 129.77, 128.71, 128.08, 127.93, 127.46, 127.41, 127.38, 127.36, 127.26, 127.24, 127.21, 127.06, 126.95, 126.91, 126.88, 125.81, 51.36 (36 signals, 7 unaccounted for); IR (ATR) ṽ 3025 (m), 2923 (w), 1590 (m), 1479 (s), 1392 (w), 1351 (w), 1263 (m), 1002 (m), 816 (s), 738 (s); HRMS (ASAP, positive mode) *m/z* calcd for $C_{63}H_{43}N_3$: 841.3457 $[M]^+$, found 841.3365.

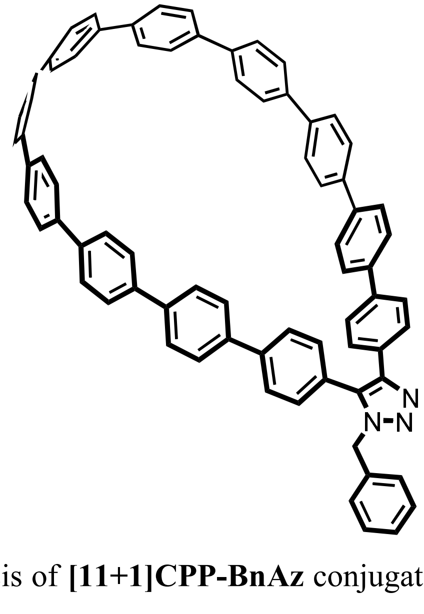

[11+1]CPP-BnAz. The synthesis of **[11+1]CPP-BnAz** conjugate has been described previously. As our kinetics experiments were performed in *d*-DMSO, we include here NMR information for this compound in *d*-DMSO. ^{1}H NMR (500 MHz, DMSO-d_6) δ 7.85 – 7.64 (m, 36H), 7.59 (d, *J* = 8.1 Hz, 2H), 7.53 (d, *J* = 8.0 Hz, 2H), 7.38 – 7.29 (m, 7H), 7.13 (d, *J* = 7.3 Hz, 2H), 5.63 (s, 2H); ^{13}C NMR (126 MHz, DMSO) δ 144.44, 140.14, 139.16, 138.64, 138.59, 138.35, 138.09, 137.98, 137.91, 137.76, 137.72, 137.59, 137.44, 137.40, 137.35, 137.29, 137.08, 137.05, 137.02, 135.82, 134.32, 130.76, 129.88, 128.72, 127.94, 127.68, 127.31, 127.26, 127.18, 127.14, 126.99, 126.94, 126.88, 126.04, 51.34 (35 signals, 16 unaccounted for).

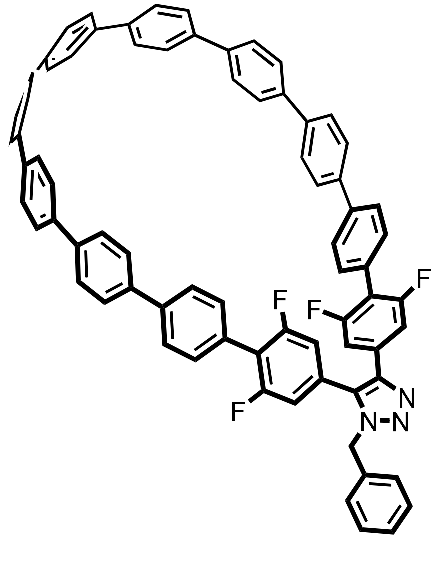

fluor[11+1]CPP-BnAz. fluor[11+1]CPP (0.016 g, 0.017 mmol, 1.0 equiv.) was dissolved in toluene (5.7 mL, 0.003 M). Benzyl azide (0.015 mL, 0.12 mmol, 7.0 equiv.) was added and the reaction was allowed to proceed for 18 hours at 45 °C. The toluene was removed *via* rotary evaporator. The crude product was purified *via* a short plug (basic AlO_x, 100% CH_2Cl_2). The resultant solid was sonicated in ether and vacuum filtered to yield the final product as a light yellow solid (0.013 g, 0.012 mmol, 69%); R_f = 0.35 (SiO_2, 100% CH_2Cl_2); ^{1}H NMR (500 MHz, Methylene Chloride-d_2) δ 7.69 – 7.62 (m, 32H), 7.56 (d, *J* = 8.1 Hz, 2H), 7.43 (d, *J* = 8.0 Hz, 2H), 7.39 – 7.33 (m, 3H), 7.20 – 7.15 (m, 2H), 7.03 (d, *J* = 8.1 Hz, 2H), 6.81 (d, *J* = 7.1 Hz, 2H), 5.58 (s, 2H); ^{1}H NMR (500 MHz, DMSO-d_6) δ 7.79 – 7.71 (m, 32H), 7.55 (d, *J* = 8.0 Hz, 2H), 7.44 (d, *J* = 8.0 Hz, 2H), 7.40 – 7.30 (m, 5H), 7.17 (d, 2H), 7.07 (d, *J* = 8.5 Hz, 2H), 5.70 (s, 2H); ^{19}F NMR (471 MHz, Methylene Chloride-d_2) δ -111.86 (d, *J* = 7.4 Hz), -113.99 (d, *J* = 8.4 Hz); ^{19}F NMR (471 MHz, DMSO-d_6) δ -112.66 (d, *J* = 7.0 Hz), -113.61 (d, *J* = 7.8 Hz); ^{13}C NMR (126 MHz, Methylene Chloride-d_2) δ 160.75 (dd, *J* = 251.5, 8.1 Hz), 160.43 (d, *J* = 248.2, 8.1 Hz), 144.05 (t, *J* = 1.9 Hz), 141.40, 140.53, 139.71, 139.62, 139.26, 139.10, 139.02, 138.82, 138.79, 138.64, 138.59, 138.53, 138.51, 138.47, 133.04 (t, *J* = 2.4 Hz), 132.23 (t, *J* = 11.1 Hz), 131.21 (t, *J* = 2.5 Hz), 131.08 (t, *J* = 1.8 Hz), 129.38, 128.98, 128.31 (t, *J* = 11.2 Hz), 128.09, 127.99, 127.92, 127.90, 127.88, 127.86, 127.84, 127.81, 127.79, 127.77, 127.75, 127.73, 127.70, 127.65, 127.30, 127.18, 126.96, 120.14 (t, *J* = 17.7 Hz), 117.96 (t, *J* = 18.9 Hz), 114.32 (dd, *J* = 19.3, 8.0 Hz), 110.63 (dd, *J* = 20.4, 7.6 Hz), 52.95 (46 signals, 5 unaccounted for); IR (ATR) ṽ 3024 (w), 1907 (w), 1630 (w), 1557 (w), 1485 (m), 1395 (m), 1365 (m), 1199 (m), 1111 (w) 1022 (m), 1002 (m), 867 (m), 808 (s), 726 (m); HRMS (ASAP, positive mode) *m/z* calcd for $C_{75}H_{48}N_3F_4$: 1066.3784 $[M+H]^+$, found 1066.3641.

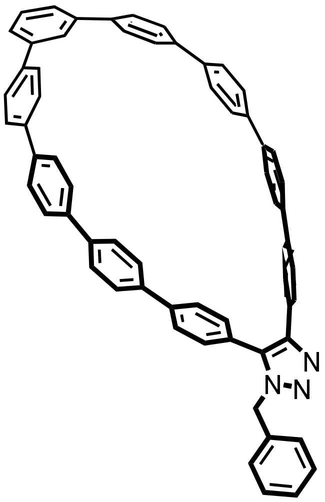

***m*[9+1]CPP-BnAz.** ***m*[9+1]CPP** (0.014 g, 0.020 mmol, 1.0 equiv.) was dissolved in tetrahydrofuran (3.0 mL, 0.0065 M). Benzyl azide (0.040 mL, 0.32 mmol, 16 equiv.) was added and the reaction was allowed to stir for 2 hours. The tetrahydrofuran was removed *via* rotary evaporator. The crude product was purified *via* a short plug (basic AlO_x, 50-100% CH_2Cl_2/hexanes). The resultant solid was sonicated in ether and vacuum filtered to yield the final product as a yellow solid (0.0047 g, 0.0056 mmol, 28%); $R_f = 0.58$ (SiO_2, 5% MeOH/CH_2Cl_2); ^1H NMR (500 MHz, DMSO-d_6) δ 7.73 – 7.63 (m, 22H), 7.61 – 7.53 (m, 3H), 7.47 – 7.40 (m, 6H), 7.39 – 7.28 (m, 3H), 7.26 (d, J = 8.3 Hz, 2H), 7.22 (d, J = 8.0 Hz, 2H), 7.16 (d, J = 6.7 Hz, 2H), 6.28 (t, J = 1.9 Hz, 1H), 5.66 (s, 2H); ^1H NMR (600 MHz, Methylene Chloride-d_2) δ 7.65 – 7.51 (m, 23H), 7.48 (d, J = 8.1 Hz, 2H), 7.41 – 7.31 (m, 9H), 7.23 (d, J = 8.4 Hz, 4H), 7.11 (d, J = 8.1 Hz, 2H), 6.31 (d, J = 1.9 Hz, 1H), 5.61 (s, 2H); ^{13}C NMR (151 MHz, CD_2Cl_2) δ 146.95, 143.11, 143.02, 142.41, 142.36, 141.84, 140.54, 140.03, 139.79, 139.58, 139.56, 139.52, 139.32, 138.85, 138.73, 138.51, 138.48, 136.15, 135.39, 131.33, 130.32, 129.61, 129.48, 129.45, 129.21, 129.01, 128.63, 128.02, 127.98, 127.87, 127.83, 127.81, 127.68, 127.50, 127.48, 127.46, 127.37, 126.59, 123.51, 52.57 (40 signals, 5 unaccounted for); IR (ATR) $\tilde{v}$ 3026 (m), 1596 (m), 1478 (s), 1391 (w), 1352 (w), 1263 (m), 1110 (w), 1002 (m), 831 (s), 811 (s), 736 (s), 714 (s); HRMS (ASAP, positive mode) *m*/*z* calcd for $C_{63}H_{44}N_3$: 842.3535 $[M+H]^+$, found 842.3501.

2.4.3 Photophysical characterization

For molar absorptivity measurements, the compound of interest was first dissolved at known concentration using volumetric glassware. This solution was then added incrementally to a cuvette containing a known amount of solvent and absorbance measurements were taken after each addition. Three trials were performed for each compound.

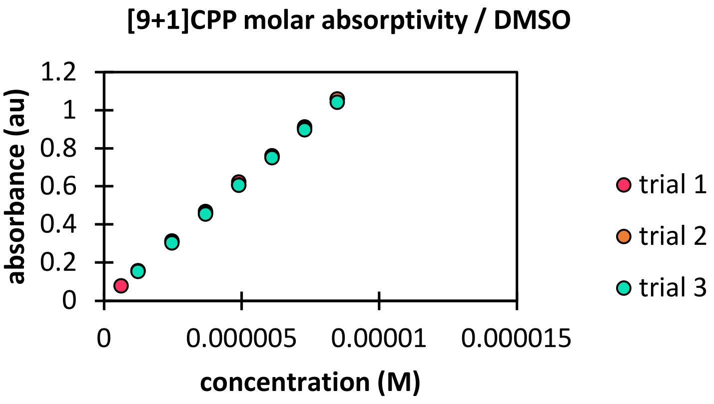

Figure 2.7. Beer's law plot for **[9+1]CPP** in DMSO.

Table 2.3. Measured molar absorptivity for **[9+1]CPP** in DMSO; $\lambda_{max,abs}$ = 351 nm.

Trial	Slope (M^{-1} cm^{-1})
1	1.3×10^5
2	1.2×10^5
3	1.2×10^5
average	1.2×10^5
std. dev.	0.0087×10^5

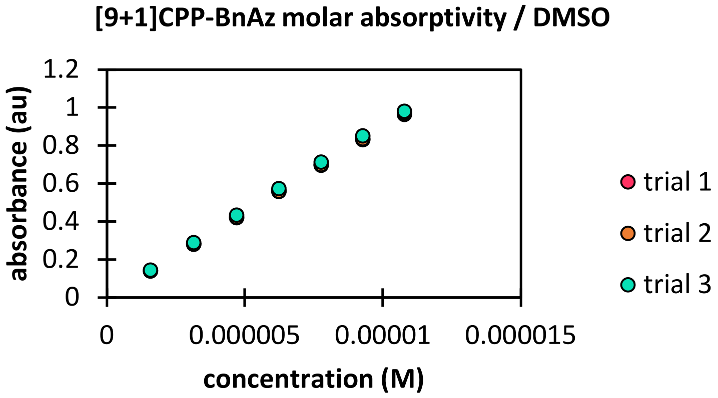

Figure 2.8. Beer's law plot for **[9+1]CPP-BnAz** in DMSO.

Table 2.4. Measured molar absorptivity for **[9+1]CPP-BnAz** in DMSO; $\lambda_{max,abs}$ = 335 nm.

Trial	Slope (M^{-1} cm^{-1})
1	9.0×10^4
2	9.1×10^4
3	9.1×10^4
average	9.1×10^4
std. dev.	0.069×10^4

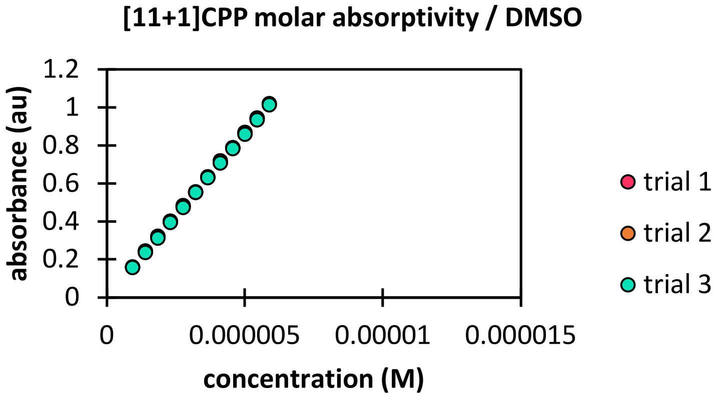

Figure 2.9. Beer's law plot for **[11+1]CPP** in DMSO.

Table 2.5. Measured molar absorptivity for **[11+1]CPP** in DMSO; $\lambda_{max,abs}$ = 350 nm.

Trial	Slope (M^{-1} cm^{-1})
1	1.7×10^5
2	1.7×10^5
3	1.7×10^5
average	1.7×10^5
std. dev.	0.0023×10^5

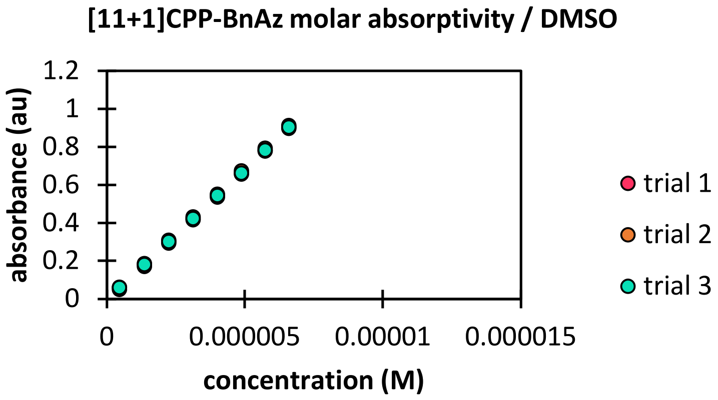

Figure 2.10. Beer's law plot **for [11+1]CPP-BnAz** in DMSO.

Table 2.6. Measured molar absorptivity for **[11+1]CPP-BnAz** in DMSO; $\lambda_{max,abs}$ = 338 nm.

Trial	Slope (M^{-1} cm^{-1})
1	1.4×10^5
2	1.4×10^5
3	1.4×10^5
average	1.4×10^5
std. dev.	0.0070×10^5

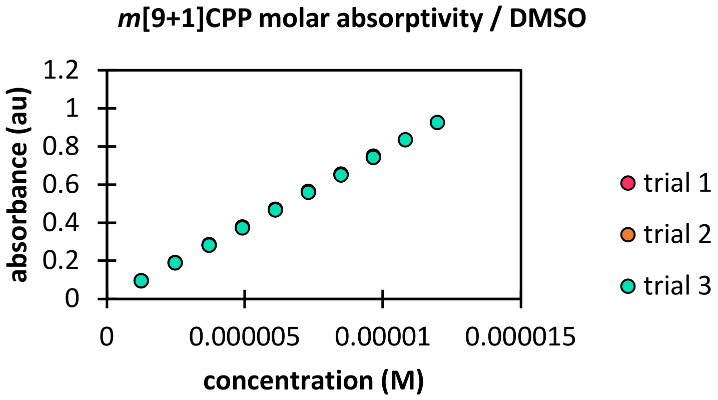

Figure 2.11. Beer's law plot for ***m*[9+1]CPP** in DMSO.

Table 2.7. Measured molar absorptivity for ***m*[9+1]CPP** in DMSO; $\lambda_{\text{max,abs}} = 333$ nm.

Trial	Slope (M^{-1} cm^{-1})
1	7.8×10^4
2	7.8×10^4
3	7.7×10^4
average	7.8×10^4
std. dev.	0.039×10^4

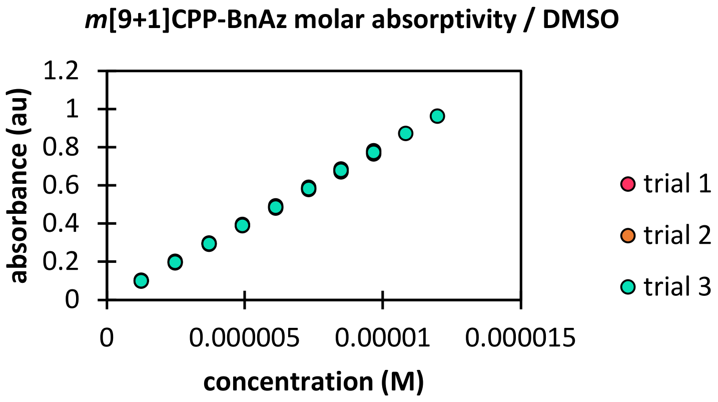

Figure 2.12. Beer's law plot for ***m*[9+1]CPP-BnAz** in DMSO.

Table 2.8. Measured molar absorptivity for ***m*[9+1]CPP-BnAz** in DMSO; $\lambda_{\text{max,abs}} = 323$ nm.

Trial	Slope (M^{-1} cm^{-1})
1	7.9×10^4
2	8.1×10^4
3	8.1×10^4
average	8.0×10^4
std. dev.	0.082×10^4

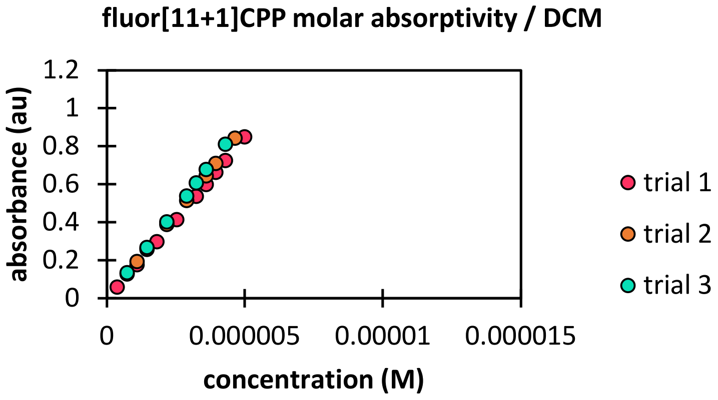

Figure 2.13. Beer's law plot for **fluor[11+1]CPP** in DCM.

Table 2.9. Measured molar absorptivity for **fluor[11+1]CPP** in DCM; $\lambda_{max,abs}$ = 337 nm.

Trial	Slope (M^{-1} cm^{-1})
1	1.7×10^5
2	1.8×10^5
3	1.9×10^5
average	1.8×10^5
std. dev.	0.097×10^5

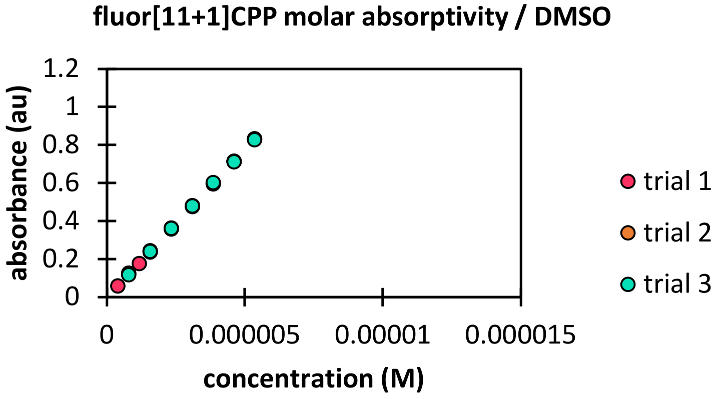

Figure 2.14. Beer's law plot for **fluor[11+1]CPP** in DMSO.

Table 2.10. Measured molar absorptivity for **fluor[11+1]CPP** in DMSO; $\lambda_{max,abs}$ = 343 nm.

Trial	Slope (M^{-1} cm^{-1})
1	1.6×10^5
2	1.6×10^5
3	1.6×10^5
average	1.6×10^5
std. dev.	0.0073×10^5

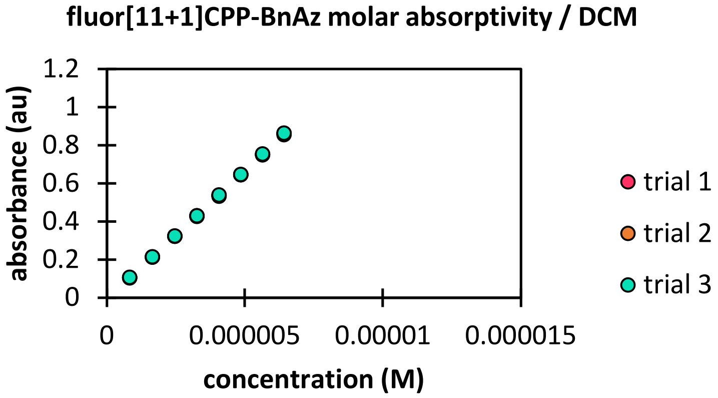

Figure 2.15. Beer's law plot for **fluor[11+1]CPP-BnAz** in DCM.

Table 2.11. Measured molar absorptivity for **fluor[11+1]CPP-BnAz** in DCM; $\lambda_{max,abs}$ = 328 nm.

Trial	Slope (M^{-1} cm^{-1})
1	1.4×10^5
2	1.3×10^5
3	1.4×10^5
average	1.4×10^5
std. dev.	0.0052×10^5

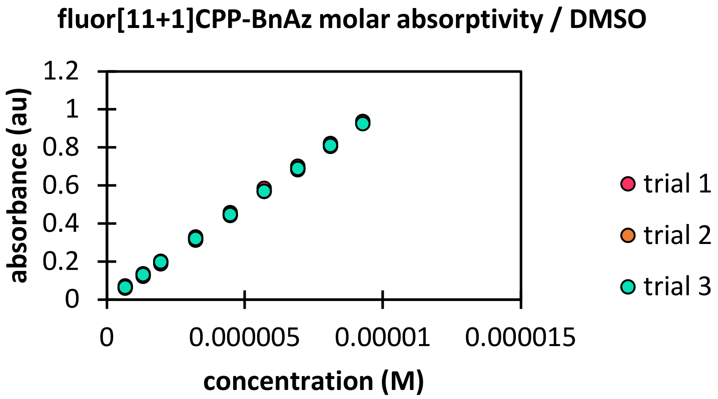

Figure 2.16. Beer's law plot for **fluor[11+1]CPP-BnAz** in DMSO.

Table 2.12. Measured molar absorptivity for **fluor[11+1]CPP-BnAz** in DMSO; $\lambda_{max,abs}$ = 336 nm.

Trial	Slope (M^{-1} cm^{-1})
1	1.0×10^5
2	1.0×10^5
3	1.0×10^5
average	1.0×10^5
std. dev.	0.0045×10^5

Quantum yield measurements were performed using the method described in "A Guide to Recording Fluorescence Quantum Yields" by Horiba Scientific.[61] The internal standards used were quinine sulfate (0.1 M H_2SO_4, aqueous, lit. value $\Phi = 0.60$, fluorescence signal integrated from 400-600 nm) and anthracene (ethanol, lit. value $\Phi = 0.27$, fluorescence signal integrated from 360-480 nm). For fluorescence measurements, all compounds were excited at a wavelength of 340 nm with consistent excitation and emission slit widths of 1 nm. Absorbance values plotted below were as measured at 340 nm. Fluorescence signal integrations for compounds of interest are listed below:

Table 2.13. Compound integration ranges for each [*n*+1]CPP and [*n*+1]CPP-BnAz in DMSO and DCM.

Compound of interest	Integration range (DCM, nm)	Integration range (DMSO, nm)
[9+1]CPP	400 – 600	400 – 600
[9+1]CPP-BnAz	400 – 600	400 – 600
[11+1]CPP	measured previously	400 – 600
[11+1]CPP-BnAz	400 – 600	400 – 600
m[9+1]CPP	390 – 590	390 – 590
m[9+1]CPP-BnAz	350 – 550	350 – 550
fluor[11+1]CPP	390 – 600	390 – 700
fluor[11+1]CPP-BnAz	390 – 600	400 – 600

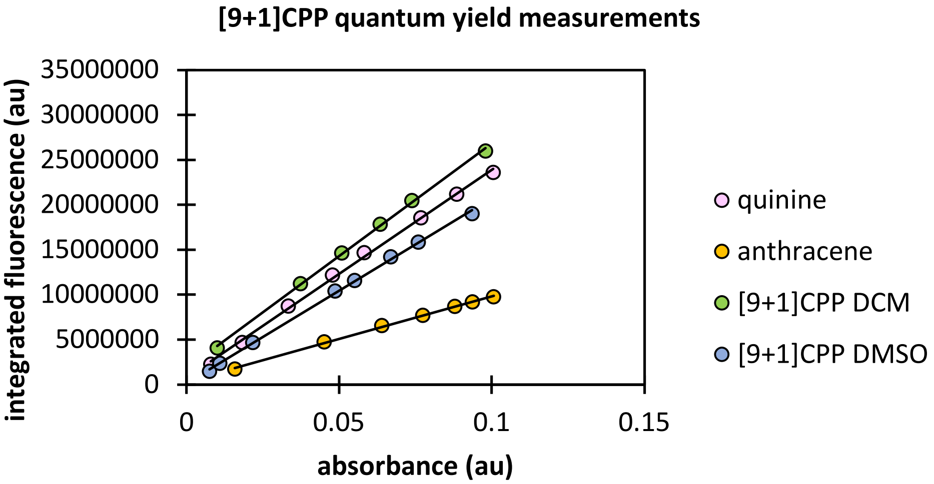

Figure 2.17. Quantum yield plot for **[9+1]CPP**.

Table 2.14. Quantum yield data for **[9+1]CPP**.

Compound	Solvent	Slope	Φ w.r.t. quinine	Φ w.r.t. anthracene	Avg. Φ	Std. dev.
quinine	0.1 M H_2SO_4 (*aq*)	2.32×10^8	0.60 (lit)	0.63	0.62	0.011
anthracene	ethanol	9.48×10^7	0.26	0.27 (lit)	0.26	0.0049
[9+1]CPP	DCM	2.50×10^8	0.74	0.78	0.76	0.014
[9+1]CPP	DMSO	2.06×10^8	0.66	0.69	0.67	0.013

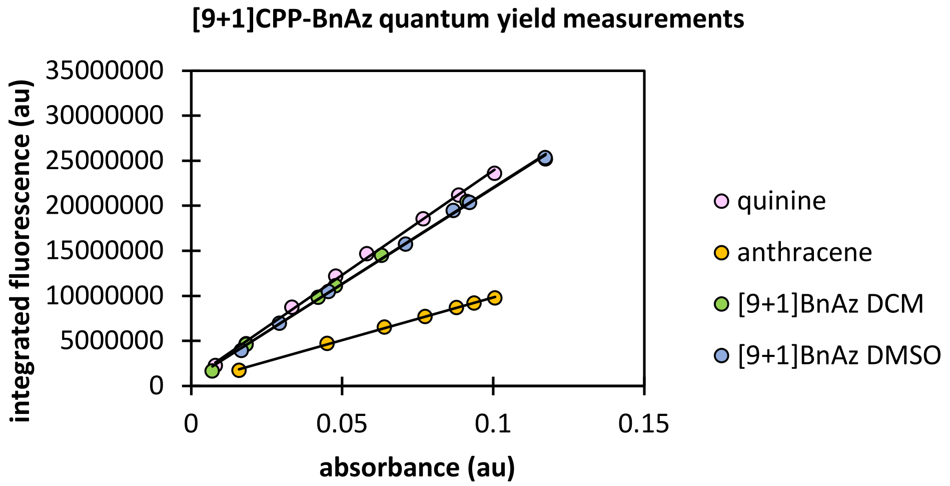

Figure 2.18. Quantum yield plot for **[9+1]CPP-BnAz**.

Table 2.15. Quantum yield data for **[9+1]CPP-BnAz**.

Compound	Solvent	Slope	Φ w.r.t. quinine	Φ w.r.t. anthracene	Avg. Φ	Std. dev.
quinine	0.1 M H_2SO_4 (*aq*)	2.32×10^8	0.60 (lit)	0.63	0.62	0.011
anthracene	ethanol	9.48×10^7	0.26	0.27 (lit)	0.26	0.0049
[9+1]BnAz	DCM	2.14×10^8	0.63	0.67	0.65	0.012
[9+1]BnAz	DMSO	2.13×10^8	0.68	0.72	0.70	0.013

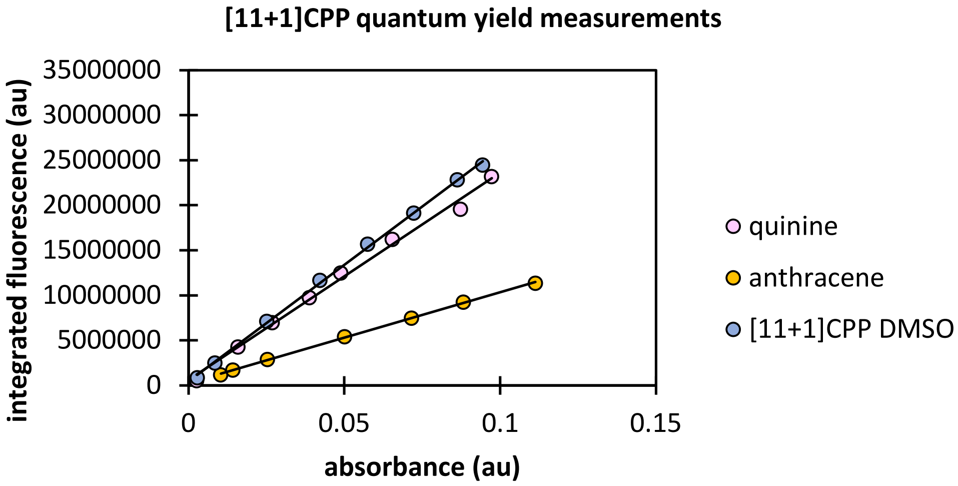

Figure 2.19. Quantum yield plot for **[11+1]CPP**.

Table 2.16. Quantum yield data for **[11+1]CPP**.

Compound	Solvent	Slope	Φ w.r.t. quinine	Φ w.r.t. anthracene	Avg. Φ	Std. dev.
quinine	0.1 M H_2SO_4 (*aq*)	2.30×10^8	0.60 (lit)	0.59	0.60	0.0028
anthracene	ethanol	1.01×10^8	0.27	0.27 (lit)	0.27	0.0013
[11+1]CPP	DMSO	2.59×10^8	0.83	0.82	0.83	0.0038

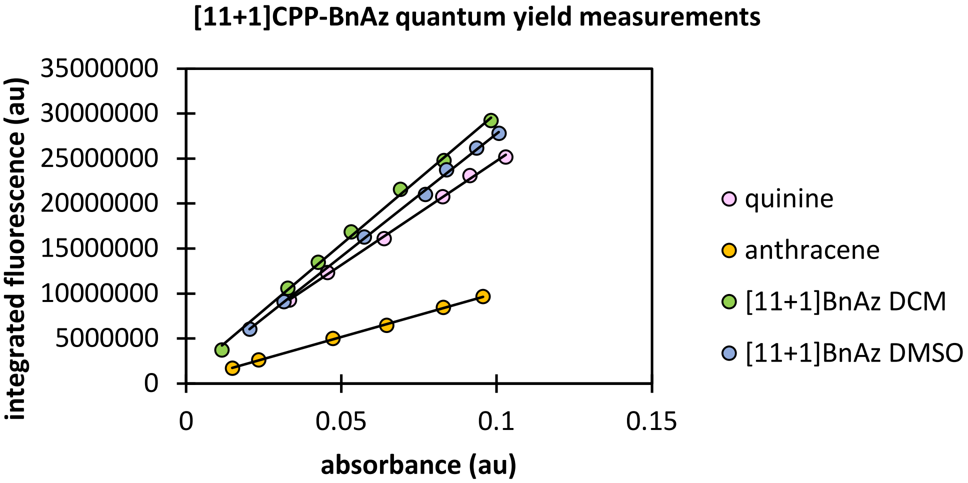

Figure 2.20. Quantum yield plot for **[11+1]CPP-BnAz**.

Table 2.17. Quantum yield data for **[11+1]CPP-BnAz**.

Compound	**Solvent**	**Slope**	**Φ w.r.t. quinine**	**Φ w.r.t. anthracene**	**Avg. Φ**	**Std. Dev.**
quinine	0.1 M H_2SO_4 (*aq*)	2.31×10^8	0.60 (lit)	0.61	0.60	0.0034
anthracene	ethanol	9.81×10^7	0.27	0.27 (lit)	0.27	0.0015
[11+1]BnAz	DCM	2.92×10^8	0.87	0.88	0.87	0.0050
[11+1]BnAz	DMSO	2.73×10^8	0.87	0.88	0.88	0.0049

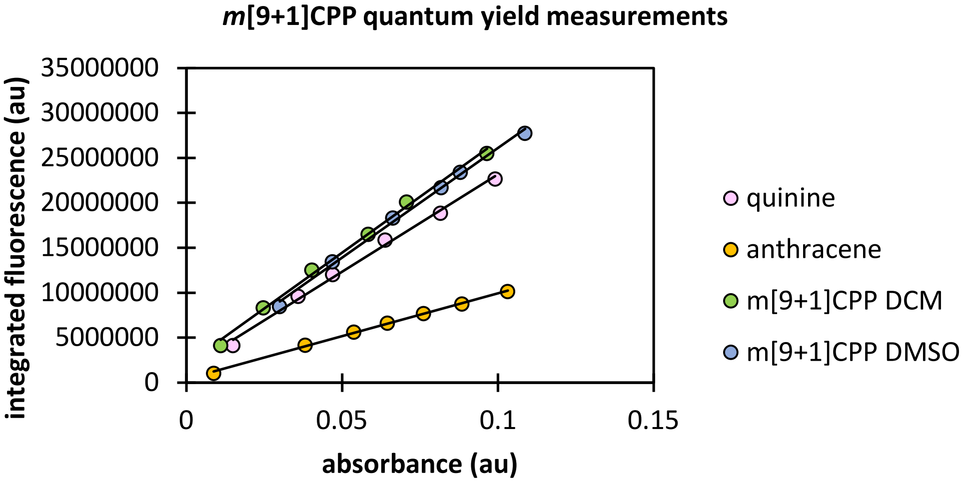

Figure 2.21. Quantum yield plot for ***m*[9+1]CPP**.

Table 2.18. Quantum yield data for ***m*[9+1]CPP**.

Compound	**Solvent**	**Slope**	**Φ w.r.t. quinine**	**Φ w.r.t. anthracene**	**Avg. Φ**	**Std. dev.**
quinine	0.1 M H_2SO_4 (*aq*)	2.16×10^8	0.60 (lit)	0.59	0.59	0.0053
anthracene	ethanol	9.57×10^7	0.28	0.27 (lit)	0.27	0.0024
m[9+1]CPP	DCM	2.49×10^8	0.79	0.77	0.78	0.0069
m[9+1]CPP	DMSO	2.44×10^8	0.83	0.81	0.82	0.0073

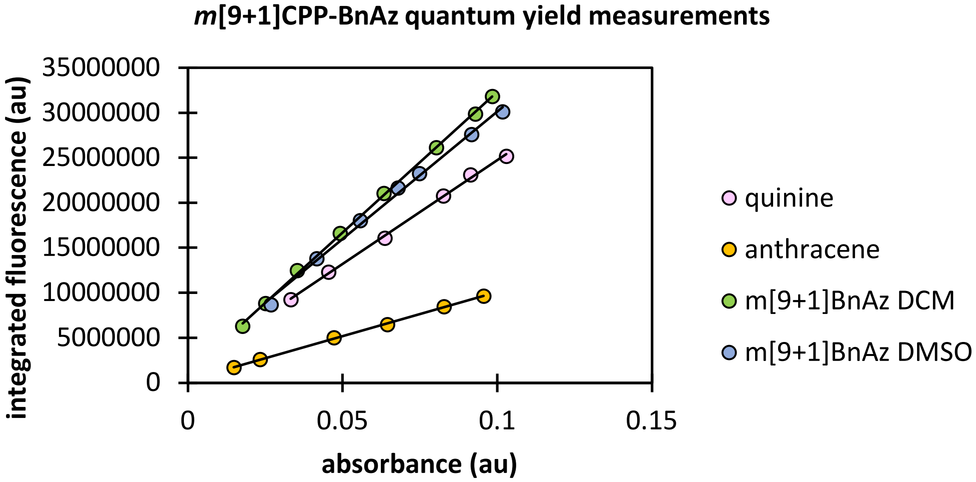

Figure 2.22. Quantum yield plot for ***m*[9+1]CPP-BnAz**.

Table 2.19. Quantum yield data for ***m*[9+1]CPP-BnAz**.

Compound	**Solvent**	**Slope**	**Φ w.r.t. quinine**	**Φ w.r.t. anthracene**	**Avg. Φ**	**Std. dev.**
quinine	0.1 M H_2SO_4 (*aq*)	2.31×10^8	0.60 (lit)	0.61	0.60	0.0034
anthracene	ethanol	9.81×10^7	0.27	0.27 (lit)	0.27	0.0015
m[9+1]BnAz	DCM	3.13×10^8	0.93	0.94	0.93	0.0053
m[9+1]BnAz	DMSO	2.83×10^8	0.91	0.92	0.91	0.0052

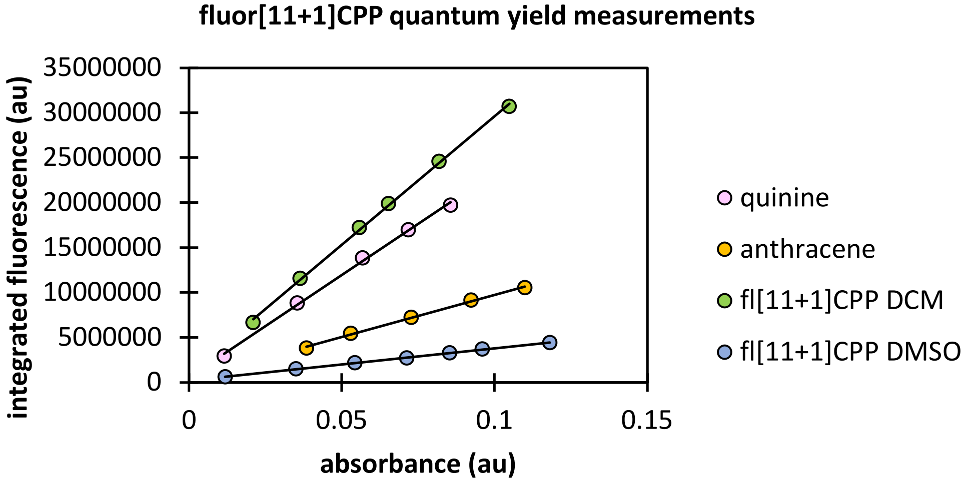

Figure 2.23. Quantum yield plot for **fluor[11+1]CPP**.

Table 2.20. Quantum yield data for **fluor[11+1]CPP**.

Compound	Solvent	Slope	Φ w.r.t. quinine	Φ w.r.t. anthracene	Avg. Φ	Std. dev.
quinine	0.1 M H_2SO_4 (*aq*)	2.27 × 10^8	0.60 (lit)	0.63	0.61	0.0092
anthracene	ethanol	9.40 × 10^7	0.26	0.27 (lit)	0.26	0.0040
fluor[11+1]CPP	DCM	2.86 × 10^8	0.86	0.90	0.88	0.013
fluor[11+1]CPP	DMSO	3.59 × 10^7	0.12	0.12	0.12	0.0018

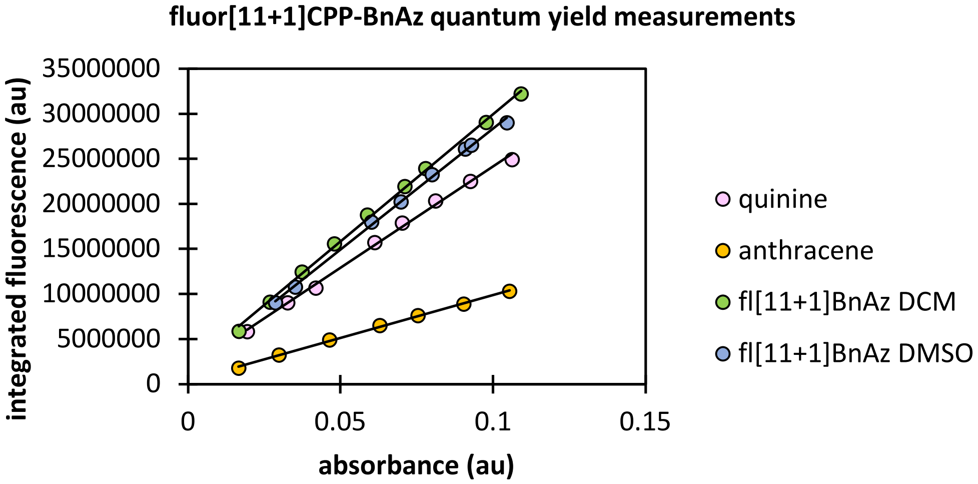

Figure 2.24. Quantum yield plot for **fluor[11+1]CPP-BnAz**.

Table 2.21. Quantum yield data for **fluor[11+1]CPP-BnAz**.

Compound	Solvent	Slope	Φ w.r.t. quinine	Φ w.r.t. anthracene	Avg. Φ	Std. dev.
quinine	0.1 M H_2SO_4 (*aq*)	2.25 × 10^8	0.60 (lit)	0.61	0.61	0.0038
anthracene	ethanol	9.53 × 10^7	0.27	0.27 (lit)	0.27	0.0017
fluor[11+1]BnAz	DCM	2.82 × 10^8	0.86	0.88	0.87	0.0054
fluor[11+1]BnAz	DMSO	2.68 × 10^8	0.88	0.90	0.89	0.0056

The following absorbance/emission traces show each [*n*+1]CPP and [*n*+1]CPP-BnAz in DCM or DMSO. Each compound of interest was dissolved in the appropriate solvent to an absorbance value of approx. 0.1. This sample was immediately measured in the fluorimeter. For fluorescence measurements, all compounds were excited at a wavelength of 340 nm with consistent excitation and emission slit widths of 1 nm. Absorbance and emission traces for **[11+1]CPP** were measured previously.[56]

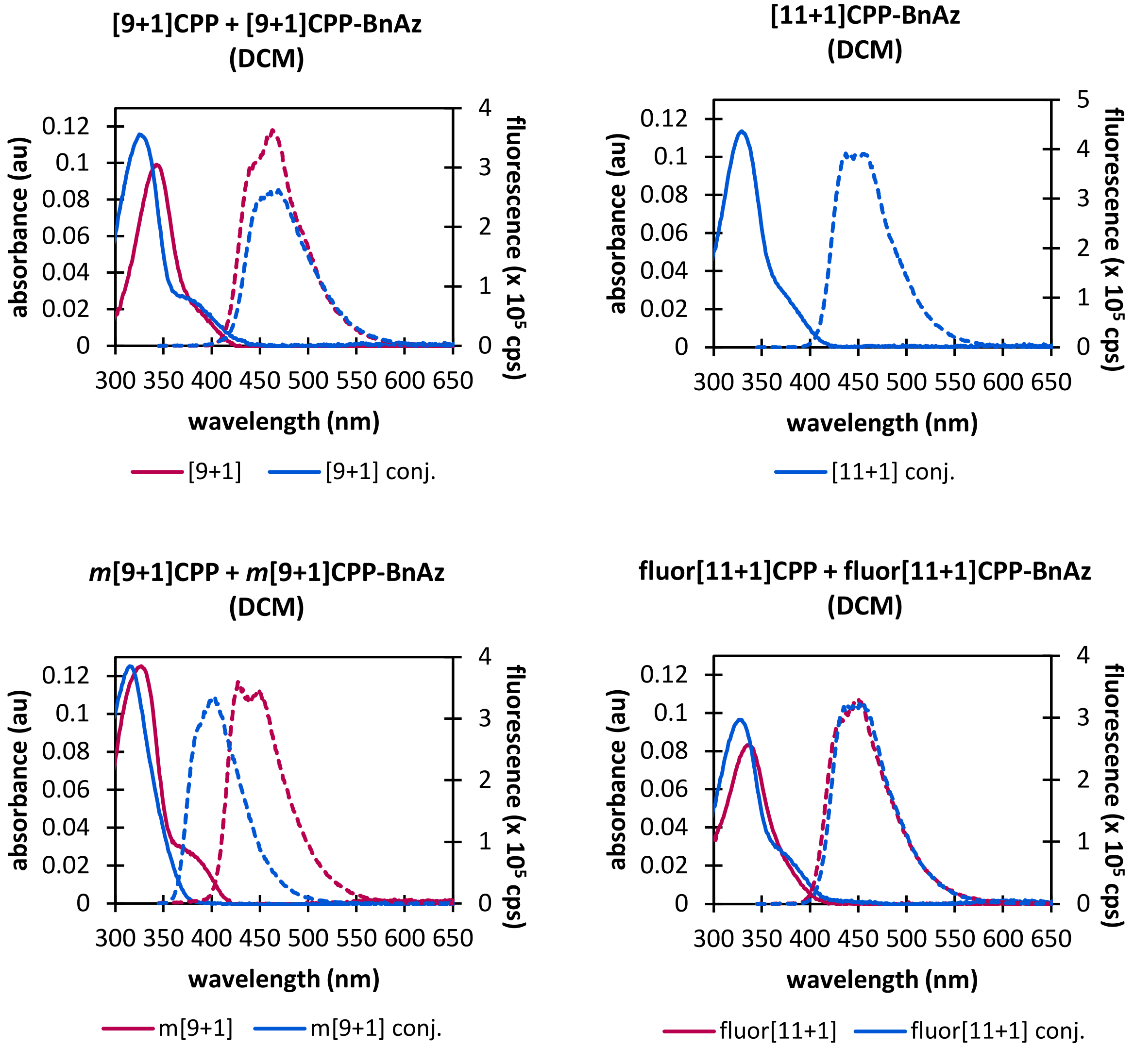

Figure 2.25. Absorbance and emission traces for [*n*+1]CPPs and their benzyl azide click products in DCM.

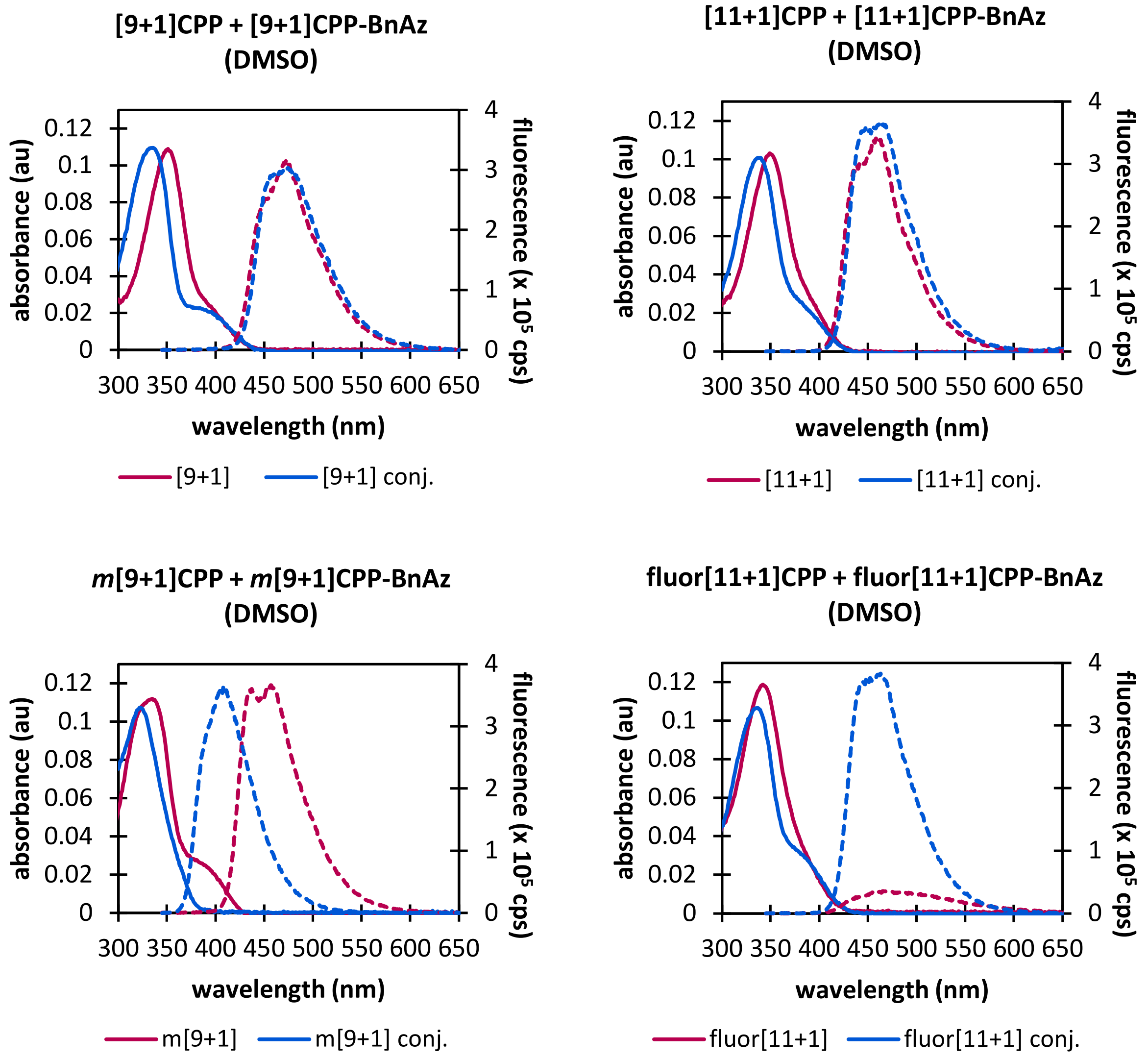

Figure 2.26. Absorbance and emission traces for [*n*+1]CPPs and their benzyl azide click products in DMSO.

Table 2.22. Wavelengths of maximum absorbance and fluorescence emission for each compound.

	$\lambda_{max,abs}$ (nm)		**$\lambda_{max,em}$ (nm)**	
Compound	**DCM**	**DMSO**	**DCM**	**DMSO**
[9+1]CPP	343	351	463	473
[9+1]CPP-BnAz	325	335	469	474
[11+1]CPP	341*	350	449*	460
[11+1]CPP-BnAz	329	338	437	464
m[9+1]CPP	327	333	427	457
m[9+1]CPP-BnAz	315	323	403	408
fluor[11+1]CPP	337	343	450	472
fluor[11+1]CPP-BnAz	328	336	451	463

*measured in previous publication.[56]

2.4.4 Kinetics Analysis with Benzyl Azide

All kinetics experiments were performed with the same stock of DMSO-d_6 with added dimethyl sulfone as an internal standard (14.5 mM, prepared by dissolving 0.0683 g dimethyl sulfone in 50.0 mL DMSO-d_6 from a fresh bottle with analytical glassware). This solution was kept under inert atmosphere in a Schlenk flask at room temperature. In each experiment, a batch of the [*n*+1]CPP was dissolved to saturation in the DMSO-d_6 stock solution. The solution was syringe-filtered and then transferred to a clean NMR tube. An initial quantitative ^{1}H NMR (4 scans, pre-scan delay of 25 s, 90° pulse) was collected for the [*n*+1]CPP. Then, benzyl azide (5-12 equivalents, actual concentration determined by comparison to internal standard) was added to the NMR tube and the solution was thoroughly vortexed to ensure adequate mixing. The tube was placed back in the NMR, the instrument was reshimmed, and set to collect quantitative ^{1}H NMR spectra at specific time increments (longer increments for slower reactions, shorter increments for faster reactions).

At the end of the experiments, the spectra were analyzed with Mestrenova software. Each spectrum was referenced at the DMSO residual solvent peak to 2.50 ppm. Automatic phase correction and baseline correction was applied. The NMRs were stacked and an integrals graph was prepared, with integrations performed over the full width of the peak. Integration widths for each peak were consistent for all experiments for the same [*n*+1]CPP. The initial concentration for each [*n*+1]CPP was determined by comparison of its most upfield doublet peak integration to peak integration for the internal standard. Concentration of benzyl azide for all spectra was determined by comparing integration of the benzyl azide peak at approx. 4.44 ppm to the peak integration for the internal standard. Product concentration was determined by comparing integration of the benzylic peak of the [*n*+1]CPP-BnAz at approx. 5.7 ppm to the peak integration for the internal standard. For all spectra except the initial [*n*+1]CPP spectrum, the concentration of [*n*+1]CPP was determined by subtracting the product concentration at that time point from the initial [*n*+1]CPP concentration.

Having determined the concentrations for each species at each time point, it was possible to plot

$$\frac{1}{[\mathrm{BnAz}]_0 - [\mathrm{CPP}]_0} \times \ln \frac{[\mathrm{CPP}]_0[\mathrm{BnAz}]}{[\mathrm{CPP}][\mathrm{BnAz}]_0}$$

as a function of time. Plotting the reaction until 30% completion* resulted in a linear data curve, the slope of which was taken as the second-order rate constant for the SPAAC reaction between the [*n*+1]CPP of interest and benzyl azide.

*in two cases, the reaction of **[11+1]CPP** was only monitored until 20% completion due to time constraints on the NMR instrument.

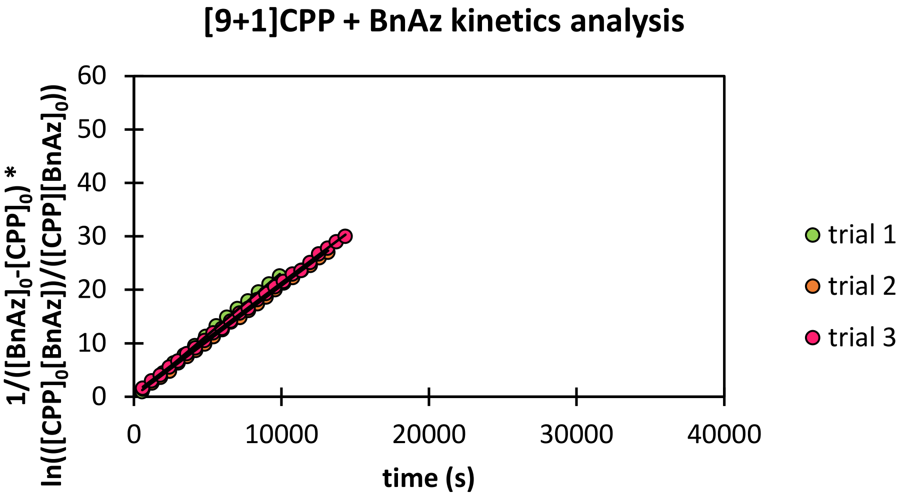

Figure 2.27. Kinetics analysis for SPAAC reaction of **[9+1]CPP** with benzyl azide in DMSO-d_6.

Table 2.23. Linear regression and derived second order rate constant for each trial of the SPAAC reaction of **[9+1]CPP** with benzyl azide in DMSO-d_6.

Trial	**Equation of line**	**Second-order rate constant**
1	y = 2.33E-03x + 1.21E-02	2.33×10^{-3} M^{-1} s^{-1}
2	y = 2.07E-03x + 1.07E-01	2.07×10^{-3} M^{-1} s^{-1}
3	y = 2.07E-03x + 6.44E-01	2.07×10^{-3} M^{-1} s^{-1}
avg.	-	2.2×10^{-3} M^{-1} s^{-1}
std. dev.	-	0.15×10^{-3} M^{-1} s^{-1}

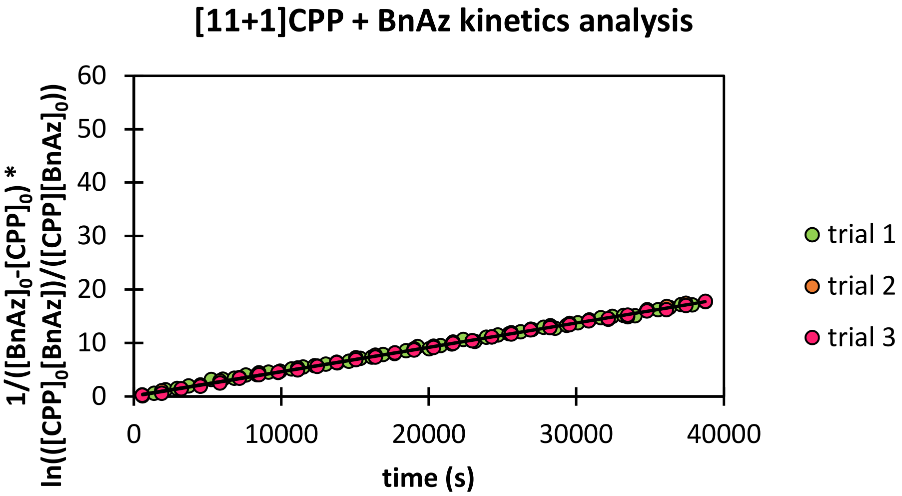

Figure 2.28. Kinetics analysis for SPAAC reaction of **[11+1]CPP** with benzyl azide in DMSO-d_6.

Table 2.24. Linear regression and derived second order rate constant for each trial of the SPAAC reaction of **[11+1]CPP** with benzyl azide in DMSO-d_6.

Trial	Equation of line	Second-order rate constant
1	y = 4.50E-04x + 2.32E-01	4.50×10^{-4} M^{-1} s^{-1}
2	y = 4.55E-04x + 1.70E-01	4.55×10^{-4} M^{-1} s^{-1}
3	y = 4.58E-04x - 4.75E-02	4.58×10^{-4} M^{-1} s^{-1}
avg.	-	4.5×10^{-4} M^{-1} s^{-1}
std. dev.	-	0.04×10^{-4} M^{-1} s^{-1}

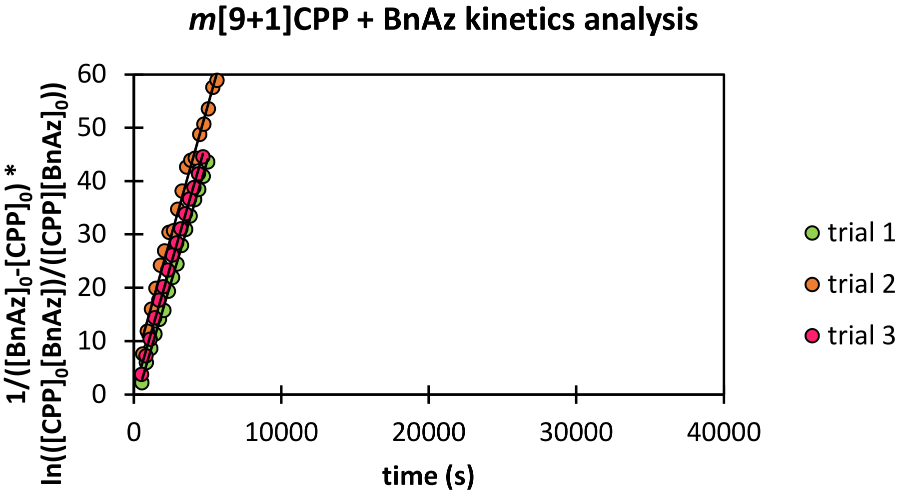

Figure 2.29. Kinetics analysis for SPAAC reaction of ***m*[9+1]CPP** with benzyl azide in DMSO-d_6.

Table 2.25. Linear regression and derived second order rate constant for each trial of the SPAAC reaction of ***m*****[9+1]CPP** with benzyl azide in DMSO-d_6.

Trial	Equation of line	Second-order rate constant
1	y = 9.26E-03x - 2.19E+00	9.26×10^{-3} M^{-1} s^{-1}
2	y = 9.86E-03x + 4.82E+00	9.86×10^{-3} M^{-1} s^{-1}
3	y = 9.58E-03x + 3.59E-01	9.58×10^{-3} M^{-1} s^{-1}
avg.	-	9.6×10^{-3} M^{-1} s^{-1}
std. dev.	-	0.3×10^{-3} M^{-1} s^{-1}

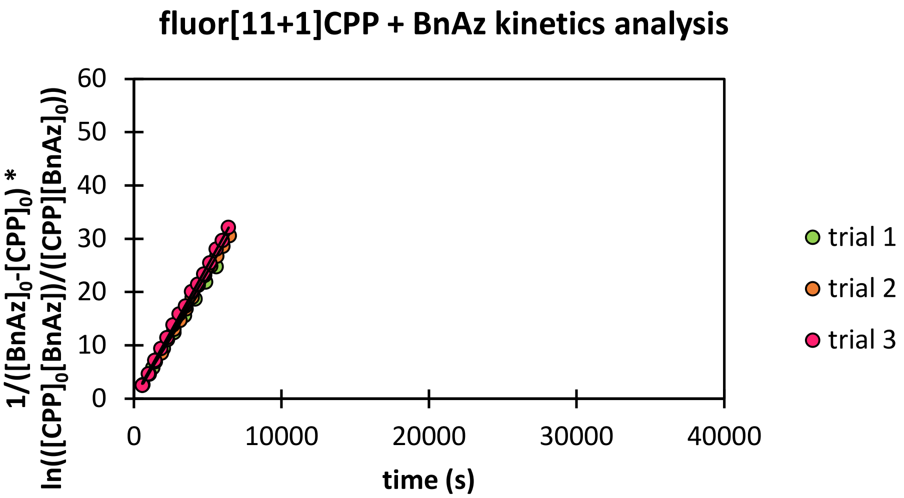
fluor[11+1]CPP + BnAz kinetics analysis

Figure 2.30. Kinetics analysis for SPAAC reaction of **fluor[11+1]CPP** with benzyl azide in DMSO-d_6.

Table 2.26 Linear regression and derived second order rate constant for each trial of the SPAAC reaction of **fluor[11+1]CPP** with benzyl azide in DMSO-d_6

Trial	Equation of line	econd-order rate constant
1	y = 4.44E-03x + 3.60E-01	4.44×10^{-3} M^{-1} s^{-1}
2	y = 4.80E-03x - 8.65E-02	4.80×10^{-3} M^{-1} s^{-1}
3	y = 4.98E-03x + 2.27E-01	4.98×10^{-3} M^{-1} s^{-1}
avg.	-	4.7×10^{-3} M^{-1} s^{-1}
std. dev.	-	0.3×10^{-3} M^{-1} s^{-1}

2.4.5 StrainViz

All input files, fragment geometries, and output files are available for download *via* Figshare at https://figshare.com/projects/Supporting_Information_of_Computational_results_StrainViz_for_Experimental_and_Theoretical_Elucidation_of_SPAAC_Kinetics_for_Strained_Alkyne-Containing_Cycloparaphenylenes/155192. Fragment geometries are shown below and in .xyz format.

Note: one alkyne fragment for each molecule with the smoothest optimization was included to emphasize the local strain between each [*n*+1]CPP and troubleshoot failed optimizations due to linear angles present in alkyne fragments.

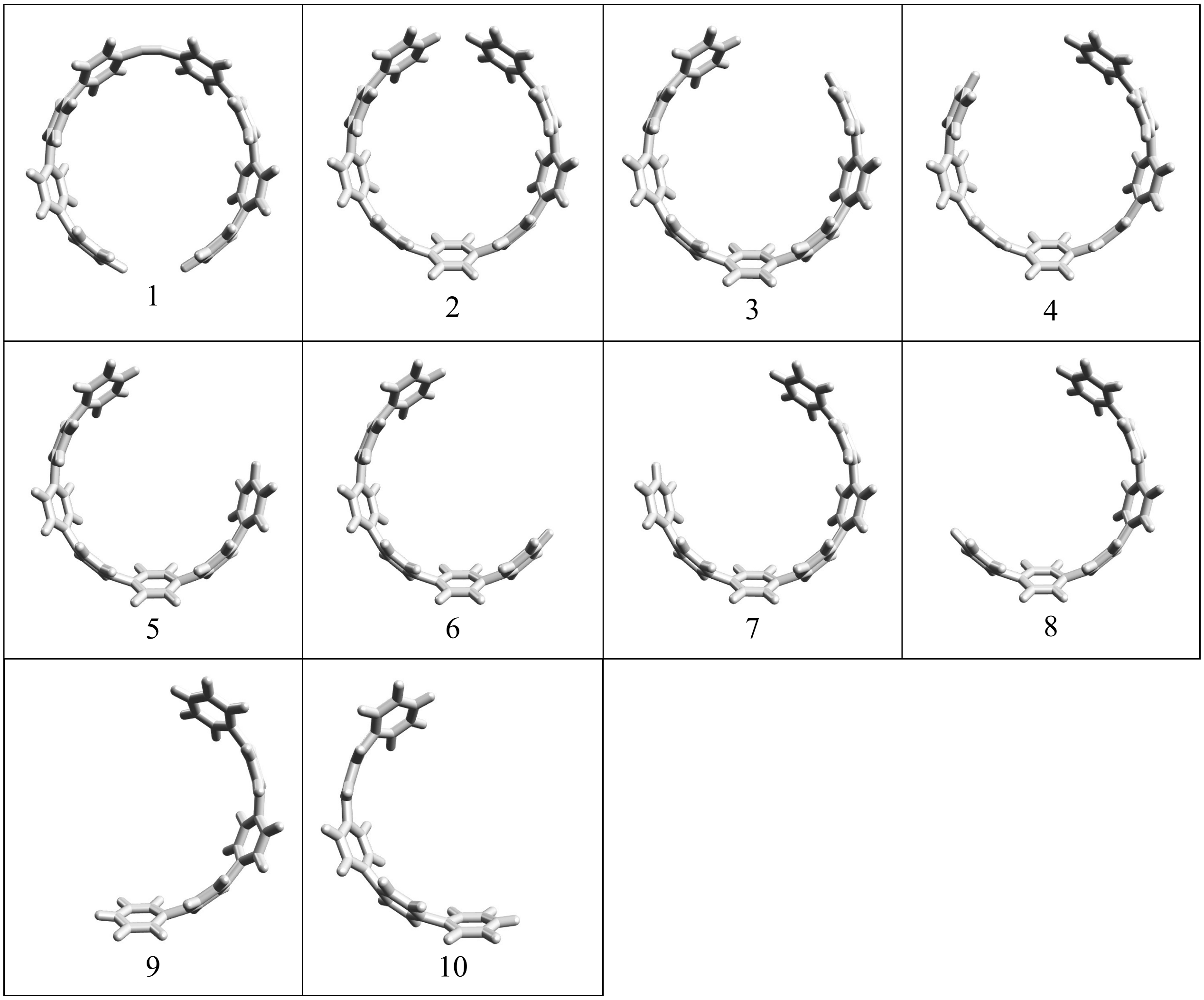

Figure 2.31. [9+1]CPP molecule fragments used for StrainViz.

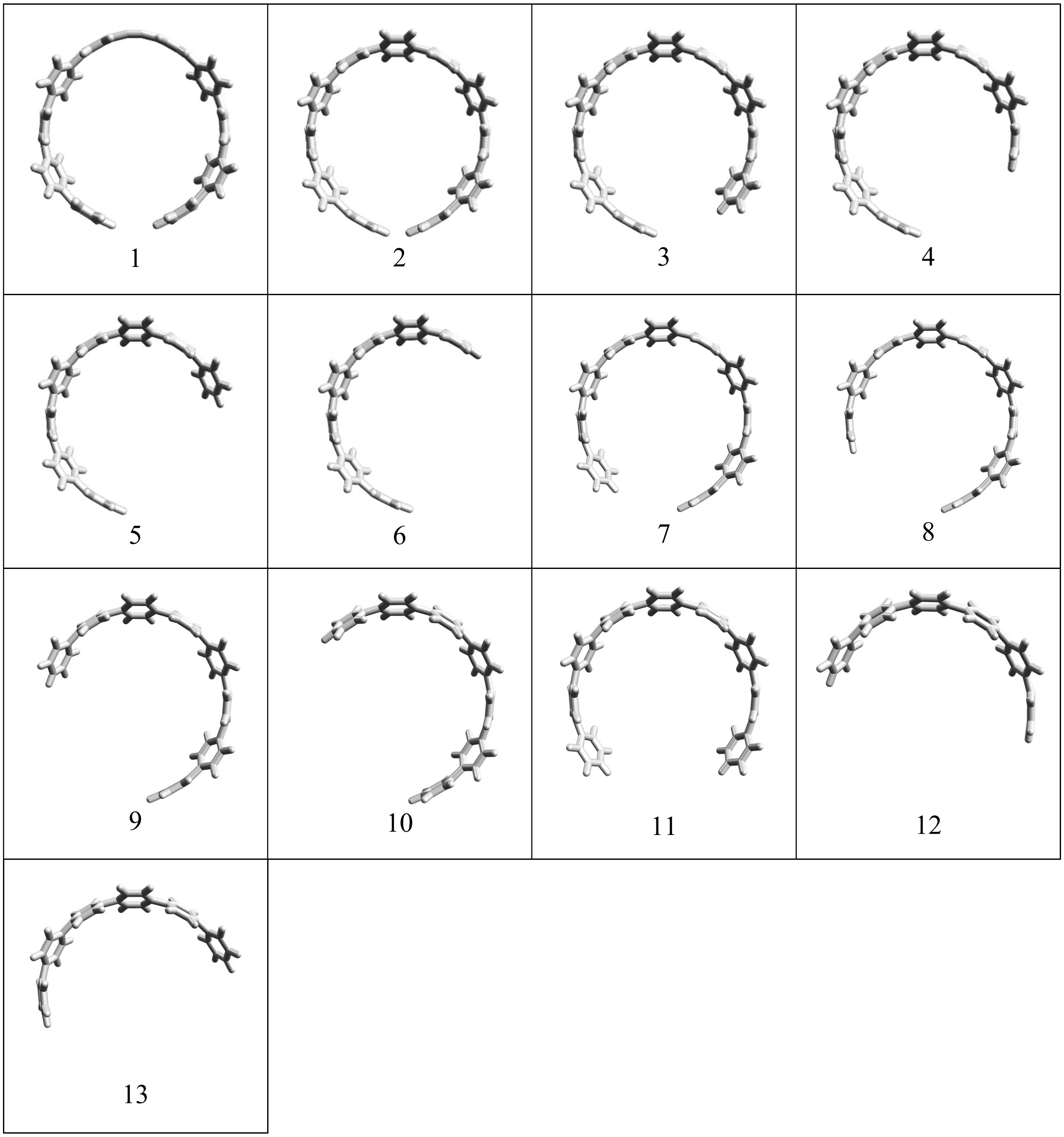

Figure 2.32. [11+1]CPP molecule fragments used for StrainViz.

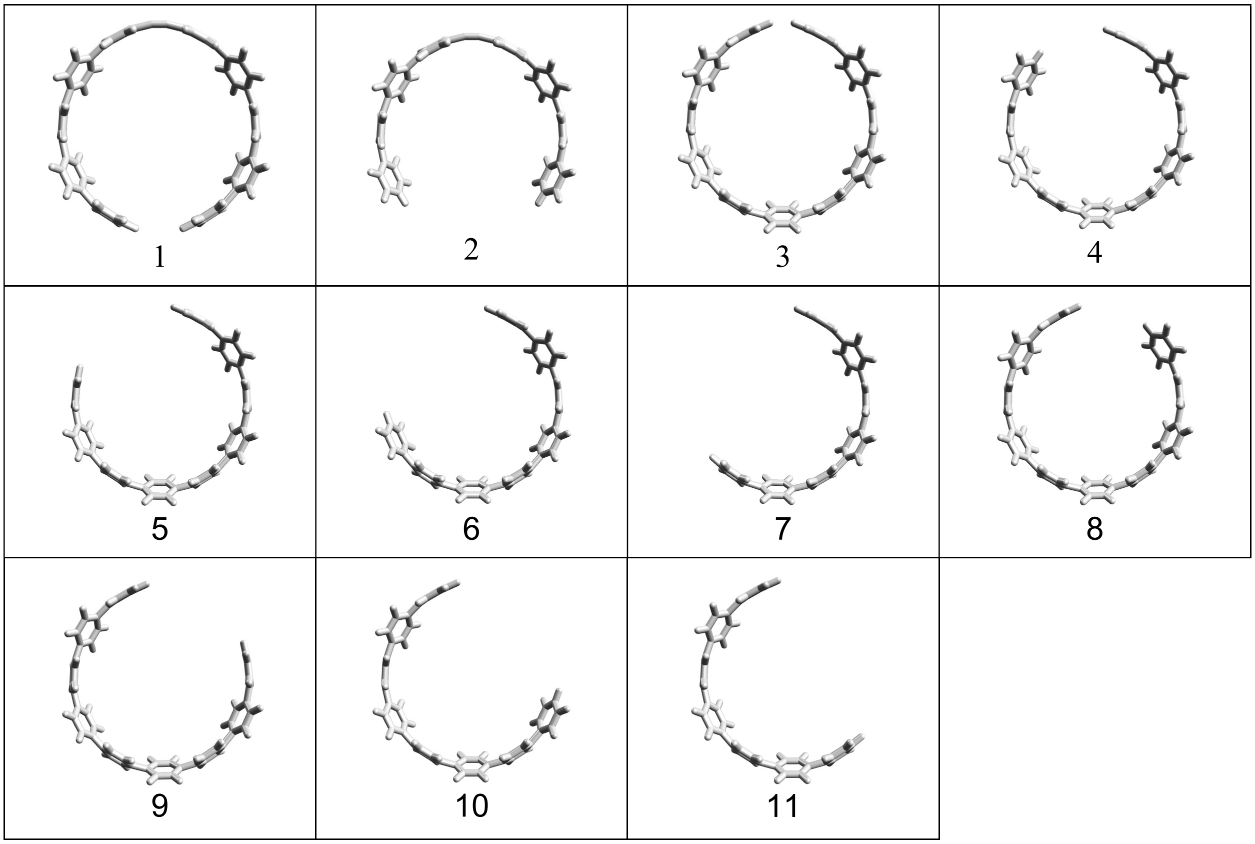

Figure 2.33. fluor[11+1]CPP molecule fragments used for StrainViz.

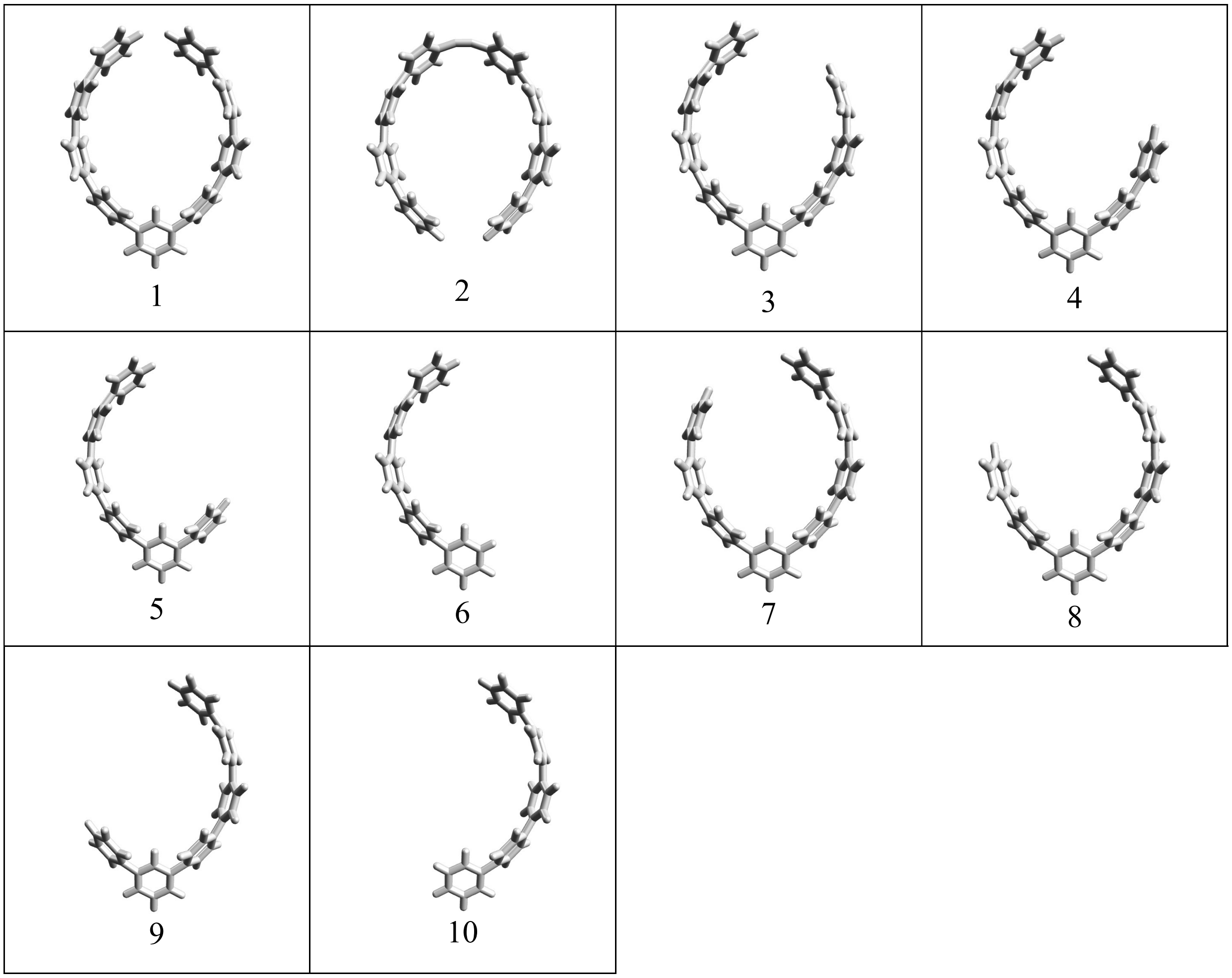

Figure 2.34. ***m*[9+1]CPP** molecule fragments used for StrainViz.

2.4.6 Transition State and Energy Calculations

All Gaussian output files for stationary points are available via Figshare with the following link, https://figshare.com/articles/figure/test/21648506

Table 2.27. Computed M06-2X/6-31+G(d,p) electronic and free energies, and activation barrier energies for **[11+1]CPP, [9+1]CPP, fluor[11+1]CPP, *m*[9+1]CPP, II.13, and II.14**, with benzyl azide in DMSO.

Compound	**E_{DMSO} (Hartree)**	**G_{DMSO} (Hartree)**	**$\Delta G^{‡}_{DMSO}$ (Hartree)**	**$\Delta G^{‡}_{DMSO}$ (kcal mol^{-1})**
benzyl azide	–434.9815687	–434.884810	---	---
[11+1]CPP	–2616.77369375	–2615.956344	---	---
fluor[11+1]CPP	–3013.60729751	–3012.827492	---	---
[9+1]CPP	–2154.80926912	–2154.142347	---	---
m[9+1]CPP	–2154.82946060	–2154.163188	---	---
II.13	–2985.63402421	–2984.833285	---	---
II.14	–2985.63609487	–2984.834431	---	---
[11+1]CPP-TS	–3051.73881391	–3050.800792	0.040362	25.3
[9+1]CPP-TS	–2589.77633131	–2588.988587	0.038273	24.2
fluor[11+1]CPP-TS	–3448.57505364	–3447.674029	0.03857	24.0
m[9+1]CPP-TS	–2589.79813545	–2589.011416	0.036582	23.0
II.13-TS	–3420.606007	–3419.682297	0.035798	22.5
II.14-TS	–3420.613547	–3419.687368	0.031873	20.0

Table 2.28. Computed activation free energies, distortion, and interaction energies for the reactions of **BnAz** with **[11+1]CPP, [9+1]CPP, fluor[11+1]CPP,** and ***m*[9+1]CPP** in DMSO. Energies are in Hartrees.

Compound	**E (TS)**	**$E_{\text{dist. hoop}}$**	**$E_{\text{dist. azide}}$**	**$E_{\text{int.}}$**
[11+1]CPP	–3051.73881391	–2616.76428495	–434.957454127	–0.017074833
[9+1]CPP	–2589.77633131	–2154.801036	–434.9586488	–0.016646434
fluor[11+1]CPP	–3448.57505364	–3013.59805123	–434.958366023	–0.018636387
m[9+1]CPP	–2589.79813545	–2154.821985	–434.960042404	–0.016108016
II.13	–2985.63402421	–2985.62430794	–434.956442407	–0.025256813
II.14	–3420.613547	–2985.62673930	–434.958292536	–0.028515524

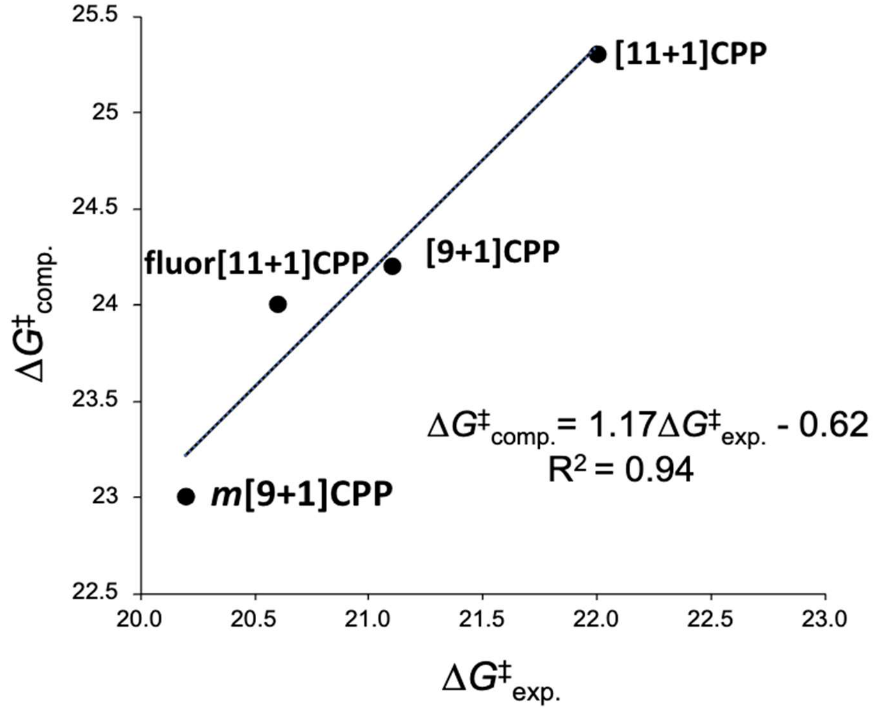

Figure 2.35. The computed activation free energies for **[11+1]CPP**, **[9+1]CPP**, **fluor[11+1]CPP**, and ***m*[9+1]CPP** versus the experimentally determined values. The activation free energies were determined in kcal mol^{-1}.

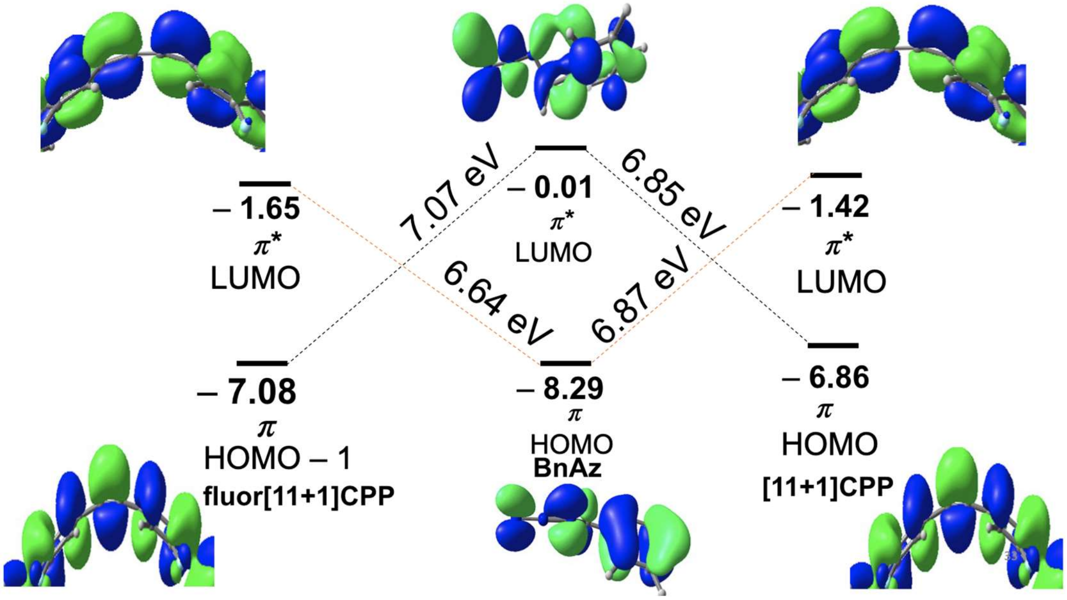

Figure 2.36. FMO diagram for the cycloaddition of **[11+1]CPP** and **fluor[11+1]CPP** with benzyl azide (**BnAz**) as calculated by M06-2X/6-31+G(d,p) using IEF-PCM: DMSO. Values are reported in eV. The HOMO-LUMO gap energies between the HOMO of **BnAz** and the LUMO of **[11+1]CPP** or **fluor[11+1]CPP** are shown using the dotted orange lines. The black dotted lines

are the HOMO-LUMO gap between the HOMO of **[11+1]CPP** or **fluor[11+1]CPP** versus the LUMO of **BnAz**.

2.5 Bridge to Chapter III

Chapter II focuses on the synthesis of new [*n*+1]CPPs with strain and electronic modulations which alter their kinetic and photophysical properties. As we worked to synthesize more reactive versions of the [*n*+1]CPP scaffold, we began to observe the formation of highly symmetrical [*n*+1]CPP derivatives which were eventually identified as trimeric versions of [*n*+1]CPPs produced *via* an alkyne cyclotrimerization reaction. Chapter III focuses on the systematic synthesis and characterization of such [*n*+1]CPP trimers.

CHAPTER III

PINWHEEL-LIKE CURVED AROMATICS FROM THE CYCLOTRIMERIZATION OF STRAINED ALKYNE CYCLOPARAPHENYLENES

Chapter III is adapted from a manuscript in preparation for submission entitled "Pinwheel-Like Curved Aromatics from the Cyclotrimerization of Strained Alkyne Cycloparaphenylenes." Synthesis of the molecules described herein was performed by myself and Tara Clayton. Characterization, photophysical measurements, and reaction screening were carried out by myself and Tara Clayton. StrainViz calculations were performed by Tavis Price. The manuscript was written primarily by myself with contributions from Tara Clayton and Tavis Price. Editorial assistance was provided by Prof. Ramesh Jasti. Crystallographic data collection and analysis was performed by Dr. Lev Zakharov. Prof. Ramesh Jasti provided guidance on the project.

3.1 Introduction

Curved aromatic hydrocarbons are a useful and continuously evolving class of carbon nanomaterials. Their deviation from the flat, planar topology expected of aromatic molecules can grant them advantages such as: (1) narrower HOMO-LUMO gaps due to poorer p-orbital overlap,[26] (2) heightened solubility due to less efficient self-stacking,[27] and (3) more productive intermolecular interactions such as convex-concave π-interactions.[28,86]

Since the landmark discoveries of fullerenes and carbon nanotubes,[36,37] many molecular topologies of curved aromatic hydrocarbons have been synthesized. Small molecules such as helicenes, corannulenes, saddle-shaped polyaromatics, and a variety of conjugated macrocycles are now accessible *via* controlled, bottom-up synthetic methods.[87] The structure-property relationships present in these molecules are complex, unique, and warrant further study.

Macrocycles in this class combine the attractive properties of curved aromatics with the added benefits of shape-persistent pores and host-guest capabilities.[28,86] Our group focuses on carbon nanohoops (also known as cycloparaphenylenes, abbrev. [*n*]CPP where *n* = number of phenylene units): strained aromatic macrocycles that represents the smallest cross-section of an armchair carbon nanotube.[39] Carbon nanohoops possess excellent solubility in many organic solvents.[41] Their photophysical properties are highly unusual, with most carbon nanohoops possessing a $\lambda_{max,abs}$ around 340 nm but varying fluorescence emission dictated by nanohoop size and functionality.[54] All carbon nanohoops possess a shape-persistent pore amenable to host-guest applications, and [10]CPP in particular has been shown to effectively host C_{60} and C_{70}.[28,88–93] Significantly, their syntheses are highly modular and tunable, allowing for the synthesis and study of nanohoops of many different sizes, shapes, functionalities, and properties.

Since 2018, our group has published three studies describing a subclass of nanohoops we refer to as [*n*+1]CPPs, wherein *n* refers to the number of phenylenes in the nanohoop "+1" internal alkyne incorporated into the macrocyclic backbone.[56,94,95] We have shown that this alkyne group is capable of undergoing strain-promoted reactions such as a [2+2] cycloaddition-retrocyclization with tetracyanoethylene and the strain-promoted azide-alkyne cycloaddition (SPAAC) with azides.[56] We have also shown that post-click reaction, **[11+1]CPP** is converted to a lasso shape capable of hosting C_{60} and C_{70}.[94] Our most recent paper focused on modulating the strain and electronics of this new family of CPPs in order to affect the kinetics of the SPAAC reaction.[95] We found that fluorination of the scaffold and incorporation of a *meta*-linkage to increase local strain at the alkyne were effective strategies for heightening SPAAC reactivity.

While working to synthesize more strained and electronically activated [*n*+1]CPPs, we observed a byproduct of the final reductive aromatization step with the same symmetry as the desired carbon nanohoop but lacking characteristic alkyne ^{13}C signals and any reactivity towards strain-promoted reactions. Further investigation of this byproduct revealed it to be a pinwheel-like molecule produced by alkyne cyclotrimerization involving three [*n*+1]CPPs.

These new molecules possess three shape-peresistent pores, and mark the next installment to a class of carbon nanohoop derivatives with multiple shape-persistent openings. Some other examples include 3D carbon nanocages from the groups of Itami, Tanaka, and Yamago, and the carbon nanopropellor and spiro[*n*,*n*]CPPs from our group (**Figure 3.1**).[96–101] Such void space grants the molecule intrinsic porosity—a useful attribute for the production of materials capable of gas adsorption.[102] In addition, the molecules described in this study demonstrate three-fold symmetry, which has been identified as a useful attribute in the field of quantum computing.[103,104] Herein, we describe the synthesis of four [*n*+1]CPP trimers—two derived from previously published [*n*+1]CPPs[56] and two derived from new [*n*+1]CPPs. We also provide detailed analysis of their photophysical properties, crystal packing structure where applicable, and strain profile.

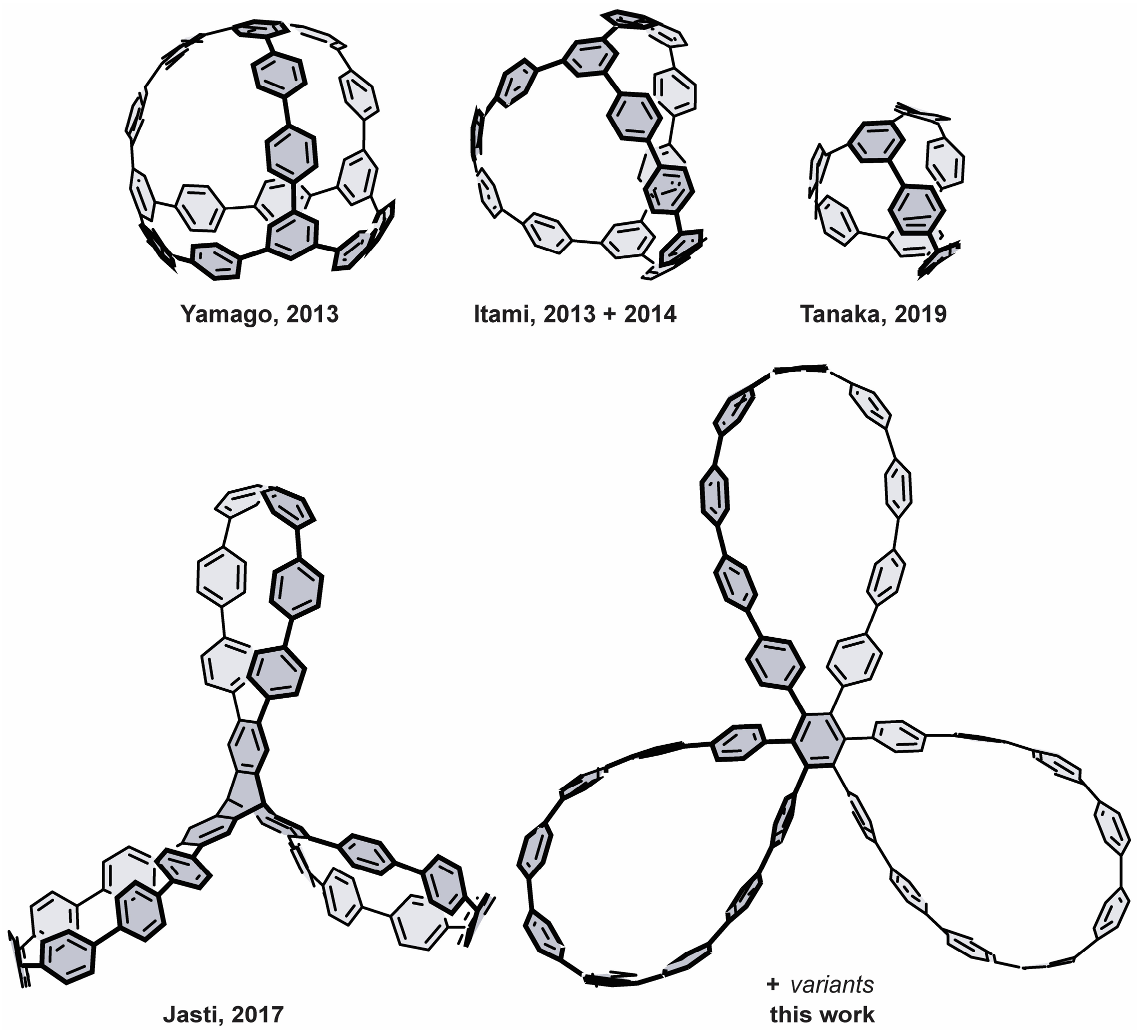

Figure 3.1. Previous examples of large nanohoop-type scaffolds with three-fold symmetry as well as the trimeric hoop molecules described in this work.

3.2 Results and Discussion

3.2.1 Synthesis

We first focused our efforts on the synthesis of **fluor[9+1] trimer** and ***meta*-fluor[9+1] trimer**. These two trimers are synthesized *via* nanohoops which have not yet been reported by our group and therefore will be described in detail here. The synthesis of macrocyclic precursor **III.1** was achieved by coupling two previously described CPP building blocks, **III.2** and **III.3** in a dilute Suzuki-Miyaura cross-coupling reaction. Through the same strategy, the synthesis of ***meta*-fluor[9+1] trimer** began with the coupling of **III.2** and **III.4** to yield macrocycle **III.5** (**Scheme 3.1**).

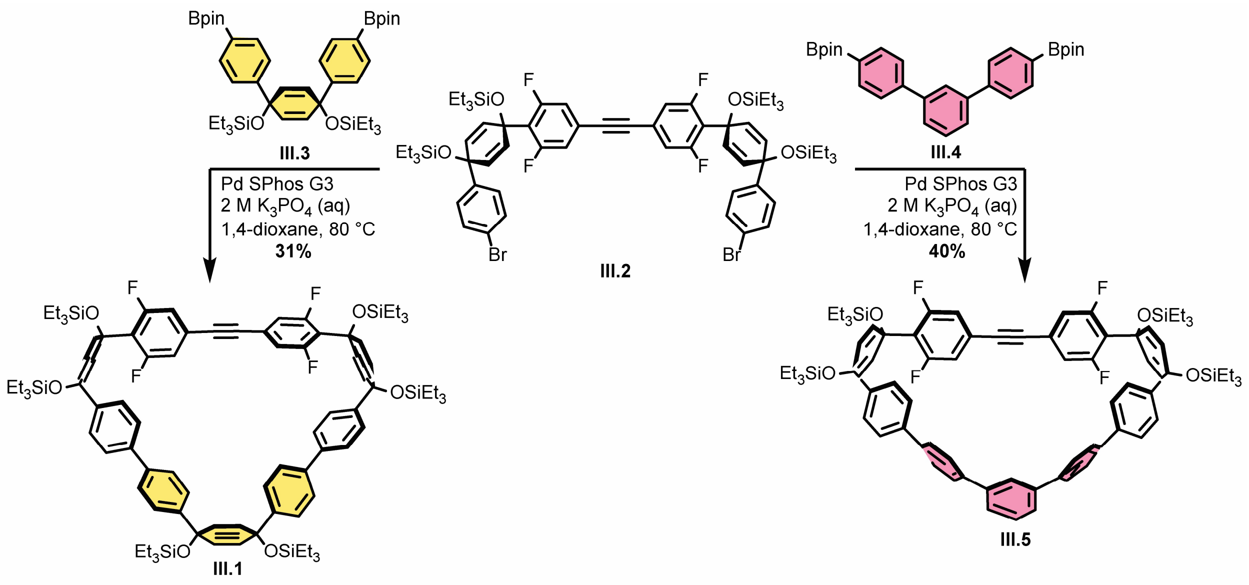

Scheme 3.1. Synthesis of macrocyclic intermediates **III.1** and **III.5**.

The remainder of the synthetic route for **fluor[9+1] trimer** is shown in **Scheme 3.2**. Deprotection of the silyl protecting groups with tetrabutylammonium fluoride (TBAF) in the presence of acetic acid yielded the free alcohol macrocyclic precursor which was converted *via* tin-mediated reductive aromatization to **fluor[9+1]CPP**. Finally, the treatment of **fluor[9+1]CPP** with $Pd_2(dba)_3$ (0.2 equiv.) in DCM yielded trimer **fluor[9+1] trimer** in 70% yield.

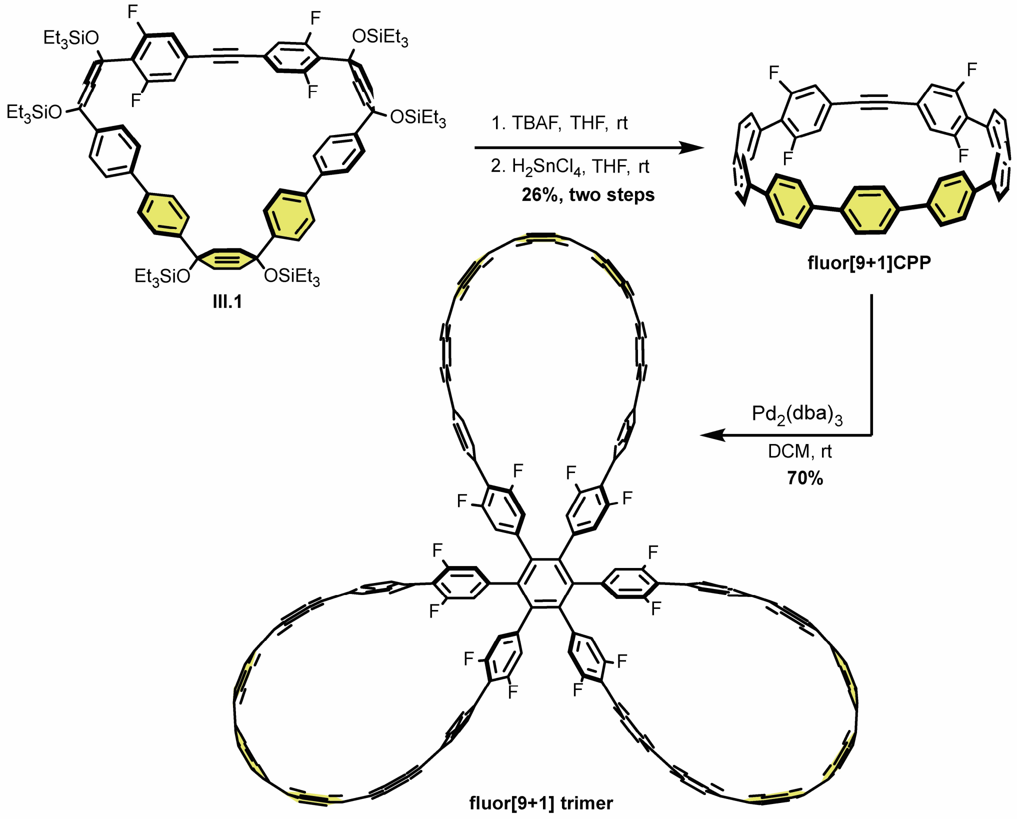

Scheme 3.2. Synthesis of **fluor[9+1] trimer**.

The synthesis of ***meta*-fluor[9+1] trimer** is shown in **Scheme 3.3** and began with the coupling of **III.2** and **III.4** to yield **III.5**. Deprotection of the silyl protecting groups *via* TBAF and acetic acid yielded the alcohol-containing macrocyclic precursor. Interestingly, treatment of this macrocycle with H_2SnCl_4 under a variety of reaction and workup conditions yielded only fleeting glimpses of the CPP product, **fluor-*m*[9+1]CPP**, making isolation and characterization unfeasible. However, small amounts of the **fluor-*m*[9+1] trimer** in these same mixtures suggested that it was possible to synthesize the trimer *via* a one-pot approach, starting from the free alcohol-containing macrocyclic precursor. In the event, treatment of the deprotected macrocycle with H_2SnCl_4 for one hour, followed by the addition of Ni(cod)DQ for one hour, yielded the **fluor-*m*[9+1] trimer** in good yield (52%) over three steps (see section 3.2.2 for more details).

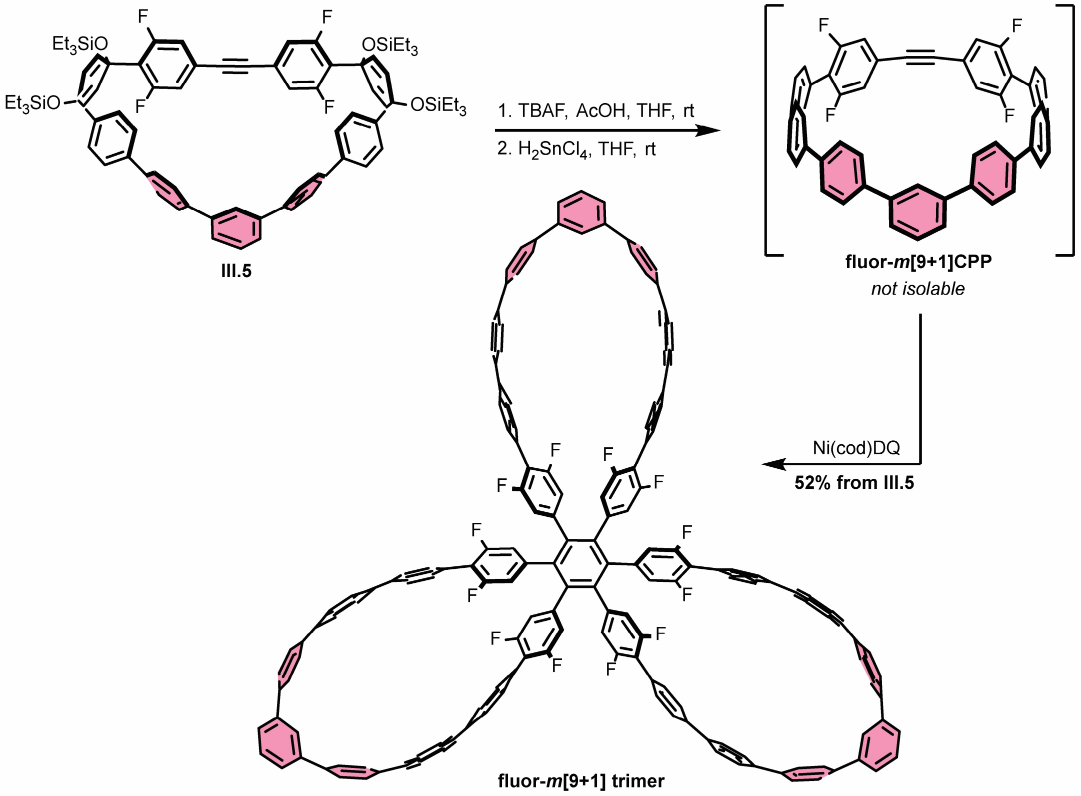

Scheme 3.3. Synthesis of **fluor-*m*[9+1] trimer**.

Trimerization of previously reported[56] **[9+1]CPP** and **[11+1]CPP** proceeded as shown in **Scheme 3.4**. From **[9+1]CPP**, treatment with $Pd_2(dba)_3$ in DCM yielded the **[9+1] trimer** in 95% yield; treatment of **[11+1]CPP** with $Pd_2(dba)_3$ yielded the **[11+1] trimer** in 63% yield.

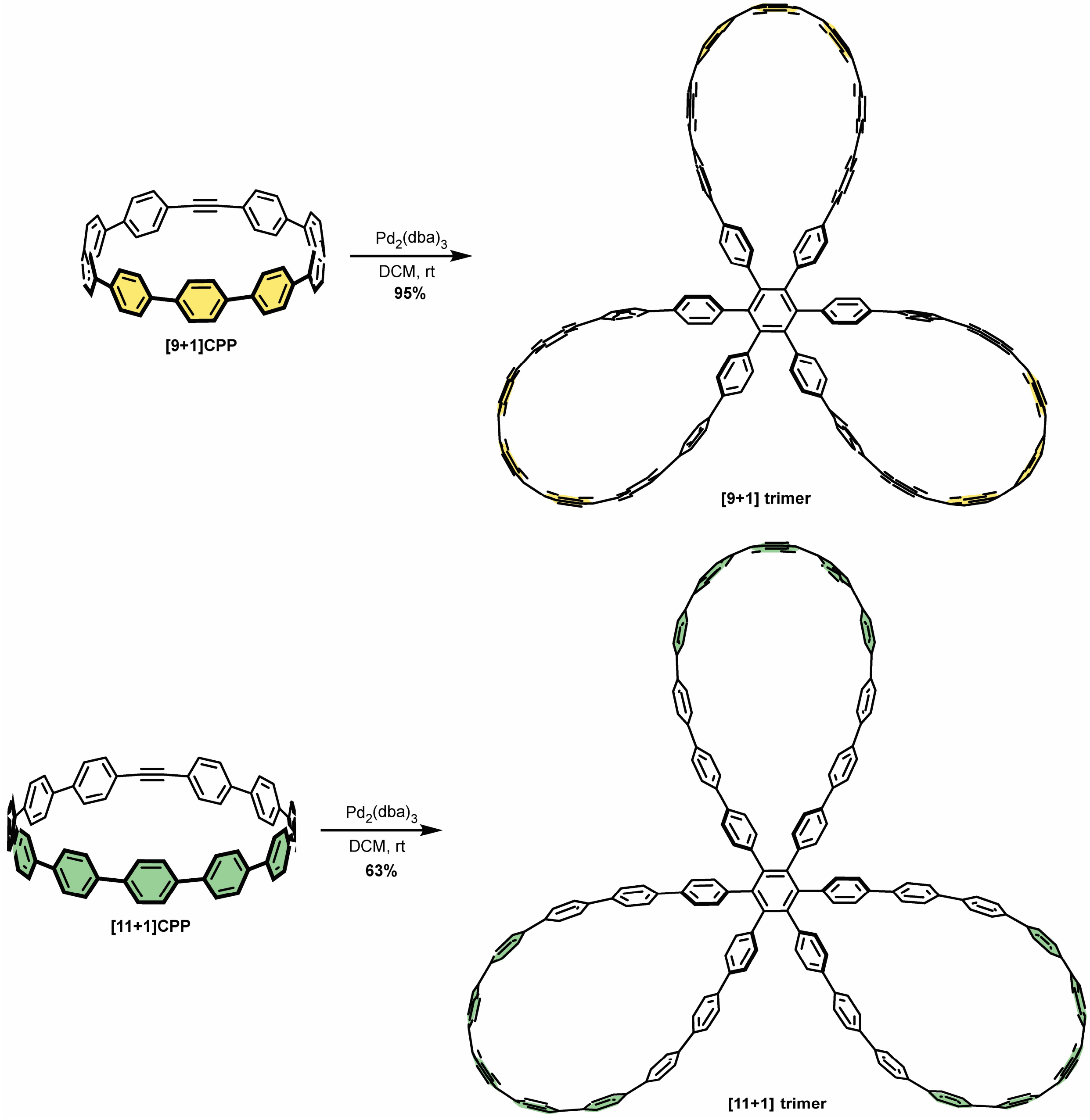

Scheme 3.4. Synthesis of **[9+1] trimer** and **[11+1] trimer**.

3.2.2 Screening of Alkyne Cyclotrimerization Transition Metal Catalysts

The formation of benzene derivatives *via* the transition metal-catalyzed [2+2+2] cycloaddition of alkynes has been known for over 70 years.[105] Several transition metals have proven useful in promoting cyclotrimerization including Ni, Co, Pd, Rh, Ru, Zr, and Ir.[106] Factors such as symmetry, sterics, stability, and functional group tolerance of the alkyne precursors inform choice of transition metal. In this work we study the self-trimerization of symmetric alkynes.

Cobalt has previously been reported to catalyze the formation of hexaarylbenzene systems *via* trimerization of diphenylacetylene derivatives.[107–109] The strained alkyne nanohoops contain curved diphenylacetylene units, inspiring our initial attempts to use of $Co_2(CO)_8$ as a catalyst. This failed to yield product despite the use of elevated temperatures and extended reaction times. The formation of a red-colored precipitate with ^1H NMR resembling starting material led us to believe that an unidentified cobalt complex may have been forming ($Co_2(CO)_8$ has been shown to act as an alkyne protecting group for strained alkynes). Considering these findings, we turned our attention to screening other commonly used transition metals.[110]

Quantitative ^{19}F NMR was used to determine percent conversion of **fluor[9+1]CPP** to **fluor[9+1] trimer** in the presence of a catalytic amount of Ni(cod)DQ, Wilkinson's catalyst ($RhCl(PPh_3)_3$), and $Pd_2(dba)_3$ at room temperature. Ni(0) was chosen because it has been shown to efficiently trimerize symmetric linear alkynes at lower temperatures and reaction times than cobalt.[111–113] Ni(cod)DQ is a relatively air-stable source of Ni(0). Rhodium-based catalysts are some of the most well-known for [2+2+2] cycloadditions, and among rhodium catalysts, Wilkinson's catalyst is one of the most frequently employed as it is stable and works well with a variety of alkyne substrates.[114,115] $Pd_2(dba)_3$ is a common catalyst for the trimerization of arynes, and we hypothesized that catalysts which promote cycloadditions of aryne species may be well suited for our inherently strained alkyne nanohoops.[106,116,117] As shown in **Figure 3.2**, we observed less than 1% conversion to **fluor[9+1] trimer** in the absence of catalyst, a modest 12% and 6% conversion in the presence of Ni(cod)DQ and Wilkinson's catalyst, respectively, and 100% conversion in the presence of $Pd_2(dba)_3$. As a control experiment, we subjected unstrained diphenylacetylene to very similar reaction conditions in the presence of $Pd_2(dba)_3$ and saw no reaction *via* ^1H NMR.

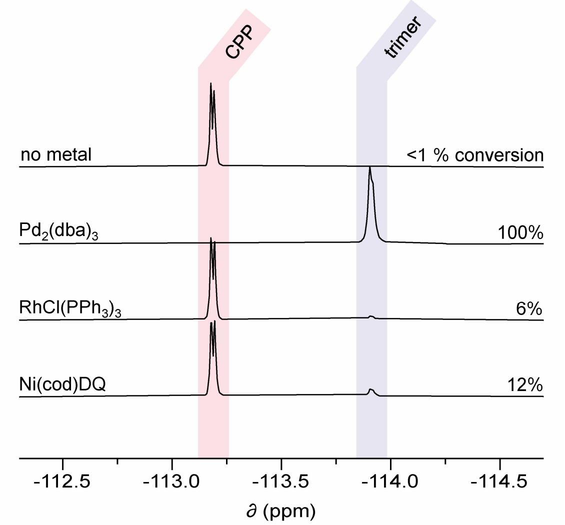

Figure 3.2. Quantitative ^{19}F NMR spectra and percent conversion of **fluor[9+1]CPP** to **fluor[9+1] trimer** in the presence of various transition metal catalysts. Experiment performed in $CDCl_3$ with 20% catalyst loading at 2 mM concentration (with respect to **fluor[9+1]CPP**).

As described in section 3.2.1, we were unable to isolate **fluor-*m*[9+1]CPP** due to its low stability. As such, **fluor-*m*[9+1] trimer** was synthesized by directly adding a cyclotrimerization catalyst to the H_2SnCl_4/CPP reaction mixture during the final aromatization step. We found that Ni(cod)DQ was the best cyclotrimerization catalyst for this system, and $Pd_2(dba)_3$ did not afford any isolable product in this two-step/one-pot procedure. All other strained alkyne nanohoops reported in this study were efficiently trimerized upon exposure to catalytic amounts of $Pd_2(dba)_3$ at room temperature with short reaction times.

3.2.3 X-ray Crystallographic Analysis

Single crystals suitable for x-ray analysis were successfully grown for **fluor[9+1] trimer** and **fluor-*m*[9+1] trimer** (**Figure 3.3**) with R factors of 11.56% and 9.51%, respectively. Despite our efforts, we were unable to grow suitable single crystals for **[9+1] trimer** and **[11+1] trimer**. The unit cells shown in **Figure 3.3** indicate the very different packing patterns observed between the two isomers. The all-para **fluor[9+1] trimer** packs much more loosely with few close contacts between trimer molecules and a significant amount of solvent (1,4-dioxane), some of which could be resolved though they are not included in **Figure 3.3** for clarity. In contrast, the packing for **fluor-*m*[9+1] trimer** appears denser.

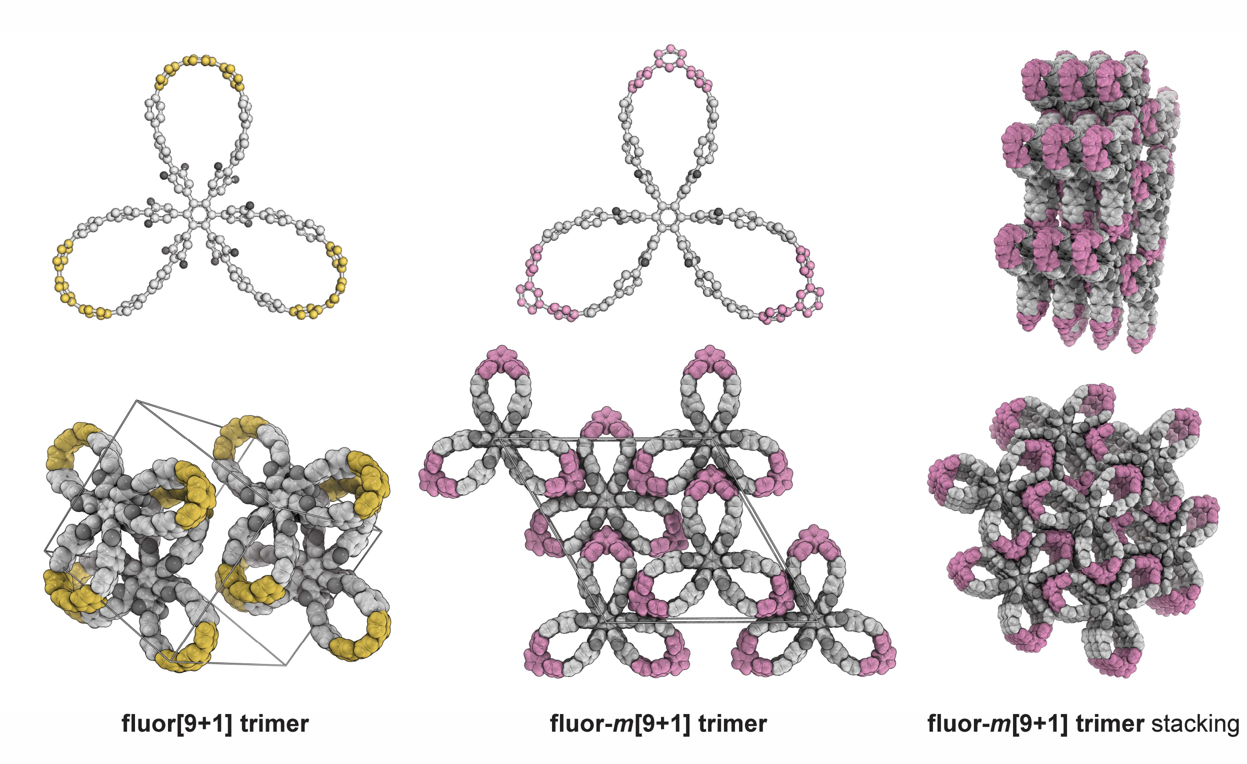

Figure 3.3. X-ray crystallographic data for **fluor[9+1] trimer** (yellow) and **fluor-*m*[9+1] trimer** (pink).

The packing of the **fluor-*m*[9+1] trimer** is noteworthy due to the fact that the extended structure would possess solvent-filled columnar channels. Unfortunately, the single crystals of **fluor-*m*[9+1] trimer** were extremely fragile, leading us to suspect that they may not be amenable to solvent removal in preparation for gas adsorption studies. Nonetheless, the close and ordered packing we observe for **fluor-*m*[9+1] trimer** could prove a good jumping-off point for design of future trimers with a similar shape and stronger intermolecular interactions that could withstand solvent evacuation.

3.2.4 Photophysical Properties

Like many carbon nanohoops and their derivatives,[41,48,54,118] the molecules synthesized herein possess interesting photophysical characteristics. The photophysical data for each trimer as well as **fluor[9+1]CPP** is displayed in **Figure 3.4** and **Table 3.1**. The absorbance and fluorescence traces of each molecule in polar (DMSO) and nonpolar (DCM) solvent display a few general trends. In every case, the observed $\lambda_{max,abs}$ and $\lambda_{max,em}$ are bathochromically shifted when measured in DMSO, though generally only by a few nanometers (with the exception of **fluor[9+1]CPP**, *vide infra*). We observe that in almost all cases, the $\lambda_{max,abs}$ occurs at approximately 340 nm as is typical for carbon nanohoops and their derivatives.[54]

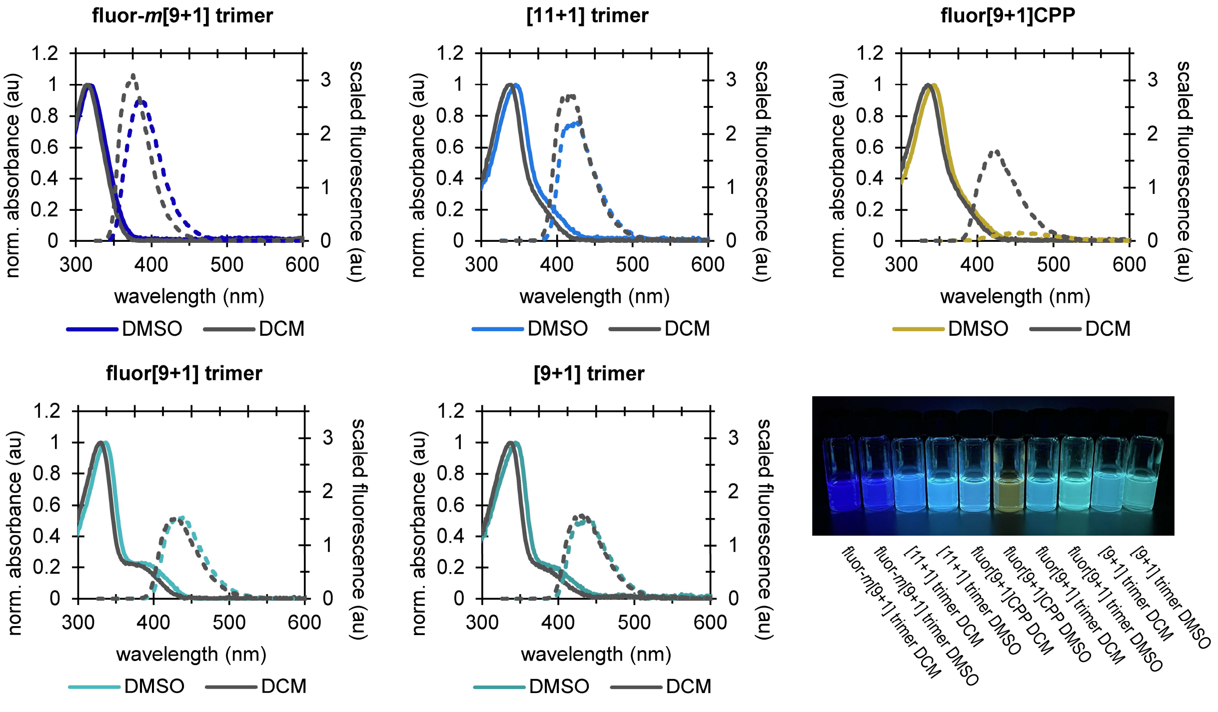

Figure 3.4. Photophysical data for **fluor[9+1]CPP** and the **trimer** molecules described herein. Absorbance traces (solid lines) were normalized such that each abs_{max} had a value of 1. Fluorescence traces (dashed lines, collected with an excitation wavelength of 330 nm and slit widths of 1 nm) were scaled accordingly.

Table 3.1. Photophysical data for **fluor[9+1]CPP** and **trimers**.

Compound	**λ_{max} Absorbance (nm)**		**λ_{max} Emission (nm)**		**Quantum yield (Φ)**		**Molar absorptivity (M^{-1} cm^{-1})**
	DCM	**DMSO**	**DCM**	**DMSO**	**DCM**	**DMSO**	**DCM**
[11+1] trimer	338	345	454	468	0.69	0.67	
[9+1] trimer	337	344	472	487	0.42	0.48	
fluor[9+1]CPP	335	343	463	507	0.49	0.07	$1.03 \pm 0.04 \times 10^5$
fluor[9+1] trimer	329	337	472	485	0.4	0.46	$3.18 \pm 0.21 \times 10^5$
fluor-*m*[9+1] trimer	315	317	401	418	0.88	0.88	$3.33 \pm 0.08 \times 10^5$

Full characterization of all-hydrocarbon **[9+1]** and **[11+1] trimers** is ongoing, but these molecules seems to possess photophysical properties very similar to the parent **[9+1]CPP** and **[11+1]CPP** which were described previously.[56,95] As would be expected, $\lambda_{max,em}$ is redder for the smaller nanohoop derivative, **[9+1] trimer**, in comparison to **[11+1]CPP**. **Fluor[9+1] trimer** shares many photophysical characteristics with **[9+1] trimer**, with the most notable attribute of both molecules being a significant absorbance shoulder at approximately 400 nm. As has been observed previously, we speculate that this shoulder could be due to more symmetry-allowed transitions at the approximate energy of the HOMO-LUMO transition, which is symmetry-forbidden in most carbon nanohoops.[48] **Fluor[9+1]CPP** exhibits a red-shifted and significantly diminished fluorescence emission in DMSO as compared to DCM, as has been observed for closely related **fluor[11+1]CPP**.[95] We hypothesize that **fluor[9+1]CPP** has a polar excited state, caused by the electron-withdrawing fluorines, that is more stabilized in polar solvent; this resultant narrowing of the energy gap between lowest energy excited state and ground state in turn results in the red-shifted maximum emission.[119] Finally, **fluor-*m*[9+1] trimer** displays the most hypsochromic absorbance and emission, which we attribute to a significant lack of strain in the structure.[48]

Quantum yield measurements were performed using the relative quantum yields method as described by Horiba Scientific,[61] with a consistent excitation wavelength (330 nm) for all compounds and standards. **Fluor-*m*[9+1] trimer** exhibits the highest quantum yields of the series: 0.88 in both DCM and DMSO. **[11+1] trimer**, **[9+1] trimer**, and **fluor[9+1] trimer** possess good quantum yields in both DCM and DMSO ranging from 0.69 to 0.4. Finally, **fluor[9+1]CPP** displays a quantum yield of 0.49 in DCM but this value drops to only 0.07 in DMSO. This result can most likely be ascribed to a polarized donor-acceptor-type excited state, which, in polar solvents, favors relaxation *via* nonradiative pathways.[119,120]

The available results of molar absorptivity measurements for these molecules are reported in **Table 3.1**. Interestingly, it was observed for **fluor[9+1]CPP** and **fluor[9+1] trimer** that trimerization essentially produced a molecule with triple the molar absorptivity as the parent nanohoop (within error). This is an exciting result suggesting that the light absorption ability of the nanohoop is additive and maintained even after trimerization.

3.2.5 StrainViz Analysis

Calculations were performed with the Gaussian09 package at the B3LYP/6-31G(d) level of theory for all structures.[62] Optimized geometries were obtained by requesting Rational Function Optimization "rfo" methods. Each parent nanohoop and cyclotrimerized products were analyzed *via* StrainViz[59] and referenced to the most strained structure, **fluor-*m*[9+1]CPP** (**Figure 3.5**). The quantitative results of these calculations are shown in **Figure 3.6** and **Table 3.2**.

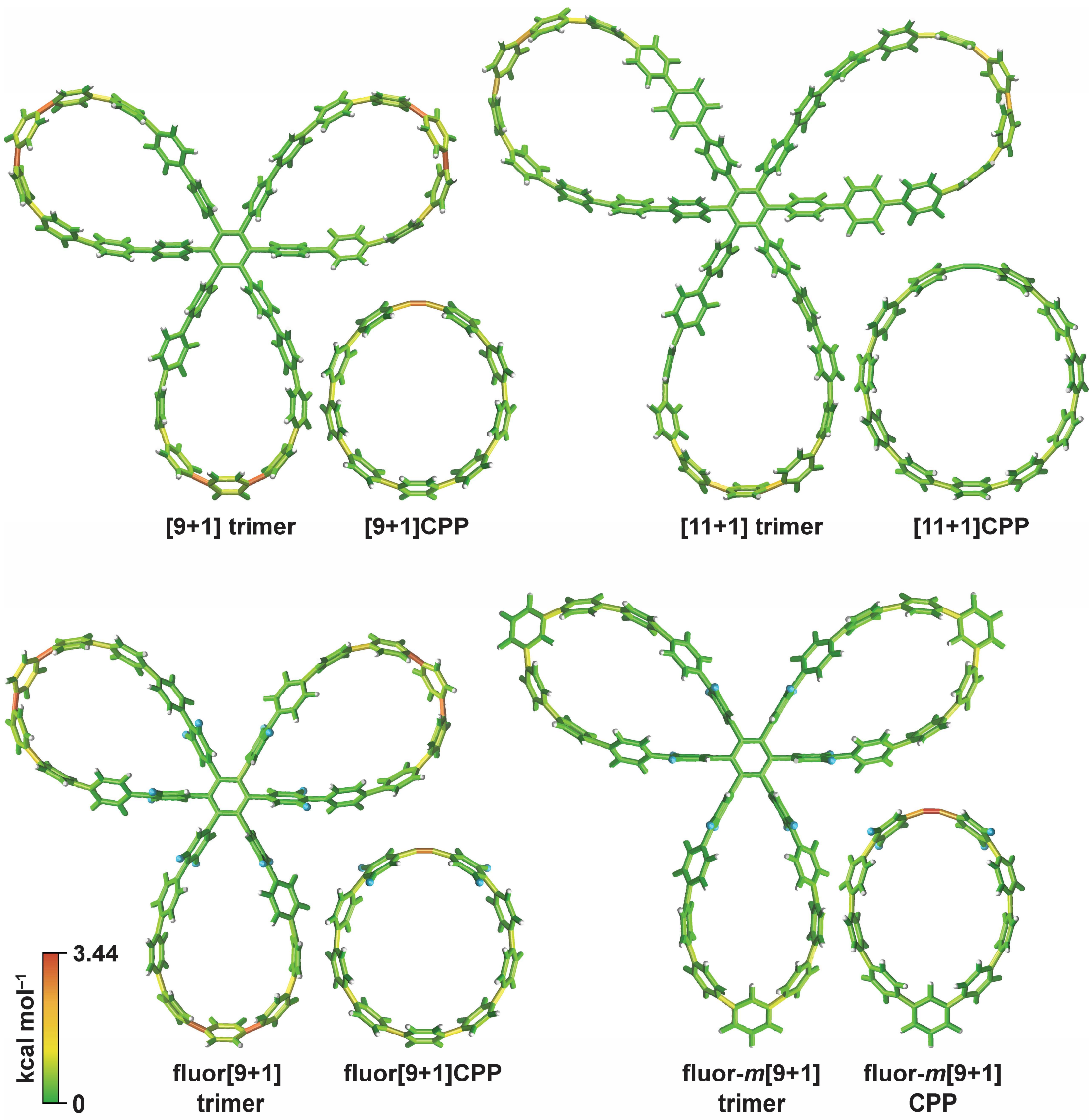

Figure 3.5. StrainViz structures for each trimer and its respective [*n*+1]CPP (**fluor-*m*[9+1]CPP** was not isolated but is shown here for completeness).

Overall, the strain of the nanohoops is localized onto the alkyne as we have observed previously.[95] However, upon trimerization, the strain becomes localized at the opposite side of the nanohoop—this is consistent with our understanding of how strain is distributed in macrocycles.[59] Linear strips of phenylenes tend to localize the strain as the substitution pattern on the opposite side of the nanohoop changes from *para* to *meta* or *ortho* connectivity. Trimers, other than the **fluor-*m*[9+1] trimer**, have greater localized strain due to the change in connectivity from alkyne to *ortho*-phenylene. Additionally, all of the trimers have total strain values equivalent to less than three times the total strain of the precursor alkyne nanohoops (*e.g.* 130 kcal mol^{-1} for **fluor[9+1] trimer** vs. 56 kcal mol^{-1} for **fluor[9+1]CPP**). These findings indicate that the total strain decreases post-trimerization. However, the local strain is increased for the *para* substituted alkyne nanohoops post-trimerization: 3.10 kcal kcal mol^{-1} for **fluor[9+1] trimer** vs. 2.78 kcal kcal mol^{-1} for **fluor[9+1]CPP**. Understanding how the strain is allocated within the alkyne-containing nanohoop and trimers could serve as a useful tool for altering the photophysical properties of these materials. As addressed computationally, localizing strain onto electron acceptors within a nanohoop can result in larger bathochromic shifts in the emission profile.[121]

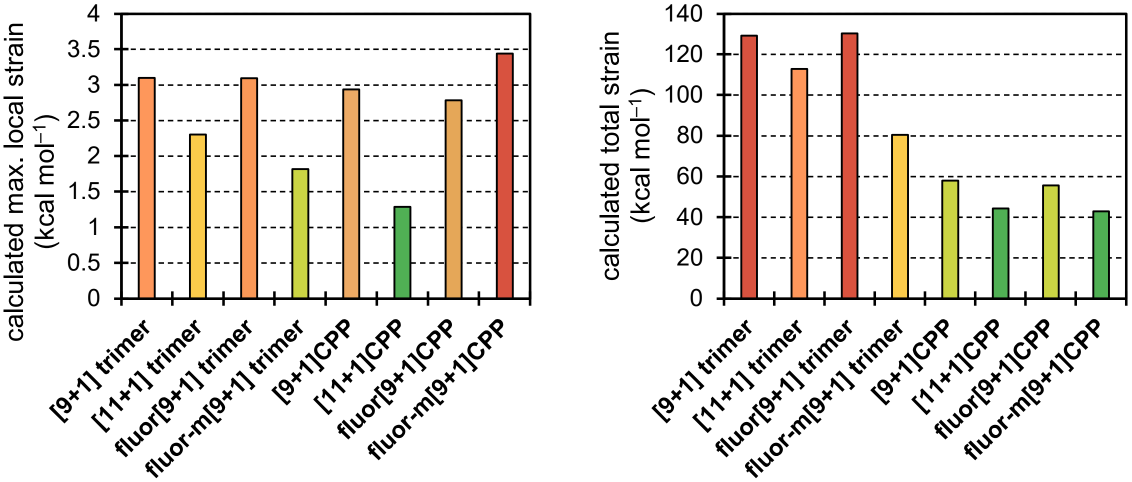

Figure 3.6. Maximum local strain (left) and total strain (right) for each trimer and [*n*+1]CPP, as calculcated *via* StrainViz.

Table 3.2. Tabulated strain data as determined by StrainViz.

Molecule	Maximum local strain (kcal mol^{-1})	Total strain (kcal mol^{-1})
[9+1] trimer	3.1	129.3
[11+1] trimer	2.3	112.8
fluor[9+1] trimer	3.1	130.3
fluor-*m*[9+1] trimer	1.8	80.5
[9+1]CPP	2.9	58.0
[11+1]CPP	1.3	44.4
fluor[9+1]CPP	2.8	55.6
fluor-*m*[9+1]CPP	3.4	42.9

3.3 Conclusion

Our previous studies of strained alkyne carbon nanohoops focused on efficiently attaching them *via* click chemistry methods to other molecules of interest.[56,94,95] Herein, we have described a synthetically simple and high yielding method for derivatizing these molecules further by a metal-catalyzed trimerization reaction. The result is high molecular weight pinwheel-shaped [*n*+1] trimers that maintain nanohoop-type photophysics and excellent solubility. $Pd_2(dba)_3$, typically utilized to catalyze the trimerization of benzyne derivatives, was found to significantly outperform Wilkinson's catalyst $RhCl(PPh_3)_3$ and Ni(cod)DQ, which are catalysts typical of unstrained alkyne trimerization. We have thoroughly characterized the trimers in this study in terms of their strain profiles and photophysics.

Finally, we successfully collected X-ray crystallographic data for **fluor[9+1] trimer** and **fluor-*m*[9+1] trimer**. The packing structure of **fluor-*m*[9+1] trimer** is particularly interesting due to close associations between adjacent trimers that result in a column-like packing motif. While the crystals of **fluor-*m*[9+1] trimer** were too fragile for gas absorption studies, we anticipate that stronger crystals could be engineered with similar topologies. This is an exciting avenue of research that we plan to explore in future publications.

3.4 Experimental Section

3.4.1 General Experimental Details

Unless otherwise noted, commercially available materials were used without purification. Compounds **III.2**, **III.3**, **III.4**, and Pd Sphos G3 were prepared according to the literature.[56,84,95] Moisture and oxygen sensitive reactions were carried out in flame-dried glassware and under an inert atmosphere of purified nitrogen using syringe/septa technique. Tetrahydrofuran (THF), dimethylformamide (DMF), and 1,4-dioxane were dried by filtration through alumina according to the methods described by Grubbs.[85] Thin-layer chromatography (TLC) was performed on aluminum plates coated with 0.20 mm thickness of Silica Gel 60 F254 (Macherey-Nagel). Developing plates were visualized using UV light at wavelengths of 254 and 365 nm. Silica column chromatography was conducted with Zeochem Zeoprep n60 Eco 40-63 µm silica gel. Alumina column chromatography was conducted with SorbTech basic alumina (pH 10), Act. II-III, 50-200 µm. ^1H and ^{13}C NMR spectra were recorded on either a Bruker Avance III HD 500 (^1H: 500 MHz, ^{13}C: 126 MHz) or Bruker Avance III HD 600 MHz (^1H: 600 MHz, ^{13}C: 151 MHz) NMR spectrometer. The samples were measured at 25 °C. The chemical shifts (δ) were reported in parts per million (ppm) and were referenced to the residual protio-solvent (CD_2Cl_2, ^1H: $\delta = 5.32$

ppm and ^{13}C: δ = 53.84 ppm) or to tetramethylsilane (for $CDCl_3$, TMS, δ = 0.00 ppm). Coupling constants (J) are given in Hz and the apparent resonance multiplicity is reported as s (singlet), d (doublet), t (triplet), q (quartet), dd (doublet of doublets) or m (multiplet). Infrared absorption (IR) spectra were recorded on a Thermo Scientific Nicolet 6700 spectrometer equipped with a diamond crystal Smart ATR. Characteristic IR absorptions are reported in cm^{-1} and denoted as strong (s), medium (m), and weak (w). UV/Vis absorption and fluorescence spectra were recorded on an Agilant Cary 100 spectrophotometer and a Horiba Jobin Yvon Fluoromax-4 Fluorimeter, respectively. All measurements were carried out under ambient conditions in a Spectrocell RF-1010-T threaded top vacuum formed borosilicate fluorometer cell (10 mm light path). The absorption maxima (λ_{max}) are reported in nm and the extinction coefficient (ε) in M^{-1} cm^{-1}.

3.4.2 Synthetic Details

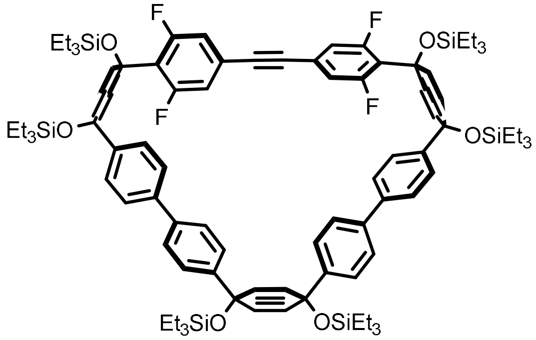

III.1. III.3 (0.358 g, 0.48 mmol, 1.1 equiv.), **III.2** (0.540 g, 0.44 mmol, 1 equiv.), and Pd SPhos G3 (0.035 g, 0.044 mmol, 0.1 equiv.) were dissolved in 1,4-dioxane (480 mL, 0.001 M, sparged with N_2 for one hour prior to use). The resulting solution was sparged with N_2 for an additional 15 minutes. The reaction mixture was heated to 80 °C over the course of 15 minutes. Deoxygenated aqueous K_3PO_4 solution (48 mL, 2.0 M, sparged with N_2 for one hour prior to use) was added via syringe. The reaction mixture was allowed to stir at 80 °C overnight. It was then cooled to room temperature and the 1,4-dioxane was removed via rotary evaporator. The organic products were then extracted with DCM (4 × 50 mL), washed with brine (2 × 50 mL), dried over sodium sulfate, filtered and concentrated to yield the crude product as an orange solid. The crude product was purified via automated column chromatography (0 – 18% DCM/hexanes). The resultant light yellow solid was recrystallized in DCM and ethanol to yield the final product as a crystalline white

solid (0.212 g, 0.14 mmol, 31%). R_f = 0.50 (SiO_2, 35% DCM/hexanes); ^{1}H NMR (500 MHz, Methylene Chloride-d_2) δ 7.53 (d, J = 8.5 Hz, 4H), 7.50 – 7.42 (m, 8H), 7.27 (d, J = 8.3 Hz, 4H), 7.07 (d, J = 9.8 Hz, 4H), 6.46 (dt, J = 9.9, 3.4 Hz, 4H), 6.01 (s, 4H), 5.97 (d, J = 10.2 Hz, 4H), 1.01 (t, J = 7.9 Hz, 18H), 0.98 – 0.90 (m, 36H), 0.71 (q, J = 7.9 Hz, 12H), 0.67 – 0.57 (m, 24H). ^{13}C NMR (126 MHz, Methylene Chloride-d_2) δ 160.82 (dd, J = 252.2, 9.2 Hz), 146.07, 145.12, 139.69, 139.47, 133.02, 131.83, 129.88 (d, J = 3.2 Hz), 127.03, 126.86, 126.59, 126.23, 124.01 (t, J = 13.3 Hz), 123.65 (t, J = 13.7 Hz), 116.38 (dd, J = 30.2, 6.8 Hz), 89.46 (t, J = 3.5 Hz), 72.06, 71.37, 70.11 (t, J = 2.8 Hz), 7.26, 7.25, 6.97, 6.80, 6.77, 6.54. ^{19}F NMR (471 MHz, Methylene Chloride-d_2) δ -104.76 (d, J = 9.3 Hz). IR (ATR) ṽ 2952 (m), 2909 (w), 2874 (m), 1622 (m), 1553 (m), 1489 (w), 1456 (w), 1415 (m), 1238 (w), 1193 (w), 1174 (w), 1074 (s), 1016 (s), 955 (s), 853 (m), 819 (m), 722 (s); HRMS (ASAP, positive mode) m/z calcd for $C_{92}H_{122}O_6F_4Si_6$: 1566.7793 $[M]^+$, found 1566.7737.

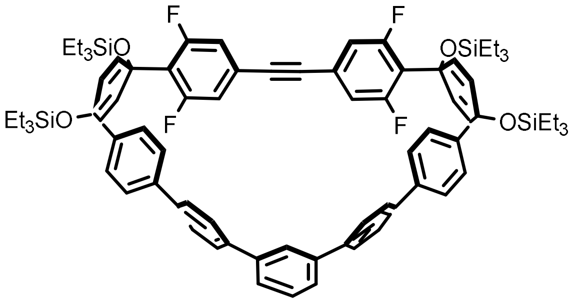

III.5. III.4 (0.146 g, 0.302 mmol, 1.1 equiv.), **III.2** (0.340 g, 0.275 mmol, 1 equiv.), and Pd SPhos GIII (0.022 g, 0.028 mmol, 0.1 equiv.) were dissolved in 1,4-dioxane (336 mL, 0.0009 M, sparged with N_2 for one hour prior to use). The resulting solution was sparged with N_2 for an additional 15 minutes. The reaction mixture was heated to 80 °C over the course of 15 minutes. Deoxygenated aqueous K_3PO_4 solution (34 mL, 2.0 M, sparged with N_2 for one hour prior to use) was added via syringe. The reaction mixture was allowed to stir at 80 °C for two hours. It was then cooled to room temperature and the aqueous layer was removed. The dioxane was removed via rotary evaporator. The resultant oily solid was dissolved in DCM, washed with brine, dried over sodium sulfate, filtered and concentrated to yield the crude product as an orange solid. The crude product was purified via automated column chromatography (0 – 30% DCM/hexanes), then sonicated in methanol to yield the final product as a white solid (0.143 g, 0.11 mmol, 40%). R_f = 0.42 (SiO_2, 35% DCM/hexanes); ^{1}H NMR (500 MHz, Methylene Chloride-d_2) δ 7.64 – 7.60 (m, 2H), 7.59 –

7.50 (m, 9H), 7.39 (d, *J* = 8.5 Hz, 4H), 7.32 (d, *J* = 8.5 Hz, 4H), 7.17 (t, *J* = 1.9 Hz, 1H), 6.98 (d, *J* = 9.9 Hz, 4H), 6.43 (dt, *J* = 10.3, 3.4 Hz, 4H), 6.04 (d, *J* = 10.2 Hz, 4H), 1.02 (t, *J* = 7.9 Hz, 18H), 0.91 (t, *J* = 7.9 Hz, 18H), 0.72 (q, *J* = 7.9 Hz, 12H), 0.59 (q, *J* = 8.0 Hz, 12H). ^{13}C NMR (126 MHz, Methylene Chloride-*d*$_2$) δ 161.90 (d, *J* = 9.3 Hz), 159.89 (d, *J* = 9.3 Hz), 144.96, 142.42, 141.50, 140.37, 139.89, 133.88, 133.47, 129.88 (t, *J* = 3.2 Hz), 129.50, 128.57, 127.70, 127.34, 126.11, 124.36, 124.07 (t, *J* = 13.3 Hz), 123.52 (t, *J* = 14.0 Hz), 116.33 (dd, *J* = 21.0, 7.2 Hz), 89.01 (t, *J* = 3.5 Hz), 72.18, 70.26 (t, *J* = 2.7 Hz), 7.25, 6.95, 6.80, 6.54. ^{19}F NMR (471 MHz, Methylene Chloride-*d*$_2$) δ -105.02 (d, *J* = 10.3 Hz); IR (ATR) ṽ 2952 (m), 2909 (m), 2874 (m), 1619 (m), 1549 (m), 1477 (w), 1457 (w), 1069 (s), 1014 (s), 955 (s), 853 (m), 823 (m), 792 (m), 720 (s); HRMS (ASAP, positive mode) m/z calcd for $C_{80}H_{93}O_4F_4Si_4$: 1305.6087 $[M+H]^+$, found 1305.6215.

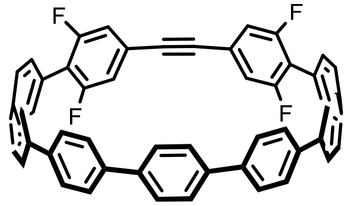

fluor[9+1]CPP. *Deprotection of silyl ether groups.* **III.1** (0.150 g, 0.096 mmol, 1 equiv.) was dissolved in THF (12 mL, 0.008 M) at room temperature. Acetic acid (0.27 mL, 4.79 mmol, 50 equiv.) was added dropwise, closely followed by dropwise addition of tetra-*n*-butylammonium fluoride (1 M solution in THF, 2.39 mL, 2.39 mmol, 25 equiv.). The reaction mixture was allowed to stir for 18 hours at room temperature. Deionized water (10 mL) was added. The organic layer was almost completely removed *via* rotary evaporator, and the resultant white suspension was vigorously sonicated. The now-deprotected intermediate (a white solid) was isolated *via* vacuum filtration and thorough washing with DI water and dichloromethane (0.109 g, 0.12 mmol, 96% crude).

Reductive aromatization. $SnCl_2{\cdot}2H_2O$ (0.181 g, 0.8 mmol, 1.0 equiv. with respect to HCl) was dissolved in tetrahydrofuran (20 mL, 0.040 M). HCl (0.13 mL, 1.6 mmol, 2.0 equiv. with respect to $SnCl_2{\cdot}2H_2O$) was added and the reaction was allowed to stir for 20 minutes. Concurrently in a separate flask, the deprotected macrocycle (0.109 g, 0.12 mmol, 1 equiv.) was dissolved in THF (15 mL, 0.008 M). After the 20 minutes had elapsed, prepared H_2SnCl_4 solution (9.3 mL, 0.37 mmol, 3 equiv.) was added to the solution of deprotected macrocycle. The reaction was allowed to stir for 40 minutes. The reaction was quenched with a saturated aqueous solution of $NaHCO_3$ (20 mL) and rotovapped to remove the THF. The organic products were extracted with DCM (5 X 20 mL), washed with brine (1 X 30 mL), dried over sodium sulfate, filtered, and concentrated to yield the crude product as an orange oil. The crude product was subjected to purification via a short plug (basic AlO_x, 30% DCM/70% hexanes). The product was a light yellow solid (0.026 g, 0.03 mmol, 27%). $R_f = 0.64$ (50% DCM/hexanes). ^{1}H NMR (500 MHz, Methylene Chloride-d_2) δ 7.70 – 7.46 (m, 28H), 6.96 (d, $J = 8.9$ Hz, 4H); ^{13}C NMR (126 MHz, Methylene Chloride-d_2) δ 160.33 (dd, $J = 250.5, 8.8$ Hz), 141.05, 138.95, 138.78 (2 overlapping signals), 138.64, 138.04, 131.30 (t, $J = 3.6$ Hz), 128.28, 127.99, 127.95, 127.88, 127.63, 127.55, 127.40, 125.57 (t, $J = 12.8$ Hz), 118.81 (t, $J = 17.3$ Hz), 115.23 (dd, $J = 21.2, 7.7$ Hz), 99.24 (t, $J = 3.9$ Hz); ^{19}F NMR (471 MHz, Methylene Chloride-d_2) δ -113.87 (d, $J = 10.2$ Hz). IR (ATR) ṽ 3025 (w), 2921 (w), 1615 (w), 1593 (w), 1558 (w), 1546 (w), 1482 (m), 1391 (w), 1264 (w), 1193 (m), 1176 (m), 1024 (s), 1001 (m), 854 (m), 807 (s), 746 (s); HRMS (ESI, positive mode) m/z calcd for $C_{56}H_{32}F_4$: 780.2435 $[M]^+$, found 780.2417.

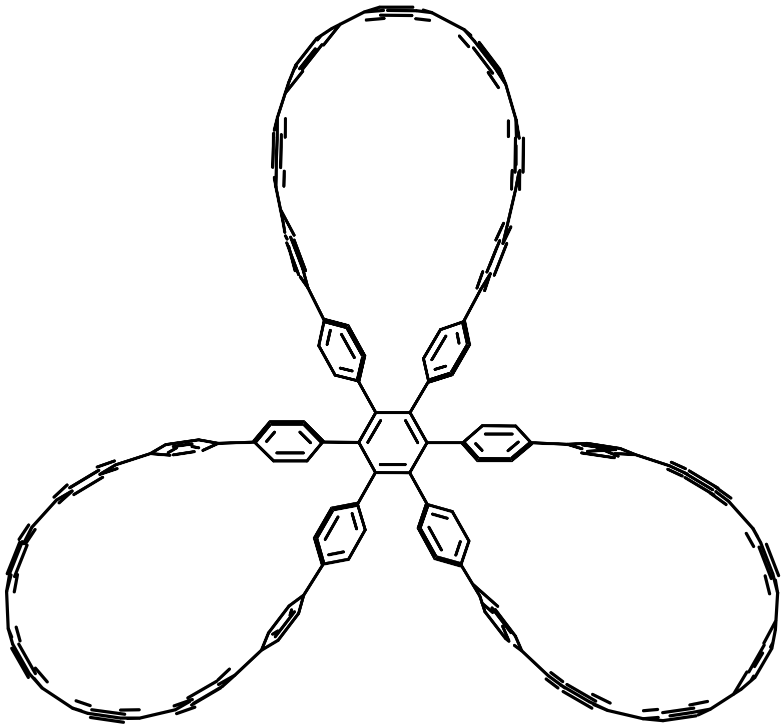

[9+1] trimer. [9+1]CPP (0.0097 g, 0.014 mmol, 1 equiv.) and $Pd_2(dba)_3$ (0.0013 g, 0.0014 mmol, 0.1 equiv.) were dissolved in DCM (5 mL, 0.003 M). The red mixture was allowed to stir at room temperature for 1 hour. The crude mixture was directly purified *via* column chromatography (basic AlO_x, 0-100% DCM/hexanes). Product containing fractions were combined and solvent was removed via rotary evaporation. This afforded the product as a yellow solid (9.3 mg, 0.0045 mmol, 95%). ^1H NMR (500 MHz, Methylene Chloride-d_2) δ 7.60 – 7.42 (m, 84H), 7.20 (d, J = 8.4 Hz, 12H), 6.99 (d, J = 8.5 Hz, 12H). HRMS (MALDI) m/z: [M]+ calculated for $C_{168}H_{108}$, 2124.8451; found, 2124.8375.

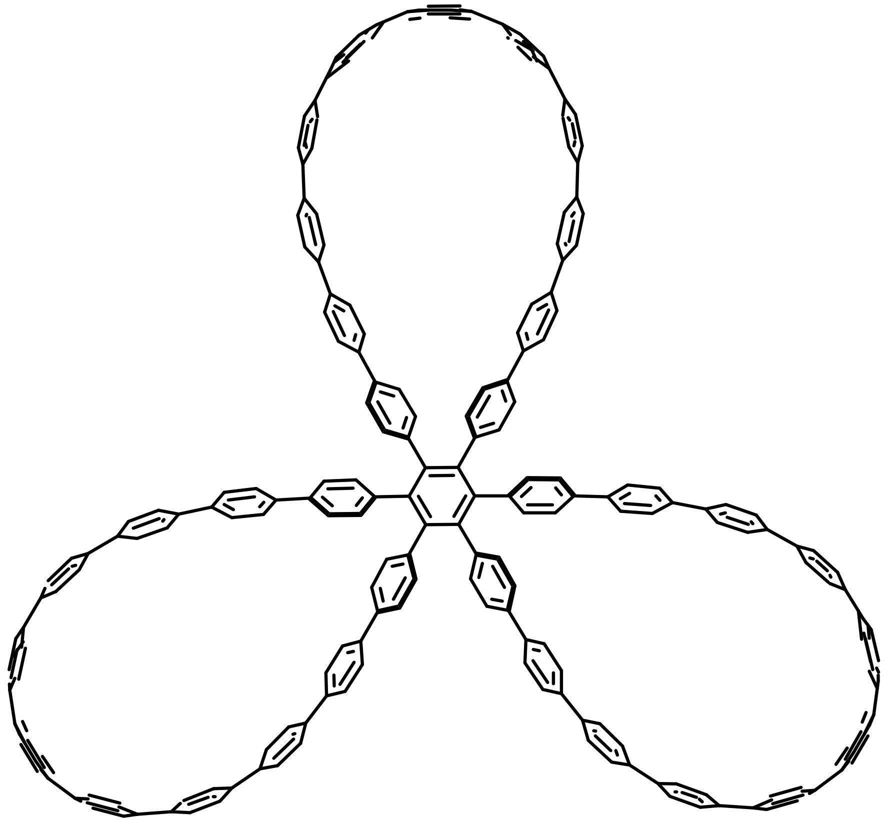

[11+1] trimer. [11+1]CPP (0.005 g, 0.0058 mmol, 1 equiv.) and $Pd_2(dba)_3$ (0.0021 g, 0.0023 mmol, 0.4 equiv.) were dissolved in DCM (2 mL, 0.003 M). The resultant red mixture was allowed to stir at room temperature for 1 hour. The crude mixture was directly purified *via* column chromatography (basic AlO_x, 0-100% DCM/hexanes). Product containing fractions were combined and solvent was removed via rotary evaporation This afforded the product as a slightly yellow/white solid (0.0031 g, 0.0019 mmol, 63%). ^1H NMR (500 MHz, Methylene Chloride-d2) δ 7.59 (m, 84H), 7.51 (m, 24H), 7.26 (d, J = 8.2 Hz, 12H), 7.05 (d, J = 8.3 Hz, 12H). HRMS (MALDI) m/z: $[M]^+$ calculated for $C_{204}H_{132}$, 2581.0329; found, 2581.0409.

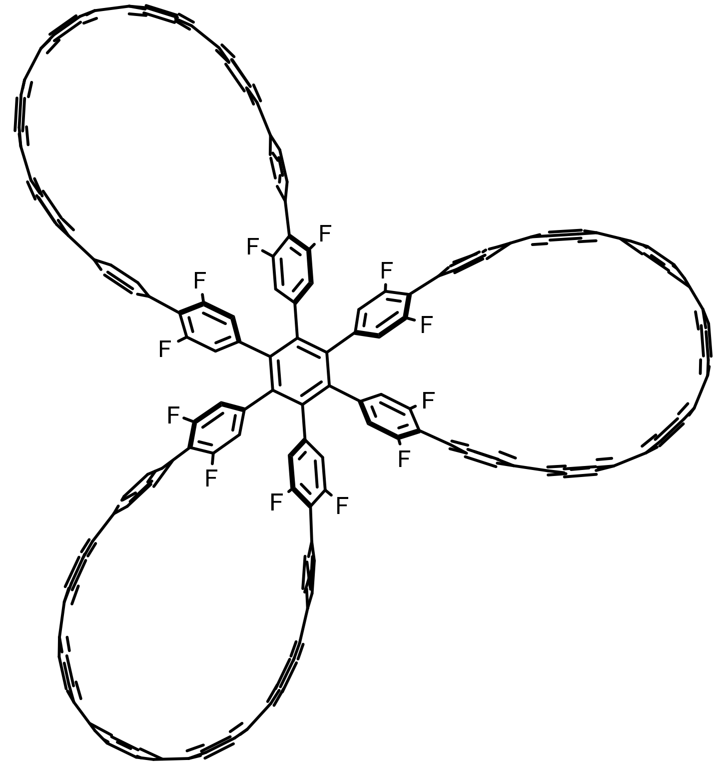

fluor[9+1] trimer. Fluor[9+1]CPP (0.0125 g, 1 equiv., 0.016 mmol) and $Pd_2(dba)_3$ (0.003 g, 0.2 equiv., 0.0032 mmol) were dissolved in DCM (4 mL, 0.004 M). The reaction was allowed to stir for 30 minutes. The solvent was then removed via rotary evaporator and the resultant crude mixture was purified *via* column chromatography (basic AlO_x, 50-100% DCM/hexanes). The final product was a yellow-green solid (0.0087 g, 0.0037 mmol, 70%). $R_f = 0.60$ (70% DCM/hexanes). IR (ATR) ṽ 3029 (w), 1627 (w), 1559 (w), 1482 (m), 1394 (m), 1288 (w), 1199 (w), 1110 (2), 1025 (s), 1007 (m), 811 (s), 751 (m); ^{1}H NMR (500 MHz, Methylene Chloride-d_2) δ 7.62 – 7.42 (m, 72H), 7.35 (d, J = 8.6 Hz, 12H), 6.65 (d, J = 8.1 Hz, 12H); ^{13}C NMR (126 MHz, Methylene Chloride-d_2) δ 159.69 (dd, J = 250.1, 8.3 Hz), 140.69, 140.24 (d, J = 10.4 Hz), 139.46, 139.23, 138.74, 138.51, 137.99, 137.65, 131.19, 128.15, 128.08, 127.77 (2 overlapping signals), 127.53, 126.92, 116.83 (t, J = 17.7 Hz), 114.88 (dd, J = 19.2, 7.4 Hz) (one signal unaccounted for); ^{19}F NMR (471 MHz, Methylene Chloride-d_2) δ -115.09 (d, J = 7.9 Hz); HRMS (ESI, positive mode) m/z calcd for $C_{168}H_{96}F_{12}$: 2340.7315 $[M]^+$, found 2340.7319.

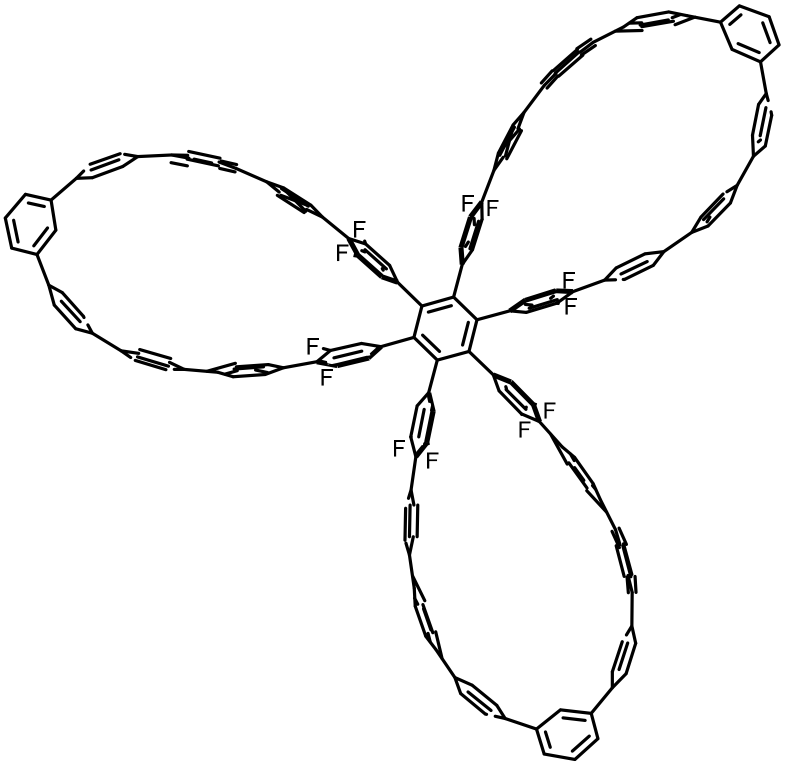

fluor-*m*[9+1] trimer. *Deprotection of silyl ether groups*. **III.5** (0.140 g, 0.011 mmol, 1 equiv.) was dissolved in THF (13.4 mL, 0.008 M) at room temperature. Acetic acid (0.31 mL, 5.36 mmol, 50 equiv.) was added dropwise, closely followed by dropwise addition of tetra-*n*-butylammonium fluoride (1 M solution in THF, 2.68 mL, 2.68 mmol, 25 equiv.). The reaction mixture was allowed to stir for 18 hours at room temperature. Deionized water (10 mL) was added. The organic layer was almost completely removed *via* rotary evaporator, and the resultant white suspension was vigorously sonicated. The now-deprotected intermediate (a white solid) was isolated *via* vacuum filtration and thorough washing with DI water and dichloromethane (assumed quantitative yield, 0.091 g, 0.11 mmol).

From deprotected macrocycle. $SnCl_2{\cdot}2H_2O$ (0.181 g, 0.8 mmol, 1.0 equiv. with respect to HCl) was dissolved in tetrahydrofuran (20 mL, 0.040 M). HCl (0.13 mL, 1.6 mmol, 2.0 equiv. with respect to $SnCl_2{\cdot}2H_2O$) was added and the reaction was allowed to stir for 20 minutes. Concurrently in a separate flask, the deprotected macrocycle (0.091 g, 0.11 mmol, 1 equiv.) was dissolved in THF (10 mL, 0.011 M). After the 20 minutes had elapsed, prepared H_2SnCl_4 solution (5.9 mL, 0.24 mmol, 2.2 equiv.) was added to the solution of deprotected macrocycle. The reaction was allowed to stir for 40 minutes. Concurrently, Ni(cod)DQ (0.053 g, 0.16 mmol, 1.5 equiv.) was dissolved in THF (8 mL, 0.02 M). After the 40 minutes had elapsed, the Ni(cod)DQ solution was transferred to the reaction flask and the reaction was allowed to stir for an additional 40 minutes. The reaction was quenched with a saturated aqueous solution of sodium bicarbonate (20 mL). THF was removed via rotary evaporator and the organic products were extracted with DCM (5 X 30 mL), washed with brine (1 X 30 mL), dried over sodium sulfate, filtered, and concentrated to yield the crude product as a yellow solid. Purification via column chromatography (basic AlOx, 50–100% DCM/hexanes) yielded the final product as a white solid (0.044 g, 0.056 mmol, 52%). R_f = 0.61 (60% DCM/hexanes). ^{1}H NMR (500 MHz, Methylene Chloride-d_2) δ 7.62 – 7.50 (m, 57H), 7.41 – 7.35 (m, 24H), 6.74 (d, J = 7.9 Hz, 12H), 6.13 (t, J = 1.9 Hz, 3H). ^{13}C NMR (126 MHz, Methylene Chloride-d_2) δ 159.73 (dd, J = 249.8, 8.1 Hz), 143.12, 142.68, 140.78, 140.28 (t, J = 10.4 Hz), 139.93, 139.69, 139.45, 139.16, 138.95, 131.15 (d, J = 2.4 Hz), 129.69, 129.61, 127.84, 127.70, 127.61, 127.29, 127.10, 123.19, 116.95 (t, J = 18.0 Hz), 114.86 (d, J = 27.7 Hz). ^{19}F NMR (471 MHz, Methylene Chloride-d_2) δ -115.04 (d, J = 8.1 Hz). IR (ATR) ṽ 3023 (w), 2974 (w), 2853 (w), 1629 (w), 1574 (w), 1563 (w), 1550 (w), 1483 (m), 1390 (s), 1290 (m), 1197 (m), 1111 (m), 1021 (s), 1003 (s), 806 (s), 756 (s); HRMS (ESI, positive mode) m/z calcd for $C_{168}H_{96}F_{12}$: 2340.7315 $[M]^+$, found 2340.7425.

3.4.3 Photophysical characterization

For molar absorptivity measurements, the compound of interest was first dissolved at known concentration using volumetric glassware. This solution was then added incrementally to a cuvette containing a known amount of solvent and absorbance measurements were taken after each addition. The process was repeated three times.

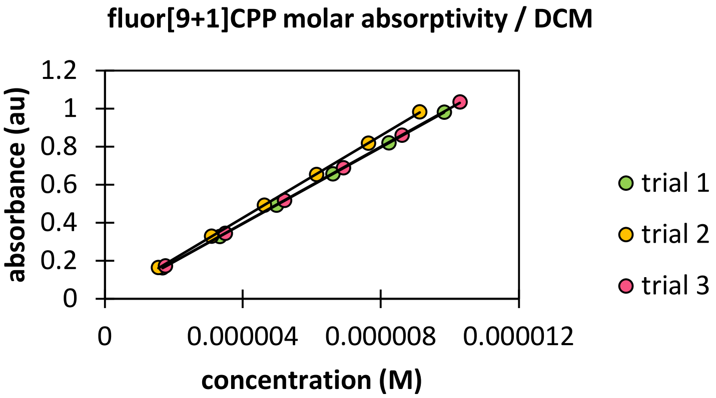

Figure 3.7. Beer's law plot for **fluor[9+1]CPP** in DCM.

Table 3.3. Measured molar absorptivity for **fluor[9+1]CPP** in DCM; $\lambda_{max,abs}$ = 335 nm.

Trial	Slope (M^{-1} cm^{-1})
1	1.00×10^5
2	1.08×10^5
3	1.01×10^5
average	1.03×10^5
std. dev.	0.04×10^5

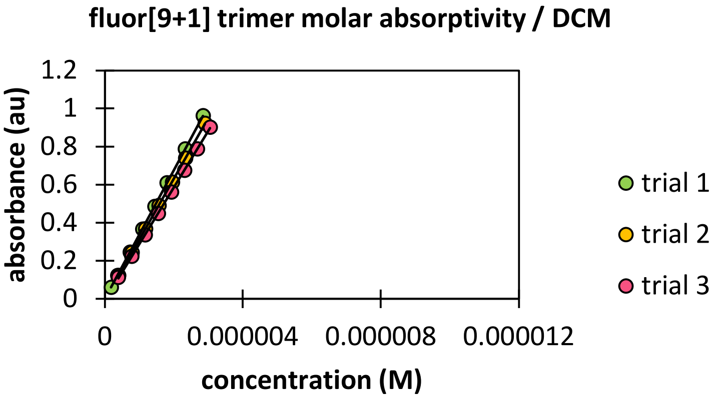

Figure 3.8. Beer's law plot for **fluor[9+1] trimer** in DCM.

Table 3.4. Measured molar absorptivity for **fluor[9+1] trimer** in DCM; $\lambda_{max,abs}$ = 329 nm.

Trial	Slope (M^{-1} cm^{-1})
1	3.39×10^5
2	3.18×10^5
3	2.96×10^5
average	3.18×10^5
std. dev.	0.21×10^5

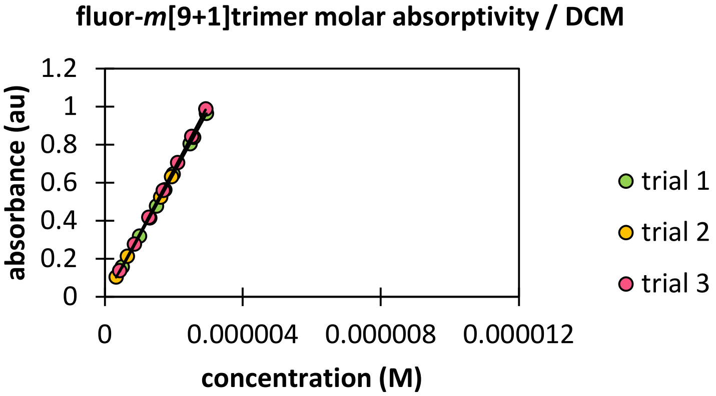

Figure 3.9. Beer's law plot for **fluor-*m*[9+1] trimer** in DCM.

Table 3.5. Measured molar absorptivity for **fluor-*m*[9+1] trimer** in DCM; $\lambda_{\text{max,abs}} = 315$ nm.

Trial	Slope (M^{-1} cm^{-1})
1	3.30×10^5
2	3.27×10^5
3	3.41×10^5
average	3.33×10^5
std. dev.	0.08×10^5

Quantum yield measurements were performed using the method described in "A Guide to Recording Fluorescence Quantum Yields" by Horiba Scientific.[61] The internal standards used were quinine sulfate (0.1 M H_2SO_4, aqueous, lit. value $\Phi = 0.54$, fluorescence signal integrated from 400-600 nm) and anthracene (ethanol, lit. value $\Phi = 0.27$, fluorescence signal integrated from 360-480 nm). For fluorescence measurements, all compounds were excited at a wavelength of 330 nm with consistent excitation and emission slit widths of 1 nm. Absorbance values plotted below were as measured at 330 nm. Fluorescence signal integrations for compounds of interest are listed below:

Table 3.6. Compound integration ranges in DMSO and DCM.

Compound of interest	Integration range (DCM, nm)	Integration range (DMSO, nm)
[9+1] trimer	400 – 600	400 – 600
[11+1] trimer	400 – 600	400 – 600
fluor[9+1]CPP	400 – 600	400 – 600
fluor[9+1]trimer	400 – 600	400 – 600
fluor-m[9+1]trimer	345 – 550	345 – 600

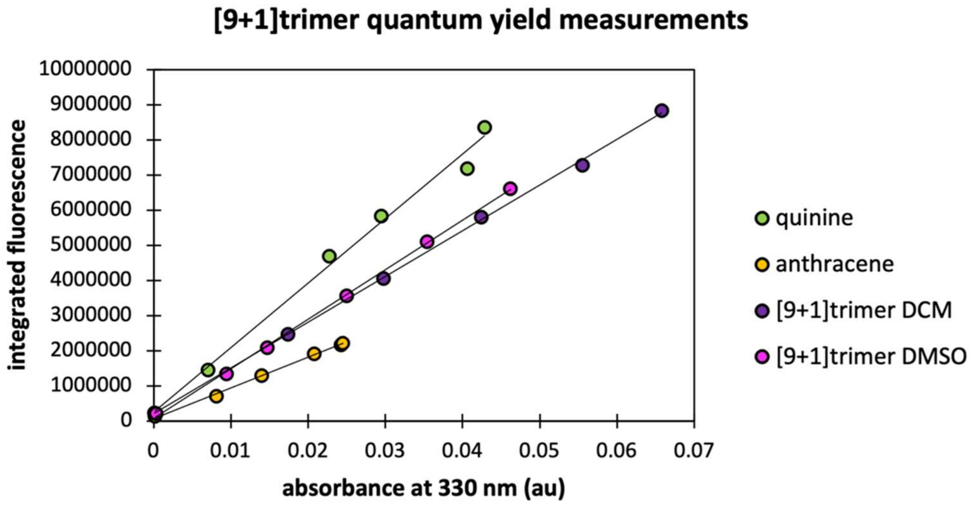

Figure 3.10. Quantum yield plot for **[9+1] trimer**.

Table 3.7. Quantum yield data for **[9+1] trimer**.

Compound	Solvent	Slope	Φ w.r.t. quinine	Φ w.r.t. anthracene	Avg. Φ	Std. dev.
quinine	0.1 M H_2SO_4 (*aq*)	1.83×10^8	0.54 (lit)	0.56	0.55	0.008
anthracene	ethanol	8.72×10^7	0.26	0.27 (lit)	0.27	0.005
[9+1]trimer	DCM	1.30×10^8	0.41	0.42	0.42	0.005
[9+1]trimer	DMSO	1.41×10^8	0.46	0.48	0.47	0.008

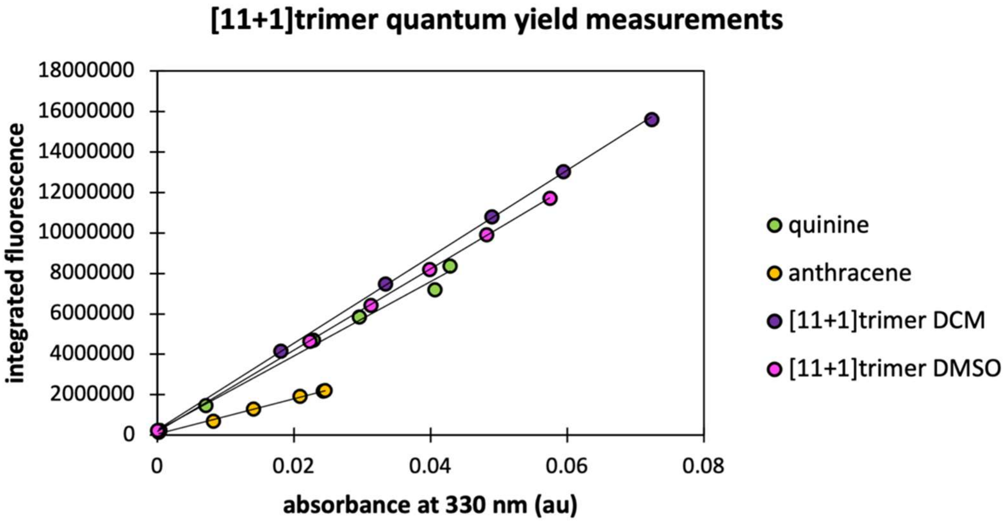

Figure 3.11. Quantum yield plot for **[11+1] trimer**.

Table 3.8. Quantum yield data for **[11+1] trimer**.

Compound	Solvent	Slope	Φ w.r.t. quinine	Φ w.r.t. anthracene	Avg. Φ	Std. dev.
quinine	0.1 M H_2SO_4 (*aq*)	1.83×10^8	0.54 (lit)	0.56	0.55	0.008
anthracene	ethanol	8.72×10^7	0.26	0.27 (lit)	0.27	0.005
[11+1]trimer	DCM	2.14×10^8	0.68	0.69	0.69	0.005
[11+1]trimer	DMSO	2.01×10^8	0.66	0.68	0.67	0.008

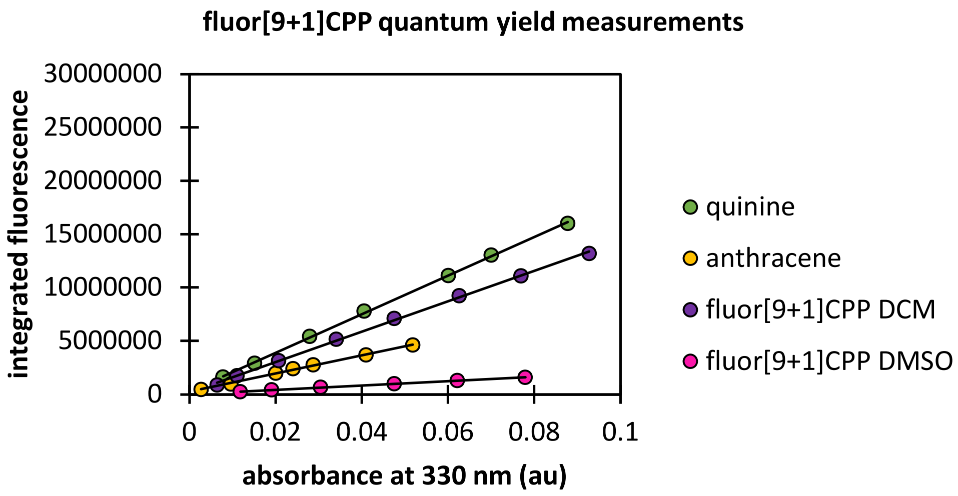

Figure 3.12. Quantum yield plot for **fluor[9+1]CPP**.

Table 3.9. Quantum yield data for **fluor[9+1]CPP**.

Compound	Solvent	Slope	Φ w.r.t. quinine	Φ w.r.t. anthracene	Avg. Φ	Std. dev.
quinine	0.1 M H_2SO_4 (*aq*)	1.81×10^8	0.54 (lit)	0.55	0.54	0.007
anthracene	ethanol	8.51×10^7	0.26	0.27 (lit)	0.27	0.003
fluor[9+1]CPP	DCM	1.42×10^8	0.49	0.49	0.49	0.006
fluor[9+1]CPP	DMSO	2.01×10^7	0.07	0.08	0.07	0.001

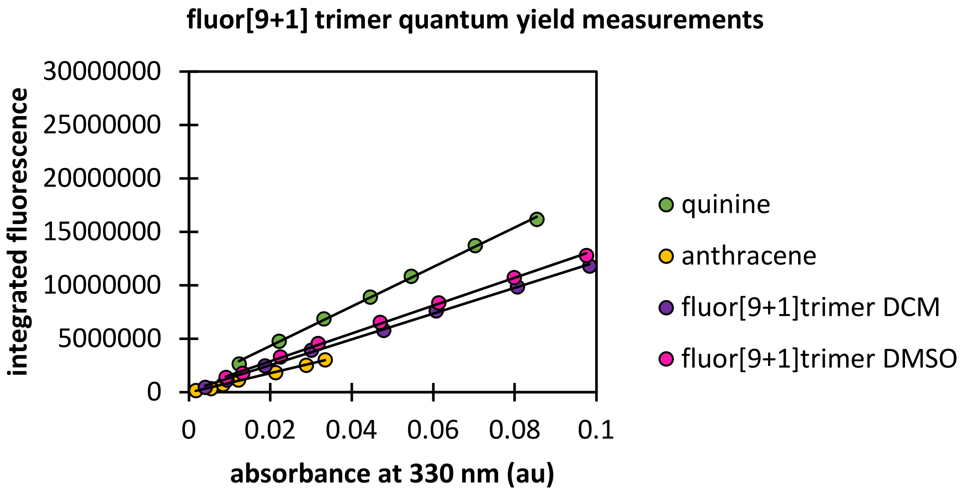

Figure 3.13. Quantum yield plot for **fluor[9+1] trimer**.

Table 3.10. Quantum yield data for **fluor[9+1] trimer**.

Compound	Solvent	Slope	Φ w.r.t. quinine	Φ w.r.t. anth.	Avg. Φ	Std. dev.
quinine	0.1 M H_2SO_4 (*aq*)	1.85×10^8	0.54 (lit)	0.53	0.53	0.004
anthracene	ethanol	9.05×10^7	0.28	0.27 (lit)	0.27	0.002
fluor[9+1]trimer	DCM	1.20×10^8	0.40	0.39	0.40	0.003
fluor[9+1]trimer	DMSO	1.30×10^8	0.47	0.46	0.46	0.003

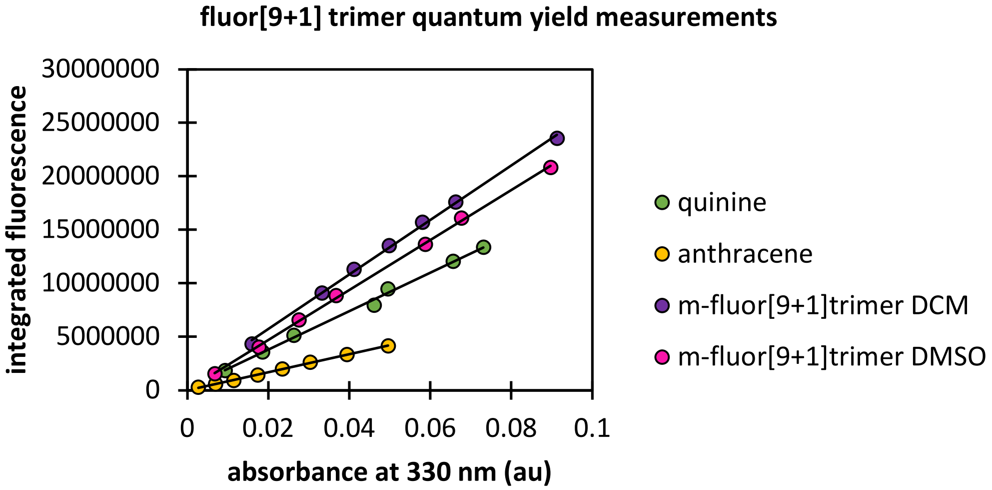

Figure 3.14. Quantum yield plot for **fluor-*m*[9+1]trimer**.

Table 3.11. Quantum yield data for **fluor-*m*[9+1]trimer**.

Compound	Solvent	Slope	Φ w.r.t. quin.	Φ w.r.t. anth.	Avg. Φ	Std. dev.
quinine	0.1 M H_2SO_4 (*aq*)	1.79×10^8	0.54 (lit)	0.55	0.55	0.008
anthracene	ethanol	8.43×10^7	0.26	0.27 (lit)	0.27	0.004
fluor-*m*[9+1]tri.	DCM	2.55×10^8	0.88	0.89	0.88	0.013
fluor-*m*[9+1]tri.	DMSO	2.34×10^8	0.87	0.88	0.88	0.013

3.4.4 StrainViz

Computations were performed using Gaussian09[62] at the B3LYP/6-31G(d) level of theory. Keywords “Opt=(rfo,NoSymm)” were added to account for the fragments with an alkyne and to ensure minimal negative energies in the case of the trimer fragments. The alkyne piece was present in one fragment for the ***m*-fluor[9+1]CPP** StrainViz analysis because of the error associated with optimizing fragments with a 180° angle. Outputs from individual StrainViz calculations were submitted with the maximum bond energy set as the highest strained bond between all four molecules (***m*-fluor[9+1]CPP**) to generate a relative strain scale. This setting recolors each bond to generate a comparative heat map. Replacing the “max(norm_values)” on line 171 in the “bond_scripts.py” with the max bond strain in the “total_bond.tcl” file, a recolored output is generated by rerunning the StrainViz script for each molecule. All fragment geometries are available for download. Fragment geometries are shown below.

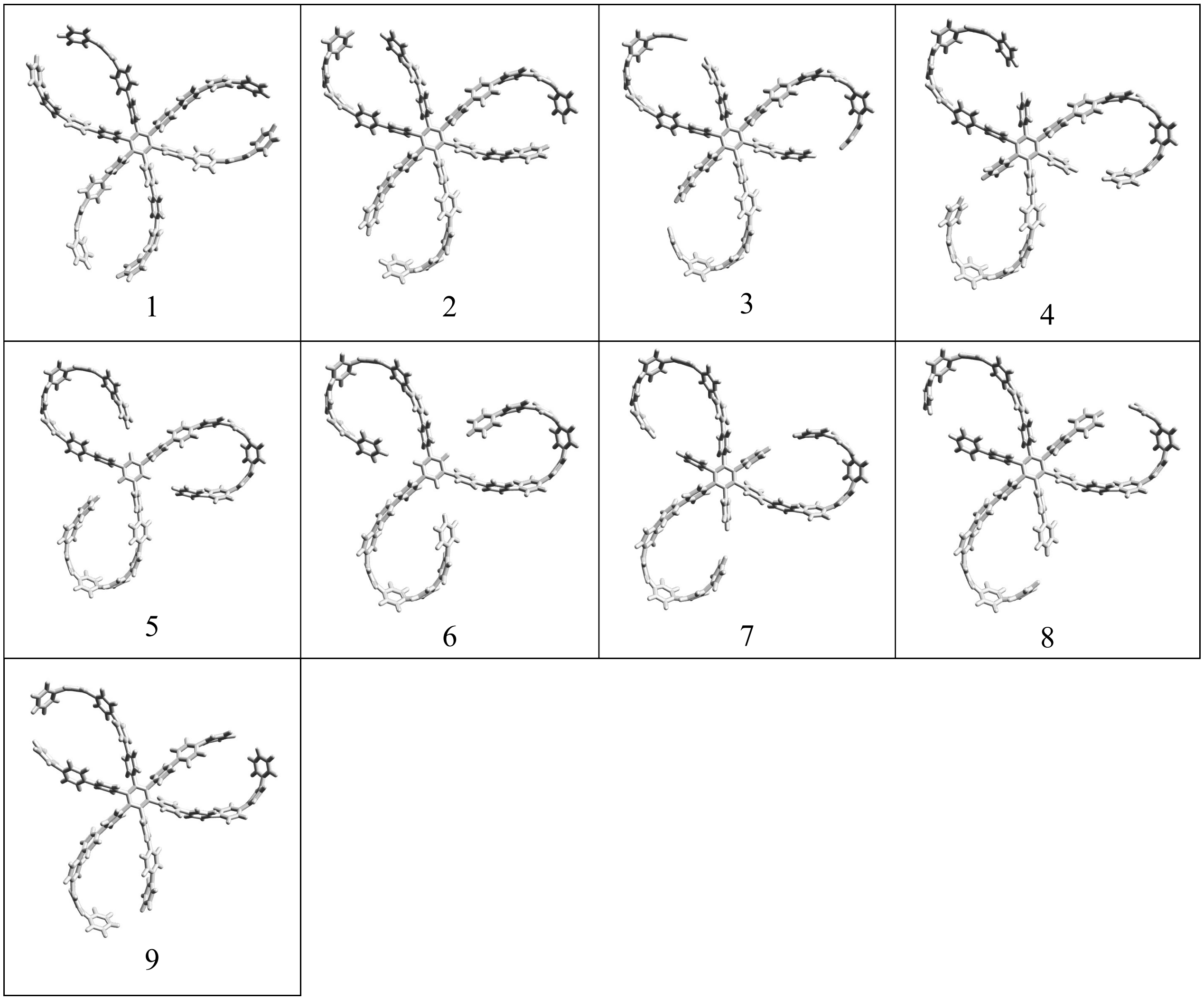

Figure 3.15. [9+1] trimer molecule fragments for use in StrainViz.

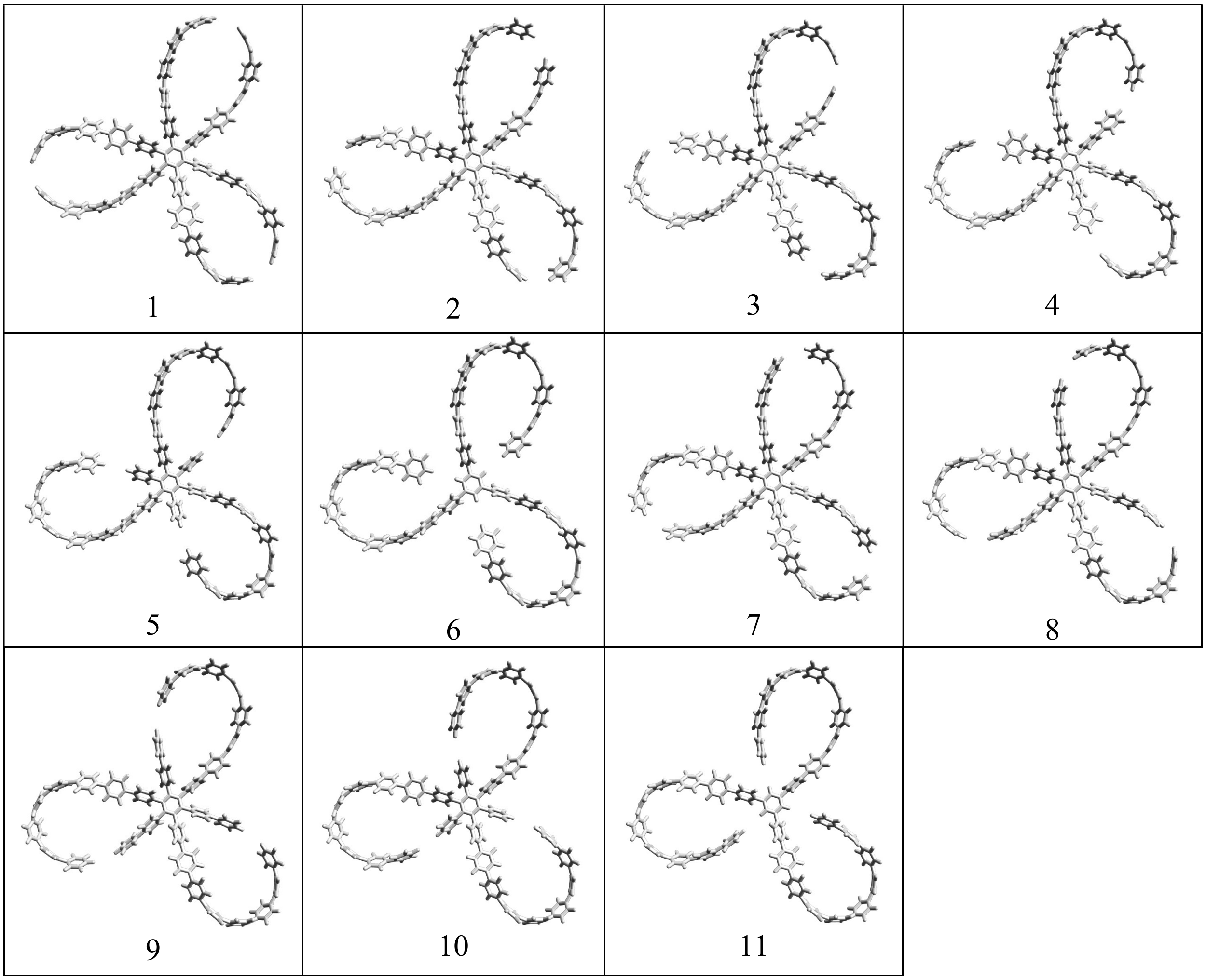

Figure 3.16. [11+1] trimer molecule fragments for use in StrainViz.

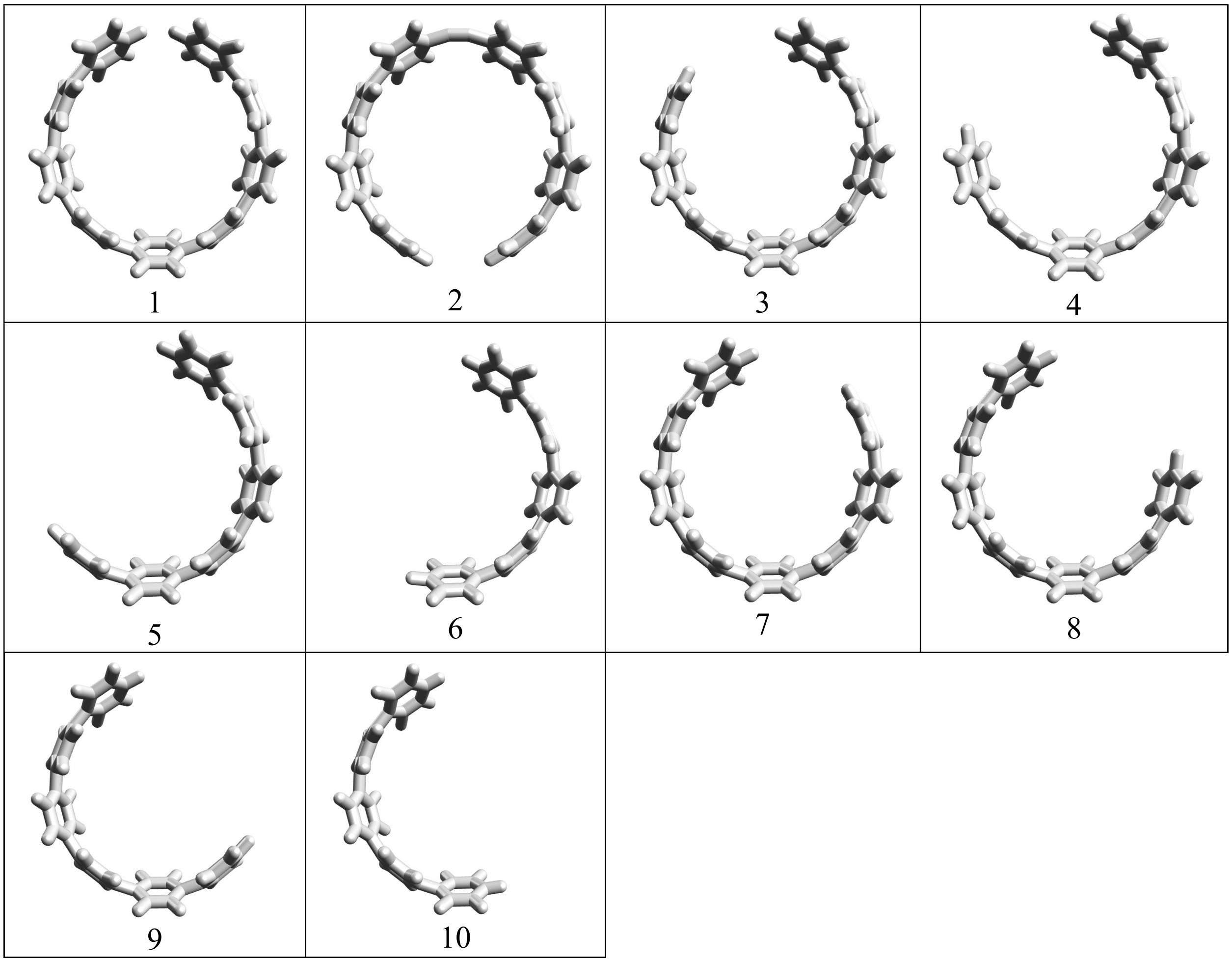
1 2 3 4
5 6 7 8
9 10

Figure 3.17. fluor[9+1]CPP molecule fragments for use in StrainViz.

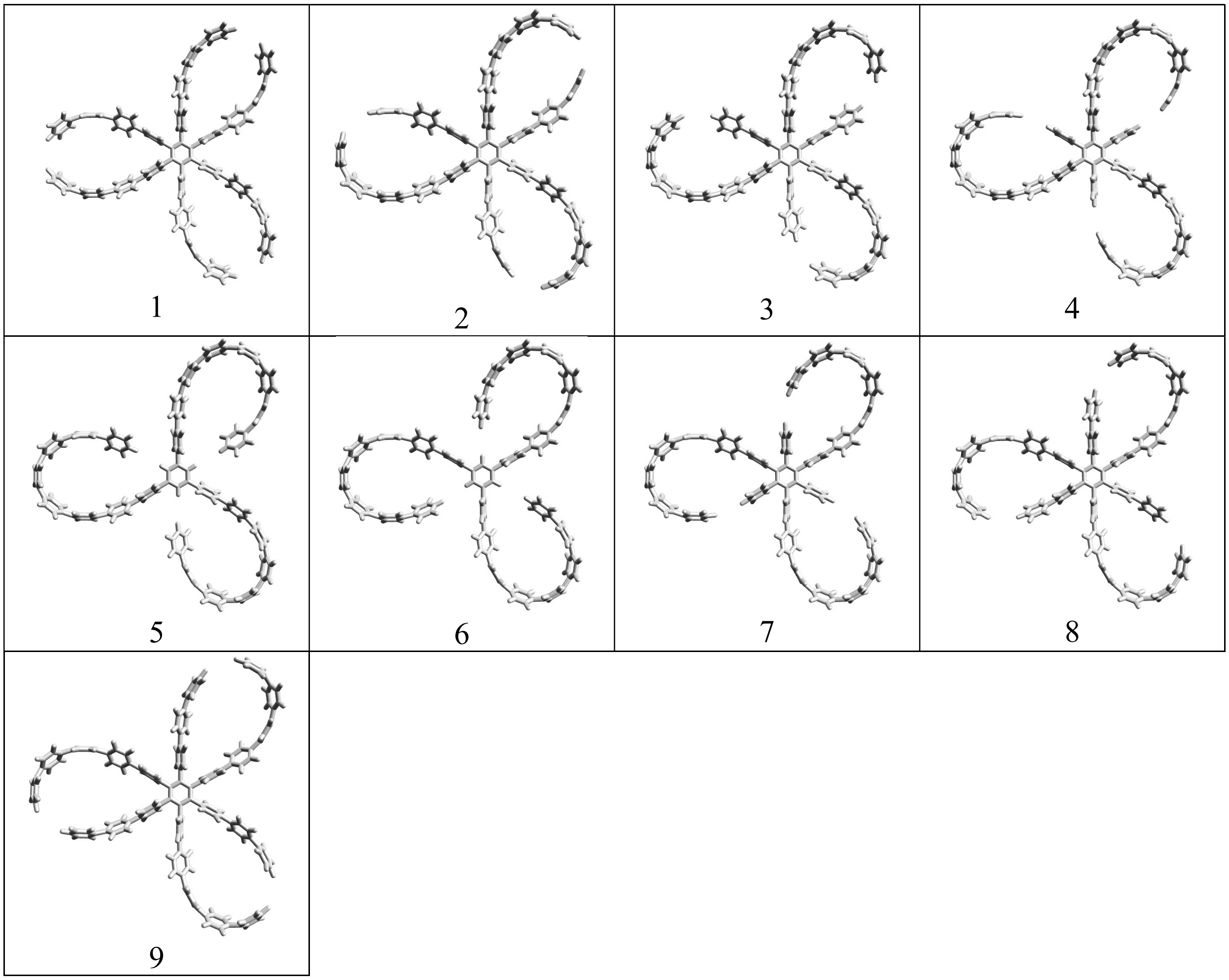

Figure 3.18. fluor[9+1] trimer molecule fragments for use in StrainViz.

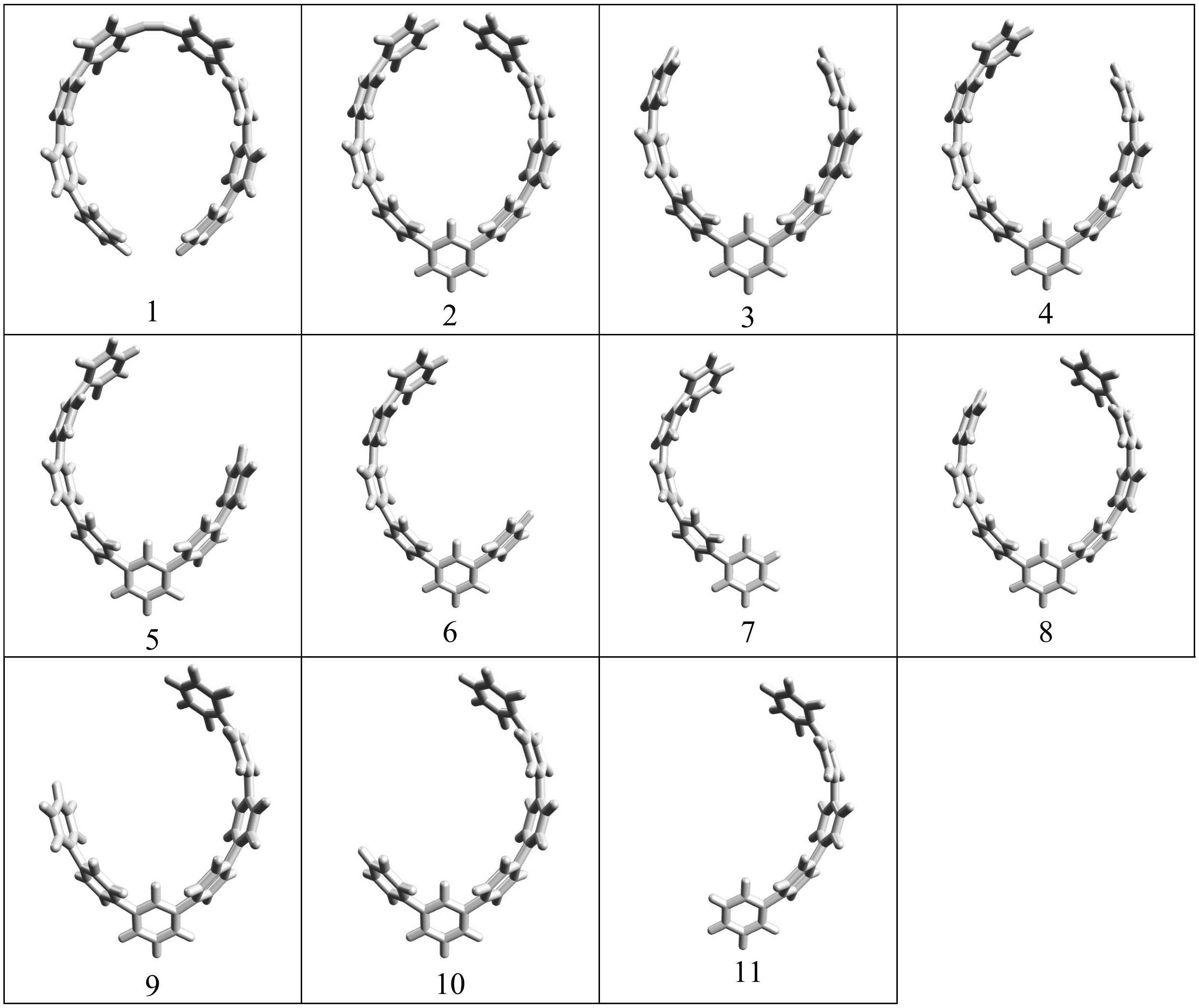

Figure 3.19. fluor-*m*[9+1]CPP molecule fragments for use in StrainViz.

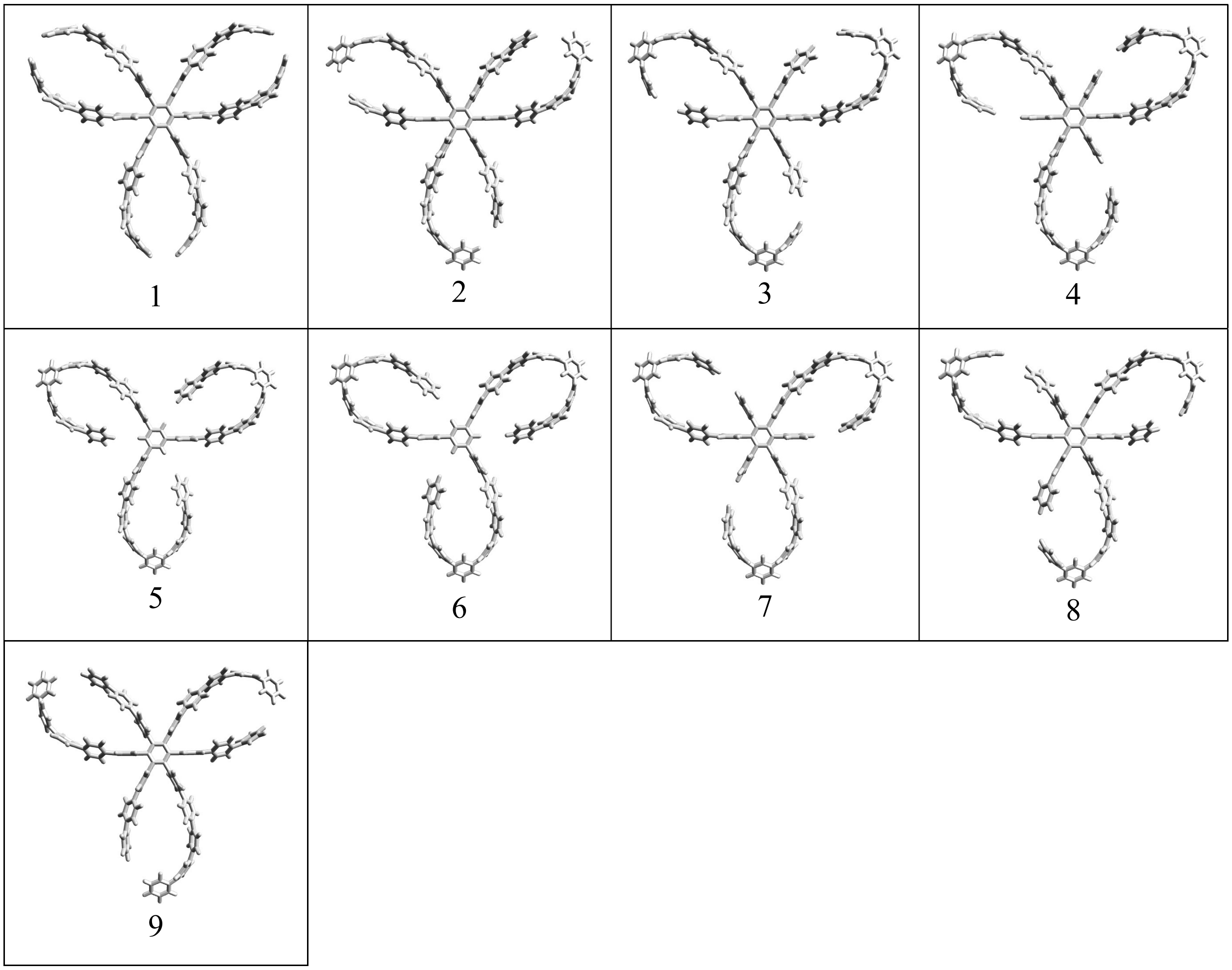
1 2 3 4 5 6 7 8 9

Figure 3.20. fluor-*m*[9+1] trimer molecule fragments for use in StrainViz.

3.5 Bridge to Chapter IV

Chapter III has focused on trimeric versions of carbon nanohoops synthesized *via* a metal-catalyzed alkyne cyclotrimerization reaction. Chapter IV continues to focus on carbon nanohoops that can undergo unusual transformations or otherwise display unique photophysical properties. The first nanohoop discussed is **BT[11+1]CPP**, a strained-alkyne-containing donor-acceptor nanohoop with red-shifted emission in comparison to parent **[11+1]CPP**. The second nanohoop is **[12+2]CPP**, which contains two alkyne units capable of strain-promoted reactivity. Finally, **DMAC-Tz[12]CPP** is a nanohoop which incorporates both a donor and an acceptor unit into its backbone; while the synthesis of this molecule has not yet been completed, it is predicted to display a unique photophysical property called thermally-activated delayed fluorescence.

CHAPTER IV

PROGRESS TOWARDS OPTICALLY AND TOPOLOGICALLY UNIQUE STRAINED ALKYNE CYCLOPARAPHENYLENES

This chapter was written by myself with editorial assistance from Professor Ramesh Jasti. Calculations for the fluorescence properties of the DMAC-Tz[12]CPP were performed by the research group of Prof. Eli Zysman-Colman.

4.1 Introduction

Due to the modular nature of carbon nanohoop syntheses, it is possible to explore new chemical space without necessarily synthesizing a large number of new building blocks. Herein, we describe the synthesis of two new carbon nanohoops, **BT[11+1]CPP** and **[12+2]CPP**, which were made with comparative ease as their syntheses both derive from previously studied starting materials.[56]

The synthesis of **BT[11+1]CPP** was inspired by the rising demand for bright, red-shifted fluorophores for use in biology.[122,123] Red-emitting fluorophores are highly desirable as they tend to have larger signal-to-noise ratios in biological tissues.[124] This is due to the fact that most autofluorescence (*i.e.* the inherent fluorescence of native biomolecules in a biological sample) occurs in the blue to yellow region of the visible light spectrum. Eliminating this "noise" by filtering out all but red emission of a suitable fluorophore can allow for much finer and efficient imaging.[124] Our lab and others have previously designed carbon nanohoops with redder emission by the incorporation of electron accepting units such as benzothiadiazole (BT) into the scaffold.[41,42,118] **BT[11+1]CPP** follows this same design strategy, and includes the added benefit of a strained alkyne which could undergo the SPAAC reaction.

[12+2]CPP provided an interesting synthetic target as a molecule that could potentially undergo two strain-promoted reactions wherein the second reaction would be even more strain-promoted than the first.[59] We envision that this molecule could serve as an interesting monomer in polymerization reactions with an azide-containing co-monomer, or as a cross-linking agent between polymer strands decorated with azide groups.[125,126]

Finally, we introduce in this section the proposed synthesis for an optically unique nanohoop that could display thermally-activated delayed fluorescence (TADF).[127] Thermally-activated delayed fluorescence (TADF) is a highly attractive property for fluorophores used in organic light-emitting diodes. TADFs can maximally absorb and re-emit light due to the fact that upon excitation, an electron that is excited into a triplet state can reverse-intersystem cross from the triplet state into the singlet state using energy from its surroundings and then undergo fluorescence. The important factor that determines whether or not a molecule is capable of undergoing TADF is the energy gap between the triplet and singlet state, denoted ΔE_{ST}.[127] We have been in communication with Professor Eli Zysman-Colman's group (St. Andrew's University) who are experts in TADF molecules. They have computationally predicted that a **[12]CPP** containing both a triazine (Tz) electron-acceptor unit and a dimethyl-dihydroacridine (DMAC) electron-donor unit is a likely TADF compound with a ΔE_{ST} of 0.30 eV.

4.2 Results and Discussion

4.2.1 Synthesis of BT[11+1]CPP

Highlighting the modularity of the syntheses of [*n*+1]CPPs, the synthesis of **BT[11+1]CPP** begins with **IV.1**—a building block common to the syntheses of **[9+1]CPP**, **[11+1]CPP**, ***m*[9+1]CPP**, and **[12+2]CPP** (*vide infra*). The synthesis of **IV.1** has been detailed elsewhere.[56] As shown in **Scheme 4.1**, **IV.1** underwent a double lithium-halogen exchange in the presence of *n*-Butyllithium at –78 °C in THF. This was followed by the addition of an electrophilic ketone **IV.2** to the reaction mixture to afford **IV.3** in 35% yield. Protection of the free alcohol groups *via* reaction with triethylsilyl chloride and imidazole yielded the fully silyl ether protected building block **IV.4**. **IV.4** and commercially-available 2,1,3-benzothiadiazole-4,7-bis(boronic acid pinacol ester) underwent dilute Suzuki-Miyaura cross-coupling conditions at elevated temperatures to yield **IV.5** in 19% yield. Next, deprotection of the silyl ether units to liberate the free alcohols was accomplished *via* exposure of the macrocycle to tetrabutylammonium fluoride (TBAF) in the presence of acetic acid. Finally, the deprotected macrocycle was subjected to reductive aromatization conditions with H_2SnCl_4 to convert the cyclohexadiene units into their final phenylene form and yield the fully aromatized **BT[11+1]CPP**.

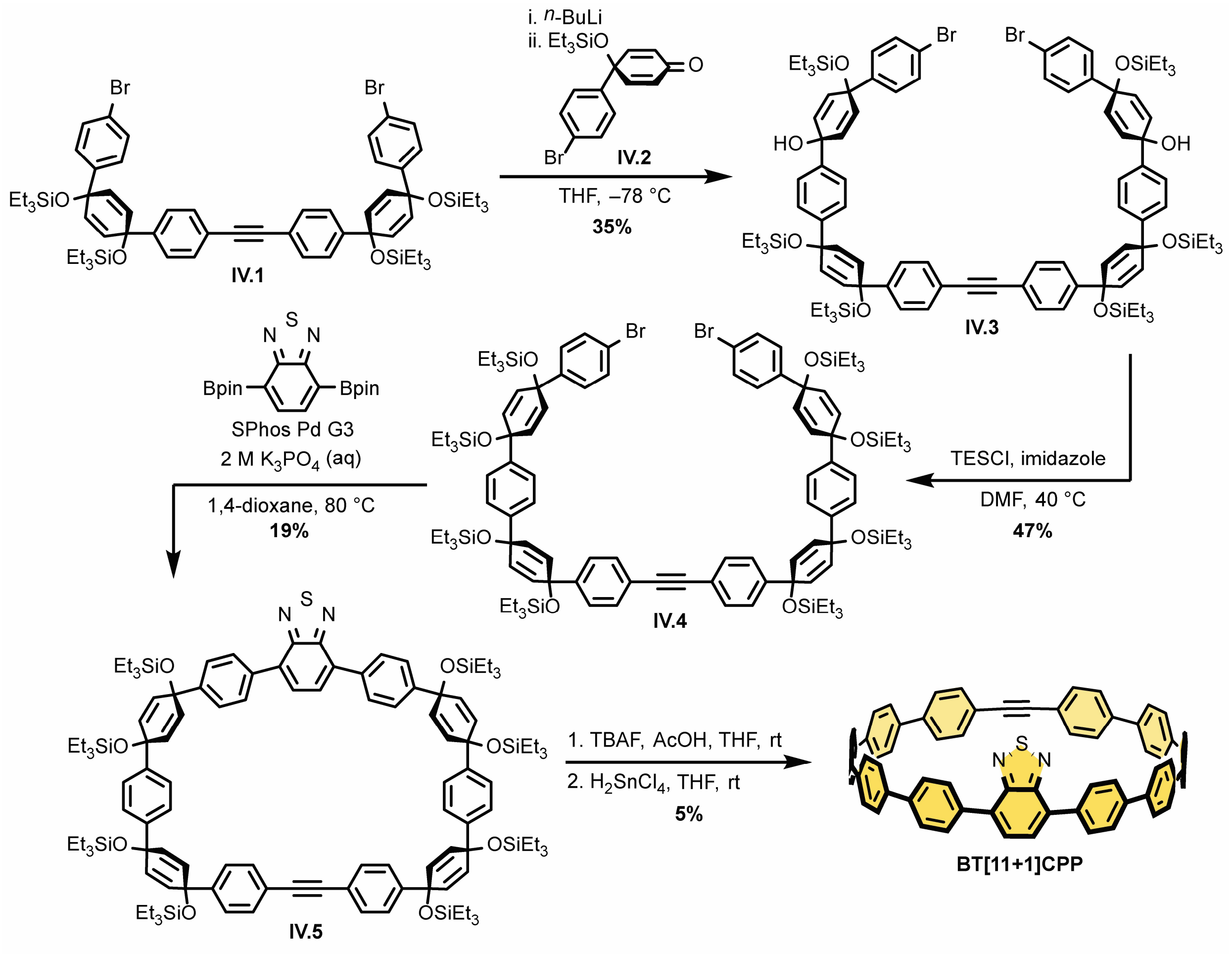

Scheme 4.1. Synthesis of **BT[11+1]CPP**.

4.2.2 Photophysical Properties of BT[11+1]CPP

The incorporation of electron-accepting heterocycles into the backbone of a carbon nanohoop has been shown to strongly impact its photophysical properties.[41–43,118,128] Generally, incorporation of an electron-accepting unit will decrease the energy of the lowest unoccupied molecular orbital (LUMO), which in turn decreases the size of the HOMO-LUMO gap (HOMO = highest occupied molecular orbital). Decreasing the magnitude of the HOMO-LUMO gap will result in a decrease in the energy of the fluorescence emission of the nanohoop, thereby red-shifting that emission. This effect has been demonstrated by our lab and others, with BT as well as other electron-accepting heterocycles.[41–43,118,128]

A negative consequence to this strategy is a decrease in the photoluminescence quantum yield (Φ), which is a ratio of the number of photons emitted to the number of photons absorbed by the molecule.[119] This effect is summarized by the energy gap law, which describes the close-to-exponential relationship between the size of the energy gap (*i.e.* the difference in energy between the molecule's lowest energy excited state and its ground state) and the rate of nonradiative decay.[120] In essence, for a given system, rates of nonradiative decay increase and therefore quantum yields decrease as the energy gap for a fluorophore decreases. This has been observed in carbon nanohoops incorporating electron-accepting units.[95,118]

In many cases, this strategy also enhances the donor-acceptor character of the nanohoop. When excited, donor-acceptor-type molecules will undergo intramolecular charge transfer (ICT) wherein the donor part of the molecule (in the case of **BT[11+1]CPP**, the alkyne unit and the surrounding curved phenylene backbone) will transfer electron density to the acceptor (BT unit and nearby phenylenes) part of the molecule. This results in a molecule with a polarized excited state. As such, a key marker of ICT (and therefore donor-acceptor character) is positive solvatofluorochromism.[119] Positive solvatofluorochromism describes a red-shift in the fluorescence emission wavelength of the fluorophore as the polarity of the solvent increases. This is due to the fact that polar excited states are more stabilized by polar solvents and therefore lower in energy in those solvents. In conjunction with the energy gap law, it is often observed for donor-acceptor-type molecules that quantum yield decreases with increasing polarity of the solvent.[119,120]

BT[11+1]CPP was first evaluated in terms of its absorbance and emission profiles (**Figure 4.1** and **Table 4.1**). This data was collected in both DCM and DMSO, a nonpolar and polar solvent respectively, to observe any solvent effects on the molecule's photophysics. Both the parent **[11+1]CPP** and **BT[11+1]CPP** have very similar maximum absorbance wavelengths in DCM of 341 nm and 336 nm, respectively.[56,95] Like most carbon nanohoops, the absorbance profiles appear to not depend significantly on the magnitude of the HOMO-LUMO gap.[54] One notable feature of the **BT[11+1]CPP** absorbance profile—not present in parent **[11+1]CPP**—is the minor peak at approximately 470 nm, observed in both DCM and DMSO. We hypothesize that this peak is representative of the HOMO-LUMO transition which is formally forbidden in most carbon nanohoops.[48] Generally, it can be seen that the absorbance trace of **BT[11+1]CPP** undergoes a minor red shift in the more polar DMSO.

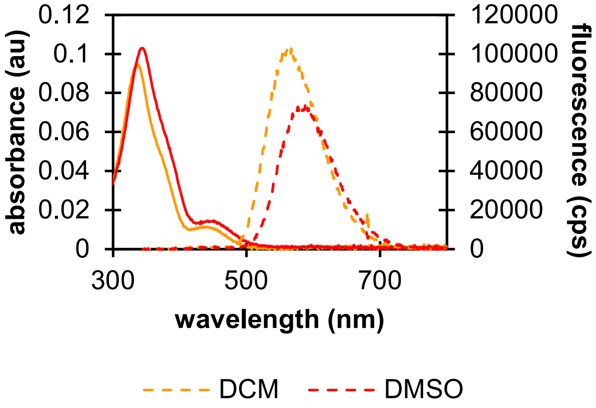

Figure 4.1. Absorbance (solid lines) and emission (dotted lines) traces for **BT[11+1]CPP** in DCM (yellow-orange) and DMSO (red). Excitation wavelength of 340 nm, slit widths (exc. and em.) of 1 nm.

Table 4.1. Photophysical data for **BT[11+1]CPP**. Quantum yields determined *via* comparison to known standards—quinine sulfate in 0.1 M H_2SO_4 (*aq*) and anthracene in ethanol.

Solvent	**$\lambda_{max,abs}$ (nm)**	**$\lambda_{max,em}$ (nm)**	**Quantum yield Φ**
DCM	336	562	0.32
DMSO	343	588	0.24

The fluorescence emission profile of **BT[11+1]CPP** is very representative of electron acceptor-containing, donor-acceptor-type molecules as described above. In comparison to the parent **[11+1]CPP**, which has a maximum emission wavelength of 449 nm in DCM,[56] we observe a red-shifted maximum emission wavelength of 562 nm in DCM for **BT[11+1]CPP**. We also observe positive solvatofluorochromism as demonstrated in **Figure 4.2**. As the polarity of solvent increases, the emission color of the molecule moves towards red in the visible light spectrum.

The quantum yields for **BT[11+1]CPP** were measured in both DCM and DMSO. In DCM, **BT[11+1]CPP** demonstrated a significantly lower quantum yield of 0.32 in comparison to parent **[11+1]CPP** (Φ = 0.80 in DCM), measured previously by a slightly different method.[56] A further lowering of the quantum yield was observed in more polar DMSO for **BT[11+1]CPP**, as is typical of fluorophores with a polarized excited state.[119] Notably, **[11+1]CPP** was shown to maintain its high quantum yield in DMSO (Φ = 0.83),[95] indicating a lack of donor-acceptor character and therefore solvent-dependent quantum yield for the parent CPP.

Figure 4.2. BT[11+1]CPP dissolved in various solvents from least polar (left) to most polar (right) and illuminated with longwave UV light.

4.2.3 Synthesis of [12+2]CPP

The synthesis of **[12+2]CPP** is shown in **Scheme 4.2**. It begins with **IV.1** undergoing lithium-halogen exchange with *n*-BuLi followed by the addition of electrophilic boron source isopropoxy-4,4,5,5-tetramethyl-1,3,2-dioxaborolane to furnish borylated **IV.6**. **IV.6** and **IV.1** were combined under dilute Suzuki-Miyaura cross-coupling conditions to yield macrocyclic precursor **IV.7** in 39% yield. **IV.7** then underwent deprotection of its silyl ether groups in the presence of TBAF. Without rigorous purification, the macrocycle was then subjected to reductive aromatization *via* H_2SnCl_4 to yield the final product **[12+2]CPP**.

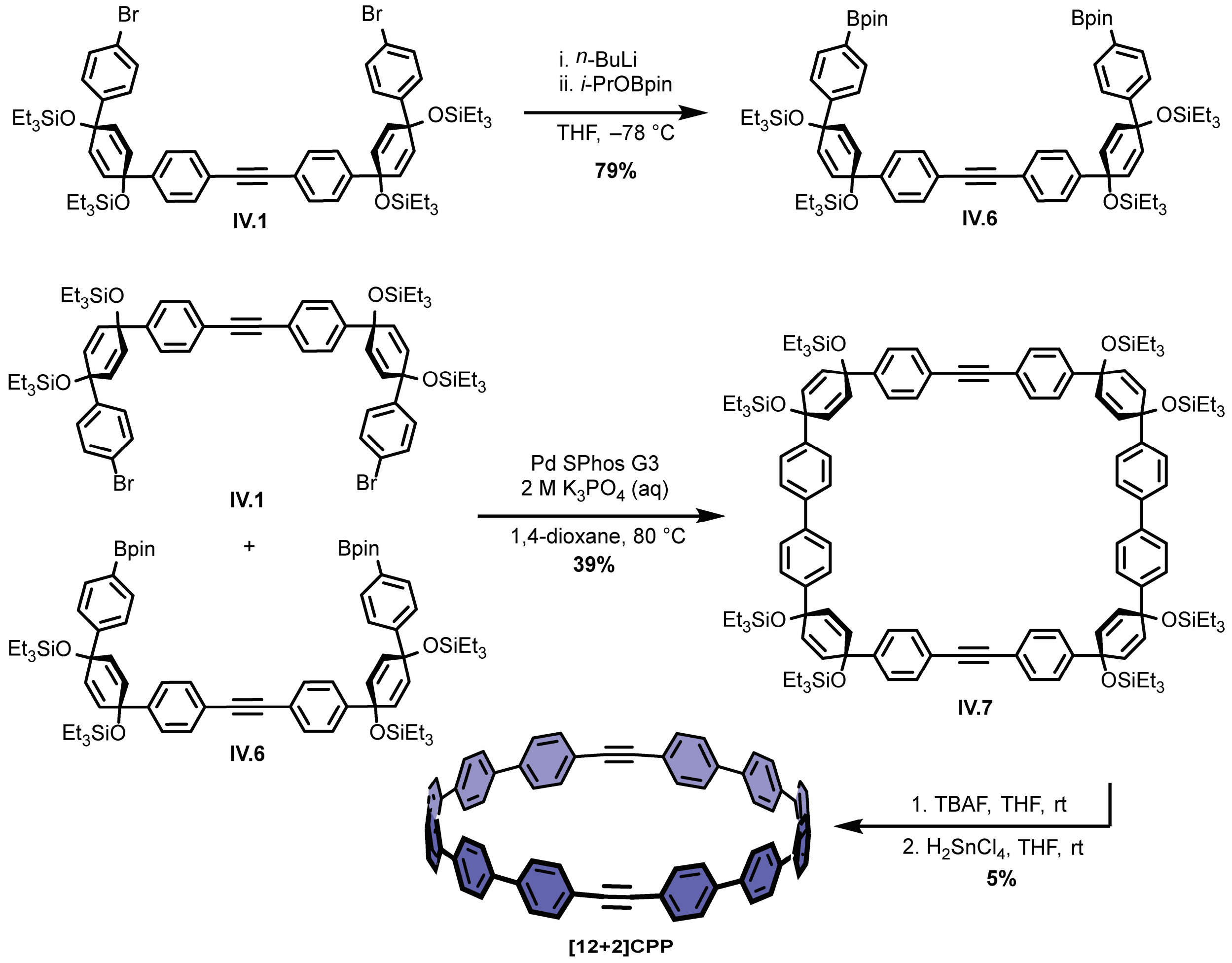

Scheme 4.2. Synthesis of **[12+2]CPP**.

4.2.4 Preliminary Click Chemistry Studies with [12+2]CPP

[12+2]CPP was generated in small yields from the above unoptimized synthetic scheme. Nonetheless, efforts were made to assess the ability of **[12+2]CPP** to undergo two SPAAC reactions at its alkynes (**Scheme 4.3**). When exposed to multiple equivalents of benzyl azide, **[12+2]CPP** appears to react to potentially form a doubly clicked product (see NMR spectra in **Figure 4.4**). Notably, two isomers would be expected to form from this reaction. We hypothesize that the product observed in **Figure 4.4** could be a combination of both these isomers, ***trans*** **[12+2]CPP-BnAz** and ***cis*** **[12+2]CPP-BnAz**.

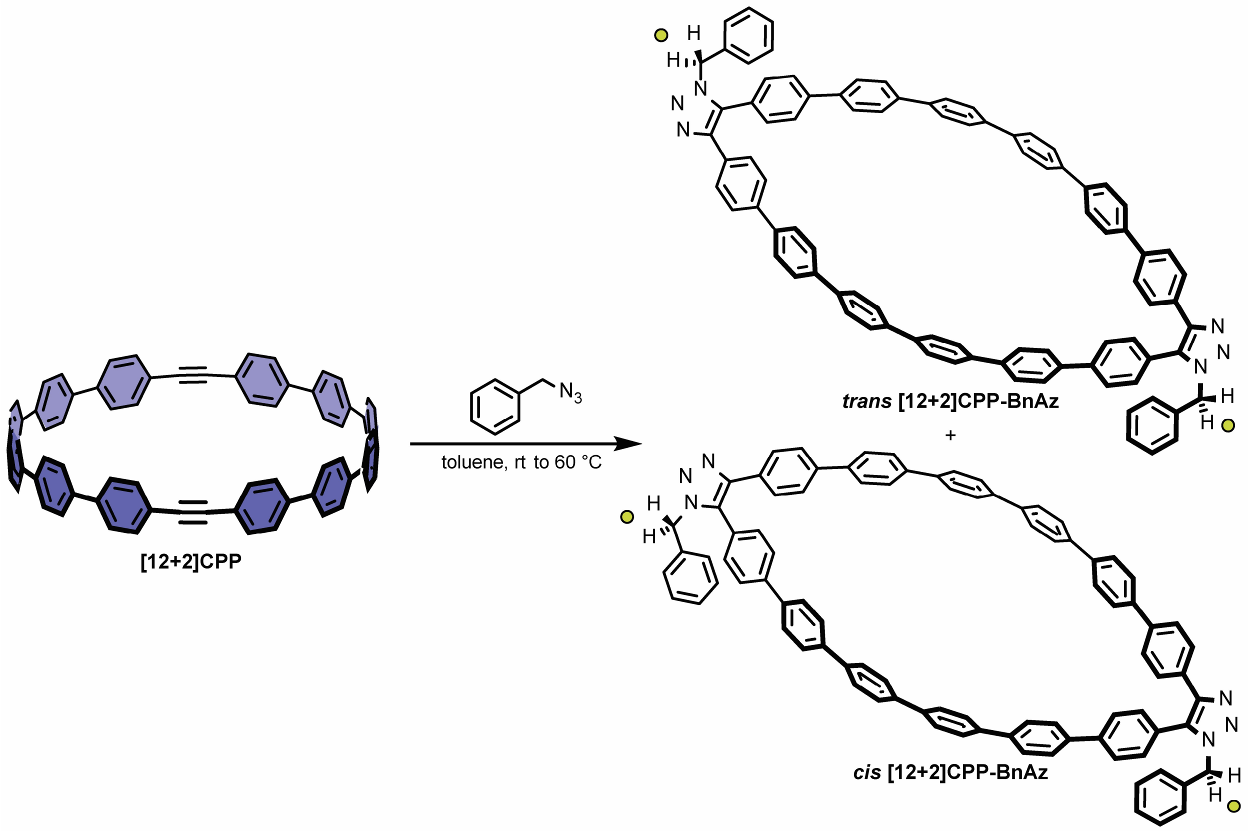

Scheme 4.3. Proposed reaction between **[12+2]CPP** and benzyl azide to form *cis* and *trans* isomers. Green dots indicate the benzylic protons which seem to be present in the NMR spectrum shown in **Figure 4.3**.

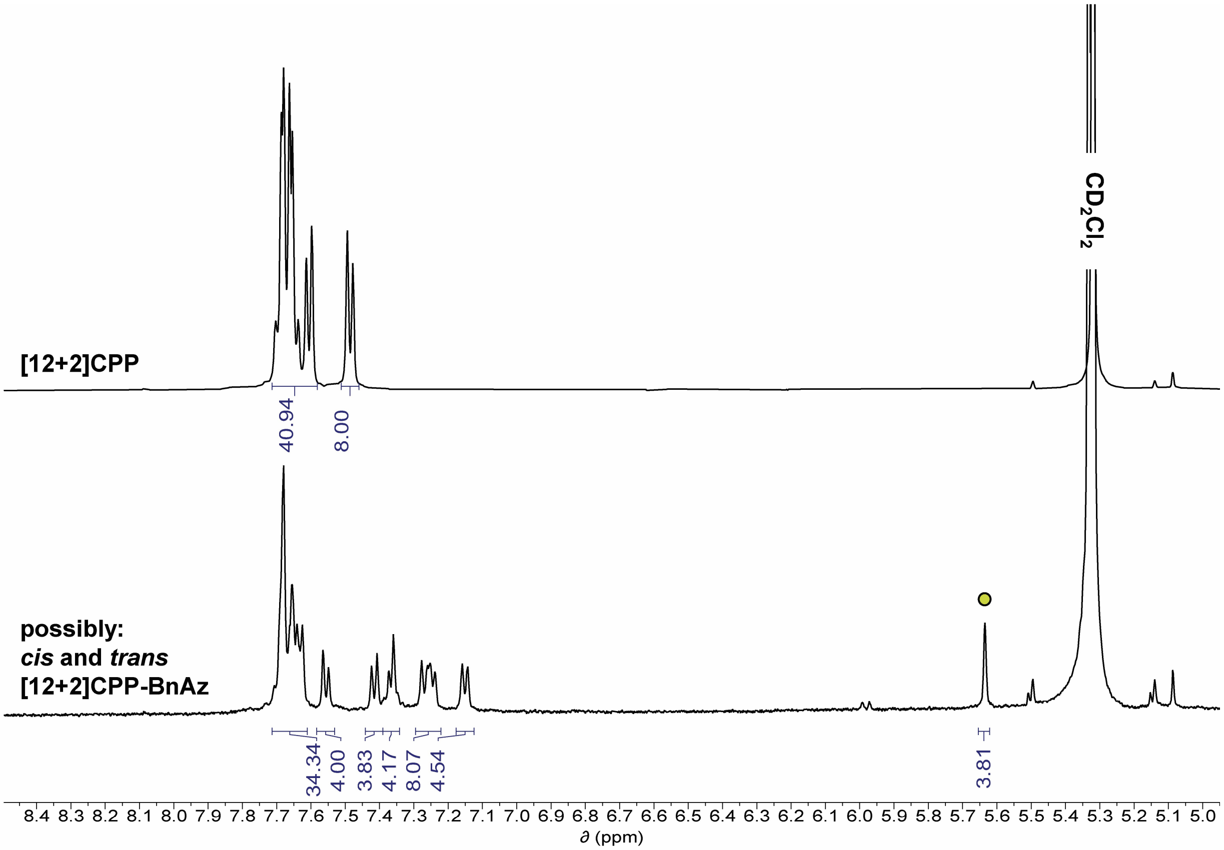

Figure 4.3. ^{1}H NMR in CD_2Cl_2 of **[12+2]CPP** (top) and possible click products, isomers ***cis*** and ***trans*** **[12+2]CPP-BnAz** (bottom). We hypothesize that the peak marked with the green dot represents the benzylic protons of the products (see **Scheme 4.3**).

4.2.5 Synthetic Progress Towards a Thermally-Activated Delayed Fluorescence DMAC-Tz[12]CPP

The synthesis of **DMAC-Tz[12]CPP** is incomplete due to difficulty in the final reductive aromatization step of our synthetic strategy (*vide infra* and **Table 4.2**). However, we have been able to successfully incorporate the electron-donating DMAC and electron-accepting Tz units into an unaromatized macrocyclic precursor (**IV.14**).

As shown in **Scheme 4.4**, the synthesis begins with the benzylation of 2,7-Dibromo-9,9-dimethyl-9,10-dihydroacridine to form **IV.8**. Previously described precursor **IV.9** was converted to **IV.10** in 47% yield by lithium-halogen exchange and addition into electrophilic ketone **IV.2**, followed by silyl ether protection. **IV.10** was in turn converted to boronate **IV.11** by lithium-halogen exchange and treatment with an electrophilic source of pinacol boronic ester. Two equivalents of coupling partner **IV.11** were combined with DMAC derivative **IV.8** under Suzuki-

Miyaura cross-coupling conditions to form **IV.12**, which subsequently underwent Miyaura borylation to yield **IV.13**. Subjection of **IV.13** and 2,4-dichloro-6-phenyl-1,3,5-triazine to very dilute Suzuki-Miyaura cross-coupling conditions furnished silyl-protected **IV.14**. Deprotection with tetrabutylammonium fluoride yielded **IV.15** containing eight free alcohol groups.

Unfortunately, attempts to reductively aromatize precursors **IV.14** and **IV.15** under a variety of conditions were unsuccessful (**Table 4.2**).

Table 4.2. Summary of results for reductive aromatization of DMAC-Tz[12]CPP.

Trial	Starting material	Reducing agent	Outcome
1	**IV.15**	H_2SnCl_4	decomposition
2	**IV.14**	$Na^+[C_{10}H_8]^-$	decomposition
3	**IV.15**	$SnCl_2$, PBr_3	decomposition

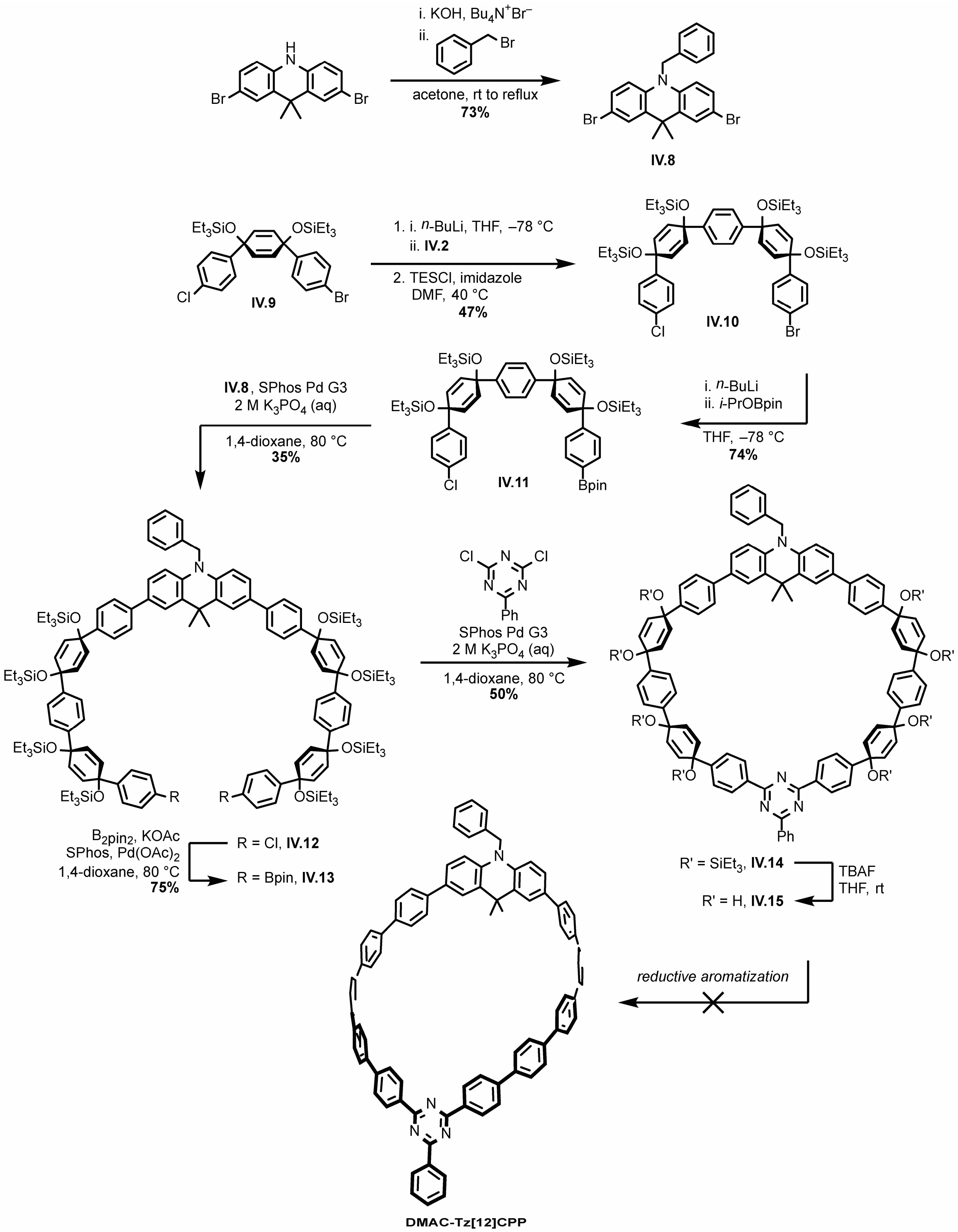

Scheme 4.4. Synthetic scheme for **DMAC-Tz[12]CPP**.

4.3 Conclusion and Future Directions

4.3.1 Electron Acceptor-Incorporating [*n*+1]CPPs

BT[11+1]CPP incorporates two avenues of study in our lab—donor-acceptor and strained alkyne nanohoops—into a unique molecule that can productively undergo strain-promoted reactions. We have demonstrated that **BT[11+1]CPP** displays fluorescence emission red-shifted by over 100 nm (in DCM and DMSO) in comparison to parent **[11+1]CPP**.[56,95] Crucially, we have also shown that **BT[11+1]CPP** has strong donor-acceptor character as indicated by its solvent-dependent maximum emission wavelengths and quantum yields.

An important next step forward is to assess the ability of **BT[11+1]CPP** to undergo the SPAAC reaction with a model azide (*e.g.* benzyl azide). This is important for two reasons. Firstly, a previous study from our group has shown that the BT unit is sensitive to strain.[118] As this unit is located directly across the nanohoop from the alkyne, it will likely experience heightened local strain post-click reaction as the nanohoop is bent into a tear-drop shape.[59] Assessing the stability of the SPAAC product is therefore important. Secondly, computational findings from our group suggest that increasing strain at electron-accepting units leads to a further increase in their electron affinity and therefore lowers the energy of the LUMO further.[121] Assessing whether **BT[11+1]CPP-BnAz** could have even further red-shifted emission than **BT[11+1]CPP** itself would therefore be of interest in the future design of electron acceptor-containing nanohoops.

4.3.2 [12+2]CPP as a Double Click Reagent

Carbon nanohoops capable of undergoing late-stage transformations are especially useful. The design of **[12+2]CPP** is particularly interesting as the reaction at one alkyne will result in heightened local strain on the opposite side of the nanohoop.[59] This in turn should accelerate reaction at the second alkyne. Finally, the product of such reactions should be very stable due to its diminished strain.

We have shown herein that **[12+2]CPP** can be synthesized efficiently from the building block common to many strained alkyne nanohoop syntheses, **IV.1**. Furthermore, preliminary study suggests that **[12+2]CPP** can undergo two SPAAC reactions with model system benzyl azide to form a stable product, **[12+2]CPP-BnAz**, which most likely is a mixture of *trans* and *cis* isomers. We envision that many derivatives of **[12+2]CPP** could be synthesized from sequential strain-promoted reactions of the nanohoop. Such chemistry could find use in the field of material chemistry as a reagent for polymerizations and cross-linkings.

4.3.3 Synthesis of a TADF Nanohoop DMAC-Tz[12]CPP

A carbon nanohoop displaying thermally-acetivated delayed fluorescence remains an elusive goal for our group and others.[128] The current bottleneck for our efforts is the final reductive aromatization step of a promising DMAC and triazine-containing macrocycle to form the final DMAC-Tz[12]CPP. We have tried several strategies used frequently in our group for this aromatization step but have thus far only observed decomposition of the starting material. Future efforts will work to identify better conditions for this transformation.

4.4 Experimental Section

4.4.1 General Experimental Details

Unless otherwise noted, commercially available materials were used without purification. Compounds **IV.1**, **IV.2**, **IV.9**, and Pd Sphos G3 were prepared according to the literature.[48,56,84] Moisture and oxygen sensitive reactions were carried out in flame-dried glassware and under an inert atmosphere of purified nitrogen using syringe/septa technique. Tetrahydrofuran (THF), dimethylformamide (DMF), and 1,4-dioxane were dried by filtration through alumina according to the methods described by Grubbs.[85] Thin-layer chromatography (TLC) was performed on aluminum plates coated with 0.20 mm thickness of Silica Gel 60 F254 (Macherey-Nagel). Developing plates were visualized using UV light at wavelengths of 254 and 365 nm. Silica column chromatography was conducted with Zeochem Zeoprep n60 Eco 40-63 μm silica gel. Alumina column chromatography was conducted with SorbTech basic alumina (pH 10), Act. II-III, 50-200 μm. ^{1}H and ^{13}C NMR spectra were recorded on either a Bruker Avance III HD 500 (^{1}H: 500 MHz, ^{13}C: 126 MHz) or Bruker Avance III HD 600 MHz (^{1}H: 600 MHz, ^{13}C: 151 MHz) NMR spectrometer. The samples were measured at 25 °C. The chemical shifts (δ) were reported in parts per million (ppm) and were referenced to the residual protio-solvent (CD_2Cl_2, ^{1}H: $\delta = 5.32$ ppm and ^{13}C: $\delta = 53.84$ ppm) or to tetramethylsilane (for $CDCl_3$, TMS, $\delta = 0.00$ ppm). Coupling constants (J) are given in Hz and the apparent resonance multiplicity is reported as s (singlet), d (doublet), t (triplet), q (quartet), dd (doublet of doublets) or m (multiplet). Infrared absorption (IR) spectra were recorded on a Thermo Scientific Nicolet 6700 spectrometer equipped with a diamond crystal Smart ATR. Characteristic IR absorptions are reported in cm^{-1} and denoted as strong (s), medium (m), and weak (w). UV/Vis absorption and fluorescence spectra were recorded on an Agilant Cary 100 spectrophotometer and a Horiba Jobin Yvon Fluoromax-4 Fluorimeter, respectively. All measurements were carried out under ambient conditions in a Spectrocell RF-1010-T threaded top vacuum formed borosilicate fluorometer cell (10 mm light path). The absorption maxima (λ_{max}) are reported in nm and the extinction coefficient (ε) in M^{-1} cm^{-1}.

4.4.2 Synthesis

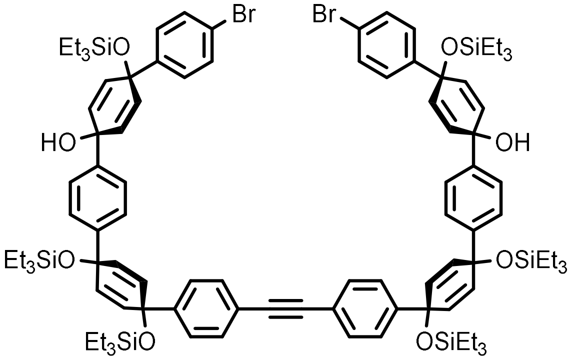

IV.3. IV.1 (0.318 g, 0.27 mmol, 1.05 equiv.) was dissolved in THF (2.6 mL, 0.2 M) and the solution cooled to –78 °C over the course of 45 minutes. *n*-Butyllithium (2.5 M in hexanes, 0.21 mL, 0.53 mmol, 2.05 equiv.) was added dropwise. The mixture was stirred for 5 minutes, then **IV.2** (0.197 6, 0.51 mmol, 2 equiv., diluted with 2 mL THF) was added dropwise. The reaction was allowed to stir at -78 °C for one hour. Deionized water (15 mL) was added. The organic solvent was removed via rotary evaporator. The mixture was extracted with ethyl acetate (3 × 50 mL). The combined organic layers were washed with brine (3 × 50 mL), dried over sodium sulfate, filtered and concentrated to yield the crude product as a yellow oil. The crude product was purified via automated column chromatography (SiO_2, 20 – 60% DCM/hexanes). Product-containing fractions were concentrated and subjected to recrystallization in ethanol to yield the final product as a white solid (0.16 g, 0.091 mmol, 35%). $R_f = 0.54$ (70% DCM/hexanes). ^1H NMR (500 MHz, Methylene Chloride-d_2) δ 7.45 (d, $J = 8.2$ Hz, 4H), 7.40 (d, $J = 8.5$ Hz, 4H), 7.38 – 7.32 (m, 12H), 7.25 (d, $J = 8.5$ Hz, 4H), 6.03 (m, 12H), 5.96 (d, $J = 9.9$ Hz, 4H), 2.13 (s, 2H), 1.03 – 0.93 (m, 54H), 0.70 (q, $J = 7.7$ Hz, 12H), 0.68 – 0.58 (m, 24H). ^{13}C NMR (126 MHz, CD_2Cl_2) δ 146.80, 145.97, 145.49, 143.86, 132.98, 132.21, 131.82, 131.63, 131.58, 131.56, 127.90, 126.47, 126.43,

125.90, 122.51, 121.38, 89.78, 71.78, 71.72, 71.68, 69.48, 7.24 (multiple peaks overlapping), 6.84 (multiple peaks overlapping). HRMS (ASAP, positive mode) *m/z* calcd for $C_{98}H_{133}O_8Si_6Br_2$: 1763.6983 $[M+H]^+$, found 1763.6841; IR (ATR) ṽ 3592 (w), 3033 (w), 2952 (m), 2909 (m), 2874 (m), 1456 (m), 1406 (m), 1238 (m) 1187 (m), 1070 (s), 1008 (s), 960 (s), 861 (m), 821 (m), 711 (s), 558 (m).

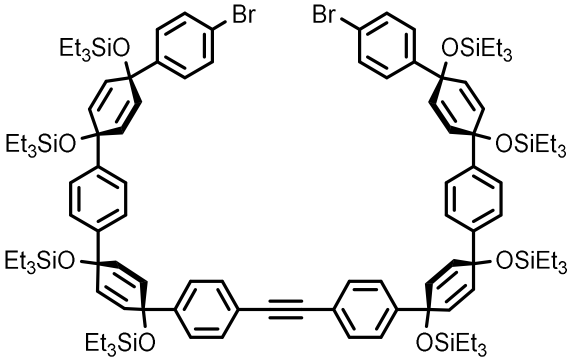

IV.4. IV.3 (0.152 g, 0.086 mmol, 1 equiv.) and imidazole (0.023 g, 0.34 mmol, 4 equiv.) was dissolved in *N,N*-dimethylformamide (1.3 mL, 0.2 M). Chlorotriethylsilane (0.04 mL, 0.26 mmol, 3 equiv.) was added *via* syringe. The reaction mixture was heated to 40 °C and allowed to stir overnight. It was then cooled to room temperature and saturated aqueous solution of sodium bicarbonate (5 mL) was added. The reaction was extracted with ethyl acetate (3 × 50 mL). The combined organic layers were then washed with aqueous 5% LiCl (3 × 50 mL), washed with brine (3 × 50 mL), dried over sodium sulfate, filtered, and concentrated *via* rotary evaporator to yield the crude product as a colorless oil. The crude product was purified *via* automated column chromatography (SiO_2, 0 – 28% CH_2Cl_2/hexanes) to yield a white solid (0.081 g, 0.041 mmol, 47%). $R_f = 0.55$ (30% DCM/hexanes). ^1H NMR (500 MHz, Methylene Chloride-d_2) δ 7.41 (d, *J* = 8.0 Hz, 4H), 7.36 (d, *J* = 8.3 Hz, 4H), 7.34 – 7.24 (m, 12H), 7.19 (d, *J* = 8.2 Hz, 4H), 6.05 (dd, *J* = 10.2, 2.2 Hz, 8H), 5.98 (d, *J* = 9.9 Hz, 4H), 5.93 (d, *J* = 9.8 Hz, 4H), 0.99 – 0.85 (m, 72H), 0.69 – 0.54 (m, 48H). ^{13}C NMR (126 MHz, CD_2Cl_2) δ 146.78, 145.75, 145.60, 145.43, 132.20, 132.17, 131.72, 131.59, 131.55, 131.47, 128.12, 126.34, 126.21, 126.19, 122.43, 121.37, 89.72, 71.85, 71.70, 71.64, 71.58, 7.24, 7.22, 6.83, 6.79, 6.77 (26 signals, some peaks overlapping). HRMS (ASAP, positive mode) *m/z* calcd for $C_{110}H_{160}O_8Si_8Br_2$: 1990.8634 $[M]^+$, found 1990.8658. IR (ATR) ṽ 2952 (m), 2909 (m), 2875 (m), 1457 (m), 1405 (m), 1238 (m), 1188 (m), 1059 (s), 1010 (s), 957 (s), 879 (m), 862 (m), 726 (s), 554 (m).

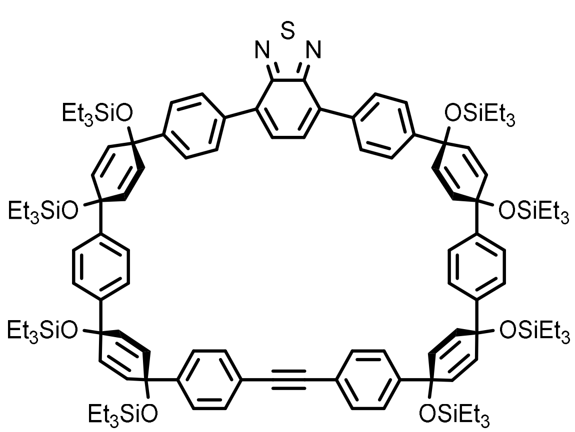

IV.5. IV.4 (0.630 g, 0.32 mmol, 1.0 equiv.), 2,1,3-benzothiadiazole-4,7-bis(boronic acid pinacol ester) (0.135 g, 0.34 mmol, 1.1 equiv.), and Pd SPhos Gen III (0.025 g, 0.032 mmol, 0.1 equiv.) were dissolved in 1,4-dioxane (451 mL, 0.0007 M, sparged with N_2 for one hour prior to use). The resulting solution was sparged with N_2 for an additional 15 minutes. The reaction mixture was heated to 80 °C over the course of 15 minutes. Deoxygenated aqueous K_3PO_4 solution (45 mL, 2.0 M, sparged with N_2 for one hour prior to use) was added via syringe. The reaction mixture was allowed to stir at 80 °C for 1.5 hours. It was then cooled to room temperature and filtered through a plug of Celite (DCM) and dried over sodium sulfate. Concentration *via* rotary evaporator yielded the crude product as a brown solid. The crude product was purified *via* automated column chromatography (0 – 25% DCM/hexanes). The resultant solid was sonicated in methanol and vacuum filtered to yield the final product as a bright yellow solid (0.117 g, 0.06 mmol, 19%). R_f = 0.32 (40% DCM/hexanes). ^{1}H NMR (500 MHz, Methylene Chloride-d_2) δ 7.83 (d, J = 8.0 Hz, 4H), 7.70 (s, 2H), 7.44 (d, J = 8.0 Hz, 4H), 7.36 – 7.29 (m, 8H), 7.26 (d, J = 8.1 Hz, 4H), 7.19 (d, J = 8.0 Hz, 4H), 6.07 (dt, J = 21.6, 10.2 Hz, 12H), 5.93 (d, J = 9.8 Hz, 4H), 0.96 (ddt, J = 25.3, 13.2, 7.9 Hz, 72H), 0.71 (q, J = 7.9 Hz, 12H), 0.61 (ddt, J = 14.9, 10.0, 7.5 Hz, 36H). ^{13}C NMR (126 MHz, CD_2Cl_2) δ 154.36, 146.94, 146.36, 145.61, 145.45, 136.78, 132.77, 132.27, 132.15, 131.99, 131.52, 131.33, 129.30, 128.61, 126.44, 126.22, 125.98, 122.06, 89.52, 72.18, 71.93, 71.68, 71.62, 7.29, 7.25, 7.21, 6.87, 6.83, 6.76 (29 signals, some peaks overlapping). HRMS (ASAP, positive mode) *m/z* calcd for $C_{116}H_{162}N_2O_8Si_8S$: 1967.0206 $[M]^+$, found 1967.0089. IR (ATR) ṽ 2952 (m), 2909 (m), 2874 (m), 1456 (m), 1408 (m), 1238 (m), 1189 (m), 1068 (s), 1004 (s), 960 (s), 880 (m), 862 (m), 823 (m), 715 (s), 555 (m).

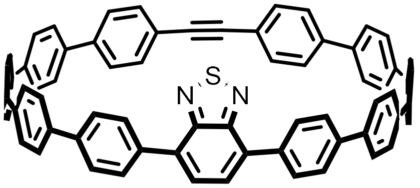

BT[11+1]CPP. *Deprotection of silyl ethers*. **IV.5** (0.032 g, 0.030 mmol, 1 equiv.) was dissolved in THF (3.8 mL, 0.008 M). Acetic acid (0.09 mL, 1.5 mmol, 50 equiv.) was added dropwise, followed closely by the addition of tetrabutyl ammonium fluoride (1 M solution in THF, 0.76 mL, 0.76 mmol, 25 equiv.) was added dropwise and the reaction was allowed to stir for 18 hours at room temperature. The reaction was diluted with ethyl acetate (100 mL). This organic phase was washed with DI water (2 × 50 mL) and brine (2 × 50 mL). Concentration of the organic layer yielded the crude product as a yellow solid which was not purified further (0.032 g, 0.03 mmol, yield assumed quantitative).

Reductive aromatization. $SnCl_2{\cdot}2H_2O$ (0.181 g, 0.8 mmol, 1.0 equiv. with respect to HCl) was dissolved in tetrahydrofuran (20 mL, 0.040 M). HCl (0.13 mL, 1.6 mmol, 2.0 equiv. with respect to $SnCl_2{\cdot}2H_2O$) was added and the reaction was allowed to stir for 20 minutes. Concurrently in a separate flask, the deprotected macrocycle (0.032 g, 0.03 mmol, 1 equiv.) was dissolved in THF (8 mL, 0.0038 M). After the 20 minutes had elapsed, prepared H_2SnCl_4 solution (6.1 mL, 0.2 mmol, 8 equiv.) was added to the solution of deprotected macrocycle. The reaction was allowed to stir for 1.5 hours. The mixture was diluted with hexanes (30 mL) and subjected directly to a plug (basic AlO_x, 50% DCM/50% hexanes). Product-containing fractions were concentrated and washed with pentanes to yield the final product as a yellow solid. (0.0015 g, 0.0016 mmol, 5%). R_f = 0.58 (70% DCM/hexanes). ^{1}H NMR (500 MHz, DMSO-d_6) δ 8.08 (d, *J* = 8.4 Hz, 4H), 7.85 – 7.69 (m, 36H), 7.63 (s, 2H), 7.47 (d, *J* = 8.3 Hz, 4H).

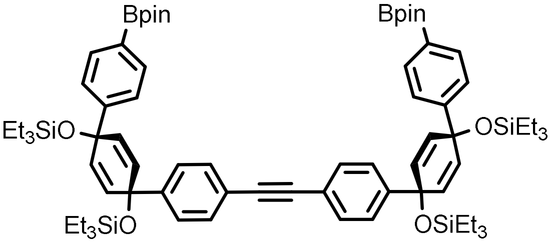

IV.6. IV.1 (2.30 g, 2.0 mmol, 1 equiv.) was dissolved in THF (15 mL, 0.2 M) and the solution cooled to –78 °C over the course of 45 minutes. *n*-Butyllithium (2.5 M in hexanes, 1.8 mL, 4.5

mmol, 2.3 equiv.) was added dropwise. This was followed by the dropwise addition of 2-isopropoxy-4,4,5,5-tetramethyl-1,3,2-dioxaborolane (1.2 mL, 4.5 mmol, 3 equiv.). The reaction was allowed to stir at -78 °C for one hour. Deionized water (15 mL) was added. The organic solvent was removed via rotary evaporator. The mixture was extracted with ethyl acetate (3 × 50 mL). The combined organic layers were washed with brine (3 × 25 mL), dried over sodium sulfate, filtered and concentrated to yield the crude product as a yellow oil. Trituration with DCM and ethanol yielded the final product as a white solid. (1.966 g, 1.6 mmol, 79%). ^{1}H NMR (500 MHz, Chloroform-*d*) δ 7.72 (d, *J* = 8.2 Hz, 4H), 7.45 (d, *J* = 8.4 Hz, 4H), 7.39 – 7.30 (m, 8H), 6.05 – 5.96 (m, 8H), 1.36 (s, 24H), 0.97 – 0.89 (m, 36H), 0.65 – 0.55 (m, 24H).

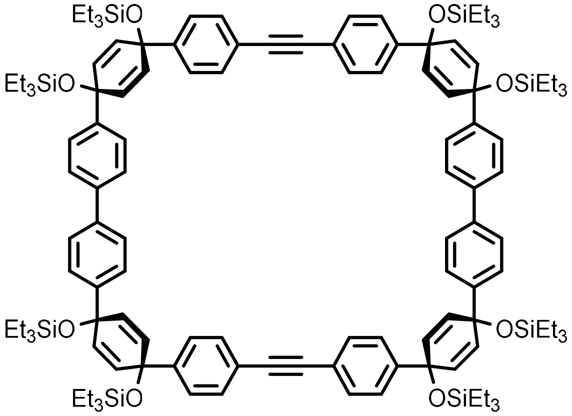

IV.7. IV.1 (0.15 g, 0.129 mmol, 1 equiv.), **IV.6** (0.178 g, 0.142 mmol, 1.1 equiv.), and Pd SPhos Gen III (0.010 g, 0.013 mmol, 0.1 equiv.) were dissolved in 1,4-dioxane (142 mL, 0.001 M, sparged with N_2 for one hour prior to use). The resulting solution was sparged with N_2 for an additional 15 minutes. The reaction mixture was heated to 80 °C over the course of 15 minutes. Deoxygenated aqueous K_3PO_4 solution (14 mL, 2.0 M, sparged with N_2 for one hour prior to use) was added *via* syringe. The reaction mixture was allowed to stir at 80 °C overnight. It was then cooled to room temperature and the 1,4-dioxane was removed *via* rotary evaporator. The resultant mixture was extracted with DCM (3 × 100 mL). The organic layers were combined and washed with brine (3 × 50 mL), dried over sodium sulfate, filtered, and concentrated to yield the crude product as a brown oily solid. The crude product was purified via automated column chromatography (SiO_2, 0 – 20% DCM/hexanes). The resultant solid was sonicated in methanol and filtered to yield the final product as a white solid (0.10 g, 0.05 mmol, 39%). ^{1}H NMR (500

MHz, Chloroform-*d*) δ 7.46 (d, *J* = 8.3 Hz, 8H), 7.40 – 7.32 (m, 16H), 7.30 (d, *J* = 8.1 Hz, 8H), 6.06 – 5.96 (m, 16H), 0.99 – 0.93 (m, 72H), 0.61 (dq, *J* = 11.6, 7.9 Hz, 48H).

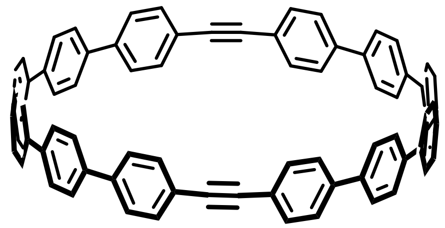

[12+2]CPP. *Deprotection of silyl ethers*. **IV.7** (0.086 g, 0.043 mmol, 1 equiv.) was dissolved in THF (5.3 mL, 0.008 M). Tetrabutyl ammonium fluoride (1 M solution in THF, 0.34 mL, 0.34 mmol, 8 equiv.) was added dropwise and the reaction was allowed to stir for one hour at room temperature. Deionized water (10 mL) was added and the mixture was sonicated for five minutes. Excess organic solvent was removed via rotary evaporator, and the resultant white suspended solid was isolated *via* vacuum filtration. Washing with deionized water and DCM yielded the product as a white solid (0.040 g, 0.037 mmol, 85% crude).

Reductive aromatization. $SnCl_2 \cdot 2H_2O$ (0.181 g, 0.8 mmol, 1.0 equiv. with respect to HCl) was dissolved in tetrahydrofuran (20 mL, 0.040 M). HCl (0.13 mL, 1.6 mmol, 2.0 equiv. with respect to $SnCl_2 \cdot 2H_2O$) was added and the reaction was allowed to stir for 20 minutes. Concurrently in a separate flask, the deprotected macrocycle (0.040 g, 0.037 mmol, 1 equiv.) was dissolved in THF (5 mL, 0.007 M). After the 20 minutes had elapsed, prepared H_2SnCl_4 solution (3.6 mL, 0.15 mmol, 4 equiv.) was added to the solution of deprotected macrocycle. The reaction was allowed to stir for one hour. The reaction was quenched with a saturated aqueous solution of $NaHCO_3$ (15 mL) and rotovapped to remove the THF. The organic products were extracted with DCM (5 × 30 mL), washed with brine (1 × 30 mL), dried over sodium sulfate, filtered, and concentrated to yield the crude product as a yellow solid. The crude product was subjected to purification *via* a short plug (basic AlO_x, 50% DCM/50% hexanes). The product was a yellow solid (0.002 g, 0.0021 mmol, 6%). ^1H NMR (500 MHz, Chloroform-*d*) δ 7.69 – 7.54 (m, 40H), 7.47 (d, *J* = 8.5 Hz, 8H).

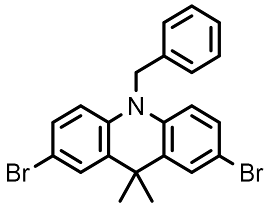

IV.8. 2,7-Dibromo-9,9-dimethyl-9,10-dihydroacridine (0.500 g, 1.37 mmol, 1 equiv.) was dissolved in acetone (18 mL, 0.076 M). Tetrabutyl ammonium bromide (0.023 g, 0.07 mmol, 0.05 equiv.) and KOH (0.23 g, 4.1 mmol, 3 equiv.) were added and the reaction was allowed to stir for 30 minutes at room temperature. Over the course of this time the solution turned yellow-orange. Benzyl bromide (0.24 mL, 2.1 mmol, 1.5 equiv.) was added. The reaction flask was fitted with a water-cooled condenser and heated to reflux for one hour. It was then removed from heat and allowed to cool. The reaction was quenched with DI water (30 mL). The organic products were extracted with ethyl acetate (3 × 150 mL) and hexanes (1 × 100 mL). The organic layers were combined and washed with brine (3 × 100 mL), dried over sodium sulfate, filtered, and concentrated to yield the crude product as an orange, somewhat crystalline solid. Vigorous sonication in hexanes followed by vacuum filtration yielded the final product as an off-white solid (0.456 g, 1.0 mmol, 73%). ^{1}H NMR (500 MHz, Chloroform-*d*) δ 7.50 (d, *J* = 2.2 Hz, 2H), 7.35 – 7.26 (m, 3H), 7.19 – 7.11 (m, 4H), 6.60 (d, *J* = 8.7 Hz, 2H), 5.14 (s, 2H), 1.56 (s, 6H).

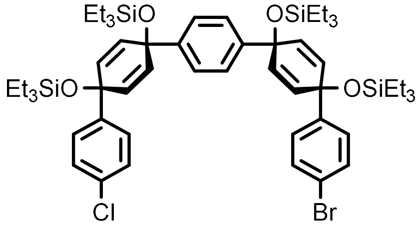

IV.10. *Lithium-halogen exchange and nucleophilic addition to ketone.* **IV.9 (**2.11 g, 3.5 mmol, 1.1 equiv.) was dissolved in THF (11 mL, 0.3 M), and the solution was cooled to –78 °C over the course of 30 minutes. *n*-Butyllithium (2.38 M in hexanes, 1.4 mL, 3.3 mmol, 1.05 equiv.) was added dropwise. After ten minutes, **IV.2** (1.2 g, 3.2 mmol, 1.0 equiv.) was added dropwise. The reaction was allowed to stir for one hour at –78 °C. The reaction was quenched with DI water (30 mL) and allowed to warm to room temperature. Excess THF was removed *via* rotary evaporator. The organic products were extracted with ethyl acetate (3 × 50 mL). The organic layers were

combined and washed with brine (3 × 50 mL), dried over sodium sulfate, filtered, and concentrated to yield the crude product as a yellow oil which was not purified further.

Silyl ether protection. The crude oil (assumed 2.86 g, 3.2 mmol, 1 equiv.) and imidazole (0.86 g, 12.6 mmol, 4 equiv.) were dissolved in *N,N*-dimethylformamide (16 mL, 0.2 M). Chlorotriethylsilane (0.64 mL, 3.8 mmol, 1.2 equiv.) was added *via* syringe and the reaction was allowed to stir overnight at 40 °C. The reaction as then removed from heat and allowed to cool to room temperature. Then, the reaction was quenched with saturated aqueous sodium bicarbonate solution (30 mL). The organic products were extracted with ethyl acetate (3 × 75 mL). The organic layers were combined and washed with aqueous 5% LiCl solution (5 × 50 mL) and brine (3 × 50 mL), dried over sodium sulfate, filtered, and concentrated to yield a yellow solid as the crude product. The crude product was purified *via* automated column chromatography (SiO_2, 0 – 18% DCM/hexanes). Product-containing fractions were combined, concentrated, and triturated with DCM/ethanol to yield the final product as a white powdery solid (1.53 g, 1.5 mmol, 47%). ^1H NMR (500 MHz, Chloroform-*d*) δ 7.34 (d, *J* = 8.5 Hz, 2H), 7.25 – 7.13 (m, 10H), 6.01 (d, *J* = 10.2 Hz, 4H), 5.93 – 5.87 (m, 4H), 0.97 – 0.89 (m, 36H), 0.65 – 0.52 (m, 24H).

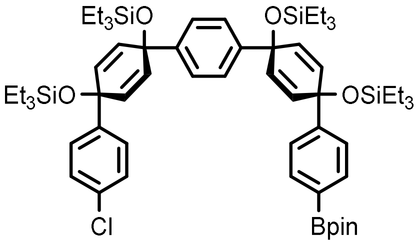

IV.11. IV.10 (1.4 g, 1.4 mmol, 1 equiv.) was dissolved in THF (6.9 mL, 0.2 M), and the solution was cooled to –78 °C over the course of 40 minutes. *n*-Butyllithium (2.38 M in hexanes, 0.66 mL, 1.6 mmol, 1.15 equiv.) was added dropwise. After ten minutes, 2-isopropoxy-4,4,5,5-tetramethyl-1,3,2-dioxaborolane (0.42 mL, 2.1 mmol, 1.5 equiv.) was added and the reaction was allowed to stir for one hour at –78 °C. The solution was quenched with DI water (15 mL) and allowed to warm to room temperature. Excess THF was removed *via* rotary evaporator. The organic products were extracted with ethyl acetate (3 × 50 mL). The organic layers were combined and washed with brine (3 × 50 mL), dried over sodium sulfate, filtered, and concentrated to yield the crude product as a colorless oil. Recrystallization in ethanol yielded the product as a white solid (1.08 g, 1.01 mmol, 74%). ^1H NMR (500 MHz, Chloroform-*d*) δ 7.70 (d, *J* = 7.8 Hz, 2H), 7.32 (d, *J* = 8.1 Hz,

2H), 7.21 (ddd, *J* = 13.6, 10.2, 5.6 Hz, 8H), 6.04 – 5.87 (m, 8H), 1.33 (s, 12H), 0.92 (m, *J* = 7.9, 4.6 Hz, 36H), 0.66 – 0.53 (m, 24H).

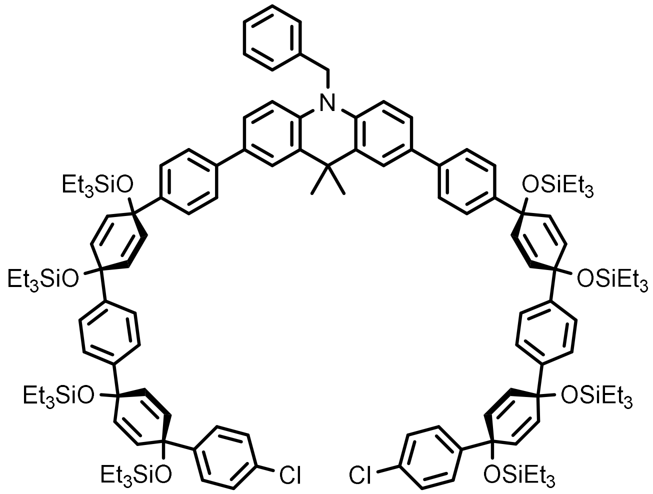

IV.12. IV.8 (0.24 g, 0.53 mmol, 1 equiv.), **IV.11** (1.16 g, 1.1 mmol, 2.05 equiv.), and Pd(dppf)Cl_2 (0.035 g, 0.042 mmol, 0.08 equiv.) were dissolved in 1,4-dioxane (5.3 mL, 0.1 M). The solution was sparged for 15 minutes, then placed into a pre-heated 80 °C oil bath for 15 minutes. Aqueous K_3PO_4 (2.0 M, 0.53 mL) was added and the reaction was allowed to stir at 80 °C overnight. The reaction was allowed to cool to room temperature, then diluted with ethyl acetate (200 mL). The solids were removed *via* a short Celite plug. The filtrate was concentrated and purified *via* automated column chromatography (SiO_2, 0 – 40% DCM/hexanes). Product-containing fractions were combined and sonicated in methanol to yield the product with minor impurities as an off-white powder (0.405 g, 0.19 mmol, 35%). ^{1}H NMR (500 MHz, Chloroform-*d*) δ 7.69 (d, *J* = 2.1 Hz, 2H), 7.48 (d, *J* = 8.3 Hz, 5H), 7.41 – 7.23 (m, 17H), 7.25 – 7.19 (m, 5H), 7.17 (d, *J* = 8.6 Hz, 4H), 6.82 (d, *J* = 8.5 Hz, 2H), 6.08 – 5.98 (m, 12H), 5.91 (d, *J* = 10.1 Hz, 4H), 5.28 (s, 2H), 1.70 (s, 6H), 1.03 – 0.86 (m, 72H), 0.71 – 0.53 (m, 48H).

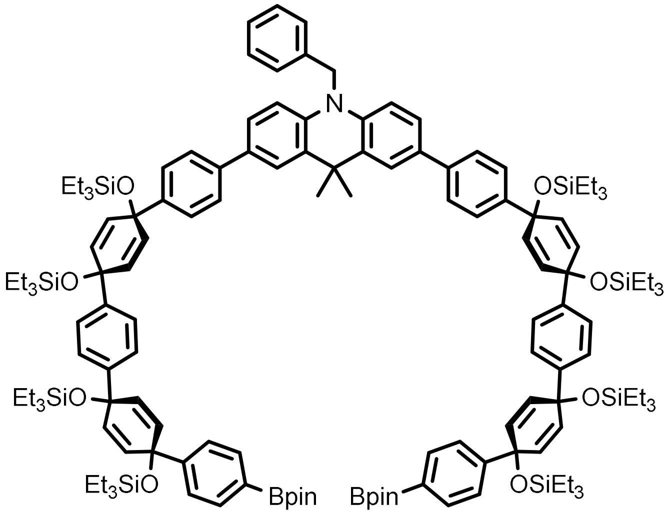

IV.13. IV.12 (0.295 g, 0.14 mmol, 1.0 equiv), KOAc (0.088 g, 0.89 mmol, 6.6 equiv.), palladium acetate (0.002 g, 0.0068 mmol, 0.05 equiv.), SPhos (0.007 g, 0.14 mmol, 0.125 equiv.), and bis(pinacolato)diboron (0.137 g, 0.54 mmol, 4.0 equiv) were dissolved in 1,4-dioxane (2.5 mL, 0.05 M). The reaction mixture was heated to 80 °C and allowed to stir for two hours. The reaction mixture was cooled to room temperature. Ethyl acetate (250 mL) was added and the reaction mixture was sonicated. It was then filtered through a plug of Celite. The filtrate was concentrated to yield the crude product as a brown oil. The product was run through a short plug (SiO_2, 70 – 100% DCM/hexanes). The filtrate was concentrated, and sonication in methanol yielded a white solid (0.238 g, 0.11 mmol, 75%). ^1H NMR (500 MHz, Chloroform-*d*) δ 7.71 – 7.65 (m, 6H), 7.48 – 7.42 (m, 5H), 7.41 – 7.22 (m, 22H), 6.78 (d, *J* = 8.5 Hz, 2H), 6.04 – 5.95 (m, 12H), 5.93 (d, *J* = 10.1 Hz, 4H), 5.25 (s, 2H), 1.67 (s, 6H), 1.29 (s, 24H), 0.99 – 0.87 (m, 72H), 0.69 – 0.52 (m, 48H).

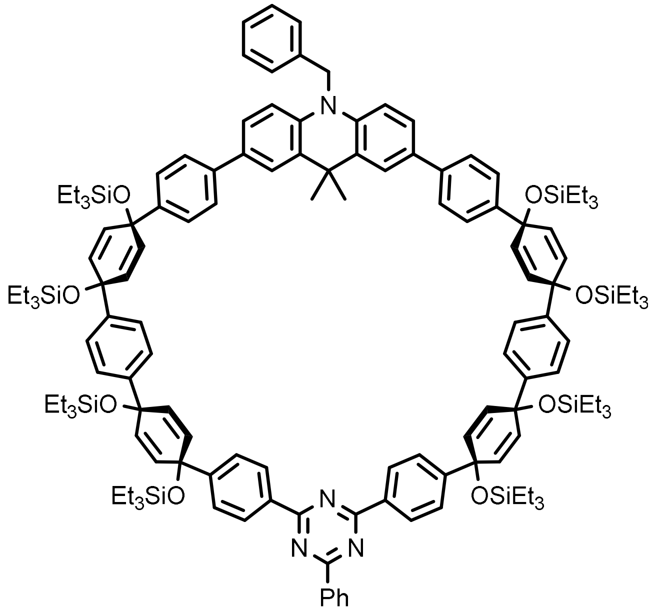

IV.14. IV.13 (0.232 g, 0.098 mmol, 1.1 equiv.), 2,4-dichloro-6-phenyl-1,3,5-triazine (0.02 g, 0.089 mmol, 1 equiv.), and Pd SPhos G3 (0.007 g, 0.0089 mmol, 0.1 equiv.) were dissolved in 1,4-dioxane (98 mL, 0.001 M). The resulting solution was sparged with N_2 for 15 minutes. The reaction mixture was heated to 80 °C over the course of 15 minutes. Deoxygenated aqueous K_3PO_4 solution (3 mL, 2.0 M, sparged with N_2 for one hour prior to use) was added *via* syringe. The reaction mixture was allowed to stir at 80 °C overnight. It was then cooled to room temperature and subjected to a short Celite plug topped with sodium sulfate. The filtrate was concentrated to yield a yellow oil as the crude product. Automated column chromatography (SiO_2, 0 – 27% DCM/hexanes) yielded mostly clean product (0.102 g, 0.045 mmol, 50%). ^{1}H NMR (500 MHz, Chloroform-*d*) δ 7.68 (d, *J* = 2.1 Hz, 2H), 7.48 – 7.42 (m, 6H), 7.38 – 7.31 (m, 5H), 7.32 – 7.26 (m, 17H), 7.19 – 7.12 (m, 5H), 7.09 – 7.03 (m, 3H), 6.81 (d, *J* = 8.5 Hz, 2H), 6.03 – 5.90 (m, 16H), 5.27 (s, 2H), 1.68 (s, 6H), 1.01 – 0.87 (m, 72H), 0.67 – 0.53 (m, 48H).

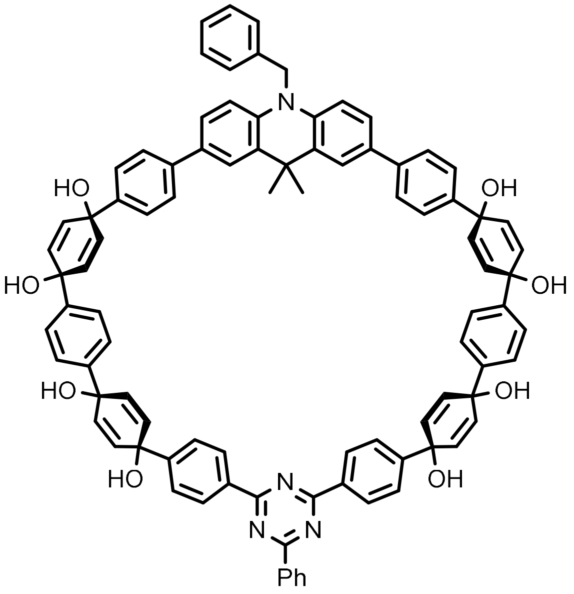

IV.15. IV.14 (0.046 g, 0.020 mmol, 1 equiv.) was dissolved in THF (2.5 mL, 0.008 M). Tetrabutylammonium fluoride (0.18 mL, 1 M in hexanes, 0.18 mmol, 8.8 equiv.) was added dropwise, turning the solution green. The reaction was allowed to stir for one hour. DI water (15 mL) was added and excess THF was removed *via* rotary evaporator. The product was extracted with ethyl acetate (3 × 30 mL), washed with DI water (1 × 15 mL), dried over sodium sulfate, filtered and concentrated to yield the product and minor impurities as a white solid. Yield not determined. ^{1}H NMR (500 MHz, Acetone-d_6) δ 7.84 (d, J = 2.2 Hz, 2H), 7.63 (d, J = 8.6 Hz, 4H), 7.55 (d, J = 8.3 Hz, 4H), 7.51 – 7.34 (m, 18H), 7.33 – 7.25 (m, 8H), 7.15 (t, J = 7.4 Hz, 2H), 6.93 (d, J = 8.5 Hz, 2H), 6.02 – 5.92 (m, 16H), 5.39 (s, 2H), 4.48 – 4.41 (m, 8H), 1.76 (s, 6H).

4.4.3 Photophysical Measurements for BT[11+1]CPP

The quantum yield of **BT[11+1]CPP** was measured *via* comparison to known standards using the method described by Horiba Scientific. Quinine sulfate in 0.1 M H_2SO_4 (aq) and anthracene in ethanol were utilized as the standards. The excitation wavelength for all measured compounds was 340 nm. The slit widths for the fluorimeter were 1 nm. **BT[11+1]CPP** was measured in both DCM and DMSO. The integration ranges for each compound's fluorescence were as follows: quinine sulfate (400-600 nm), anthracene (360-480 nm), **BT[11+1]CPP** in DCM (450-750 nm), **BT[11+1]CPP** in DMSO (450-750 nm). The experimental data is displayed in Figure 4.3 and Table 4.2.

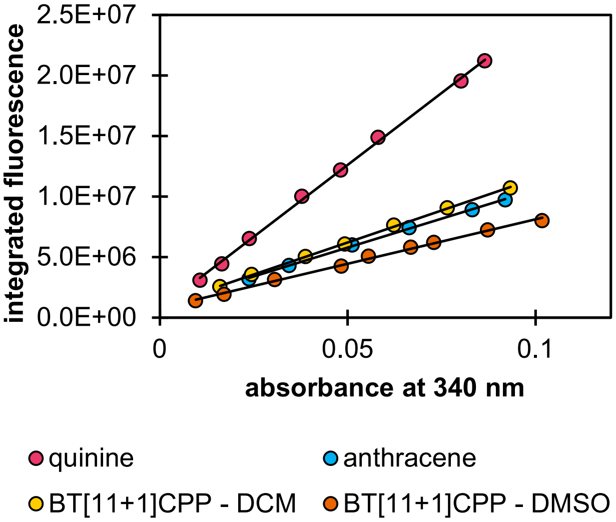

Figure 4.4. Quantum yield measurements for **BT[11+1]CPP** in DCM and DMSO as well as quinine and anthracene standards.

Table 4.3. Data for quantum yield measurement of **BT[11+1]CPP**.

Compound	Solvent	Slope	Φ w.r.t. quinine	Φ w.r.t. anthracene	Avg. Φ	Std. dev.
quinine	0.1 M H_2SO_4 (*aq*)	2.38×10^8	0.60 (lit)	0.65	0.62	0.032
anthracene	ethanol	9.53×10^7	0.25	0.27 (lit)	0.26	0.014
BT[11+1]CPP	DCM	1.06×10^8	0.30	0.33	0.32	0.017
BT[11+1]CPP	DMSO	7.33×10^7	0.23	0.25	0.24	0.012

CHAPTER 5

CONCLUDING REMARKS

The focus of this work has been a unique class of strained molecules that combine the fascinating electronic properties of strained conjugated systems with the usefulness of strained alkynes as a reactive handle. Strained alkyne carbon nanohoops exhibit reactivity that can be predicted *via* physical organic chemistry and modulated *via* organic synthesis. Through highly modular syntheses, we have described eight carbon nanohoops (**[9+1]CPP**, **[11+1]CPP**, **fluor[9+1]CPP**, **fluor[11+1]CPP**, ***m*[9+1]CPP**, **fluor-*m*[9+1]CPP**, **BT[11+1]CPP**, and **[12+2]CPP**) derived from only eight building block coupling partners. We have focused herein on the synthesis of these molecules and elucidation of their reactivity and photophysical properties. We have also described the derivatization of these molecules *via* strain-promoted azide-alkyne cycloadditions (SPAAC) and alkyne cyclotrimerization. In all, we have worked to further expand the effects that electronics and strain have on this new class of strained alkyne-containing molecules in order to better dictate their future applications. We anticipate that this research will aid in their future applications as click reagents in biology and materials chemistry.

REFERENCES CITED

(1) Kolb, H. C.; Finn, M. G.; Sharpless, K. B. Click Chemistry: Diverse Chemical Function from a Few Good Reactions. *Angew. Chem. Int. Ed.* **2001**, *40*, 2004–2021.

(2) Tornøe, C. W.; Christensen, C.; Meldal, M. Peptidotriazoles on Solid Phase: [1,2,3]-Triazoles by Regiospecific Copper(I)-Catalyzed 1,3-Dipolar Cycloadditions of Terminal Alkynes to Azides. *J. Org. Chem.* **2002**, *67*, 3057–3064.

(3) Rostovtsev, V. V.; Green, L. G.; Fokin, V. V.; Sharpless, K. B. A Stepwise Huisgen Cycloaddition Process: Copper(I)-Catalyzed Regioselective "Ligation" of Azides and Terminal Alkynes. *Angew. Chem. Int. Ed.* **2002**, *41*, 2596–2599.

(4) Huisgen, R. 1,3-Dipolar Cycloadditions. Past and Future. *Angew. Chem. Int. Ed. Engl.* **1963**, *2*, 565–598.

(5) Breugst, M.; Reissig, H.-U. The Huisgen Reaction: Milestones of the 1,3-Dipolar Cycloaddition. *Angew. Chem. Int. Ed.* **2020**, *59*, 12293–12307.

(6) Hein, J. E.; Fokin, V. V. Copper-Catalyzed Azide–Alkyne Cycloaddition (CuAAC) and beyond: New Reactivity of Copper(I) Acetylides. *Chem. Soc. Rev.* **2010**, *39*, 1302–1315.

(7) Agard, N. J.; Prescher, J. A.; Bertozzi, C. R. A Strain-Promoted [3 + 2] Azide−Alkyne Cycloaddition for Covalent Modification of Biomolecules in Living Systems. *J. Am. Chem. Soc.* **2004**, *126*, 15046–15047.

(8) Baskin, J. M.; Prescher, J. A.; Laughlin, S. T.; Agard, N. J.; Chang, P. V.; Miller, I. A.; Lo, A.; Codelli, J. A.; Bertozzi, C. R. Copper-Free Click Chemistry for Dynamic in Vivo Imaging. *Proc. Natl. Acad. Sci.* **2007**, *104*, 16793–16797.

(9) Ramil, C. P.; Lin, Q. Bioorthogonal Chemistry: Strategies and Recent Developments. *Chem. Commun.* **2013**, *49*, 11007.

(10) Hang, H. C.; Yu, C.; Kato, D. L.; Bertozzi, C. R. A Metabolic Labeling Approach toward Proteomic Analysis of Mucin-Type O-Linked Glycosylation. *Proc. Natl. Acad. Sci.* **2003**, *100*, 14846–14851.

(11) Sletten, E. M.; Bertozzi, C. R. From Mechanism to Mouse: A Tale of Two Bioorthogonal Reactions. *Acc. Chem. Res.* **2011**, *44*, 666–676.

(12) *The Nobel Prize in Chemistry 2022*. NobelPrize.org. https://www.nobelprize.org/prizes/chemistry/2022/summary/ (accessed 2023-10-16).

(13) Liu, F.; Liang, Y.; Houk, K. N. Bioorthogonal Cycloadditions: Computational Analysis with the Distortion/Interaction Model and Predictions of Reactivities. *Acc. Chem. Res.* **2017**, *50*, 2297–2308.

(14) Bickelhaupt, F. M. Understanding Reactivity with Kohn–Sham Molecular Orbital Theory: E2–SN2 Mechanistic Spectrum and Other Concepts. *J. Comput. Chem.* **1999**, *20*, 114–128.

(15) Ess, D. H.; Houk, K. N. Distortion/Interaction Energy Control of 1,3-Dipolar Cycloaddition Reactivity. *J. Am. Chem. Soc.* **2007**, *129*, 10646–10647.

(16) Bickelhaupt, F. M.; Houk, K. N. Analyzing Reaction Rates with the Distortion/Interaction-Activation Strain Model. *Angew. Chem. Int. Ed.* **2017**, *56*, 10070–10086.

(17) Harris, T.; Alabugin, I. V. Strain and Stereoelectronics in Cycloalkyne Click Chemistry. *Mendeleev Commun.* **2019**, *29*, 237–248.

(18) Ning, X.; Guo, J.; Wolfert, M. A.; Boons, G.-J. Visualizing Metabolically Labeled Glycoconjugates of Living Cells by Copper-Free and Fast Huisgen Cycloadditions. *Angew. Chem. Int. Ed.* **2008**, *47*, 2253–2255.

(19) Debets, M. F.; Van Berkel, S. S.; Schoffelen, S.; Rutjes, F. P. J. T.; Van Hest, J. C. M.; Van Delft, F. L. Aza-Dibenzocyclooctynes for Fast and Efficient Enzyme PEGylation via Copper-Free (3+2) Cycloaddition. *Chem. Commun.* **2010**, *46*, 97–99.

(20) Jewett, J. C.; Sletten, E. M.; Bertozzi, C. R. Rapid Cu-Free Click Chemistry with Readily Synthesized Biarylazacyclooctynones. *J. Am. Chem. Soc.* **2010**, *132*, 3688–3690.

(21) Chenoweth, K.; Chenoweth, D.; Goddard Iii, W. A. Cyclooctyne-Based Reagents for Uncatalyzed Click Chemistry: A Computational Survey. *Org. Biomol. Chem.* **2009**, *7*, 5255.

(22) Dommerholt, J.; Schmidt, S.; Temming, R.; Hendriks, L. J. A.; Rutjes, F. P. J. T.; van Hest, J. C. M.; Lefeber, D. J.; Friedl, P.; van Delft, F. L. Readily Accessible Bicyclononynes for Bioorthogonal Labeling and Three-Dimensional Imaging of Living Cells. *Angew. Chem. Int. Ed.* **2010**, *49*, 9422–9425.

(23) Agard, N. J.; Baskin, J. M.; Prescher, J. A.; Lo, A.; Bertozzi, C. R. A Comparative Study of Bioorthogonal Reactions with Azides. *ACS Chem. Biol.* **2006**, *1*, 644–648.

(24) Sletten, E. M.; Nakamura, H.; Jewett, J. C.; Bertozzi, C. R. Difluorobenzocyclooctyne: Synthesis, Reactivity, and Stabilization by β-Cyclodextrin. *J. Am. Chem. Soc.* **2010**, *132*, 11799–11805.

(25) Gordon, C. G.; Mackey, J. L.; Jewett, J. C.; Sletten, E. M.; Houk, K. N.; Bertozzi, C. R. Reactivity of Biarylazacyclooctynones in Copper-Free Click Chemistry. *J. Am. Chem. Soc.* **2012**, *134*, 9199–9208.

(26) Scott, L. T.; Bronstein, H. E.; Preda, D. V.; Ansems, R. B. M.; Bratcher, M. S.; Hagen, S. Geodesic Polyarenes with Exposed Concave Surfaces. *Pure Appl. Chem.* **1999**, *71*, 209–219.

(27) Bheemireddy, S. R.; Ubaldo, P. C.; Finke, A. D.; Wang, L.; Plunkett, K. N. Contorted Aromatics via a Palladium-Catalyzed Cyclopentannulation Strategy. *J. Mater. Chem. C* **2016**, *4*, 3963–3969.

(28) Xu, Y.; Kaur, R.; Wang, B.; Minameyer, M. B.; Gsänger, S.; Meyer, B.; Drewello, T.; Guldi, D. M.; von Delius, M. Concave–Convex π–π Template Approach Enables the Synthesis of [10]Cycloparaphenylene–Fullerene [2]Rotaxanes. *J. Am. Chem. Soc.* **2018**, *140*, 13413–13420.

(29) Kawase, T.; Darabi, H. R.; Oda, M. Cyclic [6]- and [8]Paraphenylacetylenes. *Angew. Chem. Int. Ed. Engl.* **1996**, *35*, 2664–2666.

(30) Lee, S.; Chénard, E.; Gray, D. L.; Moore, J. S. Synthesis of Cycloparaphenyleneacetylene via Alkyne Metathesis: C_{70} Complexation and Copper-Free Triple Click Reaction. *J. Am. Chem. Soc.* **2016**, *138*, 13814–13817.

(31) Zhou, X.; Thompson, R. R.; Fronczek, F. R.; Lee, S. Size-Selective Synthesis of Large Cycloparaphenyleneacetylene Carbon Nanohoops Using Alkyne Metathesis. *Org. Lett.* **2019**, *21*, 4680–4683.

(32) Zhou, X.; Kwon, H.; Thompson, R. R.; Herman, R. J.; Fronczek, F. R.; Bruns, C. J.; Lee, S. Scalable Synthesis of [8]Cycloparaphenyleneacetylene Carbon Nanohoop Using Alkyne Metathesis. *Chem. Commun.* **2021**, *57*, 10887–10890.

(33) Anderson, H. L.; Patrick, C. W.; Scriven, L. M.; Woltering, S. L. A Short History of Cyclocarbons. *Bull. Chem. Soc. Jpn.* **2021**, *94*, 798–811.

(34) Diederich, F.; Rubin, Y.; Knobler, C. B.; Whetten, R. L.; Schriver, K. E.; Houk, K. N.; Li, Y. All-Carbon Molecules: Evidence for the Generation of Cyclo[18]Carbon from a Stable Organic Precursor. *Science* **1989**, *245*, 1088–1090.

(35) Kaiser, K.; Scriven, L. M.; Schulz, F.; Gawel, P.; Gross, L.; Anderson, H. L. An sp-Hybridized Molecular Carbon Allotrope, Cyclo[18]Carbon. *Science* **2019**, *365*, 1299–1301.

(36) Iijima, S. Helical Microtubules of Graphitic Carbon. *Nature* **1991**, *354*, 56–58.

(37) Kroto, H. W.; Heath, J. R.; O'Brien, S. C.; Curl, R. F.; Smalley, R. E. C_{60}: Buckminsterfullerene. *Nature* **1985**, *318*, 162–163.

(38) Rao, R.; Pint, C. L.; Islam, A. E.; Weatherup, R. S.; Hofmann, S.; Meshot, E. R.; Wu, F.; Zhou, C.; Dee, N.; Amama, P. B.; Carpena-Nuñez, J.; Shi, W.; Plata, D. L.; Penev, E. S.; Yakobson, B. I.; Balbuena, P. B.; Bichara, C.; Futaba, D. N.; Noda, S.; Shin, H.; Kim, K. S.; Simard, B.; Mirri, F.; Pasquali, M.; Fornasiero, F.; Kauppinen, E. I.; Arnold, M.; Cola, B. A.; Nikolaev, P.; Arepalli, S.; Cheng, H.-M.; Zakharov, D. N.; Stach, E. A.; Zhang, J.; Wei, F.; Terrones, M.; Geohegan, D. B.; Maruyama, B.; Maruyama, S.; Li, Y.; Adams, W. W.; Hart, A. J. Carbon Nanotubes and Related Nanomaterials: Critical Advances and Challenges for Synthesis toward Mainstream Commercial Applications. *ACS Nano* **2018**, *12*, 11756–11784.

(39) Jasti, R.; Bhattacharjee, J.; Neaton, J. B.; Bertozzi, C. R. Synthesis, Characterization, and Theory of [9]-, [12]-, and [18]Cycloparaphenylene: Carbon Nanohoop Structures. *J. Am. Chem. Soc.* **2008**, *130*, 17646–17647.

(40) Leonhardt, E. J.; Jasti, R. Emerging Applications of Carbon Nanohoops. *Nat. Rev. Chem.* **2019**, *3*, 672–686.

(41) Darzi, E. R.; Hirst, E. S.; Weber, C. D.; Zakharov, L. N.; Lonergan, M. C.; Jasti, R. Synthesis, Properties, and Design Principles of Donor–Acceptor Nanohoops. *ACS Cent. Sci.* **2015**, *1*, 335–342.

(42) Van Raden, J. M.; Darzi, E. R.; Zakharov, L. N.; Jasti, R. Synthesis and Characterization of a Highly Strained Donor–Acceptor Nanohoop. *Org. Biomol. Chem.* **2016**, *14*, 5721–5727.

(43) Kuwabara, T.; Orii, J.; Segawa, Y.; Itami, K. Curved Oligophenylenes as Donors in Shape-Persistent Donor–Acceptor Macrocycles with Solvatofluorochromic Properties. *Angew. Chem. Int. Ed.* **2015**, *54*, 9646–9649.

(44) Leonhardt, E. J.; Van Raden, J. M.; Miller, D.; Zakharov, L. N.; Alemán, B.; Jasti, R. A Bottom-Up Approach to Solution-Processed, Atomically Precise Graphitic Cylinders on Graphite. *Nano Lett.* **2018**, *18*, 7991–7997.

(45) Van Raden, J. M.; Leonhardt, E. J.; Zakharov, L. N.; Pérez-Guardiola, A.; Pérez-Jiménez, A. J.; Marshall, C. R.; Brozek, C. K.; Sancho-García, J. C.; Jasti, R. Precision Nanotube Mimics via Self-Assembly of Programmed Carbon Nanohoops. *J. Org. Chem.* **2020**, *85*, 129–141.

(46) Shudo, H.; Kuwayama, M.; Shimasaki, M.; Nishihara, T.; Takeda, Y.; Mitoma, N.; Kuwabara, T.; Yagi, A.; Segawa, Y.; Itami, K. Perfluorocycloparaphenylenes. *Nat. Commun.* **2022**, *13*, 3713.

(47) Hashimoto, S.; Kayahara, E.; Mizuhata, Y.; Tokitoh, N.; Takeuchi, K.; Ozawa, F.; Yamago, S. Synthesis and Physical Properties of Polyfluorinated Cycloparaphenylenes. *Org. Lett.* **2018**, *20*, 5973–5976.

(48) Lovell, T. C.; Colwell, C. E.; Zakharov, L. N.; Jasti, R. Symmetry Breaking and the Turn-on Fluorescence of Small, Highly Strained Carbon Nanohoops. *Chem. Sci.* **2019**, *10*, 3786–3790.

(49) Van Raden, J. M.; White, B. M.; Zakharov, L. N.; Jasti, R. Nanohoop Rotaxanes from Active Metal Template Syntheses and Their Potential in Sensing Applications. *Angew. Chem. Int. Ed.* **2019**, *58*, 7341–7345.

(50) Otteson, C. E.; Levinn, C. M.; Van Raden, J. M.; Pluth, M. D.; Jasti, R. Nanohoop Rotaxane Design to Enhance the Selectivity of Reaction-Based Probes: A Proof-of-Principle Study. *Org. Lett.* **2021**, *23*, 4608–4612.

(51) Patrick, C. W.; Woods, J. F.; Gawel, P.; Otteson, C. E.; Thompson, A. L.; Claridge, T. D. W.; Jasti, R.; Anderson, H. L. Polyyne [3]Rotaxanes: Synthesis via Dicobalt Carbonyl Complexes and Enhanced Stability. *Angew. Chem. Int. Ed.* **2022**, *61*, e202116897.

(52) May, J. H.; Van Raden, J. M.; Maust, R. L.; Zakharov, L. N.; Jasti, R. Active Template Strategy for the Preparation of π-Conjugated Interlocked Nanocarbons. *Nat. Chem.* **2023**, *15*, 170–176.

(53) Segawa, Y.; Kuwayama, M.; Hijikata, Y.; Fushimi, M.; Nishihara, T.; Pirillo, J.; Shirasaki, J.; Kubota, N.; Itami, K. Topological Molecular Nanocarbons: All-Benzene Catenane and Trefoil Knot. *Science* **2019**, *365*, 272–276.

(54) Darzi, E. R.; Jasti, R. The Dynamic, Size-Dependent Properties of [5]–[12]Cycloparaphenylenes. *Chem. Soc. Rev.* **2015**, *44*, 6401–6410.

(55) Iwamoto, T.; Watanabe, Y.; Sakamoto, Y.; Suzuki, T.; Yamago, S. Selective and Random Syntheses of [*n*]Cycloparaphenylenes (*n* = 8–13) and Size Dependence of Their Electronic Properties. *J. Am. Chem. Soc.* **2011**, *133*, 8354–8361.

(56) Schaub, T. A.; Margraf, J. T.; Zakharov, L.; Reuter, K.; Jasti, R. Strain-Promoted Reactivity of Alkyne-Containing Cycloparaphenylenes. *Angew. Chem. Int. Ed.* **2018**, *57*, 16348–16353.

(57) Blomquist, A. T.; Liu, L. H. Many-Membered Carbon Rings. VII. Cycloöctyne. *J. Am. Chem. Soc.* **1953**, *75*, 2153–2154.

(58) Jackson, E. P.; Sisto, T. J.; Darzi, E. R.; Jasti, R. Probing Diels–Alder Reactivity on a Model CNT Sidewall. *Tetrahedron* **2016**, *72*, 3754–3758.

(59) Colwell, C. E.; Price, T. W.; Stauch, T.; Jasti, R. Strain Visualization for Strained Macrocycles. *Chem. Sci.* **2020**, *11*, 3923–3930.

(60) Adamska, L.; Nayyar, I.; Chen, H.; Swan, A. K.; Oldani, N.; Fernandez-Alberti, S.; Golder, M. R.; Jasti, R.; Doorn, S. K.; Tretiak, S. Self-Trapping of Excitons, Violation of Condon Approximation, and Efficient Fluorescence in Conjugated Cycloparaphenylenes. *Nano Lett.* **2014**, *14*, 6539–6546.

(61) Horiba, J. Y. A Guide to Recording Fluorescence Quantum Yields. https://static.horiba.com/fileadmin/Horiba/Application/Materials/Material_Research/Quantum_Dots/quantumyieldstrad.pdf (accessed 2022-10-28).

(62) Gaussian 09, Revision A.02, M. J. Frisch, G. W. Trucks, H. B. Schlegel, G. E. Scuseria, M. A. Robb, J. R. Cheeseman, G. Scalmani, V. Barone, G. A. Petersson, H. Nakatsuji, X. Li, M. Caricato, A. Marenich, J. Bloino, B. G. Janesko, R. Gomperts, B. Mennucci, H. P. Hratchian, J. V. Ortiz, A. F. Izmaylov, J. L. Sonnenberg, D. Williams-

Young, F. Ding, F. Lipparini, F. Egidi, J. Goings, B. Peng, A. Petrone, T. Henderson, D. Ranasinghe, V. G. Zakrzewski, J. Gao, N. Rega, G. Zheng, W. Liang, M. Hada, M. Ehara, K. Toyota, R. Fukuda, J. Hasegawa, M. Ishida, T. Nakajima, Y. Honda, O. Kitao, H. Nakai, T. Vreven, K. Throssell, J. A. Montgomery, Jr., J. E. Peralta, F. Ogliaro, M. Bearpark, J. J. Heyd, E. Brothers, K. N. Kudin, V. N. Staroverov, T. Keith, R. Kobayashi, J. Normand, K. Raghavachari, A. Rendell, J. C. Burant, S. S. Iyengar, J. Tomasi, M. Cossi, J. M. Millam, M. Klene, C. Adamo, R. Cammi, J. W. Ochterski, R. L. Martin, K. Morokuma, O. Farkas, J. B. Foresman, and D. J. Fox, Gaussian, Inc., Wallingford CT, 2016.

(63) Gaussian 16, Revision C.01, Frisch, M. J.; Trucks, G. W.; Schlegel, H. B.; Scuseria, G. E.; Robb, M. A.; Cheeseman, J. R.; Scalmani, G.; Barone, V.; Petersson, G. A.; Nakatsuji, H.; Li, X.; Caricato, M.; Marenich, A. V.; Bloino, J.; Janesko, B. G.; Gomperts, R.; Mennucci, B.; Hratchian, H. P.; Ortiz, J. V.; Izmaylov, A. F.; Sonnenberg, J. L.; Williams-Young, D.; Ding, F.; Lipparini, F.; Egidi, F.; Goings, J.; Peng, B.; Petrone, A.; Henderson, T.; Ranasinghe, D.; Zakrzewski, V. G.; Gao, J.; Rega, N.; Zheng, G.; Liang, W.; Hada, M.; Ehara, M.; Toyota, K.; Fukuda, R.; Hasegawa, J.; Ishida, M.; Nakajima, T.; Honda, Y.; Kitao, O.; Nakai, H.; Vreven, T.; Throssell, K.; Montgomery, J. A., Jr.; Peralta, J. E.; Ogliaro, F.; Bearpark, M. J.; Heyd, J. J.; Brothers, E. N.; Kudin, K. N.; Staroverov, V. N.; Keith, T. A.; Kobayashi, R.; Normand, J.; Raghavachari, K.; Rendell, A. P.; Burant, J. C.; Iyengar, S. S.; Tomasi, J.; Cossi, M.; Millam, J. M.; Klene, M.; Adamo, C.; Cammi, R.; Ochterski, J. W.; Martin, R. L.; Morokuma, K.; Farkas, O.; Foresman, J. B.; Fox, D. J. Gaussian, Inc., Wallingford CT, 2016.

(64) Zhao, Y.; Truhlar, D. G. The M06 Suite of Density Functionals for Main Group Thermochemistry, Thermochemical Kinetics, Noncovalent Interactions, Excited States, and Transition Elements: Two New Functionals and Systematic Testing of Four M06-Class Functionals and 12 Other Functionals. *Theor. Chem. Acc.* **2008**, *120*, 215–241.

(65) Ditchfield, R.; Hehre, W. J.; Pople, J. A. Self-Consistent Molecular-Orbital Methods. IX. An Extended Gaussian-Type Basis for Molecular-Orbital Studies of Organic Molecules. *J. Chem. Phys.* **1971**, *54*, 724–728.

(66) Tomasi, J.; Mennucci, B.; Cammi, R. Quantum Mechanical Continuum Solvation Models. *Chem. Rev.* **2005**, *105*, 2999–3094.

(67) Pracht, P.; Bohle, F.; Grimme, S. Automated Exploration of the Low-Energy Chemical Space with Fast Quantum Chemical Methods. *Phys. Chem. Chem. Phys.* **2020**, *22*, 7169–7192.

(68) Kochhar, G. S.; Mosey, N. J. Differences in the Abilities to Mechanically Eliminate Activation Energies for Unimolecular and Bimolecular Reactions. *Sci. Rep.* **2016**, *6*, 23059.

(69) de Cózar, A. Diastereoselectivity on Intramolecular Alder-Ene Reaction of 1,6-Dienes. *ChemPhysChem*, e202200377.

(70) Fernández, I.; Bickelhaupt, F. M.; Cossío, F. P. Type-I Dyotropic Reactions: Understanding Trends in Barriers. *Chem. – Eur. J.* **2012**, *18*, 12395–12403.

(71) Velasco-Juárez, E.; Arpa, E. M. A Novel Partitioning Scheme for the Application of the Distortion/Interaction - Activation Strain Model to Intramolecular Reactions. *Theor. Chem. Acc.* **2021**, *140*, 107.

(72) Lopez, S. A.; Houk, K. N. Alkene Distortion Energies and Torsional Effects Control Reactivities, and Stereoselectivities of Azide Cycloadditions to Norbornene and Substituted Norbornenes. *J. Org. Chem.* **2013**, *78*, 1778–1783.

(73) Liu, F.; Paton, R. S.; Kim, S.; Liang, Y.; Houk, K. N. Diels–Alder Reactivities of Strained and Unstrained Cycloalkenes with Normal and Inverse-Electron-Demand Dienes: Activation Barriers and Distortion/Interaction Analysis. *J. Am. Chem. Soc.* **2013**, *135*, 15642–15649.

(74) Paton, R. S.; Kim, S.; Ross, A. G.; Danishefsky, S. J.; Houk, K. N. Experimental Diels–Alder Reactivities of Cycloalkenones and Cyclic Dienes Explained through Transition-State Distortion Energies. *Angew. Chem. Int. Ed.* **2011**, *50*, 10366–10368.

(75) Lopez, S. A.; Munk, M. E.; Houk, K. N. Mechanisms and Transition States of 1,3-Dipolar Cycloadditions of Phenyl Azide with Enamines: A Computational Analysis. *J. Org. Chem.* **2013**, *78*, 1576–1582.

(76) Fell, J. S.; Martin, B. N.; Houk, K. N. Origins of the Unfavorable Activation and Reaction Energies of 1-Azadiene Heterocycles Compared to 2-Azadiene Heterocycles in Diels–Alder Reactions. *J. Org. Chem.* **2017**, *82*, 1912–1919.

(77) Ess, D. H.; Jones, G. O.; Houk, K. N. Conceptual, Qualitative, and Quantitative Theories of 1,3-Dipolar and Diels–Alder Cycloadditions Used in Synthesis. *Adv. Synth. Catal.* **2006**, *348*, 2337–2361.

(78) Houk, K. N. Frontier Molecular Orbital Theory of Cycloaddition Reactions. *Acc. Chem. Res.* **1975**, *8*, 361–369.

(79) Houk, K. N.; Sims, Joyner.; Duke, R. E.; Strozier, R. W.; George, J. K. Frontier Molecular Orbitals of 1,3 Dipoles and Dipolarophiles. *J. Am. Chem. Soc.* **1973**, *95*, 7287–7301.

(80) Houk, K. N.; Sims, Joyner.; Watts, C. R.; Luskus, L. J. Origin of Reactivity, Regioselectivity, and Periselectivity in 1,3-Dipolar Cycloadditions. *J. Am. Chem. Soc.* **1973**, *95*, 7301–7315.

(81) Schoenebeck, F.; Ess, D. H.; Jones, G. O.; Houk, K. N. Reactivity and Regioselectivity in 1,3-Dipolar Cycloadditions of Azides to Strained Alkynes and Alkenes: A Computational Study. *J. Am. Chem. Soc.* **2009**, *131*, 8121–8133.

(82) Houk, K. N.; Paddon-Row, M. N.; Rondan, N. G.; Wu, Y.-D.; Brown, F. K.; Spellmeyer, D. C.; Metz, J. T.; Li, Y.; Loncharich, R. J. Theory and Modeling of Stereoselective Organic Reactions. *Science* **1986**, *231*, 1108–1117.

(83) Ess, D. H.; Houk, K. N. Theory of 1,3-Dipolar Cycloadditions: Distortion/Interaction and Frontier Molecular Orbital Models. *J. Am. Chem. Soc.* **2008**, *130*, 10187–10198.

(84) Bruno, N. C.; Tudge, M. T.; Buchwald, S. L. Design and Preparation of New Palladium Precatalysts for C–C and C–N Cross-Coupling Reactions. *Chem. Sci.* **2013**, *4*, 916–920.

(85) Pangborn, A. B.; Giardello, M. A.; Grubbs, R. H.; Rosen, R. K.; Timmers, F. J. Safe and Convenient Procedure for Solvent Purification. *Organometallics* **1996**, *15*, 1518–1520.

(86) Ball, M.; Zhong, Y.; Fowler, B.; Zhang, B.; Li, P.; Etkin, G.; Paley, D. W.; Decatur, J.; Dalsania, A. K.; Li, H.; Xiao, S.; Ng, F.; Steigerwald, M. L.; Nuckolls, C. Macrocyclization in the Design of Organic N-Type Electronic Materials. *J. Am. Chem. Soc.* **2016**, *138*, 12861–12867.

(87) Majewski, M. A.; Stępień, M. Bowls, Hoops, and Saddles: Synthetic Approaches to Curved Aromatic Molecules. *Angew. Chem. Int. Ed.* **2019**, *58*, 86–116.

(88) Xia, J.; Bacon, J. W.; Jasti, R. Gram-Scale Synthesis and Crystal Structures of [8]- and [10]CPP, and the Solid-State Structure of C60@[10]CPP. *Chem. Sci.* **2012**, *3*, 3018–3021.

(89) Iwamoto, T.; Watanabe, Y.; Sadahiro, T.; Haino, T.; Yamago, S. Size-Selective Encapsulation of C60 by [10]Cycloparaphenylene: Formation of the Shortest Fullerene-Peapod. *Angew. Chem. Int. Ed.* **2011**, *50*, 8342–8344.

(90) Iwamoto, T.; Watanabe, Y.; Takaya, H.; Haino, T.; Yasuda, N.; Yamago, S. Size- and Orientation-Selective Encapsulation of C70 by Cycloparaphenylenes. *Chem. – Eur. J.* **2013**, *19*, 14061–14068.

(91) Ueno, H.; Nishihara, T.; Segawa, Y.; Itami, K. Cycloparaphenylene-Based Ionic Donor–Acceptor Supramolecule: Isolation and Characterization of Li$^+$@C60⊂[10]CPP. *Angew. Chem. Int. Ed.* **2015**, *54*, 3707–3711.

(92) Hashimoto, S.; Iwamoto, T.; Kurachi, D.; Kayahara, E.; Yamago, S. Shortest Double-Walled Carbon Nanotubes Composed of Cycloparaphenylenes. *ChemPlusChem* **2017**, *82*, 1015–1020.

(93) Xu, Y.; Wang, B.; Kaur, R.; Minameyer, M. B.; Bothe, M.; Drewello, T.; Guldi, D. M.; von Delius, M. A Supramolecular [10]CPP Junction Enables Efficient Electron Transfer in Modular Porphyrin–[10]CPP⊃Fullerene Complexes. *Angew. Chem. Int. Ed.* **2018**, *57*, 11549–11553.

(94) Schaub, T. A.; Zieleniewska, A.; Kaur, R.; Minameyer, M.; Yang, W.; Schüßlbauer, C. M.; Zhang, L.; Freiberger, M.; Zakharov, L. N.; Drewello, T.; Dral, P. O.; Guldi, D. M.; Jasti, R. Tunable Macrocyclic Polyparaphenylene Nanolassos via Copper-Free Click Chemistry. *Chem. – Eur. J.* **2023**, *29*, e202300668.

(95) Fehr, J. M.; Myrthil, N.; Garrison, A. L.; Price, T. W.; Lopez, S. A.; Jasti, R. Experimental and Theoretical Elucidation of SPAAC Kinetics for Strained Alkyne-Containing Cycloparaphenylenes. *Chem. Sci.* **2023**, *14*, 2839–2848.

(96) Matsui, K.; Segawa, Y.; Namikawa, T.; Kamada, K.; Itami, K. Synthesis and Properties of All-Benzene Carbon Nanocages: A Junction Unit of Branched Carbon Nanotubes. *Chem. Sci.* **2012**, *4*, 84–88.

(97) Matsui, K.; Segawa, Y.; Itami, K. All-Benzene Carbon Nanocages: Size-Selective Synthesis, Photophysical Properties, and Crystal Structure. *J. Am. Chem. Soc.* **2014**, *136*, 16452–16458.

(98) Kayahara, E.; Iwamoto, T.; Takaya, H.; Suzuki, T.; Fujitsuka, M.; Majima, T.; Yasuda, N.; Matsuyama, N.; Seki, S.; Yamago, S. Synthesis and Physical Properties of a Ball-like Three-Dimensional π-Conjugated Molecule. *Nat. Commun.* **2013**, *4*, 2694.

(99) Hayase, N.; Nogami, J.; Shibata, Y.; Tanaka, K. Synthesis of a Strained Spherical Carbon Nanocage by Regioselective Alkyne Cyclotrimerization. *Angew. Chem. Int. Ed.* **2019**, *58*, 9439–9442.

(100) Li, P.; Zakharov, L. N.; Jasti, R. A Molecular Propeller with Three Nanohoop Blades: Synthesis, Characterization, and Solid-State Packing. *Angew. Chem. Int. Ed.* **2017**, *56*, 5237–5241.

(101) Schaub, T. A.; Prantl, E. A.; Kohn, J.; Bursch, M.; Marshall, C. R.; Leonhardt, E. J.; Lovell, T. C.; Zakharov, L. N.; Brozek, C. K.; Waldvogel, S. R.; Grimme, S.; Jasti, R. Exploration of the Solid-State Sorption Properties of Shape-Persistent Macrocyclic Nanocarbons as Bulk Materials and Small Aggregates. *J. Am. Chem. Soc.* **2020**, *142*, 8763–8775.

(102) Holst, J. R.; Trewin, A.; Cooper, A. I. Porous Organic Molecules. *Nat. Chem.* **2010**, *2*, 915–920.

(103) Alonso, J. M.; Díaz-Álvarez, A. E.; Criado, A.; Pérez, D.; Peña, D.; Guitián, E. [16]Cloverphene: A Clover-Shaped Cata-Condensed Nanographene with Sixteen Fused Benzene Rings. *Angew. Chem. Int. Ed.* **2012**, *51*, 173–177.

(104) Soe, W.-H.; Manzano, C.; Renaud, N.; De Mendoza, P.; De Sarkar, A.; Ample, F.; Hliwa, M.; Echavarren, A. M.; Chandrasekhar, N.; Joachim, C. Manipulating Molecular Quantum States with Classical Metal Atom Inputs: Demonstration of a Single Molecule NOR Logic Gate. *ACS Nano* **2011**, *5*, 1436–1440.

(105) Reppe, W.; Schlichting, O.; Klager, K.; Toepel, T. Cyclisierende Polymerisation von Acetylen I Über Cyclooctatetraen. *Justus Liebigs Ann. Chem.* **1948**, *560*, 1–92.

(106) Kotha, S.; Brahmachary, E.; Lahiri, K. Transition Metal Catalyzed [2+2+2] Cycloaddition and Application in Organic Synthesis. *Eur. J. Org. Chem.* **2005**, *2005*, 4741–4767.

(107) Shen, X.; Ho, D. M.; Pascal, R. A. Synthesis of Polyphenylene Dendrimers Related to "Cubic Graphite." *J. Am. Chem. Soc.* **2004**, *126*, 5798–5805.

(108) Xiao, W.; Feng, X.; Ruffieux, P.; Gröning, O.; Müllen, K.; Fasel, R. Self-Assembly of Chiral Molecular Honeycomb Networks on Au(111). *J. Am. Chem. Soc.* **2008**, *130*, 8910–8912.

(109) Kobayashi, K.; Kobayashi, N.; Ikuta, M.; Therrien, B.; Sakamoto, S.; Yamaguchi, K. Syntheses of Hexakis(4-Functionalized-Phenyl)Benzenes and Hexakis[4-(4‘-Functionalized- Phenylethynyl)Phenyl]Benzenes Directed to Host Molecules for Guest-Inclusion Networks. *J. Org. Chem.* **2005**, *70*, 749–752.

(110) Gobbo, P.; Romagnoli, T.; Barbon, S. M.; Price, J. T.; Keir, J.; Gilroy, J. B.; Workentin, M. S. Expanding the Scope of Strained-Alkyne Chemistry: A Protection–Deprotection Strategy via the Formation of a Dicobalt–Hexacarbonyl Complex. *Chem. Commun.* **2015**, *51*, 6647–6650.

(111) Kumar, P.; Louie, J. Nickel-Mediated [2 + 2 + 2] Cycloaddition. In *Transition-Metal-Mediated Aromatic Ring Construction*; John Wiley & Sons, Ltd, 2013; pp 37–70.

(112) Stará, I. G.; Starý, I.; Kollárovič, A.; Teplý, F.; Vyskočil, Š.; Šaman, D. Transition Metal Catalysed Synthesis of Tetrahydro Derivatives of [5]-, [6]- and [7]Helicene. *Tetrahedron Lett.* **1999**, *40*, 1993–1996.

(113) Teplý, F.; Stará, I. G.; Starý, I.; Kollárovič, A.; Šaman, D.; Rulíšek, L.; Fiedler, P. Synthesis of [5]-, [6]-, and [7]Helicene via Ni(0)- or Co(I)-Catalyzed Isomerization of Aromatic Cis,Cis-Dienetriynes. *J. Am. Chem. Soc.* **2002**, *124*, 9175–9180.

(114) Tanaka, K. Rhodium-Mediated [2 + 2 + 2] Cycloaddition. In *Transition-Metal-Mediated Aromatic Ring Construction*; John Wiley & Sons, Ltd, 2013; pp 127–160.

(115) Pla-Quintana, A.; Roglans, A. The Choice of Rhodium Catalysts in [2+2+2] Cycloaddition Reaction: A Personal Account. *Molecules* **2022**, *27*, 1332.

(116) Peña, D.; Escudero, S.; Pérez, D.; Guitián, E.; Castedo, L. Efficient Palladium-Catalyzed Cyclotrimerization of Arynes: Synthesis of Triphenylenes. *Angew. Chem. Int. Ed.* **1998**, *37*, 2659–2661.

(117) Peña, D.; Pérez, D.; Guitián, E. Cyclotrimerization Reactions of Arynes and Strained Cycloalkynes. *Chem. Rec.* **2007**, *7*, 326–333.

(118) Lovell, T. C.; Garrison, Z. R.; Jasti, R. Synthesis, Characterization, and Computational Investigation of Bright Orange-Emitting Benzothiadiazole [10]Cycloparaphenylene. *Angew. Chem. Int. Ed.* **2020**, *59*, 14363–14367.

(119) Barnsley, J. E.; Shillito, G. E.; Mapley, J. I.; Larsen, C. B.; Lucas, N. T.; Gordon, K. C. Walking the Emission Tightrope: Spectral and Computational Analysis of Some Dual-Emitting Benzothiadiazole Donor–Acceptor Dyes. *J. Phys. Chem. A* **2018**, *122*, 7991–8006.

(120) Caspar, J. V.; Meyer, T. J. Application of the Energy Gap Law to Nonradiative, Excited-State Decay. *J. Phys. Chem.* **1983**, *87*, 952–957.

(121) Lovell, T. C.; Fosnacht, K. G.; Colwell, C. E.; Jasti, R. Effect of Curvature and Placement of Donor and Acceptor Units in Cycloparaphenylenes: A Computational Study. *Chem. Sci.* **2020**, *11*, 12029–12035.

(122) Pengshung, M.; Neal, P.; Atallah, T. L.; Kwon, J.; Caram, J. R.; Lopez, S. A.; Sletten, E. M. Silicon Incorporation in Polymethine Dyes. *Chem. Commun.* **2020**, *56*, 6110–6113.

(123) Weissleder, R. A Clearer Vision for in Vivo Imaging. *Nat. Biotechnol.* **2001**, *19*, 316–317.

(124) Jun, Y. W.; Kim, H. R.; Reo, Y. J.; Dai, M.; Ahn, K. H. Addressing the Autofluorescence Issue in Deep Tissue Imaging by Two-Photon Microscopy: The Significance of Far-Red Emitting Dyes. *Chem. Sci.* **2017**, *8*, 7696–7704.

(125) Hodgson, S. M.; McNelles, S. A.; Abdullahu, L.; Marozas, I. A.; Anseth, K. S.; Adronov, A. Reproducible Dendronized PEG Hydrogels via SPAAC Cross-Linking. *Biomacromolecules* **2017**, *18*, 4054–4059.

(126) Meichsner, E.; Fong, D.; Ritaine, D. E. M.; Adronov, A. Strain-promoted Azide-alkyne Cycloaddition Polymerization as a Route toward Tailored Functional Polymers. *J. Polym. Sci.* **2021**, *59*, 29–33.

(127) Wong, M. Y.; Zysman-Colman, E. Purely Organic Thermally Activated Delayed Fluorescence Materials for Organic Light-Emitting Diodes. *Adv. Mater.* **2017**, *29*, 1605444.

(128) Chen, D.; Wada, Y.; Kusakabe, Y.; Sun, L.; Kayahara, E.; Suzuki, K.; Tanaka, H.; Yamago, S.; Kaji, H.; Zysman-Colman, E. A Donor–Acceptor 10-Cycloparaphenylene

and Its Use as an Emitter in an Organic Light-Emitting Diode. *Org. Lett.* **2023**, *25*, 998–1002.